



# UNIVERSITÀ DEGLI STUDI DI TRIESTE

## XXX CICLO DEL DOTTORATO DI RICERCA IN NANOTECNOLOGIE

### Adsorption and interaction of atoms, molecules and nanoclusters on epitaxial graphene.

Settore scientifico-disciplinare: **FIS/03 Fisica della Materia**

DOTTORANDO  
**Francesco PRESEL**

COORDINATORE  
**Prof.ssa Lucia PASQUATO**

SUPERVISORE DI TESI  
**Prof. Alessandro BARALDI**

**ANNO ACCADEMICO 2016/2017**





## UNIVERSITY OF TRIESTE

---

Department of Physics  
Graduate School in Nanotechnology, Cycle 30

### PhD Thesis

Adsorption and interaction of atoms, molecules and nanoclusters on epitaxial graphene.

Supervisor:  
Prof. Alessandro Baraldi

Candidate:  
Francesco Presel

Coordinator:  
Prof. Lucia Pasquato

---

Academic Year 2016-2017





## Abstract

The research activity I have performed during my PhD was centred on the study of several aspects of the interaction of graphene with surfaces and adsorbates including atoms and molecules. In particular, I have investigated how the latter is modified by a metal substrate supporting graphene. The unique electronic and mechanical properties of graphene make it an ideal candidate for applications in high efficiency nanoelectronic devices. However, these properties are modified when it interacts with such species, and this represents one of the major issues still preventing its wide-spread adoption.

For this reason, in the first phase of my research I have investigated the factors which govern the intensity of the graphene-substrate interaction. In particular, by characterising and comparing the properties of several graphene/metal interfaces, I have shown that the interaction occurring between them is due to the coupling of the  $d$ -band of the substrate with the  $\pi$  band of graphene.

Following this, I have investigated the interaction between small inorganic molecules (such as CO) and atoms (Ar) with metal-supported graphene. My results show that these interactions, which are based on van der Waals forces, increase when graphene is supported on a strongly interacting surface. In collaboration with computational scientists, I have shown that the main factor influencing the adsorption energy of CO on graphene is the chemical composition of the substrate's topmost layer, while the distance between graphene and the substrate plays a negligible role. This proves that this increased adsorption energy is due to the modifications induced by the substrate on the bands of graphene by their coupling with the substrate's  $d$ -band. A contribution due to the transparency of graphene to van der Waals interaction, which had been proposed by some works in literature, could instead be refuted.

Another issue related to the wide-scale application of graphene which I have addressed here is the cost-effectiveness of its synthesis. In particular, part of my research work was dedicated to the identification of the factors which can be address to improve the existing synthesis techniques. More in detail, I have demonstrated the important role of the adsorption energy of atoms and small clusters of carbon on graphene on the dynamics of its growth, and therefore on the quality of the final product.

Finally, I have studied some possible applications which exploit the modifications induced by the interaction of graphene with its substrate and with species adsorbed on it on the properties of the latter, in fields such as magnetism and catalysis. More in detail, I have studied the dynamics leading to a magnetic superexchange between graphene supported on a magnetic material and molecular adsorbates. Furthermore, I have characterised the geometric and electronic structure of titania nanoparticles supported on different graphene/substrate interfaces, which have shown a 20-fold increase in their photocatalytic activity with respect to a graphene-less control system.

In parallel to these activities, I have worked on the development of a mass-selected nanocluster source, whose final aim is to allow the characterisation of the properties of nanoclusters as a function of their mass with space-averaging experimental techniques. To improve my knowledge on this kind of apparatus, I have made a 3-month traineeship (within the Erasmus + project) at the Chemistry Department of Technische Universität München, where I have worked on the commissioning of an analogous device.



## Sommario

L'attività di ricerca del mio dottorato è stata dedicata allo studio di diversi aspetti dell'interazione del grafene con superfici e con adsorbati quali atomi e molecole e di come quest'ultima sia modificata da un substrato metallico sotto il grafene. Le proprietà elettroniche e meccaniche uniche del grafene lo rendono un candidato ideale per lo sviluppo di dispositivi nanoelettronici ad alta efficienza. Tuttavia, le modifiche indotte alle proprietà del grafene dalla sua interazione con tali specie sono uno dei principali problemi che impediscono un suo utilizzo su scala industriale.

Pertanto, la prima fase della mia ricerca ha riguardato l'identificazione dei fattori che governano l'intensità dell'interazione grafene-substrato. In particolare, studiando e confrontando le proprietà di diverse interfacce grafene/metallo, ho dimostrato che l'interazione fra di essi dipende dall'accoppiamento fra la banda  $d$  della superficie metallica e la banda  $\pi$  del grafene.

La fase successiva della mia ricerca è stata dedicata allo studio dell'interazione di piccole molecole inorganiche (principalmente CO) ed atomi (Ar) con grafene supportato su diverse superfici metalliche. I miei risultati dimostrano che le interazioni di van der Waals tra il grafene ed i suoi adsorbati sono aumentate in presenza di un substrato fortemente interagente. Grazie ad una collaborazione con ricercatori del campo della fisica computazionale, ho dimostrato che il fattore che influenza maggiormente l'energia di adsorbimento del CO sul grafene è la composizione chimica dello strato superficiale del substrato metallico, mentre la distanza tra grafene e substrato ha un effetto molto più ridotto. Questo dimostra che l'aumento dell'energia di adsorbimento è originata dalle alterazioni indotte nelle bande del grafene dal loro accoppiamento con la banda  $d$  del substrato e non, come sostenuto da diverse fonti in letteratura, da una trasparenza del grafene alle interazioni di van der Waals.

Un altro limite alla possibilità di utilizzare il grafene su scala industriale dipende dai suoi elevati costi di produzione, rispetto alla qualità ottenuta. Ho pertanto dedicato una parte del mio lavoro di tesi anche allo studio delle tecniche di crescita del grafene su superfici metalliche, con lo scopo di identificare i possibili margini di miglioramento. Nello specifico, ho dimostrato che l'energia di adsorbimento di atomi e piccoli cluster di carbonio riveste un ruolo importante già nel determinare le dinamiche di crescita del grafene, e conseguentemente la qualità e le proprietà del prodotto.

Infine, ho studiato alcune possibili applicazioni delle modifiche indotte dall'interazione del grafene con il substrato e con specie adsorbite su di esso in alcuni campi quali il magnetismo e la catalisi. In particolare, ho studiato le dinamiche del superscambio magnetico che si instaura quando il grafene è supportato su un materiale magnetico fra quest'ultimo e le specie adsorbite sul grafene. Inoltre, ho caratterizzato la struttura geometrica ed elettronica di nanoparticelle di titania supportate sul grafene, per le quali il grafene porta ad un aumento dell'attività fotocatalitica di un ordine di grandezza.

In parallelo a queste attività, mi sono dedicato anche allo sviluppo di una sorgente di nanocluster selezionati in massa, il cui fine è di permetterne lo studio con tecniche sperimentali mediate nello spazio. Per ampliare le mie conoscenze su questo tipo di strumenti, ho svolto un tirocinio di tre mesi (nell'ambito del programma Erasmus + Traineeship) presso il Dipartimento di Chimica della Technische Universität München, dove ho partecipato alla messa in funzione di uno strumento analogo.



# Contents

<b>Introduction</b>	<b>1</b>
References . . . . .	6
<b>1 Experimental techniques and setup</b>	<b>11</b>
1.1 Sample cleaning and preparation . . . . .	12
1.1.1 Graphene growth on Ir (1 1 1) and other metal surfaces . . . . .	12
1.2 Low Energy Electron Diffraction . . . . .	13
1.2.1 Spot Profile Analysis-LEED . . . . .	16
1.3 Near Edge X-ray Absorption Fine Structure . . . . .	17
1.4 Core-level Photoelectron Spectroscopy . . . . .	20
1.5 Experimental setup . . . . .	24
1.5.1 Surface Science Laboratory . . . . .	25
1.5.2 SuperESCA beamline . . . . .	26
1.6 Density Functional Theory calculations . . . . .	27
References . . . . .	28
<b>2 Factors controlling the Gr-metal interaction</b>	<b>31</b>
2.1 Graphene growth on Ir (1 1 1) . . . . .	33
2.2 Graphene growth on Ru (0 0 0 1) . . . . .	34
2.2.1 Details on the Ru 3d and C 1s spectra analysis . . . . .	34
2.3 Intercalation of metallic monolayers below graphene . . . . .	37
2.3.1 Intercalation procedure . . . . .	37
2.3.2 Experimental results . . . . .	39
2.3.3 Theoretical calculations . . . . .	43
2.3.4 Discussion . . . . .	48
Conclusions . . . . .	49
References . . . . .	51
<b>3 Adsorption of atoms and molecules on Gr</b>	<b>55</b>
3.1 Carbon monoxide adsorption on supported Gr . . . . .	57
3.1.1 Experimental details . . . . .	57
3.1.2 Experimental results . . . . .	58
3.1.3 Theoretical results . . . . .	67
3.1.4 Discussion . . . . .	71
3.2 Noble gas atomic adsorption on graphene: the case of argon . . . . .	73
3.2.1 Argon adsorption on Gr/Ir (1 1 1) . . . . .	73
3.2.2 Argon adsorption on Gr/Co/Ir (1 1 1) . . . . .	77
3.2.3 Discussion . . . . .	78
3.3 Water adsorption on graphene: the role of inter-molecular forces . . . . .	79
Conclusion . . . . .	81
References . . . . .	83

<b>4</b>	<b>Magnetic coupling between graphene-supported molecules and the substrate: the case of metal-phthalocyanines.</b>	<b>89</b>
4.1	Experimental details . . . . .	91
4.2	Experimental results . . . . .	92
4.3	Discussion . . . . .	96
	Conclusion . . . . .	96
	References . . . . .	98
<b>5</b>	<b>Dynamics of single- and multi-layer graphene growth on Ir(1 1 1) using Molecular Beam Epitaxy</b>	<b>101</b>
5.1	Characterisation of the feedstock delivered by the solid state carbon source . . . . .	102
5.1.1	Experimental details and data analysis procedure . . . . .	103
5.1.2	Theoretical results . . . . .	106
5.1.3	Experimental results . . . . .	107
5.1.4	Discussion . . . . .	109
5.2	Dynamics of temperature-programmed MBE graphene growth . . . . .	111
5.3	Dynamics of high-temperature MBE graphene growth . . . . .	112
5.3.1	Experimental details and data analysis procedure . . . . .	112
5.3.2	Experimental results . . . . .	115
5.3.3	Discussion . . . . .	118
	Conclusion . . . . .	122
	References . . . . .	124
<b>6</b>	<b>Graphene-supported nanoclusters and nanoparticles: the role of the substrate</b>	<b>129</b>
6.1	Gr-titania nanoarchitectures for enhanced photocatalytic applications . . . . .	131
6.1.1	Experimental methods . . . . .	134
6.1.2	Experimental results . . . . .	135
6.1.3	Discussion . . . . .	143
	Conclusion . . . . .	144
	References . . . . .	145
<b>7</b>	<b>Development and characterization of a mass-selected nanocluster source</b>	<b>149</b>
7.1	Cluster source operating principles . . . . .	151
7.1.1	Nanocluster production . . . . .	151
7.1.2	Mass-selection of nanoclusters . . . . .	153
7.1.3	Differential pumping and nanocluster transport . . . . .	154
7.2	Design of the nanocluster source . . . . .	157
7.3	Characterisation of the nanocluster source . . . . .	158
7.3.1	Commissioning of the Surface Science Laboratory cluster source . . . . .	158
7.3.2	Set-up and commissioning of the cluster source at Technische Universität München	160
	References . . . . .	164
	<b>Conclusion</b>	<b>165</b>

# Introduction

Graphene (Gr), the two-dimensional allotrope of carbon, has attracted a great deal of interest among the scientific community in the last ten years, even though theoretical and experimental studies on this material had already been carried out for decades before. In fact, the first calculations of the electronic structure of single layers of graphite date back to 1947<sup>1</sup>, and Gr had been experimentally realized possibly as early as 1962<sup>2,3</sup>. Moreover, it had been observed on several metal surfaces already in the late 1960s, when it was identified as “single layer graphite”<sup>4,5</sup>. However, it was only reproducibly synthesized and characterized in its free-standing state and its outstanding properties discovered at the beginning of the 21<sup>st</sup> century<sup>6</sup>.

Gr is composed of  $sp^2$ -bonded carbon atoms, arranged on a hexagonal Bravais lattice whose lattice parameter is 2.46 Å; the unit cell contains two non-equivalent atoms, forming a honeycomb lattice whose side is 1.42 Å in length, shown in Figure 1.

The unique electronic structure of Gr (see Figure 2) is a consequence of the symmetries of its lattice, and is characterized by a zero-width direct band-gap at the K and K' points of the Brillouin zone<sup>1</sup>. Furthermore, for an ideal free-standing Gr layer, both the valence and conduction bands, which correspond to the  $\pi$  and  $\pi^*$  bands, display a linear dispersion around this point. This relation leads to a structure known as Dirac cones (see Figure 2), whose crossing point (known as Dirac point) is located at the K and K' points of the Brillouin zone and corresponds to the Fermi Energy. A consequence of this peculiar linear band dispersion is that charge carriers display the relativistic behaviour of massless Dirac fermions<sup>7,8</sup>.

Thanks to its unique electronic structure, Gr displays several peculiar phenomena, such as the anomalous quantum Hall effect, the ballistic charge transport, an extremely high electron mobility, and the electric field effect<sup>6,9,10</sup>. Beside these outstanding electronic properties, Gr has also remarkable mechanical properties – having the highest Young modulus among the known materials<sup>11</sup> –, is almost transparent to visible light<sup>12</sup>, and is characterised by a high thermal<sup>13</sup> and chemical<sup>14</sup> stability. Its unique electrical transport properties and the possibility to accurately tune its doping – not only by using substitutional

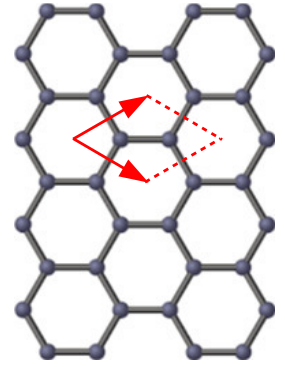


**Figure 1:** Crystal lattice of Gr. The unit cell is indicated in red.

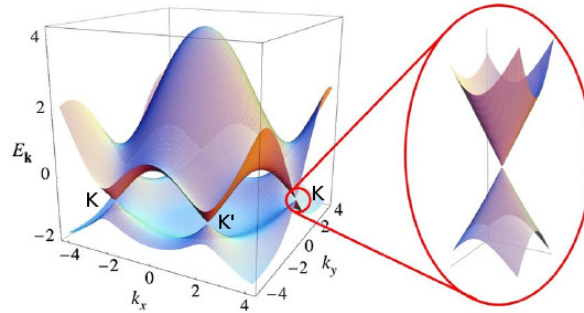


**Figure 2:** Band structure of Gr<sup>8</sup>. A zoom of the band structure around one of the Dirac points is shown in inset.

impurities but also through adsorbates<sup>15</sup> – can be exploited for innovative nanoscale devices, including high-frequency transistors and transparent and flexible electronics<sup>16,17</sup>, as well as single-molecule gas sensors<sup>18</sup>.

Thanks to these properties, it is widely believed that Gr might replace silicon as the main material for electronic devices<sup>16</sup>. However, there are several open questions and ongoing issues which still prevent its widespread adoption. In particular, for such a new technology to be adopted by industry, it must overtake the current industrial standard in efficiency and performance by at least an order of magnitude, while remaining cost effective<sup>19</sup>. Currently, very high-quality Gr can indeed be produced, which is able to significantly outperform silicon-based electronics, yet its production costs are not yet competitive nor suitable for mass production. For this reason, there is ongoing research on the techniques by which Gr is produced, in order to improve the quality and cost-effectiveness of the product<sup>20</sup>: this is therefore one of the issues which I have addressed during my PhD research work, by characterising the growth of Gr by different approaches to shed light on their main advantages and drawbacks.

There are, in fact, several known methods which allow the synthesis of Gr layers having different characteristics and properties, as shown in Figure 3. They are typically divided into three main groups<sup>16</sup>:

- exfoliation from graphite;
- catalytic growth on metallic surfaces;
- graphitization of silicon carbide.

Each of these can be further divided into several individual techniques: for example, the exfoliation procedure can be achieved using either mechanical or chemical methods, either dry or in solution<sup>6,21,22</sup>; the catalytic growth can be performed using precursors in different states and can either include chemical reactions in the precursors (Chemical Vapour Deposition techniques, CVD) or not (Molecular Beam Epitaxy, MBE). Gr has been even grown from the diffusion across a piece of metal of carbon atoms from organic waste placed in contact with it<sup>23</sup>.

The yield and applicability of each technique are very different, as well as their cost per surface area of Gr<sup>16,19</sup>. In particular, the density and the type of defects found in the product – such as mono- and di-vacancies, disclinations, dislocations, translational and rotational domain boundaries – is strongly determined by the method employed for Gr synthesis, and these defects can have significant effects on several properties of Gr, for example by reducing the electron mobility, weakening the mechanical resistance, and enhancing the chemical reactivity of Gr. In this respect, no technique has yet been found, which will perform better regardless of the target application; a compromise must always be chosen between cost and quality depending on the intended application.

Among the synthesis techniques, mechanical graphite exfoliation has long been known to produce very high quality Gr, yet is not easily scalable<sup>3,17</sup>. The ability to grow Gr at near-ambient pressure using CVD on polycrystalline copper surfaces<sup>24</sup>, on the other hand, has introduced a very promising method to obtain large Gr layers (with surfaces larger than a squared metre), with a relatively high quality and at a cost accessible by hi-tech industries. However, the main limitation of this method is the fact that CVD Gr growth can only be directly performed on a small number of metallic surfaces: therefore, if Gr is required to be supported on a different surface (for example a semiconductor or insulator), it is necessary to detach the as-grown Gr layer from its substrate and transfer it<sup>25</sup>, a process which can negatively impact on its quality<sup>26</sup>. A further drawback of the combined CVD-transfer method is that impurities including small amounts of the original copper substrate are transferred together with Gr: this makes this process unusable in those fields where extremely low concentrations of contaminants are required, such as in

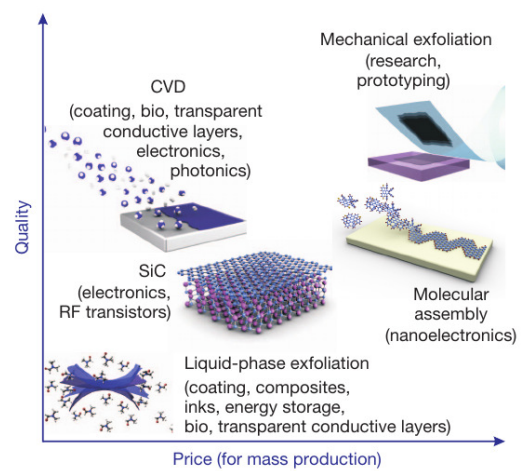


**Figure 3:** Schematic comparison of the main advantages and drawbacks of different Gr growth methods<sup>16</sup>.



the fields of micro- and nanoelectronics industry<sup>27,28</sup>. In this respect, the ability to grow high-quality Gr directly supported on a wider variety of surfaces, including semiconductors and insulators, would represent a decisive step towards the use of Gr for advanced electronic applications; a possible approach to achieve this aim is the development of new growth techniques such as Molecular Beam Epitaxy from solid state carbon sources<sup>29–31</sup>.

Finally, a very important feature of some of these methods is the possibility to precisely control the number of layers in the product. For example, chemical exfoliation procedures are known to produce a distribution of single-, bi- and multi-layer Gr, whereas for most applications Gr with a precise number of layers is required. On the other hand, CVD growth of Gr is usually a self-terminating technique which can produce pure single-layer Gr, however, it cannot produce extended areas of bi- or multi-layer<sup>24,32,33</sup>.

Another problem for the application of Gr in electronic devices which I have addressed in this work arises from its interaction with the underlying supporting substrates, such as metals or semiconductors. In fact, due to the low density of states of Gr close to the Fermi level, even a relatively small charge transfer can introduce a significant degree of doping, which moves the Dirac point away from the Fermi level<sup>3</sup>. Moreover, the lattice parameter of Gr will be in general different from that of the supporting substrate: this can lead to a deformation of Gr's lattice to become commensurate to that of the substrate – which in any case is at most of the order of 1%, due to the stiffness of C-C bonds – and to the tendency of Gr to grow along particular crystallographic directions with respect to those of the substrate<sup>34,35</sup>. In these cases, the superposition of the two crystal lattices, of Gr and its substrate, can form moiré structures, characterised by a periodicity which is several times (typically around 10 times, in each direction) larger than each of the unit cells<sup>3,34</sup>. These carbon layers often show a corrugation, where some portions of the moiré cell can be closer to the surface than the furthest almost by a factor 2. The corrugation of these structures can negatively affect Gr applications in fields such as nanoelectronics, since it leads to Gr having very different properties on the local scale. On the other hand, corrugated Gr can be exploited as highly ordered, nanoscale patterns over which nanostructures can be synthesized with high reproducibility. For example, Gr has proved effective for the synthesis of ordered layers of nanoclusters of controlled size<sup>36</sup> and molecules<sup>37</sup>. Buckled, metal-supported Gr is therefore a particularly promising substrate for catalytic active phases, since it reduces the mobility of supported nanoparticles and clusters (therefore reducing their sintering)<sup>38,39</sup>, allowing to maintain a high surface-to-bulk ratio even at high temperatures.

Besides the substrate, also the interaction of Gr with adsorbates can affect its properties, even though this interaction depends significantly, if not exclusively, on van der Waals (vdW) forces<sup>14,40–42</sup>. In particular, these interactions can introduce doping into Gr, and in some cases disrupt the Dirac cones<sup>15,43</sup>. These modifications can negatively affect the performance of its electronic applications<sup>15,44</sup>. This is particularly important since most Gr applications require it to be used in the atmosphere, therefore exposed to moisture, which is known to reduce carrier mobility in Gr<sup>44</sup>. Moreover, in order to integrate Gr within common electronics, metallic contacts need to be employed: their effects on Gr also have to be correctly taken into account to ensure Gr-based devices behave as expected<sup>45,46</sup>.

Some approaches have been investigated to be able to preserve the properties of Gr for everyday applications. For example, a possible solution to prevent the adsorption of contaminants is to encapsulate it inside an insulating material (such as hBN)<sup>10</sup>, however, the interaction with this envelope can affect the properties of Gr as well<sup>47–49</sup>. A decoupling of Gr from metallic substrates can be achieved by intercalating oxygen at the Gr-metal interface, and thereby passivating the substrate<sup>50–52</sup>. In addition, the development of an oxide film at the Gr-metal interface can also electrically insulate Gr from its substrate<sup>53,54</sup>. For all these purposes, understanding and correctly taking into account the interaction of Gr with whatever substance can come in contact with it are key steps to be able to use this material reliably in common applications<sup>3,44</sup>, and this understanding has been the main focus of my research work.

All these effects are not yet fully understood and are therefore being investigated both from an experimental and theoretical approach. In fact, several properties of Gr-based systems can be reliably predicted by *ab initio* calculations, such as the degree of interaction of Gr with different metal surfaces<sup>55</sup>. However, calculations of Gr supported on solid surfaces are often computationally demanding due to the large moiré supercells, which can contain several hundreds of atoms. Density Functional Theory (DFT) is often used

to determine the minimum energy configuration of such systems, and is often employed in combination with experimental data to fully investigate moiré structures and correctly interpret the measurements<sup>34,56</sup>. Different approximations are often employed to reduce the computational weight of DFT calculations, for example by using an approximated moiré supercell of smaller size<sup>57</sup>; moreover, different implementations of the interaction potentials are available within DFT (such as General Gradient Approximation, Linear Density Approximation), each offering a different balance between performance and accuracy<sup>40,58</sup>. In this respect, it is important to always take in mind the limits and scopes of applicability for these approximations, while ensuring that the computational cost is reasonable<sup>42,59</sup>. This is particularly important for the case of the adsorption of atoms and molecules on Gr, where vdW interaction play a key role. In fact, even though several models have been developed within the DFT framework to describe this kind of forces, their application does not always lead to consistent results<sup>40,60</sup>.

It is important therefore to understand which of the properties of Gr-based systems can significantly affect its reactivity towards adsorbates and which can instead be neglected, in order to determine the smallest system and the simulation parameters which are required to obtain reliable results from DFT on vdW – based systems. For example, there is still debate whether Gr is totally or partially transparent to vdW forces between the substrate and adsorbates, which would require the substrate below Gr to always be included in calculations, or whether this contribution can be neglected<sup>61</sup>.

It should be noted, finally, that the development of accurate methods for describing vdW forces for DFT not only affects the study of weakly interacting systems: these forces can produce significant effects even in some catalytic processes. For example, an appropriate treatment of vdW interactions is fundamental to correctly determine the CO adsorption site on some platinum surfaces<sup>62</sup>, and therefore to correctly describe the individual steps of the CO oxidation reaction on platinum, which is a key process in the field of environmental catalysis. In this respect, owing to the absence of stronger kinds of interactions, Gr-adsorbate interactions can represent an ideal testing ground to benchmark and compare the performance and accuracy of different DFT implementations of vdW forces.

The research work described in this thesis intends to identify and unravel the factors which affect and govern the interaction of Gr with different substances, and to investigate the consequences and possible applications of this interaction for the development of Gr-based nanostructures. To this aim, I have experimentally studied and compared different model systems using state of the art techniques widely used in the field of surface science. My experimental results have been also complemented by theoretical calculations by collaborating research group from University College London, Instituto de Ciencia de Materiales de Madrid and King's College London.

The experimental techniques which I have employed in my work are described in Chapter 1.

The following chapters are dedicated to the investigation of the effects of the interaction of Gr with different types of substances. In order to properly distinguish these effects, I worked in steps, every time adding a further component into the picture.

The first topic I have investigated in my research is therefore the origin of the Gr-substrate interaction occurring when Gr is supported on transition metal surfaces. In Chapter 2, I show which properties of the metallic surface play the dominant role in determining the strength of this interaction; in particular, whether the key factor is the geometric structure, which leads to a different degree of lattice mismatch between the Gr and its support, or the chemical composition – and therefore the electronic structure – of the substrate. In this research, I have shown that the Gr-metal interaction is well described in terms of a hybridization between the  $\pi_z$  orbitals of Gr with the d band of the metal, and therefore by the same model which was developed to describe molecular chemisorption on transition metal surfaces<sup>63</sup>.

Following this first step, I have proceeded to the study of the interaction of Gr with different types of adsorbates. In particular, in Chapter 3, I discuss the case of the adsorption of noble gases atoms, small inorganic molecules, as well as larger, organic molecules. In particular, I have employed the knowledge acquired during the previous research step to modify the interaction of Gr with its substrate, and investigated the effect of the substrate below Gr on the adsorption properties of Gr. These experiments have shown that the substrate below Gr significantly contributes to the adsorption energy of adsorbates on Gr. Moreover, I have also shown that the Gr-metal interaction can affect (and even completely reverse) the

ferromagnetic coupling between magnetic adsorbates and substrates, as reported in Chapter 4.

During my PhD research, besides the mechanisms, I have also investigated some of the consequences of the interactions of Gr with other adsorbed species. In particular, Chapter 5 describes the results of my research on the differences between two methods which can be used to grow Gr on metal surfaces, namely CVD and MBE. In particular, I have investigated the adsorption of different species of C precursors, namely monomers ( $C_1$ ) and dimers ( $C_2$ ), on both the metallic substrate and Gr, to understand the role of this interaction on the nucleation and accretion of the Gr islands.

The final part of my research project was dedicated to the study of nanoclusters and nanoparticles, and to the way in which depositing them on Gr can not only affect their size distribution and thermal stability, but also their electronic properties. Chapter 6 describes my studies of metal-oxide clusters ( $TiO_2$ ) grown on corrugated metal-supported Gr, as well as the effects of modifying the Gr-substrate interface on the properties of the nanoclusters. In parallel to this work, I have worked on the development of a mass-selected nanocluster source which allows to deposit clusters having a precise number of atoms on a surface: the principles and characterisation of this cluster source are described in Chapter 7.

## References

- [1] P. R. Wallace. The band theory of graphite. *Phys. Rev.* (**1947**) 71: 622–634. doi:10.1103/PhysRev.71.622.
- [2] H. P. Boehm, A. Clauss, G. O. Fischer, U. Hofmann. Dünnste Kohlenstoff-Folien. *Z. Naturforsch. B* (**1962**) 17: 150–153. doi:10.1515/znb-1962-0302.
- [3] M. Batzill. The surface science of graphene: Metal interfaces, CVD synthesis, nanoribbons, chemical modifications, and defects. *Surf. Sci. Rep.* (**2012**) 67: 83–115. doi:10.1016/j.surfrep.2011.12.001.
- [4] A. E. Morgan, G. A. Somorjai. Low energy electron diffraction studies of gas adsorption on the platinum(100) single crystal surface. *Surf. Sci.* (**1968**) 12: 405 – 425. doi:http://dx.doi.org/10.1016/0039-6028(68)90089-7.
- [5] J. W. May. Platinum surface LEED rings. *Surf. Sci.* (**1969**) 17: 267 – 270. doi:http://dx.doi.org/10.1016/0039-6028(69)90227-1.
- [6] K. S. Novoselov, A. K. Geim, S. V. Morozov, D. Jiang, Y. Zhang, S. V. Dubonos, I. V. Grigorieva, A. Firsov. Electric field effect in atomically thin carbon films. *Science* (**2004**) 306: 666–669. doi:10.1126/science.1102896.
- [7] K. S. Novoselov, A. K. Geim, S. V. Morozov, D. Jiang, M. I. Katsnelson, I. V. Grigorieva, S. V. Dubonos, A. A. Firsov. Two-dimensional gas of massless Dirac fermions in graphene. *Nature* (**2005**) 438: 197–200. doi:10.1038/nature04233.
- [8] A. H. Castro Neto, F. Guinea, N. M. R. Peres, K. S. Novoselov, A. K. Geim. The electronic properties of graphene. *Rev. Mod. Phys.* (**2009**) 81: 109–162. doi:10.1103/RevModPhys.81.109.
- [9] A. K. Geim, K. S. Novoselov. The rise of graphene. *Nat. Mater.* (**2007**) 6: 183–191. doi:10.1038/nmat1849.
- [10] A. S. Mayorov, R. V. Gorbachev, S. V. Morozov, L. Britnell, R. Jalil, L. A. Ponomarenko, P. Blake, K. S. Novoselov, K. Watanabe, T. Taniguchi, A. K. Geim. Micrometer-scale ballistic transport in encapsulated graphene at room temperature. *Nano Lett.* (**2011**) 11: 2396–2399. doi:10.1021/nl200758b.
- [11] C. Lee, X. Wei, J. W. Kysar, J. Hone. Measurement of the elastic properties and intrinsic strength of monolayer graphene. *Science* (**2008**) 321: 385–388. doi:10.1126/science.1157996.
- [12] I. Khrapach, F. Withers, T. H. Bointon, D. K. Polyushkin, W. L. Barnes, S. Russo, M. F. Craciun. Novel highly conductive and transparent graphene-based conductors. *Adv. Mater.* (**2012**) 24: 2844–2849. doi:10.1002/adma.201200489.
- [13] H. Y. Nan, Z. H. Ni, J. Wang, Z. Zafar, Z. X. Shi, Y. Y. Wang. The thermal stability of graphene in air investigated by Raman spectroscopy. *J. Raman Spectrosc.* (**2013**) 44: 1018–1021. doi:10.1002/jrs.4312.
- [14] O. Leenaerts, B. Partoens, F. M. Peeters. Adsorption of H<sub>2</sub>O, NH<sub>3</sub>, CO, NO<sub>2</sub>, and NO on graphene: A first-principles study. *Phys. Rev. B* (**2008**) 77: 125416. doi:10.1103/physrevb.77.125416.
- [15] T. O. Wehling, K. S. Novoselov, S. V. Morozov, E. E. Vdovin, M. I. Katsnelson, A. K. Geim, A. I. Lichtenstein. Molecular doping of graphene. *Nano Lett.* (**2008**) 8: 173–177. doi:10.1021/nl072364w.
- [16] K. S. Novoselov, V. I. Fal'Ko, L. Colombo, P. R. Gellert, M. G. Schwab, K. Kim. A roadmap for graphene. *Nature* (**2012**) 490: 192–200. doi:10.1038/nature11458.
- [17] A. K. Geim. Graphene: Status and prospects. *Science* (**2009**) 324: 1530–1534. doi:10.1126/science.1158877.

- [18] F. Schedin, A. K. Geim, S. V. Morozov, E. W. Hill, P. Blake, M. I. Katsnelson, K. S. Novoselov. Detection of individual gas molecules adsorbed on graphene. *Nat. Mater.* (2007) 6: 652–655. doi:10.1038/nmat1967.
- [19] A. C. Ferrari, F. Bonaccorso, V. Fal'ko, K. S. Novoselov, S. Roche, P. Bøggild, S. Borini, F. H. L. Koppens, V. Palermo, N. Pugno, J. A. Garrido, R. Sordan, A. Bianco, L. Ballerini, M. Prato, E. Lidorikis, J. Kivioja, C. Marinelli, T. Ryhänen, A. Morpurgo, J. N. Coleman, V. Nicolosi, L. Colombo, A. Fert, M. Garcia-Hernandez, A. Bachtold, G. F. Schneider, F. Guinea, C. Dekker, M. Barbone, Z. Sun, C. Galiotis, A. N. Grigorenko, G. Konstantatos, A. Kis, M. Katsnelson, L. Vandersypen, A. Loiseau, V. Morandi, D. Neumaier, E. Treossi, V. Pellegrini, M. Polini, A. Tredicucci, G. M. Williams, B. H. Hong, J.-H. Ahn, J. M. Kim, H. Zirath, B. J. van Wees, H. van der Zant, L. Occhipinti, A. D. Matteo, I. A. Kinloch, T. Seyller, E. Quesnel, X. Feng, K. Teo, N. Rupesinghe, P. Hakonen, S. R. T. Neil, Q. Tannock, T. Löfwander, J. Kinaret. Science and technology roadmap for graphene, related two-dimensional crystals, and hybrid systems. *Nanoscale* (2015) 7: 4598–4810. doi:10.1039/c4nr01600a.
- [20] A. Zurutuza, C. Marinelli. Challenges and opportunities in graphene commercialization. *Nat. Nanotechnol.* (2014) 9: 730–734. doi:10.1038/nnano.2014.225.
- [21] Y. Hernandez, V. Nicolosi, M. Lotya, F. M. Blighe, Z. Sun, S. De, I. T. McGovern, B. Holland, M. Byrne, Y. K. Gun'Ko, J. J. Boland, P. Niraj, G. Duesberg, S. Krishnamurthy, R. Goodhue, J. Hutchison, V. Scardaci, A. C. Ferrari, J. N. Coleman. High-yield production of graphene by liquid-phase exfoliation of graphite. *Nat. Nanotechnol.* (2008) 3: 563–568. doi:10.1038/nnano.2008.215.
- [22] M. Choucair, P. Thordarson, J. A. Stride. Gram-scale production of graphene based on solvothermal synthesis and sonication. *Nat. Nanotechnol.* (2008) 4: 30–33. doi:10.1038/nnano.2008.365.
- [23] G. Ruan, Z. Sun, Z. Peng, J. M. Tour. Growth of graphene from food, insects, and waste. *ACS Nano* (2011) 5: 7601–7607. doi:10.1021/nn202625c.
- [24] X. Li, W. Cai, J. An, S. Kim, J. Nah, D. Yang, R. Piner, A. Velamakanni, I. Jung, E. Tutuc, S. K. Banerjee, L. Colombo, R. S. Ruoff. Large-area synthesis of high-quality and uniform graphene films on copper foils. *Science* (2009) 324: 1312–1314. doi:10.1126/science.1171245.
- [25] X. Li, Y. Zhu, W. Cai, M. Borysiak, B. Han, D. Chen, R. D. Piner, L. Colombo, R. S. Ruoff. Transfer of large-area graphene films for high-performance transparent conductive electrodes. *Nano Lett.* (2009) 9: 4359–4363. doi:10.1021/nl902623y.
- [26] J. Kang, D. Shin, S. Bae, B. H. Hong. Graphene transfer: key for applications. *Nanoscale* (2012) 4: 5527. doi:10.1039/c2nr31317k.
- [27] A. Ambrosi, M. Pumera. The CVD graphene transfer procedure introduces metallic impurities which alter the graphene electrochemical properties. *Nanoscale* (2014) 6: 472–476. doi:10.1039/c3nr05230c.
- [28] G. Lupina, J. Kitzmann, I. Costina, M. Lukosius, C. Wenger, A. Wolff, S. Vaziri, M. Östling, I. Pasternak, A. Krajewska, W. Strupinski, S. Kataria, A. Gahoi, M. C. Lemme, G. Ruhl, G. Zoth, O. Luxenhofer, W. Mehr. Residual metallic contamination of transferred Chemical Vapor Deposited graphene. *ACS Nano* (2015) 9: 4776–4785. doi:10.1021/acs.nano.5b01261.
- [29] J. M. Garcia, R. He, M. P. Jiang, J. Yan, A. Pinczuk, Y. M. Zuev, K. S. Kim, P. Kim, K. Baldwin, K. W. West, L. N. Pfeiffer. Multilayer graphene films grown by molecular beam deposition. *Solid State Commun.* (2010) 150: 809–811. doi:10.1016/j.ssc.2010.02.029.
- [30] I. Hernández-Rodríguez, J. M. García, J. A. Martín-Gago, P. L. de Andrés, J. Méndez. Graphene growth on Pt(1 1 1) and Au(1 1 1) using a MBE carbon solid-source. *Diamond Relat. Mater.* (2015) 57: 58–62. doi:10.1016/j.diamond.2015.03.004.

- [31] G. Lippert, J. Dąbrowski, T. Schroeder, M. A. Schubert, Y. Yamamoto, F. Herziger, J. Maultzsch, J. Baringhaus, C. Tegenkamp, M. C. Asensio, J. Avila, G. Lupina. Graphene grown on Ge (0 0 1) from atomic source. *Carbon* (2014) 75: 104–112. doi:10.1016/j.carbon.2014.03.042.
- [32] R. Addou, A. Dahal, P. Sutter, M. Batzill. Monolayer graphene growth on Ni (1 1 1) by low temperature chemical vapor deposition. *Appl. Phys. Lett.* (2012) 100: 021601. doi:10.1063/1.3675481.
- [33] P. Zhao, A. Kumamoto, S. Kim, X. Chen, B. Hou, S. Chiashi, E. Einarsson, Y. Ikuhara, S. Maruyama. Self-limiting chemical vapor deposition growth of monolayer graphene from ethanol. *J. Phys. Chem. C* (2013) 117: 10755–10763. doi:10.1021/jp400996s.
- [34] J. Wintterlin, M.-L. Bocquet. Graphene on metal surfaces. *Surf. Sci.* (2009) 603: 1841–1852. doi:10.1016/j.susc.2008.08.037.
- [35] P. Merino, M. Švec, A. L. Pinardi, G. Otero, J. A. Martín-Gago. Strain-driven moiré superstructures of epitaxial graphene on transition metal surfaces. *ACS Nano* (2011) 5: 5627–5634. doi:10.1021/nn201200j.
- [36] A. T. N'Diaye, S. Bleikamp, P. J. Feibelman, T. Michely. Two-dimensional Ir cluster lattice on a graphene moiré on Ir (1 1 1). *Phys. Rev. Lett.* (2006) 97: 215501. doi:10.1103/physrevlett.97.215501.
- [37] S. K. Hämäläinen, M. Stepanova, R. Drost, P. Liljeroth, J. Lahtinen, J. Sainio. Self-assembly of cobalt-phthalocyanine molecules on epitaxial graphene on Ir (1 1 1). *J. Phys. Chem. C* (2012) 116: 20433–20437. doi:10.1021/jp306439h.
- [38] A. T. N'Diaye, T. Gerber, C. Busse, J. Mysliveček, J. Coraux, T. Michely. A versatile fabrication method for cluster superlattices. *New J. Phys.* (2009) 11: 103045. doi:10.1088/1367-2630/11/10/103045.
- [39] A. Cavallin, M. Pozzo, C. Africh, A. Baraldi, E. Vesselli, C. Dri, G. Comelli, R. Larciprete, P. Lacovig, S. Lizzit, D. Alfè. Local electronic structure and density of edge and facet atoms at Rh nanoclusters self-assembled on a graphene template. *ACS Nano* (2012) 6: 3034–3043. doi:10.1021/nn300651s.
- [40] J. Ma, A. Michaelides, D. Alfè, L. Schimka, G. Kresse, E. Wang. Adsorption and diffusion of water on graphene from first principles. *Phys. Rev. B* (2011) 84: 033402. doi:10.1103/physrevb.84.033402.
- [41] X. Lin, J. Ni, C. Fang. Adsorption capacity of H<sub>2</sub>O, NH<sub>3</sub>, CO, and NO<sub>2</sub> on the pristine graphene. *J. Appl. Phys.* (2013) 113: 034306. doi:10.1063/1.4776239.
- [42] P. L. Silvestrelli, A. Ambrosetti. Including screening in van der Waals corrected density functional theory calculations: The case of atoms and small molecules physisorbed on graphene. *J. Chem. Phys.* (2014) 140: 124107. doi:10.1063/1.4869330.
- [43] R. Balog, B. Jørgensen, L. Nilsson, M. Andersen, E. Rienks, M. Bianchi, M. Fanetti, E. Lægsgaard, A. Baraldi, S. Lizzit, Z. Sljivancanin, F. Besenbacher, B. Hammer, T. G. Pedersen, P. Hofmann, L. Hornekær. Bandgap opening in graphene induced by patterned hydrogen adsorption. *Nat. Mater.* (2010) 9: 315–319. doi:10.1038/nmat2710.
- [44] Y. Yang, K. Brenner, R. Murali. The influence of atmosphere on electrical transport in graphene. *Carbon* (2012) 50: 1727–1733. doi:10.1016/j.carbon.2011.12.008.
- [45] G. Giovannetti, P. Khomyakov, G. Brocks, V. Karpan, J. van den Brink, P. Kelly. Doping graphene with metal contacts. *Phys. Rev. Lett.* (2008) 101: 026803. doi:10.1103/PhysRevLett.101.026803.
- [46] A. Varykhalov, M. Scholz, T. Kim, O. Rader. Effect of noble-metal contacts on doping and band gap of graphene. *Phys. Rev. B* (2010) 82: 121101. doi:10.1103/PhysRevB.82.121101.

- [47] M. Yankowitz, J. Xue, D. Cormode, J. D. Sanchez-Yamagishi, K. Watanabe, T. Taniguchi, P. Jarillo-Herrero, P. Jacquod, B. J. LeRoy. Emergence of superlattice Dirac points in graphene on hexagonal boron nitride. *Nat. Phys.* (2012) 8: 382–386. doi:10.1038/nphys2272.
- [48] B. Hunt, J. D. Sanchez-Yamagishi, A. F. Young, M. Yankowitz, B. J. LeRoy, K. Watanabe, T. Taniguchi, P. Moon, M. Koshino, P. Jarillo-Herrero, R. C. Ashoori. Massive Dirac fermions and Hofstadter butterfly in a van der Waals heterostructure. *Science* (2013) 340: 1427–1430. doi:10.1126/science.1237240.
- [49] A. Principi, M. Carrega, M. B. Lundeberg, A. Woessner, F. H. L. Koppens, G. Vignale, M. Polini. Plasmon losses due to electron-phonon scattering: The case of graphene encapsulated in hexagonal boron nitride. *Phys. Rev. B* (2014) 90: 165408. doi:10.1103/physrevb.90.165408.
- [50] P. Sutter, J. T. Sadowski, E. A. Sutter. Chemistry under cover: Tuning metal-graphene interaction by reactive intercalation. *J. Am. Chem. Soc.* (2010) 132: 8175–8179. doi:10.1021/ja102398n.
- [51] R. Larciprete, S. Ulstrup, P. Lacovig, M. Dalmiglio, M. Bianchi, F. Mazzola, L. Hornekær, F. Orlando, A. Baraldi, P. Hofmann, S. Lizzit. Oxygen switching of the epitaxial graphene–metal interaction. *ACS Nano* (2012) 6: 9551–9558. doi:10.1021/nn302729j.
- [52] L. Omiciuolo, E. R. Hernández, E. Miniussi, F. Orlando, P. Lacovig, S. Lizzit, T. O. Mentes, A. Locatelli, R. Larciprete, M. Bianchi, S. Ulstrup, P. Hofmann, D. Alfè, A. Baraldi. Bottom-up approach for the low-cost synthesis of graphene-alumina nanosheet interfaces using bimetallic alloys. *Nat. Commun.* (2014) 5: 5062. doi:10.1038/ncomms6062.
- [53] S. Lizzit, R. Larciprete, P. Lacovig, M. Dalmiglio, F. Orlando, A. Baraldi, L. Gammelgaard, L. Barreto, M. Bianchi, E. Perkins, P. Hofmann. Transfer-free electrical insulation of epitaxial graphene from its metal substrate. *Nano Lett.* (2012) 12: 4503–4507. doi:10.1021/nl301614j.
- [54] R. Larciprete, P. Lacovig, F. Orlando, M. Dalmiglio, L. Omiciuolo, A. Baraldi, S. Lizzit. Chemical gating of epitaxial graphene through ultrathin oxide layers. *Nanoscale* (2015) 7: 12650–12658. doi:10.1039/c5nr02936h.
- [55] P. A. Khomyakov, G. Giovannetti, P. C. Rusu, G. Brocks, J. van den Brink, P. J. Kelly. First-principles study of the interaction and charge transfer between graphene and metals. *Phys. Rev. B* (2009) 79: 195425. doi:10.1103/physrevb.79.195425.
- [56] B. Wang, M. Caffio, C. Bromley, H. Früchtl, R. Schaub. Coupling epitaxy, chemical bonding, and work function at the local scale in transition metal-supported graphene. *ACS Nano* (2010) 4: 5773–5782. doi:10.1021/nn101520k.
- [57] B. Wang, S. Günther, J. Wintterlin, M.-L. Bocquet. Periodicity, work function and reactivity of graphene on Ru(0001) from first principles. *New J. Phys.* (2010) 12: 043041. doi:10.1088/1367-2630/12/4/043041.
- [58] J. Granatier, P. Lazar, M. Otyepka, P. Hobza. The nature of the binding of Au, Ag, and Pd to benzene, coronene, and graphene: From benchmark CCSD(T) calculations to plane-wave DFT calculations. *J. Chem. Theory Comput.* (2011) 7: 3743–3755. doi:10.1021/ct200625h.
- [59] C.-J. Shih, M. S. Strano, D. Blankschtein. Wetting translucency of graphene. *Nat. Mater.* (2013) 12: 866–869. doi:10.1038/nmat3760.
- [60] J. P. Prates Ramalho, J. R. B. Gomes, F. Illas. Accounting for van der Waals interactions between adsorbates and surfaces in density functional theory based calculations: selected examples. *RSC Adv.* (2013) 3: 13085. doi:10.1039/c3ra40713f.
- [61] Not so transparent. *Nat. Mater.* (2013) 12: 865–865. doi:10.1038/nmat3773. Editorial.

- [62] P. Janthon, F. Viñes, J. Sirijaraensre, J. Limtrakul, F. Illas. Adding pieces to the CO/Pt(1 1 1) puzzle: The role of dispersion. *J. Phys. Chem. C* **(2017)** 121: 3970–3977. doi:10.1021/acs.jpcc.7b00365.
- [63] B. Hammer, J. K. Nørskov. Theoretical surface science and catalysis-calculations and concepts. *Adv. Catal.* **(2000)** 45: 71–129. doi:10.1016/S0360-0564(02)45013-4.



# Chapter 1

## Experimental techniques and setup

The experiments described in this thesis are generally focussed on the electronic and structural characterisation of different species, such as molecules and nanostructured materials, supported on solid surfaces. The study of solid surfaces and processes occurring on them is however a challenging task, for several reasons, and has therefore required the development of a specific set of experimental techniques to overcome the problems. In particular, one of the main issues is related to the fact that a surface constitutes a minute part of bulk materials: for example, for a bulk sample whose volume is of the order of a square centimetre, the number of bulk atoms is of the order of  $10^{23}$ , while the surface atoms are just about  $10^{15}$ . For this reason, techniques probing bulk and surface at the same time are often affected by the issue that the signal from the bulk has an intensity larger by several orders of magnitude than the one from the surface, leading to a very low signal-to-background ratio.

Another very important issue in the study of surfaces is that of contamination. In fact, the surface of any body is always exposed to the environment, which contains gas molecules which can stick on the surface, covering it with a thick layer of adsorbates. For example, surfaces exposed to the atmosphere are always covered by a layer of moisture. Several metals react with the oxygen creating a thin layer of surface oxide, which dramatically changes its properties. Even inert atmospheres are often not suitable, as for a pressure of the order of the atmosphere, a balance between sticking and desorption allows an equilibrium to persist, where a certain amount of gas molecules are adsorbed on the surface at any time. For this reason, surface science experiments are usually performed in vacuum conditions.

The level of vacuum required for surface science experiments is calculated by taking into consideration the average time required for an experiment, which is often of the order of hours, and calculating the maximum pressure that allows the surface to remain clean for long enough time. For example, by calculating the average number of gas particles impinging each surface atom per unit of time from the Hertz-Knudsen formula, and assuming – as worst case scenario – that the their sticking probability is 1, it can be shown that a background pressure of  $1 \times 10^{-6}$  mbar would get the surface completely covered by contaminants in few seconds, thus preventing any accurate measurement of the actual surface<sup>1</sup>. For this reason, a pressure range of the order of  $1 \times 10^{-10}$  mbar is desirable for most experiments, to ensure that the surface remains clean of contaminants for at least a few hours. This pressure belongs to the so-called Ultra-High Vacuum (UHV) range.

These needs of working in UHV conditions, preventing contaminations and achieving surface sensitivity, greatly limit the number of possible approaches for preparing and characterising the samples. In the following sections, therefore, I will describe the methods employed in our experiments to prepare our systems, as well as the experimental techniques I have used most extensively to characterise them: Low Energy Electron Diffraction, X-ray Absorption Spectroscopy and, to a greater extent, X-ray Photoelectron Spectroscopy. Furthermore, I will briefly describe the experimental setup I have used for most experiments.

Finally, in order to improve the interpretation of our data and to acquire further understanding on our systems, we often collaborated with several groups who performed theoretical simulations of our systems. I will therefore also very briefly introduce the methods used by these research groups to this aim.

## 1.1 Sample cleaning and preparation

To ensure a high degree of homogeneity, for the benefit of the space-averaging techniques we have employed, the samples used for our experiments were single-crystal surfaces cleaved along high symmetry planes, close-packed surfaces of transition metals. The surface flatness was further improved by polishing the surfaces; however, as these samples have been originally exposed to the atmosphere, a specific cleaning in UHV environment is required to remove the contaminants originally present and further reduce the surface roughness.

The cleaning of samples in UHV is usually performed in several steps, even though the details depend on the surface composition and termination. In particular, the first step for the surface cleaning is usually its sputtering by noble gas ions of sufficiently high mass (such as  $\text{Ar}^+$ ), in order to remove a sufficient number of atomic layers from the surface. While this method is very effective in removing whatever adsorbate or thin film may be on the surface, it also induces a certain degree of roughening of the surface, which must be reduced afterwards. To this aim, the mobility of the atoms is then increased by annealing it, so that they can migrate and form large terraces with a low density of defects. This procedure is very effective in removing impurities present on the surface, and is usually sufficient to clean the most inert surfaces, such as those of noble metals.

However, on reactive surfaces such as those of transition metals, some contaminants can dissolve into the crystal bulk: in this case, they are not completely removed by sputtering: this is for example often the case of carbon. In addition, these impurities can subsequently segregate back to the surface during the annealing, making the preparation of a clean surface more challenging. In this case, a further chemical treatment is employed afterwards, by annealing the sample in an oxidising environment, for example by dosing oxygen at low pressures (*i.e.*, still in the UHV range). In this way, the residual carbon on the surface can react with the oxygen, forming gaseous species such as  $\text{CO}$  and  $\text{CO}_2$  which can desorb from the surface by thermal annealing. Finally, a similar treatment in a reducing atmosphere (such as a low  $\text{H}_2$  pressure) is performed to remove any oxygen left on the surface by the previous treatment.

While this is a general picture of the treatments required to clean a sample, some or all of them might be necessary depending on the surface, and the parameters (including sputtering energy, annealing temperature and gas pressures) have to be optimised for each case. This procedure of sample cleaning in UHV was used before each experiment, to ensure high surface crystalline quality and low levels of contaminants, well below the detection limit of our techniques, which is usually of the order of 1%, or even better when using synchrotron radiation.

### 1.1.1 Graphene growth on Ir (1 1 1) and other metal surfaces

The main topic of this thesis is the characterisation of several graphene-based systems: I will therefore briefly describe the methods we used for its synthesis. This material was always prepared *in situ* after cleaning the metal surfaces. This has several advantages as it avoids the possible contaminations which occur during the sample transfer in air and ensures a low rate of outgassing by the crystal and sample holder during subsequent thermal treatments. Moreover, it allows to follow the growth of Gr in real time, an opportunity which has been exploited extensively in the experiments described in Chapter 5.

As already mentioned in the Introduction, CVD is a method which is able to almost completely cover a metal surface with Gr, yielding a single layer of this material characterised by a high crystalline quality<sup>2</sup>. This technique consists of exposing the metal surface to a precursor gas containing carbon, and is based on a chemical reaction where the precursor is decomposed and thus produces carbon species adsorbed on the surface. These species, provided they have sufficient mobility, can then migrate on the surface and either form nucleation centres for Gr islands or attach to already nucleated ones leading to their accretion<sup>3</sup>. In this process, a parameter which plays a key role is temperature, as it must be sufficient to both allow the precursor decomposition reaction and provide a mobility to the carbon precursors sufficient for them to coalesce. Finally, it must allow the precursors to overcome the energy barriers of the nucleation and attachment processes.

More in detail, the single steps of this process have been studied with several experimental and the-

oretical approaches on different substrates for the most commonly used precursors, which are hydrocarbons<sup>4–8</sup>. In our specific case, in most of our experiments, we have grown Gr from the decomposition of ethylene ( $C_2H_4$ ) on Ir (1 1 1) at high temperature (well above 1000 K). For this particular case, the single steps by which the C feedstock is provided to the surface are the following:  $C_2H_4$  first adsorbs on the metal surface, then it undergoes a dehydrogenation reaction catalysed by the metallic substrate which progressively removes its H atoms, finally producing atomic C and H on the surface<sup>7,8</sup>. While the H atoms, because of their high mobility, combine and desorb as  $H_2$  species, atomic carbon remains on the surface. In most cases, the carbon feedstock initially forms an adatom gas on the surface, whose density increases as further carbon feedstock is provided. However, several processes can occur when this density increases. One, which is the only one occurring on surfaces such as Ir and Pt, is the nucleation of Gr islands, which usually occurs at defective sites, after which an equilibrium between the attachment and detachment of C atoms at the islands' edges leads to their progressive growth<sup>4,9</sup>. The other, which can occur in the case of strongly interacting metals such as Ni, is the diffusion of the C adatoms into the bulk<sup>3</sup>. For the case of Ni surfaces such as Ni (1 1 1), these atoms can then segregate back to the surface during cooling, forming a Gr layer<sup>10–12</sup>.

## 1.2 Low Energy Electron Diffraction

Low Energy Electron Diffraction (LEED) is an experimental technique widely used in surface science to investigate the geometry of surfaces characterised by long-range ordering. First demonstrated by Davisson and Germer in the late 1920s<sup>13</sup>, LEED was not only one of the first applications of the de Broglie hypothesis<sup>14</sup>, but also one of its first proofs. Its widespread adoption as a surface investigation technique however did not come before the 1960s, when advancements in the instrumentation – in particular those introduced by Farnsworth<sup>15</sup> – allowed it to become one of the most diffused techniques for the characterisation of solid surfaces.

Diffraction-based techniques are widely employed in the study of crystalline materials. In fact, they are based on the principle by which any wave, when interacting with an array having a periodicity of the same magnitude as the wavelength, undergoes diffraction. According to the de Broglie hypothesis of quantum mechanics, any particle can be employed as a probe in diffraction experiments, and examples which are widely used include photons, neutrons and electrons. The main requirement on the probes is that their de Broglie wavelength  $\lambda$ , which is related to their momentum  $p$  by the relation  $\lambda = \frac{h}{p}$ , is close to the lattice parameter of the system being investigated. For the particular case of electron diffraction from typical inorganic crystals, this requirement is satisfied for electrons having a kinetic energy of the order of tens or few hundreds of eV – usually referred to as low-energy electrons.

The choice of electrons as probes, and in particular the energy at which they are used, has very important consequences on the depth at which the system is probed. In fact, electrons, being charged particles, have a relatively high degree of interaction with matter, in particular when compared to photons and neutrons. At energies of tens or few hundreds of eV, in particular, there is a minimum in their penetration depth inside solids, which has been verified to be to a first approximation independent on the latter's chemical species, as shown in Figure 1.1<sup>16</sup>.

### Instrument description

A typical LEED instrument is illustrated in the scheme in Figure 1.2. A monochromatic electron beam is produced by thermionic emission by a hot filament, and subsequently accelerated to the set energy and focussed on the sample by electrostatic lenses. This system is also known as electron gun. The electrons scattered by the sample are accelerated onto a hemispherical phosphorous screen surrounding the gun, where they induce a fluorescent emission having an intensity to a first approximation proportional to their density. The position where they impinge on the screen depends on the scattering angle, and therefore on  $\vec{k}_{out} - \vec{k}_{in}$ .

However, besides undergoing diffraction (an elastic scattering process), the electrons impinging the

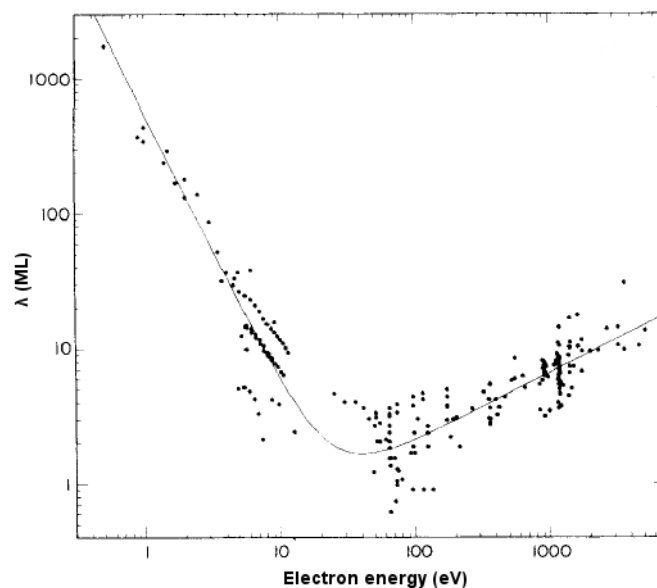


**Figure 1.1:** Universal curve of the electron inelastic mean free path in solids, expressed in monolayers, as a function of their kinetic energy<sup>16</sup>.

sample can also be involved in inelastic scattering processes. These electrons, which are scattered with an energy lower than the one at which they were accelerated, must be separated and prevented from reaching the screen, in order to ensure a high signal-to-noise ratio on the diffraction image. This is achieved by

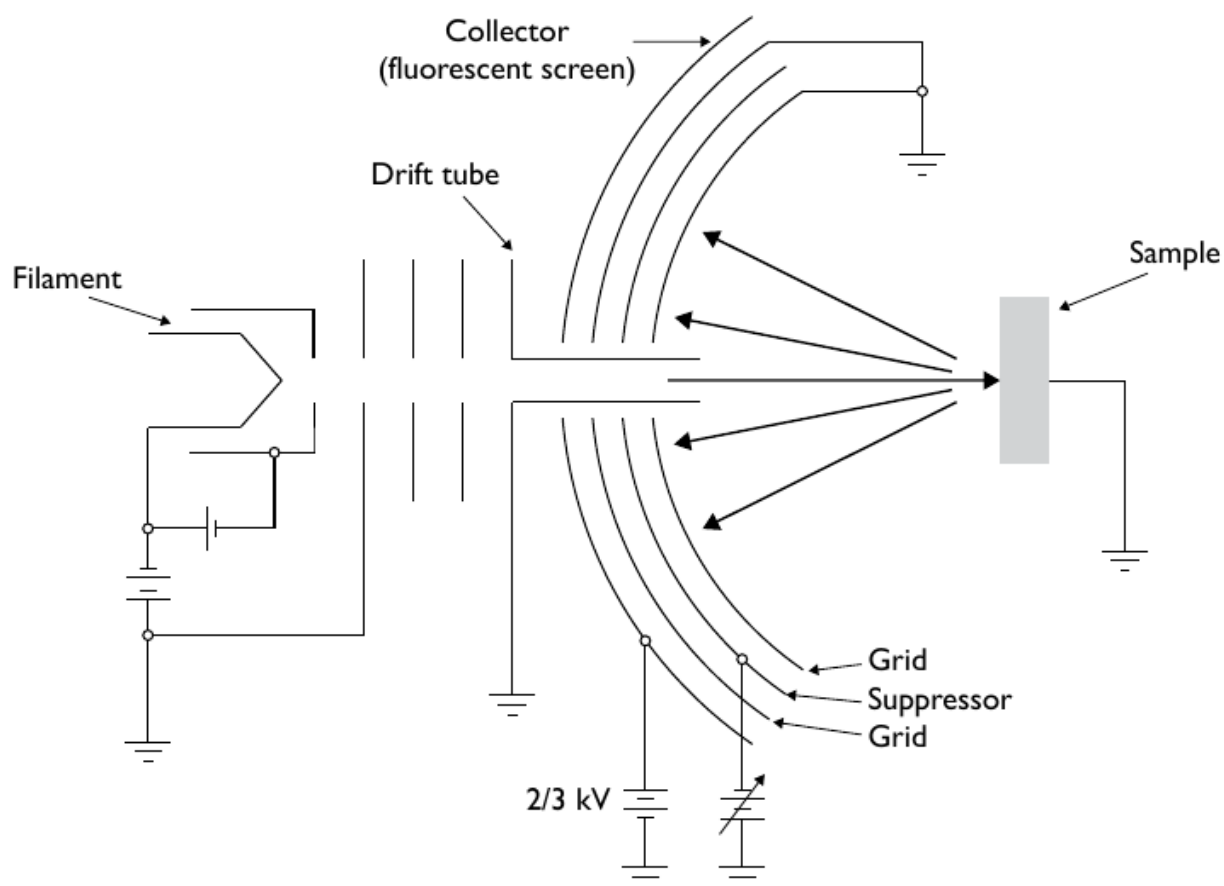


**Figure 1.2:** Scheme of a typical LEED instrument.

a set of three meshes positioned in front of the screen, set alternatively at ground potential and at the accelerating potential of the electrons. This configuration prevents those electrons having lost energy in the scattering process from crossing these meshes and thereby from reaching the screen.

It is important to note that due to the high degree of interaction of electrons with matter, LEED can only be performed in an UHV environment. In fact, at pressures of about  $10^{-4}$  mbar, the mean free path of electrons in the gas would become comparable to the distance between electron source, sample and detector, leading to a dramatic decrease in the signal. While these requirements are usually less stringent than those imposed by the necessity to prevent surface contamination, they nevertheless apply also for the most inert surfaces, in cases where other restrictions would not apply.

### Kinematic analysis

The analysis of the directions in which the electrons are scattered provides an immediate tool to probe the long-range order of the surface. In fact, this information can be achieved already by a first level of analysis, limited to the treatment of first-order scattering processes (also known as kinematic analysis). This analysis is based on the fact that the scattered electron beams have an intensity modulation as a function of the difference between the wavevector of the impinging ( $\vec{k}_{in}$ ) and diffracted ( $\vec{k}_{out}$ ) wave, and therefore to the scattering angle. According to the Laue condition, maxima are found for  $\vec{k}_{out} - \vec{k}_{in} = \vec{G}$ , where  $\vec{G}$  is a reciprocal lattice vector of the crystal lattice.

Diffraction experiments, therefore, provide a mapping of the reciprocal lattice of any long-range ordered material. This can be easily visualised from the geometric construction of the Ewald sphere, represented in Figure 1.3. For the specific case of a 2D surface in 3D space, since the momentum component perpendicular to the surface is not a good quantum number, reciprocal lattice points are actually rods perpendicular to the crystal surface, crossing it in correspondence to the points of the 2D reciprocal lattice.

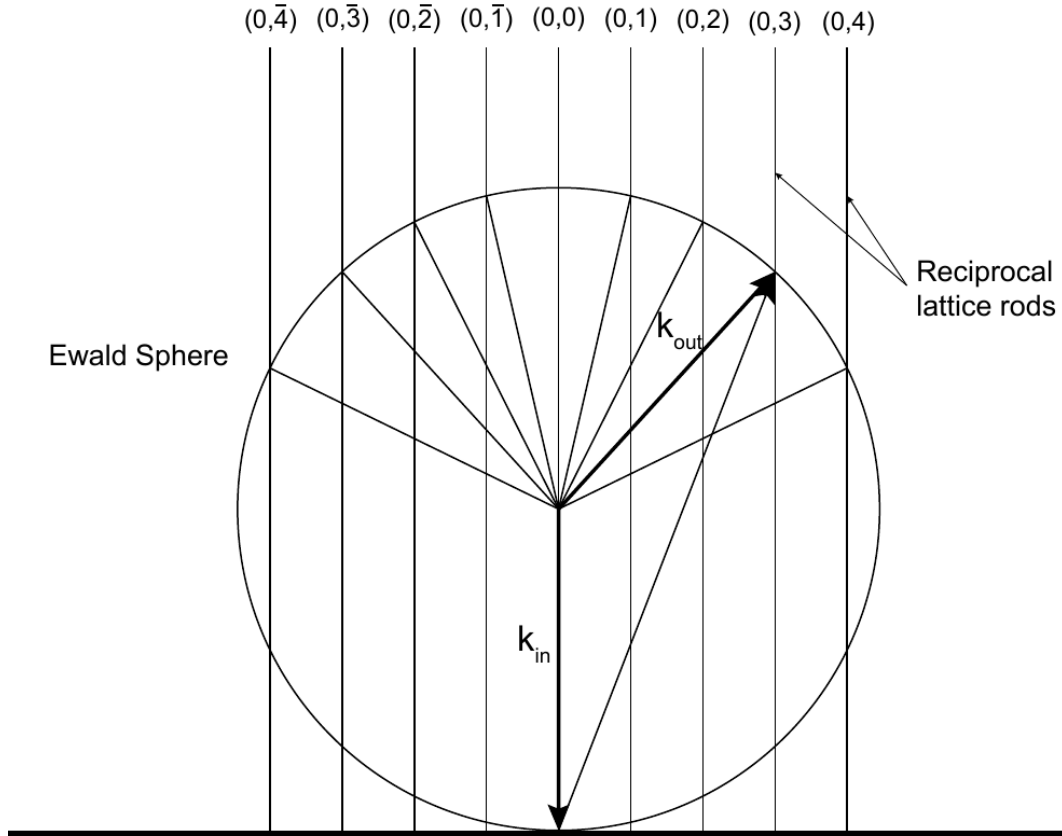


**Figure 1.3:** Ewald sphere for a 2D crystal.  $k_{in}$  is the wavevector of the impinging electrons,  $k_{out}$  of the scattered electrons; their difference is also plotted.

The points of intersection between these lines and the Ewald sphere, the radius of whom depends on the modulus of the  $k$ -vector of the incident electrons, correspond to maxima in the scattering intensity.

Finally, the broadening of the angular distribution of the modulation function around the maxima provides information about the average size of coherent domains on the surface. In fact, while for ideal, infinite surfaces the scattering intensity would be non-zero only for points satisfying the Laue condition, this is not the case when the number of scatterers are finite. In the presence of surface defects such as steps and grain boundaries, for example, the phase is not preserved on both sides, and therefore only atoms belonging to the same domain are able to scatter the electrons coherently. For the case of a finite number of in-phase scatterers, the angular distribution of the scattering intensity is broadened, showing a Lorentzian lineshape<sup>17</sup> whose full width at half-maximum (FWHM)  $L$  is related to the number of scatterers, and therefore to the average domain lateral extension  $d$ , by the relation  $\frac{L}{b} = \frac{a}{d}$ , where  $a$  is the modulus of a real space lattice vector and  $b$  that of its corresponding reciprocal vector<sup>18</sup>.

Further information about the system, and in particular on the exact position of each atom within the unit cell (including the basis of the crystal), can be obtained by a dynamic analysis of the LEED IV curves, which are obtained by measuring the intensity of the diffraction spots as a function of the electron beam energy. This level of analysis, however, requires a demanding theoretical treatment of multiple-scattering processes, and has not been employed in the experiments reported in this thesis.

Following these theoretical aspects about the kinematic analysis, I will describe some practical aspects related to LEED measurements, and in particular address the main sources of errors. In the typical LEED configuration, the electron beam impinges the sample perpendicularly to the surface. Therefore, the reflected beam is not observed as it is reflected into the electron gun.

Provided the sample is located in the exact centre of the hemisphere described by the screen, the distance of each spot from the centre of the screen is linearly proportional to the scattering angle. However, an improper alignment of the sample introduces a deformation into the pattern. Furthermore, being the screen curved, parallax errors are common when measuring the spot positions with an external tool, such as by registering the pattern with a camera. For these reasons, an error of the order of few percent usually affects the determination of the scattering angle for the spots closest to the screen edges, while it becomes negligible only close to the screen centre.

Furthermore, the main factors affecting the resolution of the instrument are given by the energy spread of the electron beam  $\Delta E$  and its angular divergence  $\Delta \vec{k}$ . This can be taken into account by including a Gaussian contribution to the lineshape broadening, which is therefore described by a Voigt function. Finally, an additional limitation of the instrument is given by the spatial coherency of the electron beam. In fact, while the size of the beam is macroscopic (about 1 mm diameter), the phase of the waves describing the electrons is not at all coherent across the whole beam. This limits the area of the surface whose atoms can scatter the electrons coherently and generate a diffraction pattern, even when the domain size is on average larger, leading to a residual minimum broadness of the spots regardless of the quality of the sample. The length describing the region of the surface over which the electron beam is coherent is called transfer width of the instrument. For a typical LEED instrument, it is of the order of about 100 Å, meaning that the size of larger domains on the surface cannot be evaluated: in those cases, only a lower boundary can be given to the domain size, corresponding to the transfer width of the instrument.

### 1.2.1 Spot Profile Analysis-LEED

Several modifications to the LEED instrument have been developed during the years, in order to overcome some of the main limitations of the traditional LEED setup. One example of this is given by Spot Profile Analysis LEED (SPA-LEED), which was specifically designed in order to improve the transfer width and reduce the experimental broadening with respect to a conventional LEED<sup>19</sup>.

In this instrument, whose scheme is shown in Figure 1.4, the scattered electrons are not collected by a 2D screen, but by a single channeltron detector. For this reason, the image is not obtained as a single image as for LEED, but by scanning the solid angle. Furthermore, the incidence angle is not fixed. Instead, several sets of electrostatic octupole lenses allow to modify the angle at which the beam impinges the sample. Being the detector close to the gun, to a first approximation, the electrons detected by the channeltron are

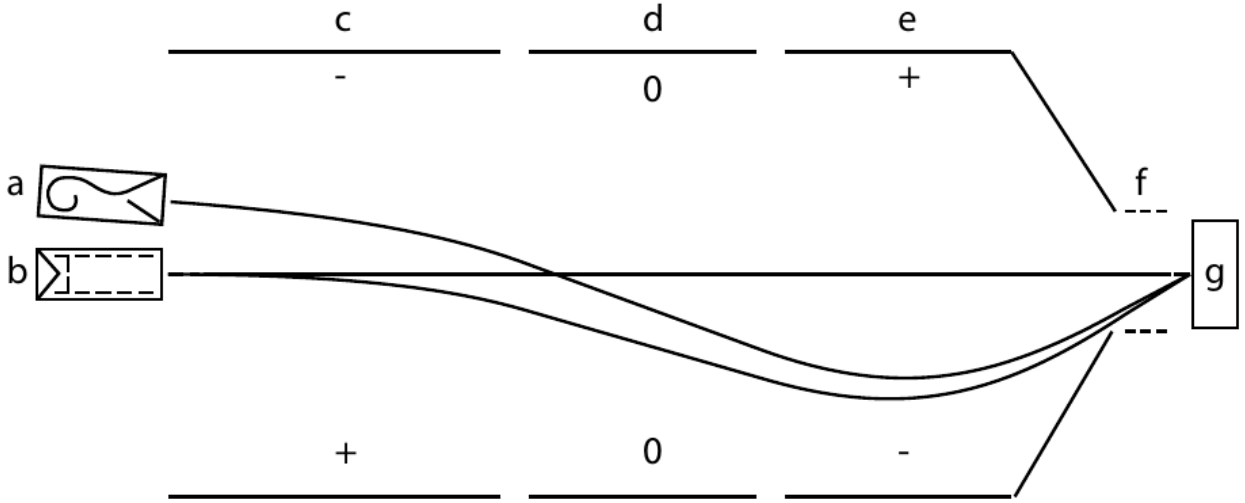


**Figure 1.4:** Scheme of a SPALEED instrument. a: channeltron detector. b: electron gun. c-f: electrostatic lenses. g: sample. The trajectory of the electrons corresponding to a generic reciprocal space point is shown, starting at b, impinging on g and travelling back to a.

those for which  $\vec{k}_{in} = -\vec{k}_{out}$ , and the reciprocal space is therefore scanned by varying the incidence angle. In this geometry, the maxima in the scattering modulation are found when  $\vec{k}_{in} = -\vec{k}_{out} = \frac{\vec{G}}{2}$ .

Thanks to this geometrical configuration, the source of error due to the parallax of the curved screen is removed. However, the electrostatic lenses introduce some aberration effect, which can be removed by carefully calibrating the instrument. In addition, this setup allows to probe the reciprocal space close to the zero-order diffraction spot, corresponding to the reflected beam. Finally, the transfer width of this instrument is larger than that of a LEED by about an order of magnitude.

### 1.3 Near Edge X-ray Absorption Fine Structure

X-ray absorption spectroscopy (XAS) is a very versatile technique to investigate the electronic structure of materials. The principle behind this technique is that when electromagnetic radiation travels through a material, it is partly absorbed due to the radiation-matter interaction, and the attenuation depends, besides the thickness  $z$  of the material, on the absorption coefficient  $\mu$ , which is a function of the photon energy:

$$I = I_0 e^{-\mu(\nu)z}$$

where  $I_0$  is the intensity of the impinging radiation and  $I$  the intensity after crossing the material<sup>20</sup>. This dependence of the cross section on the photon energy is determined by the different excitation channels available in the system: for this reason, the analysis of this dependence provides information on the electronic levels of the material. In particular, this technique allows to probe excitations involving electrons in the core level of the atoms, as the photon energies employed are of the same order of magnitude as their binding energies (BEs), which is of the order of  $10^2 - 10^4$  eV.

More in detail, this technique is based on an excitation of a system by means of monochromatic X-ray radiation: the absorption of the impinging radiation is measured as a function of the photon energy. The absorption coefficient  $\mu$  of a generic material is proportional, via its density, to its cross section  $\sigma$ , which, according to the Fermi golden rule, is given by

$$\sigma \propto \sum_i \sum_f |\langle \psi_f | H_{INT}(h\nu) | \psi_i \rangle|^2 \rho(h\nu)$$

where  $\psi_i$  is the wavefunction of the initial state,  $\psi_f$  that of the final state,  $H_{INT}$  is the interaction Hamiltonian,  $\rho$  is the density of final states, including the energy conservation condition, and the sum is performed on all initial and final states. In other words, the absorption coefficient will be given by the sum on the

initial and final states of the cross sections of each allowed transition from an occupied initial state to an unoccupied state, as shown in Figure 1.5. In a solid, the initial states will correspond to each occupied electron shell in the sample, which is usually designated with a letter such as  $K$  (corresponding to  $1s$  orbitals),  $L$  ( $2s - L_1$  - and  $2p - L_2$ , corresponding to the  $2p_{3/2}$  spin-orbit component, and  $L_3$ , corresponding to the  $2p_{1/2}$  -) and so on. The final states can be of different type: either bound states, such as unoccupied ones between the Fermi and vacuum level of the system, or unbound states. Due to the energy conservation condition, each transition to a bound state leads to an increase in the absorption coefficient for a specific value of the energy, corresponding to the difference between the initial and final states; on the other hand, transitions to the continuum give rise to a step-like increase in the absorption coefficient for photon energies larger than the energy difference between the initial state and vacuum level.

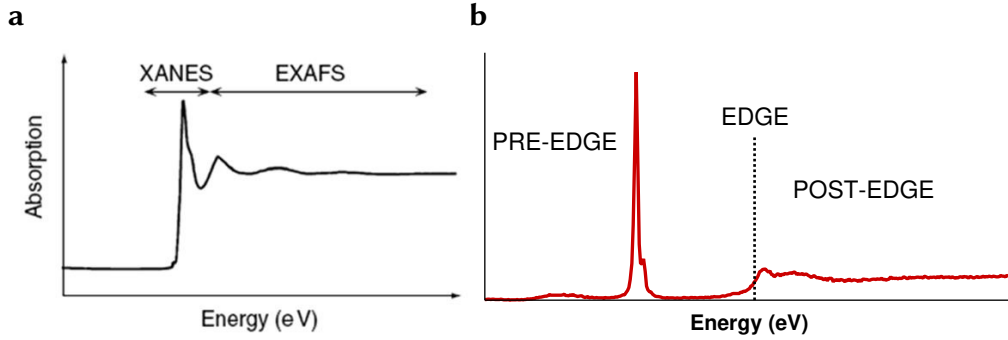


**Figure 1.5:** Typical appearance of an absorption edge. a: Distinction between the NEXAFS and EXAFS regions. b: Subdivision of the NEXAFS region into pre-edge, edge and post-edge.

Usually, the BE separation between different initial states is significantly larger than the one existing between final states, and therefore the cross section dependence on the photon energy is characterised by well-defined regions a few tens of eV wide, consisting of a step-like increase of the cross section, known as edge, sometimes preceded by one or more peaks (pre-edge features), as shown in Figure 1.5b<sup>21</sup>. The former corresponds to the onset of the transition from a bound state to the continuum, while the latter are due to transitions from the same core level to unoccupied states, as shown in Figure 1.6. As these regions, where all features originate from transitions having the same initial state, are usually well separated, each edge takes the name from the shell corresponding to the initial state. The measurement of the region of the absorption spectrum containing this onset and all features at lower energy associated to a certain shell, together with the first few tens of eV above the energy of the edge (post-edge), is known as X-ray Absorption

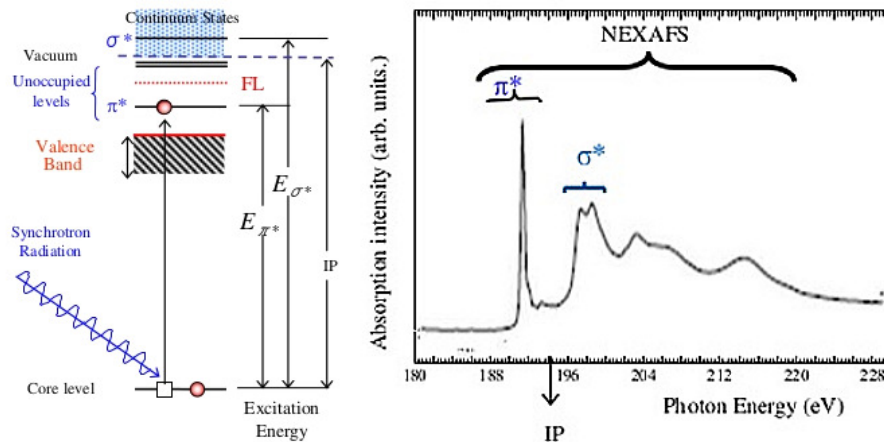


**Figure 1.6:** Schematic representation of some possible excitations activated by XAS (left), originating different features in a NEXAFS spectrum (right). The Ionisation Potential (IP) is indicated, corresponding to the edge (the onset of the transition to the continuum of unbound states); the pre-edge features are due to excitations to unoccupied bound states ( $\pi^*$  in this example)<sup>22,23</sup>.



Near Edge Spectroscopy (XANES) or Near-Edge X-ray Absorption Fine Structure (NEXAFS), as shown in Figure 1.5a. At even higher excitation energies, the cross section displays characteristic oscillations originated by the scattering of the electrons excited to the continuum: the technique studying these features, which provides information on the local geometry of the atoms where the absorption process takes place, is known as Extended X-ray Absorption Fine Structure (EXAFS).

In my work, I have mostly concentrated on the pre-edge region, which reflects the BEs and density of states (DOS) of the unoccupied conduction band states. In addition, the use of linearly polarized radiation also the characterisation of the orientation of the unoccupied orbitals in molecules. In fact, for a given initial and final state, the absorption cross section, in first order perturbation theory and by only considering the terms linearly dependent on the vector potential  $\vec{A}$ , is

$$\sigma \propto \langle \psi_f | \vec{A} \cdot \vec{p} | \psi_i \rangle$$

where  $\vec{p}$  is the momentum operator. This expression can be further expanded, in dipole approximation, to yield a dependence on a term

$$\sigma \propto \vec{\epsilon} \cdot \langle \psi_f | \vec{r} | \psi_i \rangle$$

where  $\vec{\epsilon}$  is the polarization of the radiation and  $\vec{r}$  is the position operator. In order for this factor to be non-zero, the initial and final states must satisfy some constraints related to their symmetry, known as selection rules. In particular, the matrix element  $\langle \psi_f | \vec{r} | \psi_i \rangle$  is zero unless the angular momentum  $l$  of the initial and final state differ by exactly one unit, and the magnetic quantum number  $m$  is unchanged. Also the dot product of this matrix element with the polarization vector introduces a further limitation on the allowed transitions, depending on the orientation of the states with respect to the polarization vector<sup>24-26</sup>. This dependence of the absorption cross section on the orientation of the polarization with respect to the molecule is known as linear dichroism. In particular, for the particular case of a K-edge, where  $|\psi_i\rangle$  has a spherical symmetry, this term is only dependent on the symmetry of the final state, and therefore the cross section is proportional to the component of the polarization vector parallel to the direction in which the orbital is oriented, as shown schematically in Figure 1.7.

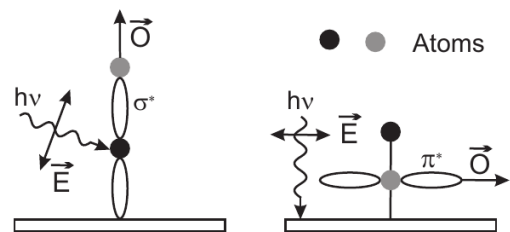


**Figure 1.7:** Schematic representation of the effect of the selection rules on the absorption cross section: depending on the polarization (denoted as  $\vec{E}$  here), only the transitions to the orbitals shown here, pointing in a direction  $\vec{O}$ , are allowed<sup>24</sup>.

Finally, different selection rules have to be considered when the radiation used is circularly polarized. In this case, in fact, the selection rules on the matrix element  $\langle \psi_f | \vec{r} | \psi_i \rangle$  require that the magnetic quantum number of the final and initial state differ, for right and left circularly polarized light, by +1 or -1 respectively. If we also consider the spin-orbit coupling, this selection rule ensures that, when using each of the circularly polarized radiation, only electrons in one of the two spin states (depending on the spin-orbit momentum of the initial state) are excited. This selection rule allows to probe the unoccupied states of the conduction band with spin sensitivity: for this reason, NEXAFS performed with circularly polarized radiation is particularly effective to study the magnetic properties of materials.

The XAS technique is very versatile thanks to the fact that the absorption coefficient can be measured not only directly. In fact, there are also a number of indirect effects of the X-ray absorption process, and in particular of the subsequent relaxation of the system, which can provide a quantitative measurement of the absorption. More specifically, after the excitation, the system is found in a highly excited state, from which it can decay, releasing the energy difference between the excited and relaxed state through various processes. In particular, the system either returns directly to the ground state, or can relax to a state at an intermediate energy, less excited than the one generated by the X-ray absorption. A common de-excitation channel is by emission of photons, a process known as fluorescence. Another common de-excitation process is by Auger, also known as auto-ionisation, which is schematically depicted in Figure 1.8. In this process, the energy obtained by filling the core-hole with an electron from a less bound shell is

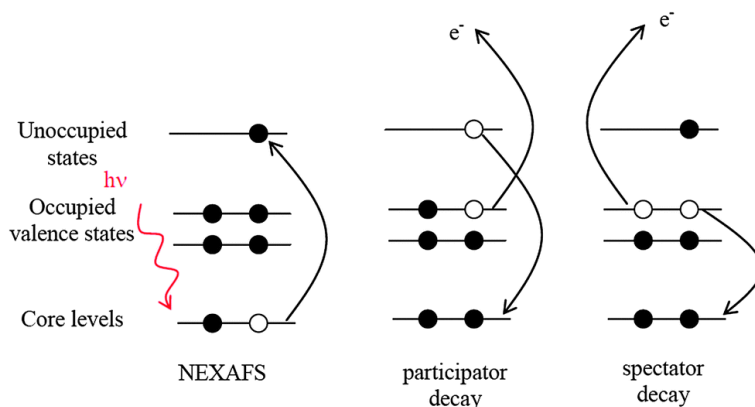


**Figure 1.8:** Schematic representation of the NEXAFS excitation (left) and Auger decay process (centre and right). The core-hole can either be filled by the same electron which had previously been excited (participant decay), or by an electron from another occupied state (spectator decay). The latter process leaves the resulting ion in a higher excited state<sup>27</sup>.

transferred to yet another electron, which acquires sufficient energy to reach the continuum and leave the material (in a process similar to the one which will be described below for Photoelectron Spectroscopy).

All by-products of the de-excitation (including fluorescence photons and Auger electrons) are proportional to the number of excitation processes occurring in the material, and therefore to the absorption cross section: for this reason, they can be used as probes in the measurement of XAS spectra instead of the direct measurement of the transmitted radiation. Depending on the probe employed, this method of measuring XAS is known as Fluorescence or Auger yield for the examples indicated above. Finally, Auger processes lead in turn to a charging of the sample as the Auger electrons are emitted from it: the current required to neutralise this charge, known as drain current, is again proportional to the number of excitations and can be also used as a probe in XAS measurements.

There can be several advantages of using different probes to measure NEXAFS spectra. For example, the use of photons as probe (direct transmission or fluorescence) is ideal for the case of insulating samples, as the emission of electrons is modified if the sample cannot efficiently replace its lost charges. Moreover, the choice of the probe can be used to tune the surface sensitivity of the measurement. In particular, the use of Auger electrons as probes allows to collect only the signal from the first few layers of the material, due to their reduced inelastic mean free path (see Chapter 1.2); on the other hand, fluorescence photons have an escape depth typically of the order of microns, while directly measuring the photon transmission ensures maximum bulk sensitivity<sup>28</sup>.

## 1.4 Core-level Photoelectron Spectroscopy

The experimental technique I have employed most extensively in the characterisation of the systems described in this thesis is Core-level Photoelectron Spectroscopy. This technique is strongly related to NEXAFS, as it is also based on the excitation of core electrons by X-rays; in this case, however, only the excitations to the unbound states of the continuum are considered. In particular, when the electrons acquire sufficient energy from the excitation to overcome their binding energy and the work function of the sample, they are able to escape it and be emitted by photoelectric effect.

Depending on the excitation energy  $h\nu$ , electrons from different shells can be excited to the continuum and be emitted as photoelectrons. The use of vacuum ultraviolet radiation, of few tens of eV photon energy, only allows the valence electrons to be photoemitted. This kind of measurement is usually known as valence band or Ultraviolet Photoemission Spectroscopy (UPS). The use of X-ray radiation provides sufficient energy also for some core level electrons to reach the continuum: this technique is known as core-level or X-ray Photoelectron Spectroscopy (XPS).

In particular, XPS measurements provide information on the BE of the electrons in the atoms of the sample. This technique allows firstly to quantitatively analyse the chemical composition of a material,

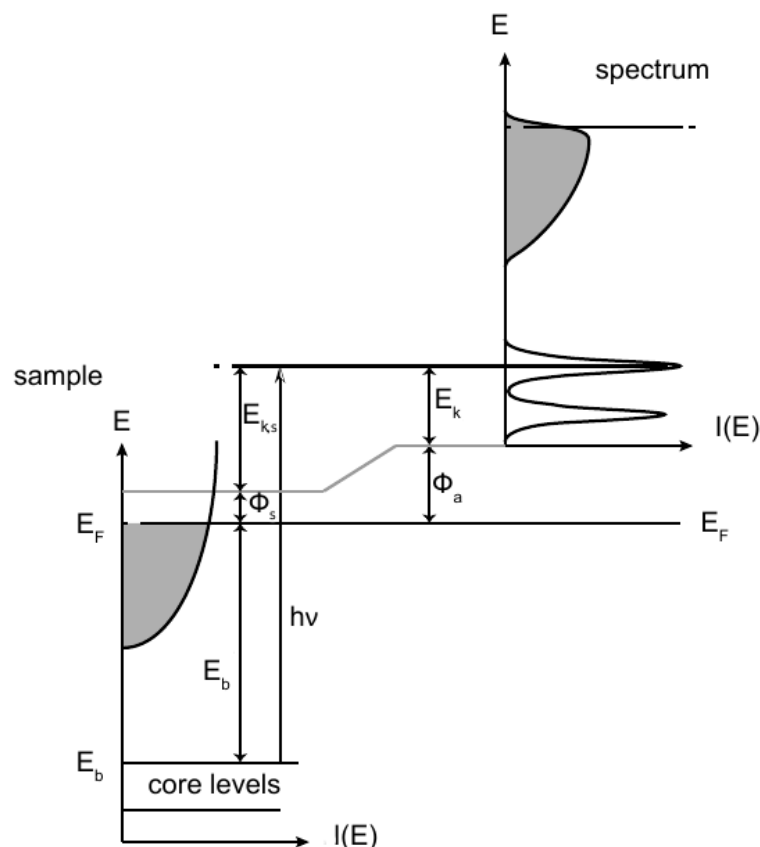


**Figure 1.9:** Schematic representation of the XPS process. The initial state is on the left; the corresponding distribution of the photoelectron kinetic energy is shown on the right.

since the BE of core levels is characteristic of each element. In addition, when atoms form chemical bonds, their electronic configuration is modified, leading to shifts in the core-level binding energies<sup>29,30</sup>. The effect by which the formation of chemical bonds, which only directly involves valence electrons, also affects the BE of core levels, is known as screening. Basically, chemical bonds modify the electron density of the valence states around the atom either by lowering it (when the element is oxidised) or by increasing it (when the element is reduced). The core electrons, then, see a different charge around the nucleus and are more or less attracted to it, respectively<sup>31</sup>. Therefore, positive shifts are observed for oxidised elements and vice versa. These core level shifts (CLS), which are usually of the order of few eV, allow to identify atoms or molecules in different chemical environments. For example, they allow to discriminate between non equivalent atoms inside a molecule. Besides chemical shifts, differences in the core-level BEs also arise between atoms which have the same oxidation state, yet a different coordination, *i.e.* a different number of nearest neighbours. This is the case, for example, of surface and bulk atoms in solids, which show a difference in their core level BE which is typically of the order of hundreds of meV, which are referred to as surface core level shifts (SCLS)<sup>32</sup>. In a similar way, molecules and atoms adsorbed in different sites of a surface can be often distinguished as both their atoms and the ones of the underlying surface show different core level BEs<sup>31,33</sup>.

### Theoretical background

The photoemission process, schematically shown in Figure 1.9, can be usually described as a three-step process<sup>31</sup> consisting of:

1. optical excitation of an electron from a bound state to the continuum;
2. travel of the electron through the material, to the surface;

### 3. exit of the electron from the material.

The theoretical treatment of the optical excitation is analogous to the one already described for XAS. Due to the energy conservation, in a first approximation, the initial state is that of the bound electron, while the final state corresponds to an electron in a plane wave, characterised by a kinetic energy inside the sample  $E_{K,s}$  related to its original BE  $E_B$  by the formula

$$E_{K,s} = h\nu - E_B - \Phi_S$$

where  $E_B$  is defined as a positive quantity and  $\Phi_S$  is the work function of the sample, corresponding to the difference between its vacuum level  $E_V$  and its Fermi level  $E_F$ .

During the travel of the electron through the material, due to the strong interaction of the electron with matter, a significant probability exists that the electron undergoes inelastic scattering processes, losing part of its energy. As already described in Chapter 1.2, the probability of inelastic scattering is a function of the thickness of the material to be crossed and of the kinetic energy of the electrons, while it is independent, to a first approximation, on the chemical composition of the material. This effect leads to an exponential attenuation of the photoemission signal as a function of the depth where the electron was photoemitted

$$I = I_0 e^{-z/\lambda(E_{K,s})}$$

where  $\lambda$  is the electrons' inelastic mean free path (IMFP), whose dependence on  $E_K$  has been shown above in Figure 1.1. Thanks to this fact, XPS, like LEED is an extremely surface-sensitive technique, especially if the photon energy can be tuned in such a way that the photoelectrons have a kinetic energy below 100 eV. This can be achieved by using a tunable X-ray source, such as synchrotron radiation, as will be shown later on in this chapter.

Finally, when the electron exits from the material, it travels through the vacuum and is subsequently collected by a detection apparatus – the electron energy analyser, which will be described below –. This instrument is also characterised by its own work function  $\Phi_A$ . As the electron exits the sample and enters the vacuum first, and the analyser then, its kinetic energy is modified by the difference between the work functions,  $\Phi_A - \Phi_S$ , and therefore, in general, depends on both. However, as can be seen in Figure 1.9, as long as the Fermi level of the sample and analyser are well aligned (which is achieved by connecting both to a common ground), the kinetic energy in the analyser  $E_K$  – which is the quantity which can be measured – is related to  $E_B$  via the formula

$$E_K = h\nu - E_B - \Phi_A$$

in other words, no dependence on  $\Phi_S$  is found, and the knowledge of  $h\nu$  and  $\Phi_A$  (or to be even less stringent, of  $h\nu - \Phi_A$ ) is sufficient to calculate  $E_B$  from the measurement of  $E_K$ .

## Instrument description

An XPS measurement requires two main components: a monochromatic X-ray source and an electron energy analyser<sup>31</sup>. Conventional photon sources exploit the fluorescence following the excitation of gasses or solids to produce monochromatic radiation which is used to excite the electrons. Alternatively, synchrotron radiation can be employed as a light source for Photoemission Spectroscopy. This kind of source has several advantages with respect to conventional sources, among which two have been extensively exploited throughout my research work:

- high brilliance of the photon beam;
- tunability of the photon energy.

The brilliance of the photon beam is a quantity which depends on the photon flux per surface area, and is also a function of the angular spreading of the beam. The high photon flux is important firstly to achieve a high signal-to-noise ratio in the measurement, and therefore to reduce the data acquisition times. In addition, it allows the beam to be monochromatised to achieve a very high photon resolving power  $E/\Delta E$ , of about  $10^4$ .

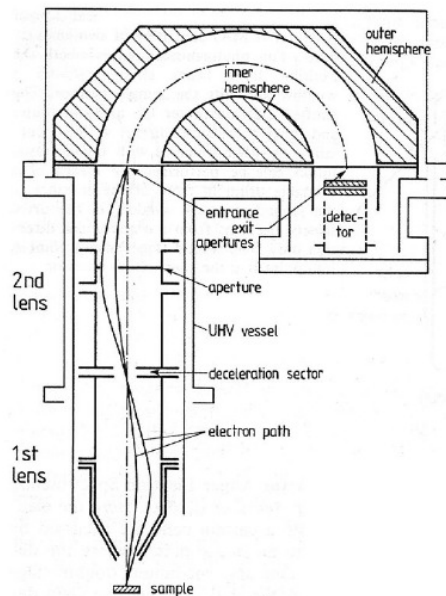


**Figure 1.10:** Schematic representation of a Concentric Hemispherical Analyser (above), together with the retarding lenses (left) and detector (right). The trajectory of the electrons having the selected kinetic energy is also shown, going from the bottom left to the right.

The electron energy analyser is the instrument which is in charge of the detection of the electrons and of the measurement of their kinetic energy. The type of analyser I have employed in my research is the Concentric Hemispherical Analyser (CHA), which is composed of two concentric metallic hemispheres, of radius  $R_1$  and  $R_2$ , separated by a vacuum region, which is shown in the top part of Figure 1.10. Two slits are located at an intermediate distance between the hemispheres, at opposite sides of the analyser, for the entrance and exit of the electrons respectively. By applying a different potential ( $V_2$  and  $V_1$ ) to the two hemispheres, an electric field is generated between them, which deflects charged particles passing between the two hemispheres. Due to the electric field, a condition exists by which only those electrons having a kinetic energy given by

$$E_K = e(V_{OUT} - V_{IN}) \left( \frac{R_{OUT}}{R_{IN}} - \frac{R_{IN}}{R_{OUT}} \right)^{-1}$$

– where  $e$  is the electron charge – follow a concentric trajectory around the geometric centre of the analyser and are able to reach the exit slit, while the others hit the hemispheres or the slit instead. Therefore, the CHA ensures that only the electrons having a specific kinetic energy reach the exit slit, and this energy (pass energy, PE) can be set by modifying the potentials  $V_1$  and  $V_2$ . An electro-multiplier and a detector are

placed after the exit slit of the analyser to count the number of electrons crossing it per unit of time.

The energy resolution of the analyser is in first approximation proportional to the PE of the electrons. For this reason, the CHA is operated in constant pass energy mode: this means that before entering the analyser, all electrons are retarded by an electrostatic potential in such a way that those electrons originally at the energy to be measured,  $E_K$ , enter the hemispheres with an energy corresponding to the PE. This ensures that the energy resolution of the analyser is constant throughout the measurement. In addition, as the PE is usually at least one order of magnitude lower than  $E_K$ , it improves the experimental resolution by the same factor.

## Data analysis

The photoemission spectrum corresponds to a curve describing the number of photoelectrons emitted per unit of time as a function of their BE in the material. As already mentioned, to calibrate the BE scale, both  $h\nu$  and  $\Phi_A$  must be precisely known, to correctly calculate  $E_B$ . Since the BE value of bound electrons is referred (by definition) to the Fermi level, the BE scale can be calibrated by measuring the kinetic energy of those electrons having  $E_B = 0$ , which corresponds to those at the Fermi level. Figure 1.9 schematically shows the typical appearance of a photoemission spectrum (right), and the electronic structure of the system originating it (left). The photoemission spectrum of core levels, in particular, is composed of peaks centred around the value  $E_B$ , which to a zero-order approximation corresponds to their BE in the solid. Actually, the value measured by photoemission spectroscopy overestimates  $E_B$ , as it neglects the effect of the relaxation of the atom after the photoemission process: this is known as Koopmans' approximation.

The lineshape of the photoemission peaks depends on the contribution of several factors, including:

- intrinsic broadening due to the finite core-hole lifetime;
- experimental resolution;
- inhomogeneous broadening;

- inelastic contribution.

In particular, the finite life-time  $\tau$  of the core-holes leads to an uncertainty on  $E_B$  of quantum origin, which introduces a broadening having a Lorentzian lineshape whose FWHM ( $L = 2\gamma$ ) is inversely proportional to  $\tau$ :

$$I_L(E) = I_0 \frac{\gamma/2\pi}{(E - E_B)^2 + (\gamma/2)^2}$$

The experimental resolution depends both on the energy resolution of the radiation and of the analyser. The inhomogeneous contribution is due to atoms in defective configuration, which have a local environment slightly different from the one of the other atoms. This different environment causes small differences in the core level shifts, which appear in the spectrum as a broadening of the lineshape. Finally, the inelastic contribution is due to the scattering with phonons in solids. Due to the energy dispersion in phonons, this scattering leads to the inelastic loss or acquisition of small amounts of energy by the photoelectrons, which results in small shifts in the measured kinetic energy. These latter three contributions can be accounted for by introducing a Gaussian broadening, which is convoluted to the intrinsic lineshape.

In addition, an important contribution to the lineshape is given by the excitation by photoelectrons of electron-hole pairs close to the Fermi level. This process has a probability which depends on the density of states close to the Fermi level, and is therefore particularly evident in metals. This process leads to a loss of energy of the photoelectrons, and therefore appears as an asymmetric broadening towards higher BE in photoemission spectra. This contribution is usually modelled by modifying the Lorentzian lineshape into the function commonly referred to as Donjach-Šunjić lineshape<sup>34</sup>:

$$DS_{\gamma,\alpha}(E) = \frac{\Gamma(1-\alpha)}{(E^2 + \gamma^2)^{(1-\alpha)/2}} \cdot \cos\left(\frac{\pi\alpha}{2} + (1-\alpha)\operatorname{atan}\left(\frac{E}{\gamma}\right)\right)$$

where  $\Gamma(x)$  is the Euler gamma function.  $\alpha$  is the asymmetry parameter, which increases for larger probabilities of electron-hole pair excitation (as is the case in transition metals), while the function reverts to a perfectly symmetric Lorentzian lineshape when this values becomes zero.

Another important feature of XPS is that it is a quantitative technique, as the number of photoelectrons is proportional to the density of the atoms originating it. In order to compare the signal of different core levels, however, several considerations have to be taken into account. Firstly, to properly evaluate the photoemission intensity, the signal must be integrated on the BE range of each component. Secondly, the photoemission intensity is proportional to the cross section of the optical excitation: this factor can be calculated theoretically and is found tabulated<sup>35</sup>. Finally, when investigating a 3D structure with several layers, the signal of each layer must be separately corrected to take into account the attenuation due to the electron IMFP.

Besides the photoemission peaks, all spectra also contain a continuous background, which is originated by photoelectrons which have undergone inelastic scattering processes and therefore exit the sample with a reduced kinetic energy. This background is increasing towards lower values of photoelectron kinetic energy, and therefore appears as a crescent function of  $E_B$ . Provided the spectral region being analysed is small enough (few eV), this background can be approximated by a polynomial: in particular, it can often be approximated with a linear dependence on  $E_B$ .

## 1.5 Experimental setup

Most of my experimental work has been performed at two facilities: the Surface Science Laboratory, jointly established by the Physics Department of the University of Trieste and by the Elettra Sincrotrone Trieste research facility, and the SuperESCA beamline, which uses the synchrotron radiation source of the latter facility. In the following paragraphs, I will briefly introduce the equipment available at both laboratories.



### 1.5.1 Surface Science Laboratory

The experimental setup of the Surface Science Laboratory (SSL), shown in Figure 1.11, consists of a large vacuum chamber with several instruments mounted on its wall, including a sputter gun for sample preparation, an electron energy analyser (CHA) with two conventional X-ray sources (an Mg source and a monochromatised Al source) for XPS, one LEED, one SPA-LEED and one quadrupole mass spectrometer for residual gas analysis and Temperature Programmed Desorption experiments.

The sample is mounted on a manipulator with five degrees of freedom (three translations, polar and azimuthal angle). This manipulator is mounted eccentrically on the cover of the chamber, which is rotatable: this allows the manipulator (and therefore the sample) to be moved in front of each instrument depending on the measurement to be performed. All degrees of freedom, of both the sample and chamber, are motorised and controlled by LabVIEW software. The same software is also used to control the data acquisition of the instrumentation.

In particular, the sample is mounted on a sample-holder which can be removed by a transfer and load-lock system without venting the vacuum chamber. It is usually spot-welded to a Ta rod, which provides electrical and thermal contact, and its temperature is read by a K-type thermocouple. Three filaments, mounted just behind the sample, are used to heat it. The heating can be performed either exclusively by radiative transmission from the filaments (when the sample is grounded) or, in addition to this method, by simultaneous electron bombardment: this is achieved by applying a positive potential of a few hundred volts to the sample, which accelerates the electrons emitted by the filament by thermionic effect against the back of the sample. Cooling of the sample is possible by means of a cryostat filled with liquid nitrogen.

For the preparation of the sample, gasses can be admitted into the chamber at a controlled pressure through leak valves mounted on a separate gas line, while evaporators can be mounted on the wall of the chamber to deposit metals or other elements from a solid. Finally, to be able to locally reach high pressures (of the order of  $10^{-3}$  mbar) on the surface of the sample, a doser can be used. This is a tube which can be

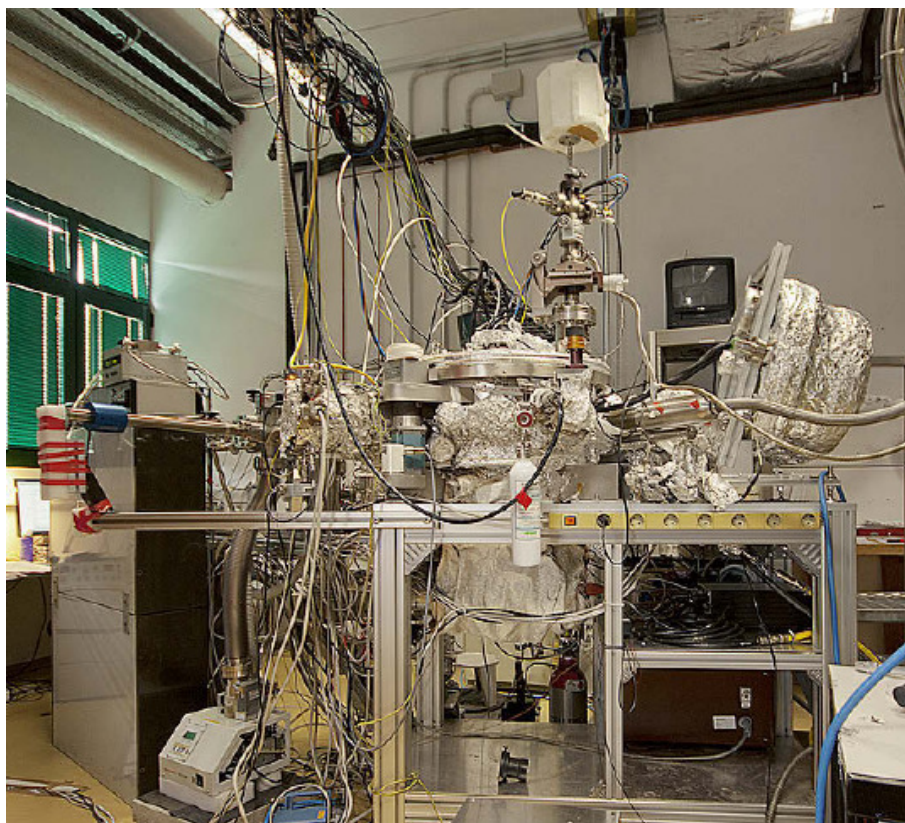


**Figure 1.11:** Surface Science Laboratory experimental chamber. The electron energy analyser is visible to the right, adjacent to the X-ray tube. The load-lock is visible on the left, beside the SPA-LEED.

brought at distances very close to the sample (below 1 mm), through which gas can be dosed in a controlled flux by the use of a leak valve; the reduced space between the sample and the tube ensures that the gas is partially trapped between the tube and the sample and therefore its pressure within that region is by at least one order of magnitude higher than in the rest of the chamber.

### 1.5.2 SuperESCA beamline

The SuperESCA beamline is optimised for spectroscopy measurements using soft X-rays with a photon energy of few hundreds eV<sup>36</sup>. The synchrotron radiation is produced by an insertion device, in particular by two consecutive 46-period undulators. The radiation thus produced has a distribution consisting of several harmonics of a fundamental frequency, with a FWHM of a few eV. The frequency at which the harmonics are centred can be shifted by changing the magnetic field inside the undulator, which is achieved by modifying the distance between the two arrays at the opposite sides of the electron beam. This photon energy distribution is further monochromatised by a grating (blaze profile), to achieve a maximum resolving power of  $1 \times 10^4$  at a typical photon energy of the order of few hundreds of eV. Besides the advantages of benefiting from this very high photon energy resolution, a high photon flux up to  $1 \times 10^{12}$  photons/s is available at the sample, depending on the photon energy.

The experimental setup is divided into a preparation chamber, provided with a sputter gun and other

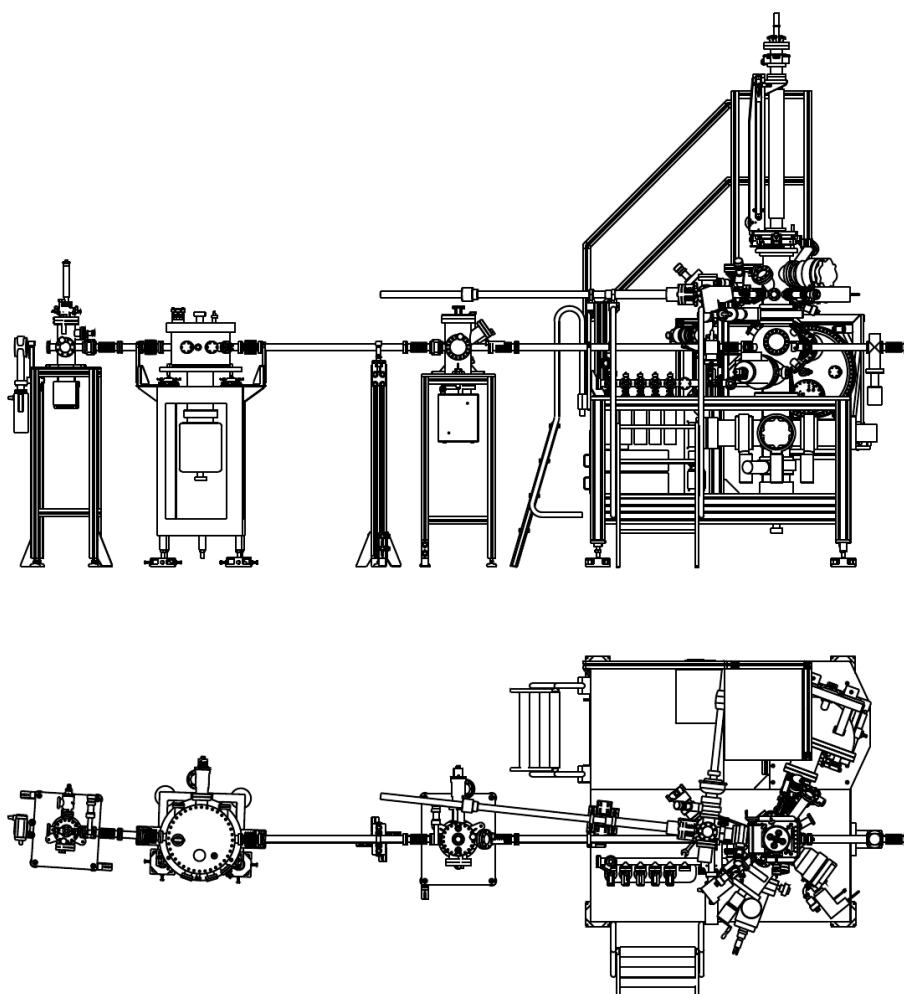


**Figure 1.12:** Technical drawing of the SuperESCA end-station at Elettra. The synchrotron radiation beam enters from the left and reaches the experimental chamber on the right side, where the electron energy analyser is also visible. Recognizable elements include the two-chamber structure, with the preparation chamber above the experimental chamber, the manipulator, and the gas line.



instrumentation, analogous to the one available at SSL, for sample preparation, and an experimental chamber with a LEED and the electron energy analyser (with a 150 mm radius). This analyser is coupled to a delay-line detector, which allows to measure spectra in snap-shot mode, rather than by counting the electrons for one kinetic energy value at a time. The snap-shot mode is based on the fact that the position where the electrons with an energy slightly different than the PE exit a CHA is to a first approximation linear with their energy. Therefore, by measuring the position where electrons impinge on the detector, it is possible to determine the kinetic energy of all electrons within a certain interval from the selected energy.

The high flux available at the sample, by allowing fast acquisition times (below 1 s for snap-shot mode, few seconds in scanning mode), make the SuperESCA beamline ideal to follow processes in real time, including chemical reactions on surfaces and the epitaxial growth of thin films and 2D materials<sup>37</sup>.

The sample is usually mounted on a manipulator with 4 degrees of freedom (three translations and polar angle). The sample heating, cooling and temperature measurement are performed in an analogous way as at SSL.

## 1.6 Density Functional Theory calculations

To acquire more in-depth knowledge on the systems we have studied, our experimental data were often complemented with Density Functional Theory calculations<sup>38,39</sup> performed by collaborating groups. The aim of these calculations was mainly two-fold: firstly, to obtain a structural characterisation of the systems, and secondly, to correlate each component we observed in the photoemission spectrum with the atoms originating it. In the following paragraphs, for the sake of completeness, I will briefly report some details about these calculations.

For the first of these aims, our collaborators calculated the spatial coordinates of each atom in the structure which minimise the energy of the system. This was obtained by using DFT with exchange-correlation effects included at the level of the PBE-GGA<sup>40</sup> functional. The Projector Augmented Wave<sup>41</sup> (PAW) method was used, as implemented in VASP<sup>42,43</sup>.

In order to describe metal-supported Gr layers, the metal surfaces were modelled using a slab with a thickness of 5 layers, with the atoms of the 2 bottom layers kept fixed at their bulk positions, while all the other atoms were allowed to relax, overlayed by a Gr sheet. A vacuum interspace of at least 15 Å between metal layers was used to minimize the interaction between periodic images of the slab along the direction perpendicular to the surface, resulting in a super-cell typically of 24 Å along the z axis. The lateral size of the cell was chosen depending on the substrate, in order to match the moiré supercell formed by Gr on that metallic surface. Typically, this size is of the order of (10 × 10) unit cells of the substrate, resulting in a slab containing well above 500 atoms.

To address the second aim of our calculations, final state core level BE can be accurately computed in the pseudopotential formalism by describing the excited atom by a pseudopotential generated in the core-excited configuration<sup>44</sup>. In this formulation, the core-level BE is given by the pseudopotential total energy difference between the initial and final state system, supplemented by an additive constant. Differences of core level energies are accurately reproduced, as this constant cancels out when calculating BE shifts<sup>45</sup>.

This kind of calculations have been extensively used in the experiments described in the following chapters, as they allowed us to interpret the photoemission spectra by indicating the atoms giving rise to each different component we could observe.

## References

- [1] P. Woodruff. *Modern Techniques of Surface Science* (Cambridge University Press, **2016**). doi:10.1017/cbo9781139149716.
- [2] M. Batzill. The surface science of graphene: Metal interfaces, CVD synthesis, nanoribbons, chemical modifications, and defects. *Surf. Sci. Rep.* (**2012**) 67: 83–115. doi:10.1016/j.surfrep.2011.12.001.
- [3] L. Zhong, J. Li, Y. Li, H. Lu, H. Du, L. Gan, C. Xu, S. W. Chiang, F. Kang. Unraveling the influence of metal substrates on graphene nucleation from first-principles study. *J. Phys. Chem. C* (**2016**) 120: 23239–23245. doi:10.1021/acs.jpcc.6b06750.
- [4] E. Loginova, N. C. Bartelt, P. J. Feibelman, K. F. McCarty. Evidence for graphene growth by C cluster attachment. *New J. Phys.* (**2008**) 10: 093026. doi:10.1088/1367-2630/10/9/093026.
- [5] P. Lacovig, M. Pozzo, D. Alfè, P. Vilmercati, A. Baraldi, S. Lizzit. Growth of dome-shaped carbon nanoislands on Ir (1 1 1): The intermediate between carbide clusters and quasi-free-standing graphene. *Phys. Rev. Lett.* (**2009**) 103: 166101. doi:10.1103/physrevlett.103.166101.
- [6] H. Chen, W. Zhu, Z. Zhang. Contrasting behavior of carbon nucleation in the initial stages of graphene epitaxial growth on stepped metal surfaces. *Phys. Rev. Lett.* (**2010**) 104: 186101. doi:10.1103/physrevlett.104.186101.
- [7] S. Lizzit, A. Baraldi. High-resolution fast X-ray photoelectron spectroscopy study of ethylene interaction with Ir (1 1 1): From chemisorption to dissociation and graphene formation. *Cat. Tod.* (**2010**) 154: 68–74. doi:10.1016/j.cattod.2010.05.028.
- [8] H. Tetlow, J. Posthuma de Boer, I. J. Ford, D. D. Vvedensky, D. Curcio, L. Omiciuolo, S. Lizzit, A. Baraldi, L. Kantorovich. Ethylene decomposition on Ir (1 1 1): initial path to graphene formation. *Phys. Chem. Chem. Phys.* (**2016**) 18: 27897–27909. doi:10.1039/c6cp03638d.
- [9] E. Loginova, N. C. Bartelt, P. J. Feibelman, K. F. McCarty. Factors influencing graphene growth on metal surfaces. *New J. Phys.* (**2009**) 11: 063046. doi:10.1088/1367-2630/11/6/063046.
- [10] Q. Yu, J. Lian, S. Siriponglert, H. Li, Y. P. Chen, S.-S. Pei. Graphene segregated on Ni surfaces and transferred to insulators. *Appl. Phys. Lett.* (**2008**) 93: 113103. doi:10.1063/1.2982585.
- [11] R. Addou, A. Dahal, P. Sutter, M. Batzill. Monolayer graphene growth on Ni (1 1 1) by low temperature chemical vapor deposition. *Appl. Phys. Lett.* (**2012**) 100: 021601. doi:10.1063/1.3675481.
- [12] E. Miniussi, M. Pozzo, T. O. Menteş, M. A. Niño, A. Locatelli, E. Vesselli, G. Comelli, S. Lizzit, D. Alfè, A. Baraldi. The competition for graphene formation on Re(0 0 1): A complex interplay between carbon segregation, dissolution and carburisation. *Carbon* (**2014**) 73: 389–402. doi:10.1016/j.carbon.2014.02.081.
- [13] C. Davisson, L. H. Germer. Diffraction of electrons by a crystal of nickel. *Phys. Rev.* (**1927**) 30: 705–740. doi:10.1103/physrev.30.705.
- [14] L. De Broglie. Recherches sur la théorie des Quanta. *Ann. Phys.* (**1925**) 10: 22–128. doi:10.1051/anphys/192510030022.
- [15] R. E. Schlier, H. E. Farnsworth. Structure and adsorption characteristics of clean surfaces of germanium and silicon. *J. Chem. Phys.* (**1959**) 30: 917–926. doi:10.1063/1.1730126.
- [16] M. P. Seah, W. A. Dench. Quantitative electron spectroscopy of surfaces: A standard data base for electron inelastic mean free paths in solids. *Surf. Interface Anal.* (**1979**) 1: 2–11. doi:10.1002/sia.740010103.

- [17] E. Bauer. In W. Schommers, P. von Blanckenhagen, (eds.) *Structure and Dynamics of Surfaces* (Springer-Verlag Berlin Heidelberg, **1987**).
- [18] G. Ertl, J. Küppers. *Low Energy Electrons and Surface Chemistry* (Wiley-VCH Verlag GmbH, **1985**), Chapter 9. 201–266.
- [19] U. Scheithauer, G. Meyer, M. Henzler. A new LEED instrument for quantitative spot profile analysis. *Surf. Sci.* (**1986**) 178: 441–451. doi:10.1016/0039-6028(86)90321-3.
- [20] P. Fornasini. Introduction to x-ray absorption spectroscopy. In S. Mobilio, F. Boscherini, C. Meneghini, (eds.) *Synchrotron Radiation* (Springer-Verlag Berlin Heidelberg, **2014**), Chapter 6. 181–211. doi:10.1007/978-3-642-55315-8\_6.
- [21] M. Benfatto, C. Meneghini. A close look into the low energy region of the XAS spectra: The XANES region. In S. Mobilio, F. Boscherini, C. Meneghini, (eds.) *Synchrotron Radiation* (Springer-Verlag Berlin Heidelberg, **2014**), Chapter 7. 213–240. doi:10.1007/978-3-642-55315-8\_7.
- [22] I. Shimoyama, Y. Baba, T. Sekiguchi, K. G. Nath. NEXAFS spectra of an epitaxial boron nitride film on Ni(111). *J. Electron Spectrosc. Relat. Phenom.* (**2004**) 137-140: 573–578. doi:10.1016/j.elspec.2004.02.040.
- [23] <https://www.slideshare.net/stsforum2016/nano-materials-to-devices-kr-koswatta>. Web site. Nano Materials to Devices - K.R Koswatta.
- [24] A. Nefedov, C. Wöll. Advanced applications of NEXAFS spectroscopy for functionalized surfaces. In G. Bracco, B. Holst, (eds.) *Surface Science Techniques* (Springer-Verlag Berlin Heidelberg, **2013**), volume 51. 277–303. doi:10.1007/978-3-642-34243-1\_10.
- [25] D. A. Outka, J. Stöhr, J. P. Rabe, J. D. Swalen. The orientation of Langmuir–Blodgett monolayers using NEXAFS. *J. Chem. Phys.* (**1988**) 88: 4076–4087. doi:10.1063/1.453862.
- [26] J. Stöhr. *NEXAFS Spectroscopy* (Springer-Verlag Berlin Heidelberg, **1992**). doi:10.1007/978-3-662-02853-7.
- [27] F. Ciccullo, S. A. Savu, M. Glaser, M. L. M. Rocco, T. Chassé, M. B. Casu. Island shape and electronic structure in diindenoperylene thin films deposited on Au(110) single crystals. *Phys. Chem. Chem. Phys.* (**2016**) 18: 13693–13700. doi:10.1039/c6cp00259e.
- [28] H. Lüth. Morphology and structure of surfaces, interfaces and thin films. In *Solid Surfaces, Interfaces and Thin Films* (Springer-Verlag Berlin Heidelberg, **2010**), Chapter 3. 5th edition, 125–130. doi:10.1007/978-3-319-10756-1\_3.
- [29] C. S. Fadley, S. B. M. Hagstrom, M. P. Klein, D. A. Shirley. Chemical effects on core-electron binding energies in iodine and europium. *J. Chem. Phys.* (**1968**) 48: 3779–3794. doi:10.1063/1.1669685.
- [30] K. Siegbahn. Electron spectroscopy - an outlook. *J. Electron Spectrosc. Relat. Phenom.* (**1974**) 5: 3–97. doi:10.1016/0368-2048(74)85005-x.
- [31] S. Hüfner. *Photoelectron spectroscopy: principles and applications*. (Springer-Verlag Berlin Heidelberg, **2003**), 3rd edition. doi:10.1007/978-3-662-09280-4.
- [32] P. H. Citrin, G. K. Wertheim, Y. Baer. Core-level binding energy and density of states from the surface atoms of gold. *Phys. Rev. Lett.* (**1978**) 41: 1425–1428. doi:10.1103/physrevlett.41.1425.
- [33] A. Baraldi, S. Lizzit, G. Paolucci. Identification of atomic adsorption site by means of high-resolution photoemission surface core-level shift: oxygen on Ru(10 $\bar{1}$ 0). *Surf. Sci.* (**2000**) 457: L354–L360. doi:10.1016/s0039-6028(00)00394-0.

- [34] S. Doniach, M. Šunjić. Many-electron singularity in X-ray photoemission and X-ray line spectra from metals. *J. Phys. C* (**1970**) 3: 285–291. doi:10.1088/0022-3719/3/2/010.
- [35] J. Yeh, I. Lindau. Atomic subshell photoionization cross sections and asymmetry parameters:  $1 \leq z \leq 103$ . *At. Data Nucl. Data Tables* (**1985**) 32: 1–155. doi:10.1016/0092-640x(85)90016-6.
- [36] A. Abrami, M. Barnaba, L. Battistello, A. Bianco, B. Brena, G. Cautero, Q. H. Chen, D. Cocco, G. Comelli, S. Contrino, F. DeBona, S. Di Fonzo, C. Fava, P. Finetti, P. Furlan, A. Galimberti, A. Gambitta, D. Giuressi, R. Godnig, W. Jark, S. Lizzit, F. Mazzolini, P. Melpignano, L. Olivi, G. Paolucci, R. Pugliese, S. N. Qian, R. Rosei, G. Sandrin, A. Savoia, R. Sergo, G. Sostero, R. Tommasini, M. Tudor, D. Vivoda, F. Wei, F. Zanini. Super ESCA: First beamline operating at ELETTRA. *Rev. Sci. Instrum.* (**1995**) 66: 1618–1620. doi:10.1063/1.1145862.
- [37] A. Baraldi, G. Comelli, S. Lizzit, M. Kiskinova, G. Paolucci. Real-time X-ray photoelectron spectroscopy of surface reactions. *Surf. Sci. Rep.* (**2003**) 49: 169 – 224. doi:https://doi.org/10.1016/S0167-5729(03)00013-X.
- [38] P. Hohenberg, W. Kohn. Inhomogeneous electron gas. *Phys. Rev.* (**1964**) 136: B864–B871. doi:10.1103/PhysRev.136.B864.
- [39] W. Kohn, L. J. Sham. Self-consistent equations including exchange and correlation effects. *Phys. Rev.* (**1965**) 140: A1133–A1138. doi:10.1103/PhysRev.140.A1133.
- [40] J. P. Perdew, K. Burke, M. Ernzerhof. Generalized gradient approximation made simple. *Phys. Rev. Lett.* (**1996**) 77: 3865–3868. doi:10.1103/PhysRevLett.77.3865.
- [41] P. E. Blöchl. Projector augmented-wave method. *Phys. Rev. B* (**1994**) 50: 17953–17979. doi:10.1103/PhysRevB.50.17953.
- [42] G. Kresse, J. Furthmüller. Efficient iterative schemes for ab initio total-energy calculations using a plane-wave basis set. *Phys. Rev. B* (**1996**) 54: 11169–11186. doi:10.1103/PhysRevB.54.11169.
- [43] G. Kresse, D. Joubert. From ultrasoft pseudopotentials to the projector augmented-wave method. *Phys. Rev. B* (**1999**) 59: 1758–1775. doi:10.1103/PhysRevB.59.1758.
- [44] E. Pehlke, M. Scheffler. Evidence for site-sensitive screening of core holes at the Si and Ge (0 0 1) surface. *Phys. Rev. Lett.* (**1993**) 71: 2338–2341. doi:10.1103/physrevlett.71.2338.
- [45] L. Bianchettin, A. Baraldi, S. de Gironcoli, S. Lizzit, L. Petaccia, E. Vesselli, G. Comelli, R. Rosei. Geometric and electronic structure of the N/Rh(1 0 0) system by core-level photoelectron spectroscopy: Experiment and theory. *Phys. Rev. B* (**2006**) 74: 045430. doi:10.1103/physrevb.74.045430.

## Chapter 2

# Factors controlling the Gr-metal interaction

In the first part of my research, I investigated the origin of the interaction of Gr with metallic substrates. This topic is of particular interest for the use of Gr in electronics, as Gr needs to be supported for most of those applications; however, when it is supported on a surface, its properties can be significantly altered with respect to the free-standing configuration. For example, Gr must be provided with conductive contacts for its use in nanoelectronic applications, or in sensoristics, and the resistance at these contacts must be low enough, as the performance of the device would be negatively affected. From this point of view, a strong interaction with the substrate would be beneficial, at least locally<sup>1,2</sup>. This issue, moreover, should be addressed already in the early stages of the Gr synthesis, as it is not trivial to establish a good contact at a later stage<sup>3</sup>: despite recent progress in Gr transfer techniques, the performance of contacts still remains a crucial issue for Gr applications in electronics<sup>4</sup>. The interaction of Gr with metal surfaces, on the other hand, induces charge transfer processes, re-hybridization and changes to its band structure<sup>2,5,6</sup>. A good understanding of the interactions occurring at the interfaces between Gr and its substrate is therefore required to create high-performance Gr-based devices<sup>5</sup>, by developing interfaces which balance the need for high-quality contacts with a limited repercussion on the band structure of Gr.

The issue of providing good Gr-metal contacts can be effectively addressed by synthesizing Gr directly on a metal surface by means of Chemical Vapour Deposition (CVD): this technique, in fact, allows to obtain high quality Gr monolayers with a low density of defects<sup>7</sup> and in direct contact with a conducting surface. The effects induced on Gr by a metallic substrate, on the other hand, require an extensive treatment, as metallic surfaces where Gr can be grown or transferred are very different from each other and therefore characterised by a variable degree of interaction with it<sup>8,9</sup>. In fact, some surfaces show a weak coupling based on vdW interactions: in these systems, the Gr-surface separation is close to the interlayer distance of graphite (around 3 Å), such as Ir(111)<sup>10</sup>, Pt(111)<sup>11</sup> and copper surfaces<sup>12</sup>. Other surfaces, instead, display a much stronger interaction, such as Ru(0001)<sup>13–15</sup> and Re(0001)<sup>16,17</sup>: in these cases, the Gr-surface distance is reduced, the nearest carbon atoms lying at approximately 2 Å from the metallic surface. Buckling of the Gr layer is present on these kinds of substrates when the lattice parameter of Gr is significantly different from that of the substrate, leading to a non-uniform degree of Gr-metal interaction on the local scale<sup>9</sup>. In addition, the band structure of Gr is strongly modified, with the disappearance of the Dirac cones and the opening of a band gap at the Fermi level<sup>18</sup>. The alterations to the electronic structure in the former case can be explained in terms of the difference between the work functions of Gr and of the metal substrate, which induces a charge transfer at the interface and a shift of the Fermi level, resulting in the formation of a surface dipole moment<sup>5</sup>. For strongly interacting systems, however, the mechanisms determining the interaction strength between Gr and its metal substrate are much more complex<sup>9,18</sup>.

One factor possibly leading to this variable interaction is the mismatch between the lattice parameter of Gr and that of the underlying surface, which induces a strain into the Gr layer and a moiré structure leading to a different degree of re-hybridization on different C atoms<sup>19,20</sup>. The geometry of the metallic surface not only causes strain on Gr as its lattice parameter adapts to that of the substrate, but could also

influence its electronic properties. It has been demonstrated, in fact, that Gr on Cu has a different degree of doping depending on the symmetry of the surface over which it has been grown: (1 1 1), (1 1 0) or (1 0 0)<sup>21</sup>. It is also interesting to notice that two metals whose lattice parameter is closest to that of Gr, *i.e.* nickel and cobalt, are also among those which exhibit a strongest interaction with Gr<sup>9</sup>.

On the other hand, the chemical bonding between molecules and surfaces can be attributed to a coupling between the valence orbitals of the adsorbates and the metal *d*-bands. In this case, it would be possible to quantify the interaction by extending the Hammer and Nørskov model for the chemisorption of molecules on transition and noble metal surfaces<sup>22</sup> also to Gr/metal systems<sup>13,23</sup>. According to this model, the coupling is maximum when the orbitals of the molecule lie close in energy to the metal *d*-band centre: in fact, it has been shown that all surfaces which exhibit the strongest interaction with Gr have a *d*-band centre lying around 1 eV below the Fermi level, whereas the interaction weakens as the barycentre moves further away from it<sup>9</sup>.

The aim of the combined experimental and theoretical investigation described in this chapter was therefore to decouple the contributions arising from the geometrical (lattice mismatch) and chemical (elemental composition of the substrate) properties of the surface on the interaction between Gr and metals. Furthermore, we investigated how C 1s core level shifts are linked to the surface chemical reactivity of the supporting metal substrates. In fact, high energy-resolution photoelectron spectroscopy of the C 1s core level allows to study the electronic structure of metal-supported Gr layers in great detail<sup>8</sup>: for example, this technique has proved particularly effective in determining the doping of weakly interacting Gr and in demonstrating its relationship with the work function of surfaces, as the energy shift of the core levels reflects that of the valence band<sup>24</sup>. In the case of strongly interacting Gr, however, chemical bonding between the substrate and Gr introduces a chemical shift in the core levels and the BE does not depend exclusively on doping any more.

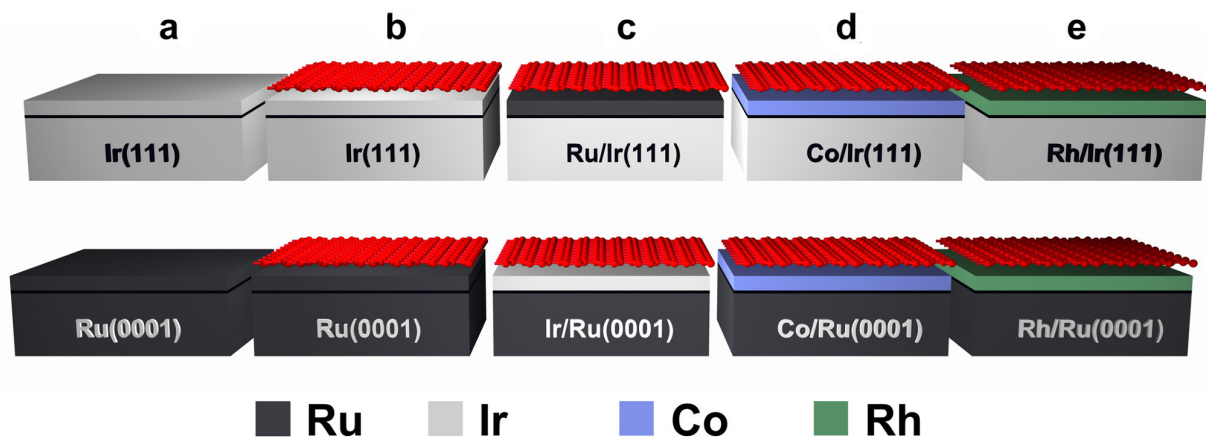


**Figure 2.1:** Schematic outline of the experimental procedure followed in the present work. a: Pristine monocrystalline Ir(1 1 1) (top row) and Ru(0 0 1) (bottom row) surfaces. b: Gr growth. c-e: Intercalation of different metallic species at the Gr/metal interface.

We have achieved this by a systematic work where different metallic species have been intercalated at Gr-metal interfaces, following the scheme reported in Figure 2.1. Intercalation is in fact a method which has proven effective in decoupling Gr from the strongly interacting Ni(1 1 1) surface<sup>25</sup>. The intercalation process, in fact, modifies the chemical composition of the first surface layer while preserving the symmetry and the lattice constant of the substrate, provided the intercalated layer is of monoatomic thickness. In order to make an extensive comparison in controlled and reproducible conditions on model systems, different single-crystal close-packed metallic surfaces were used, one which interacts strongly with Gr (Ru(0 0 1), which has a lattice parameter  $l_{Ru} = 2.70 \text{ \AA}$ ) and one which interacts weakly with it (Ir(1 1 1),  $l_{Ir} = 2.72 \text{ \AA}$ ). Both substrates have a lattice parameter which is larger than that of Gr ( $l_{Gr} = 2.46 \text{ \AA}$ ), and the lattice mismatch is larger for the latter surface by about 10%. The intercalated species were also chosen

in such a way that each of them possesses a different degree of interaction with Gr: besides Ru and Ir, we employed Rh (which exhibits an intermediate interaction strength with Gr) and Co (which is even more strongly interacting than Ru).

## 2.1 Graphene growth on Ir (1 1 1)

The synthesis of Gr on Ir (1 1 1) was performed using a Temperature Programmed CVD Growth technique, as described in Section 1.1.1, consisting of repeated cycles of annealing up to 1400 K in  $5 \times 10^{-8}$  mbar of  $C_2H_4$ . This procedure was developed in order to maximize coverage and minimise the formation of rotational domains: it is known, in fact, that Gr can grow on Ir (1 1 1) both aligned or not to the crystallographic directions of the substrate<sup>26</sup>.

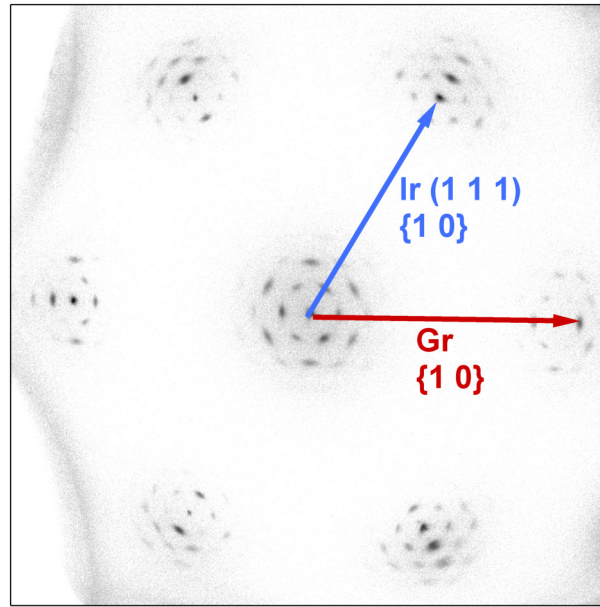


**Figure 2.2:** SPA-LEED pattern of Gr grown on Ir (1 1 1) ( $E = 110$  eV).

The long-range ordering of the Gr layer thus obtained was initially characterised by LEED. However, the width of the spots was comparable to the instrumental broadening due to the finite transfer width of the instrument, indicating that the size of the domains of Gr was at least as large as the transfer width. For this reason, we then reverted to SPA-LEED to acquire the diffraction pattern with a reduced instrumental broadening. The SPA-LEED pattern is shown in Figure 2.2 and shows the superposition of two sharp hexagonal patterns arising from the substrate and from Gr, as well as a hexagonal pattern surrounding the (0,0) spot generated by the moiré supercell, all having the same orientation. This indicates that both the Gr layer and the moiré structure are aligned to the crystallographic axes of Ir (1 1 1). Additional spots, surrounding the {1,0} spots of Ir (1 1 1) and Gr, are generated by multiple scattering processes. The FWHM of the diffraction spots indicates that Gr forms translational domains having an average diameter of at least 270 Å. The angular separation from the zero-order diffraction spot of those generated by the moiré indicates a periodicity of the latter of about 9 Ir (1 1 1) unit cells, in agreement with the value reported in literature<sup>27</sup>.

In order to assess the quality of Gr we also considered the C 1s photoemission spectrum of Gr, which is shown in Figure 2.3a and is described by a single, sharp component (W) centred at a BE of 284.12 eV. The FWHM of this peak is around 300 meV, which indicates that the quality of Gr is good; in fact, a larger value would be associated to an increased degree of inhomogeneities and to a larger density of defects<sup>28,29</sup>.

It is also interesting to compare the photoemission spectrum of the Ir  $4f_{7/2}$  core level, shown on the left of Figure 2.5, before (b) and after (c) Gr growth. The spectrum of the clean Ir (1 1 1) surface, in particular,

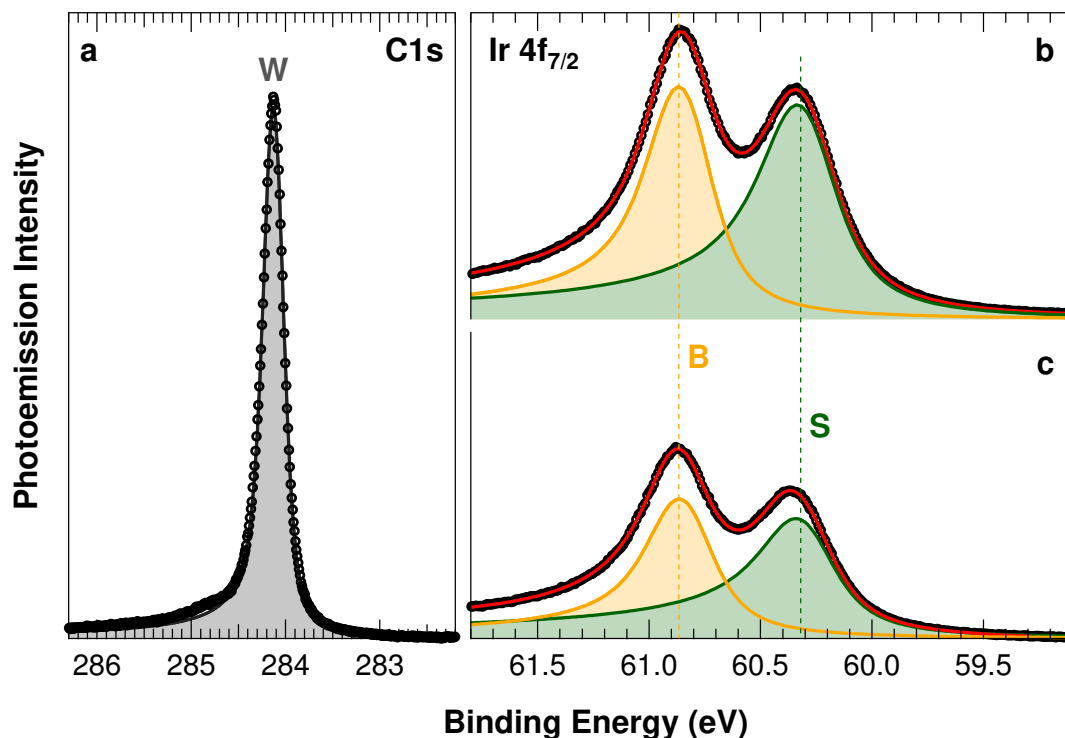


**Figure 2.3:** a: C 1s spectrum of Gr grown on Ir (1 1 1) ( $h\nu = 385$  eV). b-c: Ir  $4f_{7/2}$  photoemission spectra of Ir (1 1 1) ( $h\nu = 200$  eV) with deconvoluted bulk (B) and surface (S) components, measured before (b) and after (c) Gr growth.

can be fitted with two components<sup>30</sup>. The first one (B), at a BE of 60.84 eV, can be attributed to the bulk of the crystal, *i.e.* all layers except the surface one. This component has a lineshape described by  $L = 220$  meV,  $\alpha = 0.15$  and  $G = 180$  meV. A second component (S), shifted by 550 meV towards lower BE, is originated by the surface atoms; this component has a lineshape described by  $L = 280$  meV,  $\alpha = 0.17$  and  $G = 180$  meV.

After Gr growth, the intensity of both components is reduced by about 40%. This attenuation is due to the inelastic scattering affecting the photoelectrons from iridium as they cross the Gr layer. However, no significant changes are observed either in the lineshape or in the core level shifts: this indicates that the Gr layer does not noticeably affect the electronic structure of the underlying Ir (1 1 1).

## 2.2 Graphene growth on Ru (0 0 1)

Unlike the case of Ir (1 1 1), the growth of Gr on Ru (0 0 1) was performed by means of constant temperature (1100 K) CVD, with an increasing  $C_2H_4$  pressure up to  $5 \times 10^{-7}$  mbar<sup>15</sup>. This strategy was tuned in order to allow carbon atoms to migrate on the surface to form Gr nucleation islands, but not to diffuse into the bulk. In fact, carbon bulk dissolution can lead, upon cooling of the sample, to the formation of a second layer of Gr<sup>31</sup>.

As for the case of the Ir (1 1 1), the SPA-LEED pattern (Figure 2.4) indicates that the orientation of Gr coincides with that of the substrate. The FWHM of the diffraction spots indicates an average domain diameter of at least 150 Å. The periodicity of the moiré is compatible with the superposition of a  $(25 \times 25)$  superstructure of Gr above  $(23 \times 23)$  unit cells of Ru (0 0 1)<sup>32</sup>.

### 2.2.1 Details on the Ru 3d and C 1s spectra analysis

A particular care was required in the data acquisition and analysis to correctly deconvolute the C 1s and Ru  $3d_{3/2}$  core levels, due to the fact that their BE regions overlap. Moreover, the cross section of



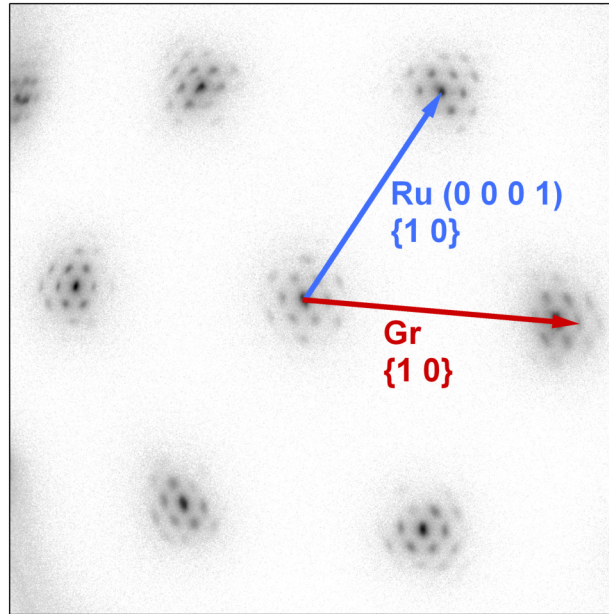


**Figure 2.4:** SPA-LEED pattern of Gr grown on Ru(0001) ( $E = 250$  eV).

the latter for the photoemission process is significantly higher than that of the former, which makes the analysis of the C 1s spectrum particularly challenging: in order to mitigate this issue, all C 1s spectra were measured using a photon energy of 385 eV, which was found to significantly enhance the photoemission cross section of the C 1s core level with respect to the Ru  $3d_{3/2}$  one<sup>33</sup>. The improved energy resolution and the tunability of the photon energy were therefore fundamental in allowing a proper deconvolution of these two photoemission components, as can be appreciated in Figure 2.5.

Nevertheless, the fitting the C 1s and Ru  $3d$  spectra required a careful use of constraints to ensure that the components arising from the two different elements were properly deconvoluted. The strategy we have adopted was based on the fact that while the C 1s and Ru  $3d_{3/2}$  core levels overlap, this is not the case of the Ru  $3d_{5/2}$  core level, whose BE is lower by about 4 eV. Therefore, it is possible to analyse the photoemission spectrum of the latter core level independently. The results of this analysis can then be used to predict the lineshape and intensity of the components of Ru  $3d_{3/2}$ .

With the aim to establish a repeatable procedure to do this, we started our analysis from the pho-

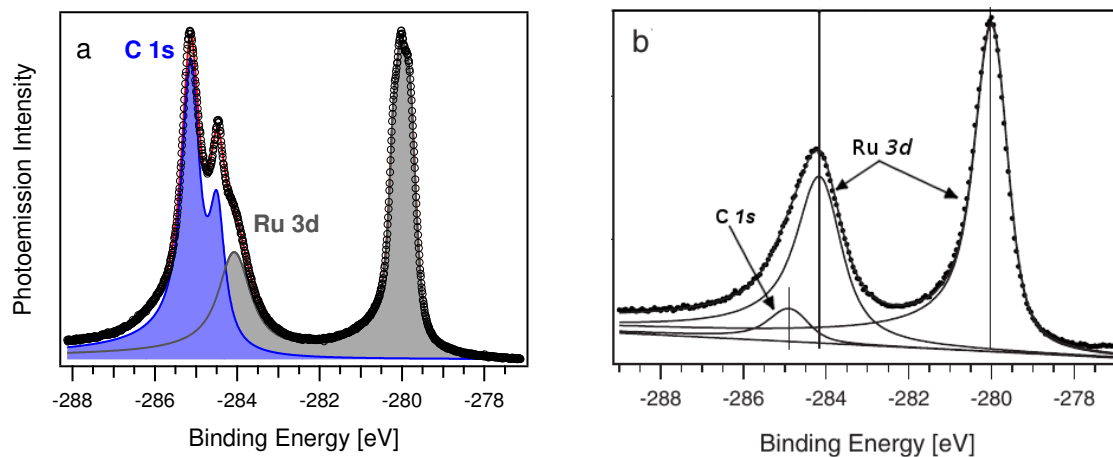


**Figure 2.5:** C 1s and Ru  $3d$  photoemission spectrum of Gr grown on Ru(0001). a: Spectrum measured at  $h\nu = 385$  eV at SuperESCA. b: Spectrum acquired using a conventional X-ray source<sup>13</sup>.

toemission spectrum of the clean Ru (0001), in order to understand the relations between the lineshapes of the two peaks. The photoemission spectrum of the Ru 3d core level of clean Ru (0001) is shown in Figure 2.6a. The spectrum shows two distinct peaks due to the spin-orbit splitting of the 3d core level. The  $3d_{5/2}$  component is found at about 280 eV and clearly shows a fine structure formed by at least two components, while the  $3d_{3/2}$  component is significantly broader and less intense and centred around a BE of about 284 eV. We started our analysis from the  $3d_{5/2}$  component, as it has a smaller broadening, in order to identify the line-shapes and core-level shifts of the different components. As previously observed<sup>34</sup>, three different photoemission components could be resolved, due to the non-equivalent Ru geometrical configuration of the first (S) and second layer ( $S_2$ ) with respect to the bulk (B). From the analysis of this spectrum, we obtained the following information:

- the asymmetry parameter  $\alpha$  and Gaussian FWHM  $G$  was equal for all components;
- the lineshape of the component generated by second layer atoms was the same as the one of bulk atoms.

In particular, the lineshape best describing the components generated by second layer and bulk atoms is characterized by  $L_B = 155$  meV,  $\alpha = 0.08$  and  $G = 130$  meV, while the surface-originated component has a Lorentzian FWHM  $L_S = 270$  meV. The core-level shifts for the surface and second layer components are  $\Delta E_S = -337 \pm 10$  meV and  $\Delta E_2 = 124 \pm 10$  meV, respectively, where a negative value indicates a shift towards lower BE values.

We then proceeded to analyse the  $3d_{3/2}$  peak, and found that the following procedure allows to obtain the  $3d_{3/2}$  level parameters from those of the  $3d_{5/2}$  level and guarantees the best agreement with the experimental results:

- the Gaussian FWHM parameter  $G$  of each component is equal to the one obtained for the corresponding component of the  $3d_{5/2}$  level;
- the asymmetry parameter  $\alpha$  was the same for all components;
- the surface and second layer core level shifts were the same as for the  $3d_{5/2}$  core level;
- according to the different degeneracy of the  $3d_{5/2}$  and  $3d_{3/2}$  core levels, the sum of the areas of all its components was constrained to  $2/3$  of the corresponding value obtained for the  $3d_{5/2}$  level.

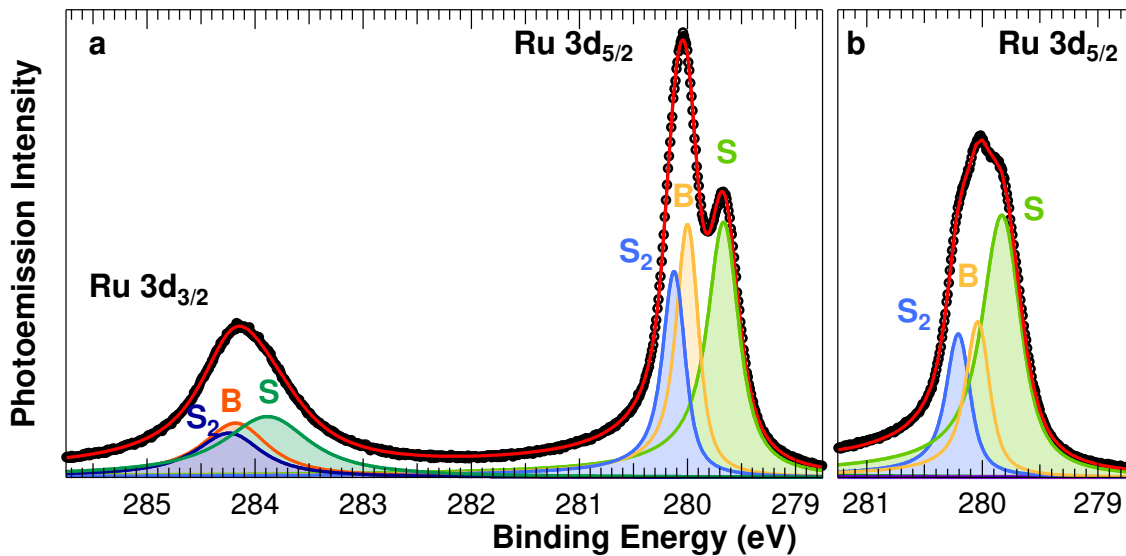


**Figure 2.6:** a: Ru 3d photoemission spectrum of the clean Ru (0001) surface ( $h\nu = 385$  eV). b: Evolution of Ru 3d<sub>5/2</sub> photoemission spectrum after Gr growth, showing a largely modified lineshape.

While this procedure is clearly based on a few approximations and over-simplifications, nevertheless it was effective in reconstructing the global line-shape of the  $3d_{3/2}$  peak. In the data analysis, therefore, only the lineshape and photoemission intensities of the Ru  $3d_{5/2}$  component were used to characterise the properties of the metal, while the calculation of the  $3d_{3/2}$  level was only performed in order to subtract it from the measured spectrum and thereby reconstruct the lineshape of the C 1s core level. The result of the subtraction of the  $3d_{3/2}$  component is shown in Figure 2.7.

The Ru  $3d$  and C 1s spectral region measured after Gr growth is shown in Figure 2.5a. Beside the new features observed above 284.5 eV, originated by the C 1s core level of Gr, the Ru  $3d_{5/2}$  component (highlighted in Figure 2.6b) is clearly very different from that of clean Ru (0 0 0 1). This indicates that the presence of Gr significantly modifies the electronic structure of the surface, unlike the Gr/Ir (1 1 1) case. To fit this spectrum, we started from the lineshape obtained for the clean surface, however, we allowed the surface and second layer core-level shifts to vary. Furthermore, we allowed the Gaussian FWHM of the surface component to relax, to account for a higher degree of disorder on the surface. The parameters we obtained from the fit were  $G_S = 190$  meV,  $\Delta E_S = -220 \pm 10$  meV and  $\Delta E_2 = 150 \pm 20$  meV. The appreciably different core level shifts observed indicate that Gr significantly alters the electronic structure of the Ru surface, which indicates that the Gr-metal interaction is strong in this system. Furthermore, the increase in the value of  $G_S$  can be explained by the large size of the moiré supercell formed by Gr on Ru (0 0 0 1) and the significant corrugation of Gr (as will be described in Section 2.3.3), which causes different atoms in the supercell to have a very different coupling to the Gr, thus resulting in a broad distribution of core-level shifts.

Finally, the C 1s spectrum of epitaxial Gr on Ru (0 0 0 1) (Figure 2.7) shows two distinct components, a weaker one ( $S_3$ ) at 284.47 eV and a more intense and narrower one ( $S_1$ ) at 285.13 eV. The presence of two components is widely recognized as a sign of the corrugation of Gr on Ru (0 0 0 1)<sup>8,13–15</sup>. They arise from a continuous distribution of non-equivalent atomic configurations where the component at lower BE is mainly generated by the atoms in the higher portion of the corrugation, and the one at higher BE is generated by atoms closer to the substrate, thus showing a more pronounced interaction with the metal underneath<sup>8,15,35</sup>, as will be shown in Section 2.3.3.

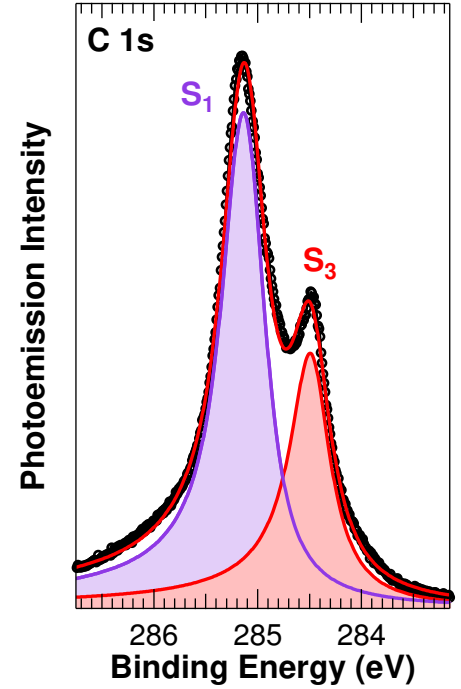


**Figure 2.7:** Reconstructed C 1s core level spectrum of Gr/Ru(0 0 0 1) ( $h\nu = 385$  eV), obtained by subtracting the calculated Ru  $3d_{3/2}$  component from the experimental data. The deconvoluted C 1s spectral components are superimposed.

## 2.3 Effects of the intercalation of metallic monolayers below graphene on the graphene/metal interaction

### 2.3.1 Intercalation procedure

The intercalation of each metal was performed by evaporation from high-purity filaments, while keeping the sample surface at 700 K. This temperature was chosen because it generally allows metal atoms to have enough mobility to diffuse above Gr, reach a suitable site for intercalation (mainly grain boundaries) and diffuse below the surface, while it has been demonstrated that metallic species deposited at ambient temperature usually tend to form clusters on top of Gr, rather than intercalate<sup>36–39</sup>.

About 1 monolayer (ML) of metal was deposited for each system, in steps of approximately 0.1 ML each. The evolution of the chemical, structural and electronic properties was followed by acquiring the C 1s core-level spectra of Gr. The photoemission spectra of the metallic substrate (either Ir  $4f_{7/2}$  or Ru  $3d_{3/2}$ )

and of the intercalated species (Ir  $4f_{7/2}$ , Ru  $3d_{5/2}$ , Co  $3p_{3/2}$  and Rh  $3d_{5/2}$ ) were also measured: the analysis of these latter peak intensities was used to determine the coverage of the intercalated metals. After each deposition step, in fact, we verified that the deposited metals had indeed intercalated by monitoring the Ir  $4f_{7/2}$  or Ru  $3d_{5/2}$  core levels' line-shape and we evaluated the amount of metal intercalated below Gr, in order to ensure that a full layer was intercalated during each experiment and that no significant dose of metal was adsorbed above Gr.

In order to understand whether or not the deposited metal had completely intercalated below Gr, we compared the C 1s spectra before and after the metal deposition. In fact, a completely intercalated metal layer causes attenuation in the photoemission signal generated by the substrate only, whereas the photoemission intensity of Gr remains more or less constant. On the contrary, when part of the metal atoms sit above Gr, the photoemission intensity of Gr is attenuated as well.

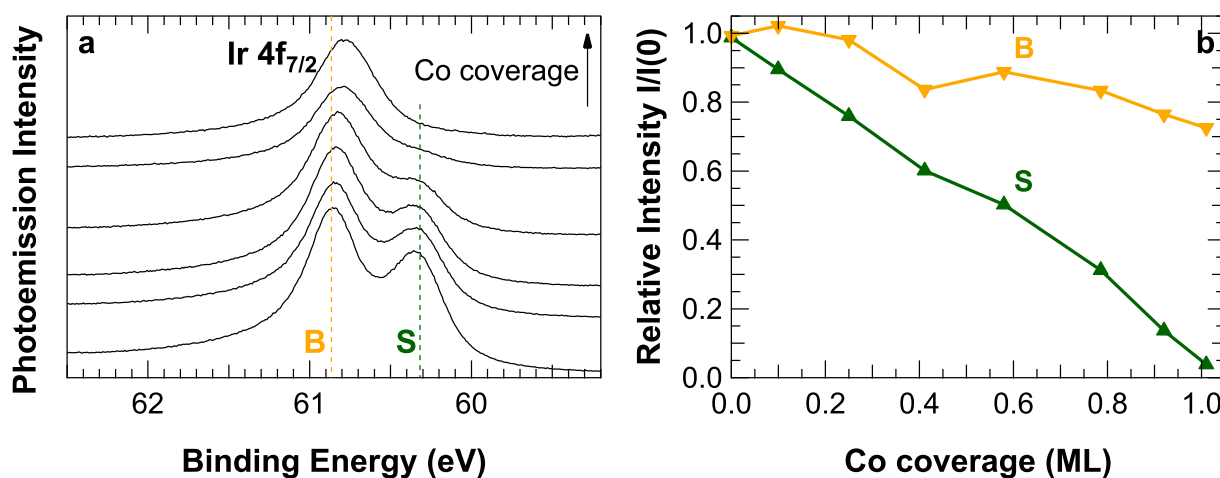


**Figure 2.8:** Ir  $4f_{7/2}$  photoemission spectrum during cobalt intercalation ( $h\nu = 200$  eV). a: Series of selected spectra; the BE of the bulk (B) and surface (S) components (see Figure 2.3c) are indicated. b: Evolution of the area of the de-convoluted components, normalised to their initial value for Gr/Ir (1 1 1), as a function of the amount of Co deposited.

On the other hand, in order to quantify the amount of metal intercalated, we exploited the fact that the high energy resolution of our experimental setup employed allows to resolve the signal generated by surface atoms from that of the underlying layers of each metal, as described in Sections 2.1 and 2.2. In particular, during the experiments described in this article, the atoms that were intercalated onto the substrate atoms modified their coordination: therefore, the BE of their core levels changes to a value similar to that of bulk atoms. This results in a progressive decrease in the intensity of the surface component, which completely vanishes after a full layer has been intercalated, as can be appreciated for example in Figure 2.8a for the selected case of cobalt intercalation on Ir (1 1 1). The intensity of the photoemission component generated by the under-coordinated surface atoms of the substrate  $I_S$  can be thus related to the coverage  $\theta$ . Our calculation is based on the fact that in our systems the intercalation leads to the epitaxial growth of a pseudomorphic ( $1 \times 1$ ) structure, as verified by LEED. Therefore, if we neglect border effects (which are only relevant at low coverages), the ratio between the area of this component after and before the intercalation is equal to the amount of surface not yet covered:  $1 - \theta = I_S(\theta)/I_S(0)$ . The evolution of the relative intensity of the surface component,  $I_S(\theta)/I_S(0)$ , and of the bulk component, during the cobalt intercalation on Ir (1 1 1), is shown as an example in Figure 2.8b. A linear decrease of  $I_S$  with the Co coverage can be clearly observed, while the intensity of the bulk component  $I_B$  does not change significantly, due to the fact that the number of subsurface layers accessible by XPS measurements is only determined by the IMFP of the photoelectrons, which is not significantly affected by the chemical composition of the surface layer.

A more accurate estimation of coverage is based on the intensity of the photoelectron signal of the intercalated species  $I_I$ , which is proportional to the number of its atoms and therefore linearly increases

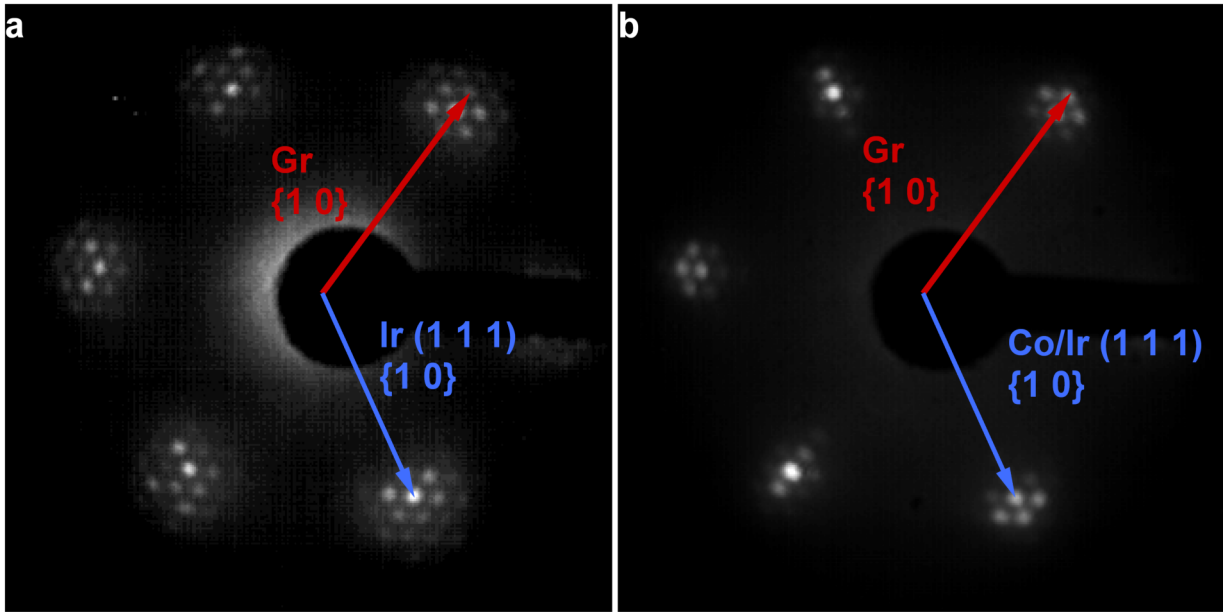


**Figure 2.9:** LEED pattern of Gr epitaxially grown on Ir (1 1 1) ( $E = 151$  eV), a: before and b: after cobalt intercalation.

with coverage, as long as a single layer is forming – as was the case for our experiment. This method however does not allow to obtain an absolute value for the coverage, since the proportionality constant between photoemission signal and coverage depends on far too many factors to be estimated *a priori*, and must be therefore obtained by combining the two aforementioned methods. Therefore, we first analysed the behaviour of  $I_S$  as a function of  $I_I$ . We then extrapolated the proportionality constant through a linear fit of this function (ignoring points at low coverage, in order to reduce border effects), and finally obtained the coverage by dividing  $I_I$  by the proportionality constant thus obtained.

The combined analysis of the XPS spectra of Gr, the substrate and the intercalated metals showed that in most cases the intercalation of metals was complete. A small reduction of the Gr photoelectron intensity was however observed after the deposition of Rh, indicating that a small amount of the deposited rhodium remained above Gr. In this case, in order to calculate the coverage  $\theta$ , all spectra were normalized by the total C 1s signal, since the screening effect was the same for all measured levels (being the kinetic energy of photoelectrons the same in all our measurements).

Finally, LEED measurements confirmed that the lattice parameters were not modified by the intercalation, *i.e.* the intercalated layer was pseudomorphic. A selected example is reported in Figure 2.9, which shows the LEED pattern of Gr on an intercalated cobalt monolayer on Ir (1 1 1).

### 2.3.2 Experimental results

In order to investigate the effects of the intercalation on the electronic properties of Gr, during each intercalation experiment we monitored the evolution of the C 1s spectrum after each deposition. The results of these measurements are shown in Figures 2.10 and 2.11.

In particular, the top graph in Figures 2.10a, b and c show the sequence of time-resolved spectra for the intercalation respectively of iridium, rhodium and cobalt below Gr/Ru(0 0 1). Already from a qualitative inspection of these sequences, it is clear that the C 1s spectrum changes dramatically as the substrate is covered by the intercalated species. A similar behaviour is observed during the intercalation of rhodium (Figure 2.11a), ruthenium (Figure 2.11b) and cobalt (Figure 2.11c) below Gr on Ir (1 1 1).

In order to accurately fit the data, we first analysed the spectra acquired at the highest coverage of the intercalated species (which are reported in the middle of Figures 2.10 and 2.11). In particular, to analyse these spectra, we used the same components used to describe the spectrum of pristine Gr, with the same



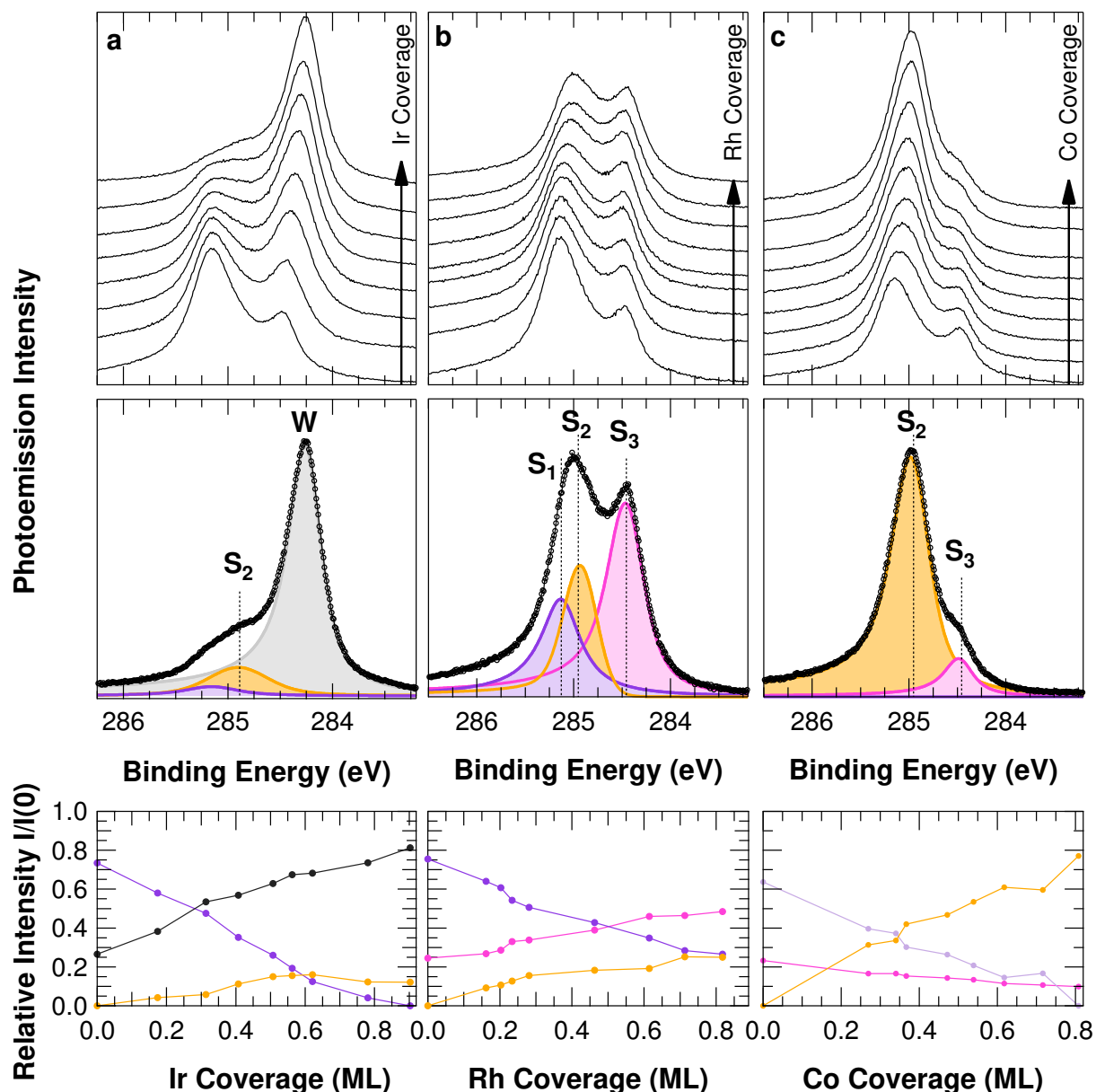


**Figure 2.10:** Background subtracted C 1s core level spectra of Gr/Ru(0001) ( $h\nu = 385$  eV) during intercalation of: a: Ir; b: Rh and c: Co. The top graph shows the evolution of the C 1s spectrum after each deposition step; the spectrum corresponding to a full monolayer intercalation is shown in the middle panel with the deconvoluted components. The area of all C 1s photoemission components corresponding to non-equivalent C populations as a function of the intercalating metal coverage is shown below, normalized to the initial area of the Gr C 1s spectrum.

lineshape – a part from the Gaussian FWHM  $G$ , which was allowed to change in order to describe possible contributions due to structural inhomogeneities – and C 1s BE, and added further components, one at a time, until the spectrum was well reproduced. All photoemission components of the C 1s core level which appear in any of the systems we analysed are reported in Table 2.1, together with their BEs. All spectra could be fitted using at most three components, whose BEs, as well as those of the pristine systems, are quite well grouped in four BE regions, which we have indicated as  $S_1$ ,  $S_2$ ,  $S_3$  and  $W$ , in order from higher to lower BE.

We then fitted all the other spectra in the sequence, by assuming that the lineshape and BE of each component ( $L$ ,  $\alpha$ ) was constant throughout all the experiment, whereas only the Gaussian parameter  $G$  was

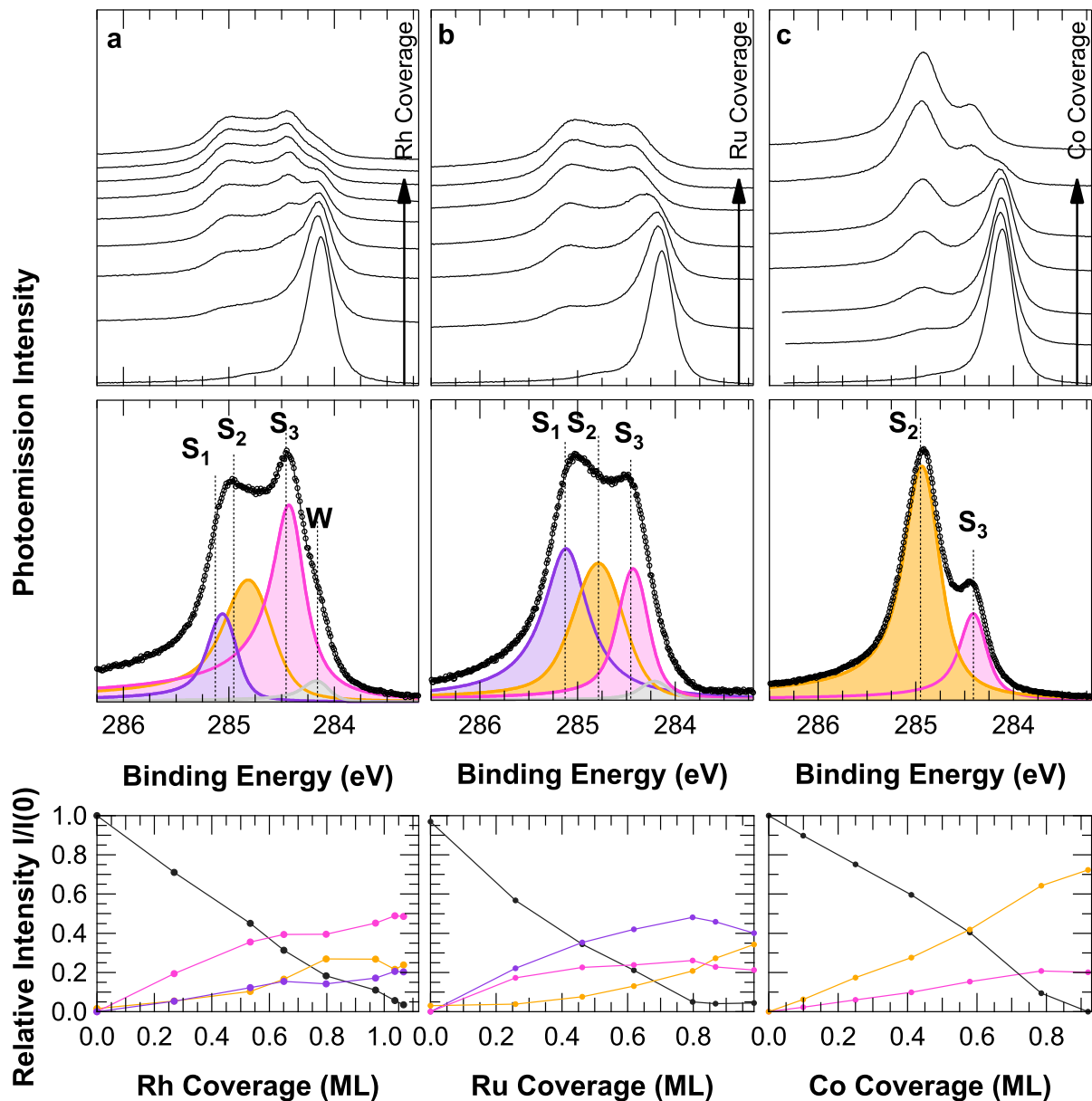


**Figure 2.11:** C 1s core level spectra of Gr/Ir (1 1 1) ( $h\nu = 385$  eV) during intercalation of: a: Rh; b: Ru and c: Co. The top graph shows the evolution of the C 1s spectrum after each deposition step; the spectrum corresponding to a full monolayer intercalation is shown in the middle panel with the deconvoluted components. The area of all C 1s photoemission components corresponding to non-equivalent C populations as a function of the intercalating metal coverage is shown below, normalized to the initial area of the Gr C 1s spectrum.

allowed to relax, to account for a different degree of structural disorder. From this analysis, we calculated the fraction of Gr originating each component by evaluating the area of each photoemission component and normalizing it to the total C 1s area of the pristine Gr. The evolution of this value as a function of the intercalated metal dose is reported in the bottom of Figures 2.10 and 2.11.

For all of the Gr/metal/Ir (1 1 1) systems (Figure 2.11), we observe that the W component loses intensity upon intercalation, almost completely vanishing for the highest coverage. On the other hand, several components appear at a higher BE, indicating a stronger degree of interaction between Gr and the substrate. The BE of these components does not depend on the coverage, only the relative intensities being modified throughout the experiment.

Specifically, after Rh intercalation (Figure 2.11a) we see a main component at 284.42 eV ( $S_3$ ) and two ad-

System	$S_1$ (eV)	$S_2$ (eV)	$S_3$ (eV)	W(eV)
<b>GR/Ru (0 0 0 1)</b>	<b>285.13 eV</b>	-	284.47 eV	-
<b>GR/Ir/Ru (0 0 0 1)</b>	-	284.89 eV	-	<b>284.23 eV</b>
<b>GR/Rh/Ru (0 0 0 1)</b>	285.13 eV	284.91 eV	<b>284.47 eV</b>	-
<b>GR/Co/Ru (0 0 0 1)</b>	-	<b>284.97 eV</b>	284.47 eV	-
<b>GR/Ir (1 1 1)</b>	-	-	-	<b>284.12 eV</b>
<b>GR/Rh/Ir (1 1 1)</b>	285.05 eV	284.83 eV	<b>284.42 eV</b>	-
<b>GR/Ru/Ir (1 1 1)</b>	<b>285.10 eV</b>	284.75 eV	284.41 eV	-
<b>GR/Co/Ir (1 1 1)</b>	-	<b>284.93 eV</b>	284.40 eV	-

**Table 2.1:** BE of each component of the C 1s core level photoemission spectrum in all systems studied in this work. The main component in the spectrum of each system is indicated in bold.

ditional components, with lower intensities, at higher BEs ( $S_{1-2}$ ) (Table 2.1). It can be noticed that the BE of the  $S_3$  peak is quite similar for this system and for the low BE component of Gr grown on Rh (1 1 1), thus suggesting that this component could arise from buckled areas of the Gr sheet. Component  $S_1$ , on the other hand, is close in BE to the high BE component of Gr on Rh (1 1 1), and is most likely related to carbon atoms strongly interacting with the substrate<sup>40–42</sup>. Component  $S_2$ , lying in between, most probably arises from atoms in an intermediate configuration between the two.

A similar behaviour is observed for the intercalation of Ru on Ir (1 1 1) (Figure 2.11b): also in this case, three components ( $S_{1-3}$ ) are detected (Table 2.1), lying between 284.41 and 285.10 eV. These components have BEs close to those found for the Rh intercalation. Their relative intensities, however, are different from the previous case, as the component at higher BE ( $S_1$ ) has a larger (almost double) spectral weight than the low BE one ( $S_3$ ): this could indicate, on average, a stronger interaction with the Ru layer than for the Rh layer. Besides the presence of the  $S_2$  component, the spectral distribution is quite similar to the one of Gr directly grown on Ru (0 0 0 1) (Fig 2.6b).

Finally, for the Co evaporation on Ir (1 1 1), we obtained a large component ( $S_2$ ) at 284.93 eV, and a weaker one ( $S_3$ ) at lower BE (Table 2.1), indicating a generally strong interaction with the Co layer.

By comparing the intercalation experiments on Ir (1 1 1), we notice that the C 1s core electrons of Gr shows significant changes depending on the chemical composition of the substrate. In particular, the interaction increases when passing from Ir to Rh, Ru and finally Co, which has, on average, the strongest interaction with Gr among the systems studied.

Also for the experiments performed on Ru (0 0 0 1), we observe a very different behaviour depending on the element being intercalated. In the case of Ir intercalation (Figure 2.10a) we notice a weakening of component  $S_1$ , which almost completely disappears, while another weak component is present at lower BE ( $S_2$ ). For this system, however, the data analysis was performed with a different strategy from the one used for the other systems. In fact, the evolution of the photoemission spectrum was better reproduced by allowing the  $S_3$  component to progressively move towards lower BE values, until it reaches values close to those of component W of Gr/Ir (1 1 1). The intensity of component  $S_3$ , therefore, increases until it becomes dominant, while its BE moves linearly towards lower values, reaching 284.23 eV at a coverage of 0.8 ML (Table 2.1). At this point, the spectrum strongly resembles that of Gr grown on Ir (1 1 1) and the dominant component is similar to component W of the latter system. This change in BE can be attributed to a smooth modification of the properties of Gr, from few-atom buckling above Ru (0 0 0 1) towards a completely raised, weakly interacting Gr above the Ir layer. The presence of the weak component  $S_2$  could be attributed to the formation of local defects and to inhomogeneities in the distribution of the Ir atoms. Also the intercalation of Rh on Ru (0 0 0 1) (Figure 2.10b) leads to an increase in the low BE component ( $S_3$ ). In addition, there are two weaker components ( $S_{1-2}$ ) at higher BE (Table 2.1). In this case, though, there are no changes in the BE of any component, indicating that the modifications are limited to a change in populations of weakly and strongly interacting atoms.

Finally, after the intercalation of Co on Ru (0 0 0 1) (Figure 2.10c) the high BE component ( $S_1$ ) is replaced by a new one ( $S_2$ ), at a slightly lower BE (Table 2.1). These two components are always distinct and their BEs remain constant with increasing Co coverage. On the other hand, the low-BE component ( $S_3$ ) decreases:



in general the spectral weight moves towards higher BE, indicating a slightly stronger interaction of Gr with Co than with Ru.

In conclusion, we observe a very similar trend to the experiments on Ir (1 1 1), in which the spectrum greatly varies depending on the chemical composition of the topmost layer of the substrate, with which Gr interacts. Also in this case, we found that the interaction with Ir is the weakest, followed by Rh and Ru. Only Co has an interaction with Gr stronger than Ru.

### 2.3.3 Theoretical calculations

Our measurements were complemented by DFT calculations performed by our collaborators from the group of Prof. Alfè, at University College London, in which the structure and core-level BE of Gr on all the substrate we investigated was calculated, as indicated in Section 1.6. The supercells used for the calculations were obtained by overlaying a  $(13 \times 13)$  Gr sheet over  $(12 \times 12)$  cells of Ru (0 0 0 1) and  $(10 \times 10)$  Gr cells over  $(9 \times 9)$  Ir (1 1 1) ones, respectively, which are good approximations of the experimentally measured supercells formed by Gr on these two systems<sup>10,43</sup>. The metal surfaces were modelled using a slab with a thickness of 5 layers: by modifying the chemical species of the topmost metallic layer, it was also possible to model the systems obtained from the intercalation of metals below Gr.

#### Theoretical results: graphene – substrate separation

The minimum-energy configuration for the systems studied in this experiment is reported in Figures 2.12 and 2.13. The colour scale indicates the vertical distance ( $Z$ ) of each carbon atom from the surface plane of the metallic substrate. It must be noted that the metallic substrate itself is actually corrugated when it strongly interacts with Gr; however, this corrugation is an order of magnitude lower than that of Gr. For this reason, the vertical distance has been referred to the mean vertical position of all atoms composing the metallic surface.

By comparing these systems, it is evident that the geometry of Gr strongly depends on the chemical composition of the topmost layer of the substrate. In particular, where the topmost layer consists of Ir (Figures 2.12a and 2.13a), the distance between Gr and the substrate is larger than 4 Å and the former has a very small corrugation. This is in contrast with all other systems, where the distribution is much wider, with the nearest atoms closer than 2 Å to the surface and the farthest between 3.4 and 3.9 Å. For all systems, the unit cells of Gr whose atoms are farthest from the surface are those where the centre of

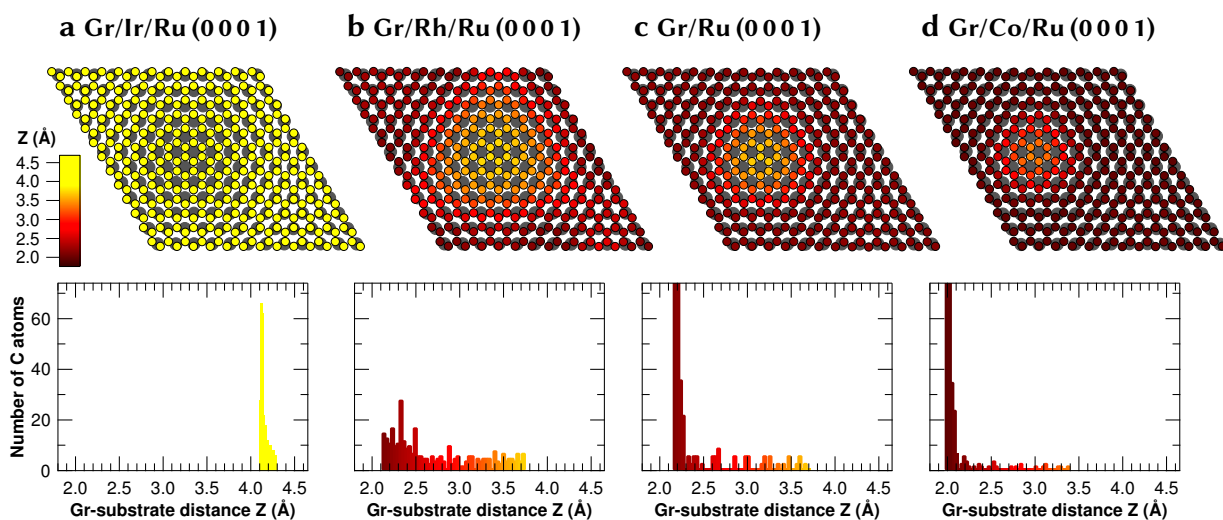


**Figure 2.12:** Theoretical results for different Gr/metal/Ru (0001) interfaces. Top panels: geometric configuration of the topmost metallic atoms (large, grey circles) and of the carbon atoms (smaller, coloured circles) inside the  $(13 \times 13)$  moiré unit cell. The C atom colour scale indicates the C to substrate distance  $Z$ . Bottom panels: distribution of all C-metal substrate distance  $Z$  in the moiré unit cell.

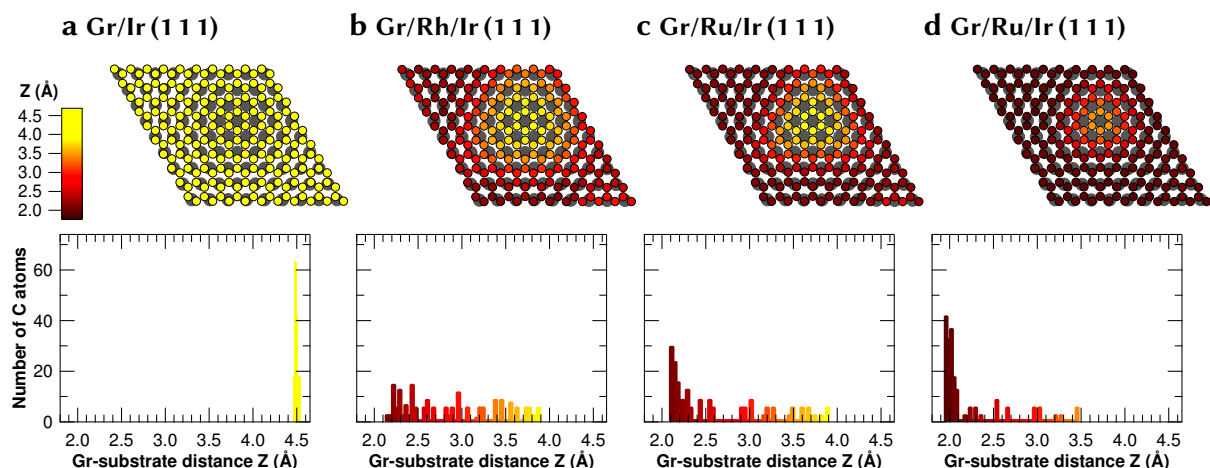


**Figure 2.13:** Theoretical results for different Gr/metal/Ir (1 1 1) interfaces. Top panels: geometric configuration of the topmost metallic atoms (large, grey circles) and of the Gr atoms (smaller, coloured circles) inside the  $(9 \times 9)$  moiré unit cell. The C atom colour scale indicates the C to substrate distance  $Z$ . Bottom panels: distribution of all C-metal substrate distance  $Z$  in the moiré unit cell.

the honeycomb lies in an on-top site of the substrate, and therefore both atoms lie in hollow sites. On the other hand, the cells closest to the substrate are those where the centre of the honeycomb lies in bridge sites, and both C atoms lie above a metallic atom.

In particular, the distribution along  $Z$  of the atoms of Gr above a Co-terminated surface (Figures 2.12d and 2.13d) has a very narrow distribution centered at low  $Z$  values (between 1.9 and 2.1 Å), with only a small number of atoms located at more than 2.1 Å from the surface (and up to 3.5 Å), 25% of all C atoms on Ir (1 1 1) and 13% on Ru (0 0 1).

In the case of Gr on Ru, most of the C atoms lie at a small distance from the substrate (between 2.1 and 2.3 Å). The others, which are more than 25% in the case of Gr/Ru (0 0 1) and almost 50% for Gr/Ru/Ir (1 1 1), lie at a larger distance, reaching up to 3.7 Å on the former substrate (Figure 2.12c) and up to 3.9 Å above the latter (Figure 2.13c). The number of weakly interacting C atoms and the range of C atoms  $Z$  values for Ru are larger than for Co, indicating a slightly weaker average interaction.

Finally, the distance of Gr from the Rh layer has a quite broad distribution which ranges from 2.1 to 3.7 Å for Ru (0 0 1) (Figure 2.12b), and from 2.1 to 3.9 Å for Ir (1 1 1) (Figure 2.13b), thus suggesting a smoother corrugation and a weaker interaction of Gr with Rh than with Co or Ru, but still stronger than with Ir.

The calculated distance between Gr and Ru (0 0 1) is in good agreement with the experimental value found in literature<sup>44</sup>. This is also the case of the separation between Gr and intercalated Co on Ir (1 1 1), which is in very good agreement with previous experiments on the same system<sup>45</sup>. Moreover, the  $Z$  value of about 2 Å found for the majority of atoms in both systems can be compared to the case of Gr above Co (0 0 1), where Gr matches the lattice of the surface forming a  $(1 \times 1)$  commensurate structure<sup>9,46</sup> and therefore all atoms lie at about 2 Å from the underlying surface. Finally, the two interfaces where Gr lies above an intercalated Rh layer have the same corrugation of Gr on Rh (1 1 1)<sup>9,47</sup>. The separation of Gr from Ir (1 1 1) appears instead to be overestimated, being by more than 1 Å larger than the reported value<sup>10</sup>. This can be attributed to the presence of dispersive forces which are not included in the present calculations<sup>23,48</sup> and which are necessary to obtain a better quantitative prediction of the Gr/substrate distance. Nevertheless, we can conclude that the trend reported in literature, with the average Gr-metal distance increasing from the case of the close-packed surfaces of cobalt, to ruthenium, rhodium and finally iridium<sup>9</sup>, is clearly observed also for our interfaces.

### Theoretical results: C 1s Binding Energy calculation

DFT was also employed to calculate the core level BEs of all C atoms, however, such theoretical methods only provide the differences between the C 1s BEs for non equivalent atoms. Therefore, we first had

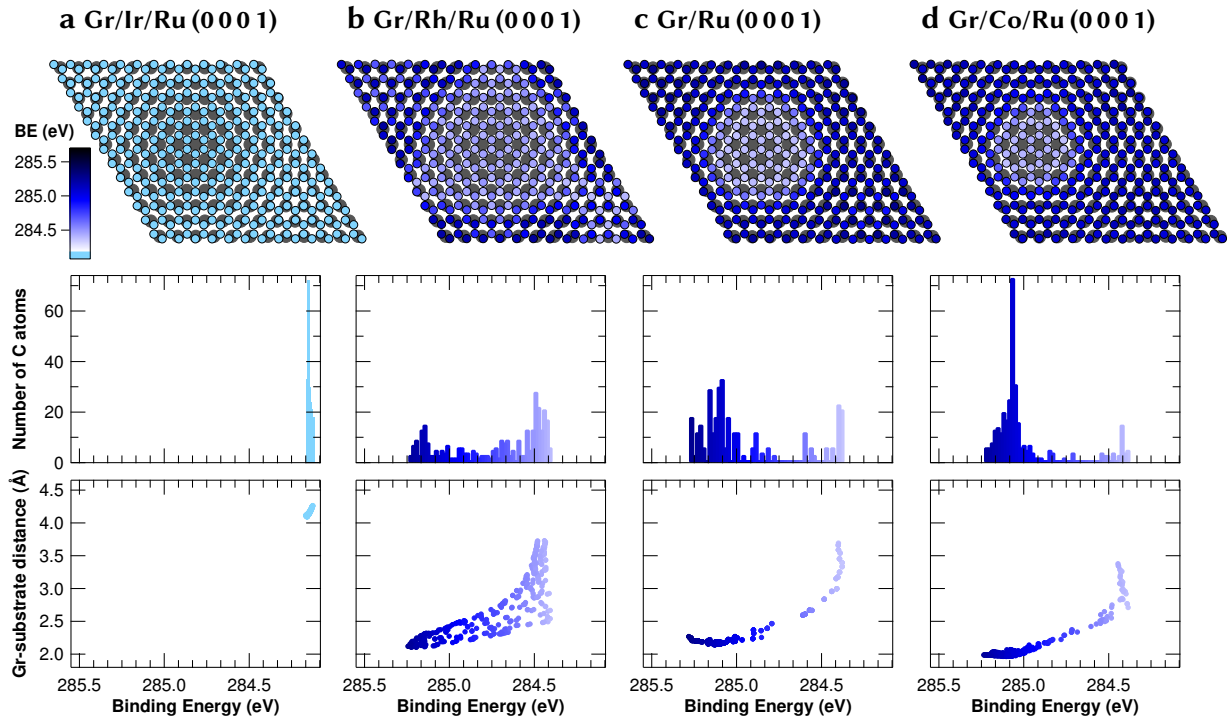


**Figure 2.14:** Theoretical results for Gr/metal/Ru(0001) system. Top panels: the C 1s core level BE is represented for each C atom (small dots) in the moiré cell using a colour scale. The larger, grey circles represent the underlying metallic atoms. Middle panels: Distribution of C 1s BEs for all C atoms. Bottom panels: correlation between C 1s BE and separation of each atom from the topmost metallic layer.

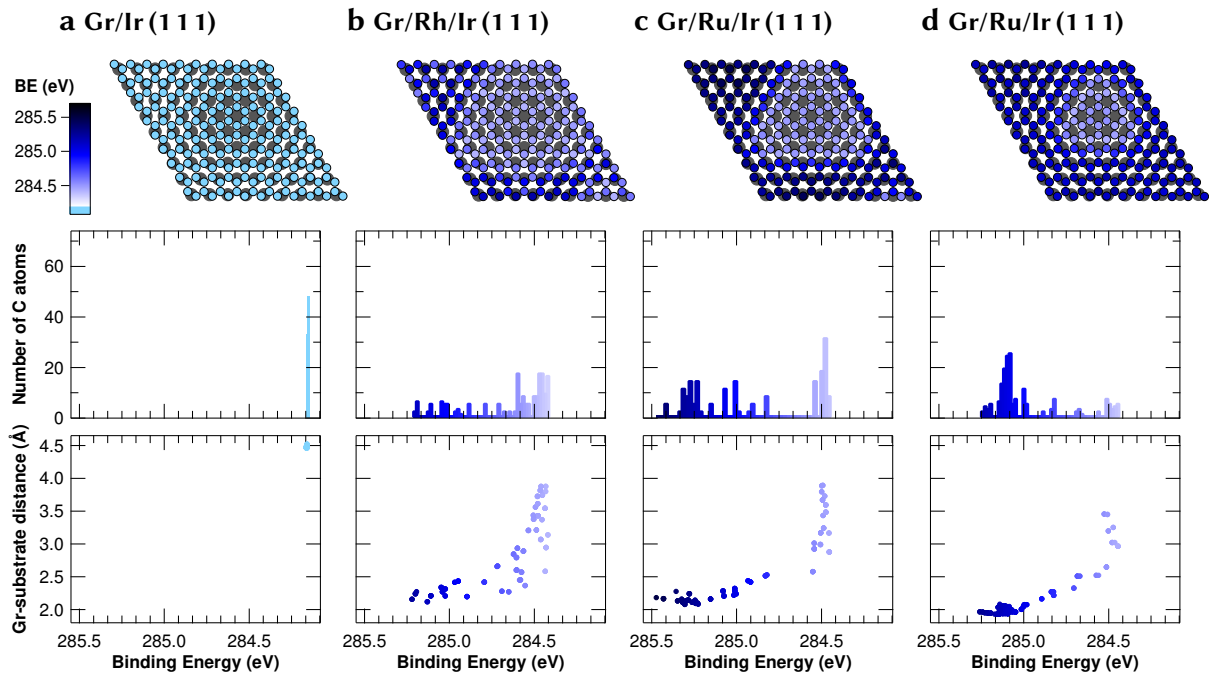


**Figure 2.15:** Theoretical results for Gr/metal/Ir(111) system. Top panels: the C 1s core level BE is represented for each C atom (small dots) in the moiré cell using a colour scale. The larger, grey circles represent the underlying metallic atoms. Middle panels: Distribution of C 1s BEs for all C atoms. Bottom panels: correlation between C 1s BE and separation of each atom from the topmost metallic layer.

to rigidly shift the energy scale to align its reference to that of the measured data. To this purpose, we first aligned the centre of the calculated BE distribution for the Ir(111) system to the actual experimental data, and then shifted the BE scale for all systems by the same offset. The Gr/Ir(111) interface was cho-

sen because it displayed both the narrowest experimental spectrum and theoretical BE distribution, thus minimizing the error in the calibration.

The distributions of the C 1s BE of each atom in each Gr supercell are reported in Figures 2.14 and 2.15. A different behaviour of the C 1s BEs distribution can be observed for different chemical compositions of the substrate's topmost layer, regardless of its geometry. Gr lying above Ir has a very narrow distribution of C 1s BEs, centred around 284.20 eV for the Gr/Ir (1 1 1) interface (Figure 2.15a), and between 284.25 and 284.28 eV for Gr on Ir-terminated Ru (0 0 0 1) (Figure 2.14a). On the other hand, the distribution is much wider for Gr sitting on Rh, Ru and Co (Figure 2.14b-d and 2.15b-d). Most of the computed C 1s BEs, in fact, fall in the range between 284.50 and 285.35 eV and in some systems — such as Ru on Ir (1 1 1) (Figure 2.15c) — can reach up to 285.5 eV. What differs among these corrugated systems, however, is the shape of the distribution, which is different depending on the topmost metallic layer. Around 50% of the C atoms lying above Rh have closely spaced C 1s BEs ranging between 284.5 and 284.7 eV, while the others are evenly distributed at higher BEs. On the other hand, most atoms of Gr above Ru have a C 1s BE between 285.1 and 285.3 eV, while only around 13% of the atoms above Ru (0 0 0 1) and 25% of those above Ru-terminated Ir (1 1 1) are concentrated at low BE. Finally, C atoms belonging to Gr lying above Co have a sharp peak C 1s BE distribution centred at around 285.20 eV, with only around 15% of the C atoms having a 1s BE lower than 284.7 eV.

As can be observed in the bottom graphs in Figure 2.14 and 2.15, there is usually a correlation between the distance of each carbon atom from the underlying surface and its C 1s BE, with the latter decreasing as the former increases. The situation is more complicated for the case of Gr on Rh (Figure 2.14b), where some adjacent atoms, despite being at the same distance from the substrate (about 2.5 Å), show a large difference (up to 500 meV) in the C 1s BE. In this case, in fact, the C 1s BE of each atom is related to the site it occupies on the surface: in particular, the BE is maximum for atoms occupying on-top or bridge sites and minimum for three-fold hollow sites. This particular behaviour has already been observed for epitaxial Gr on Rh (1 1 1) and has been explained in terms of the hybridization of the  $\pi$  states of Gr not only with the  $d_{z^2}$  but also with the  $d_{zx}$  and  $d_{zy}$  bands of Rh<sup>49</sup>. This dependence of the BE on the site is not observed for atoms either too close to the surface (around 2 Å) or too far (above 3 Å).

The similarity between the histograms representing the C 1s BE distribution and the measured XPS spectra for each of the interfaces studied in this work underlines the accuracy and validity of the calculations. In order to further confirm their agreement, we have compared the barycentre of each calculated distribution with that of the corresponding experimental spectrum. To do this with the best possible accuracy, we calculated it for all the coverages up to a monolayer, and then used the value obtained through a linear fit. In most systems, the experimental values agree with the calculated ones, within an uncertainty of 40 meV. The only cases where we found a slightly worse agreement were both interfaces obtained from Rh intercalation and the one obtained by intercalating Ru at the Gr/Ir (1 1 1) interface. All these systems were characterized by a higher disorder, suggesting that these experimental interfaces were in part different from those simulated in the calculations. In particular, in the first two cases, the reason can be ascribed to the fact that a small portion of Rh atoms were not completely intercalated but also formed clusters above Gr, a behaviour previously observed for the low temperature Rh deposition on Gr/Ir (1 1 1)<sup>37</sup> (see supporting information).

### Theoretical results: carbon – carbon separation

Figures 2.16 and 2.17 show the distribution of the averaged distance of each carbon atom from its three nearest neighbours, as obtained by our DFT calculations. In the case of Gr supported on Ir, the nearest-neighbour distance is the same for all carbon atoms: 1.45 Å for the Gr/Ir/Ru (0 0 0 1) system (fig. 2.16a) and 1.42 Å for Gr grown on bare Ir (1 1 1) (fig. 2.17a). The latter value corresponds to the nearest-neighbour distance of free-standing Gr, while the former is larger. This can be related to the fact that, when Gr is grown on Ru (0 0 0 1), the interaction with the substrate stretches it until it forms a commensurate moiré lattice, while in the case of Gr on Ir (1 1 1) the interaction with the substrate is not strong enough to modify the geometry of Gr. This average interatomic distance of the carbon atoms is preserved upon intercalation: were this not the case, it would require the breaking or a strong rippling of the Gr layer.

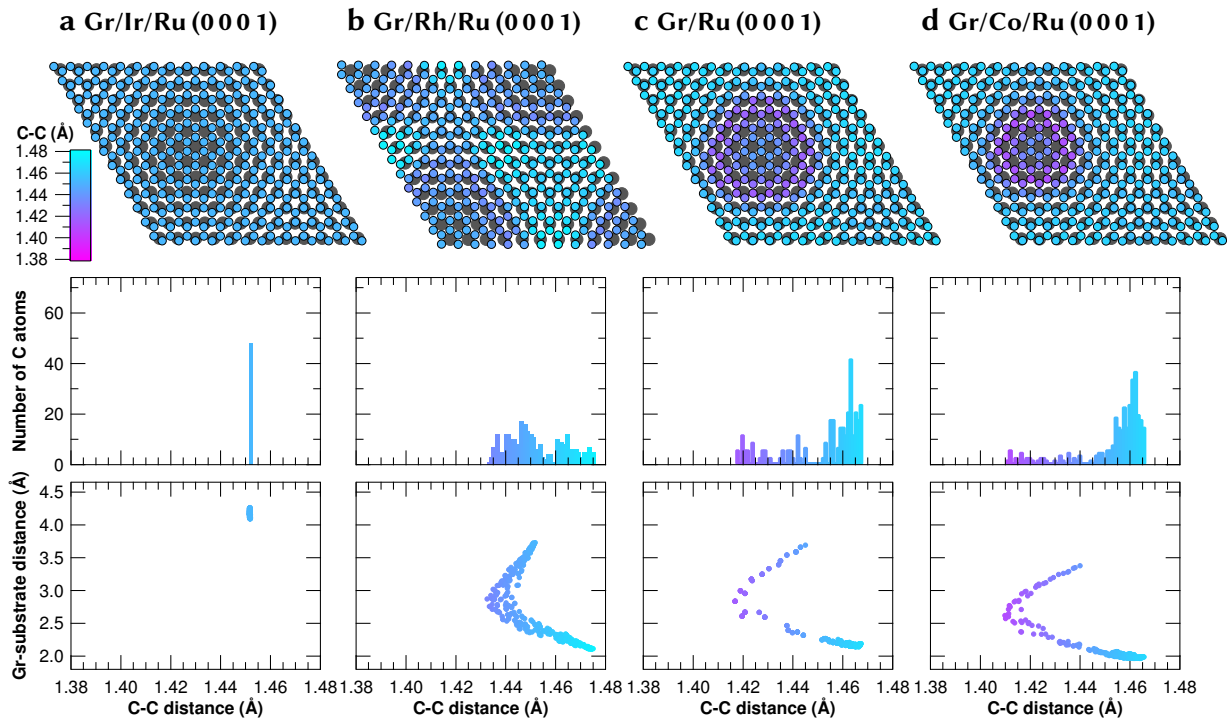


**Figure 2.16:** Theoretical results for Gr/Ru(0001) before and after intercalation. Above: geometric configuration of the topmost metallic atoms (large, grey dots) and of the Gr atoms (smaller, coloured dots) inside the moiré cell: the colour scale of the latter indicates the average distance of each C atom from its three nearest neighbours. Middle: Distribution of C-C distances of all C atoms. Below: correlation between C-C distance and separation of each atom from the topmost metallic layer.

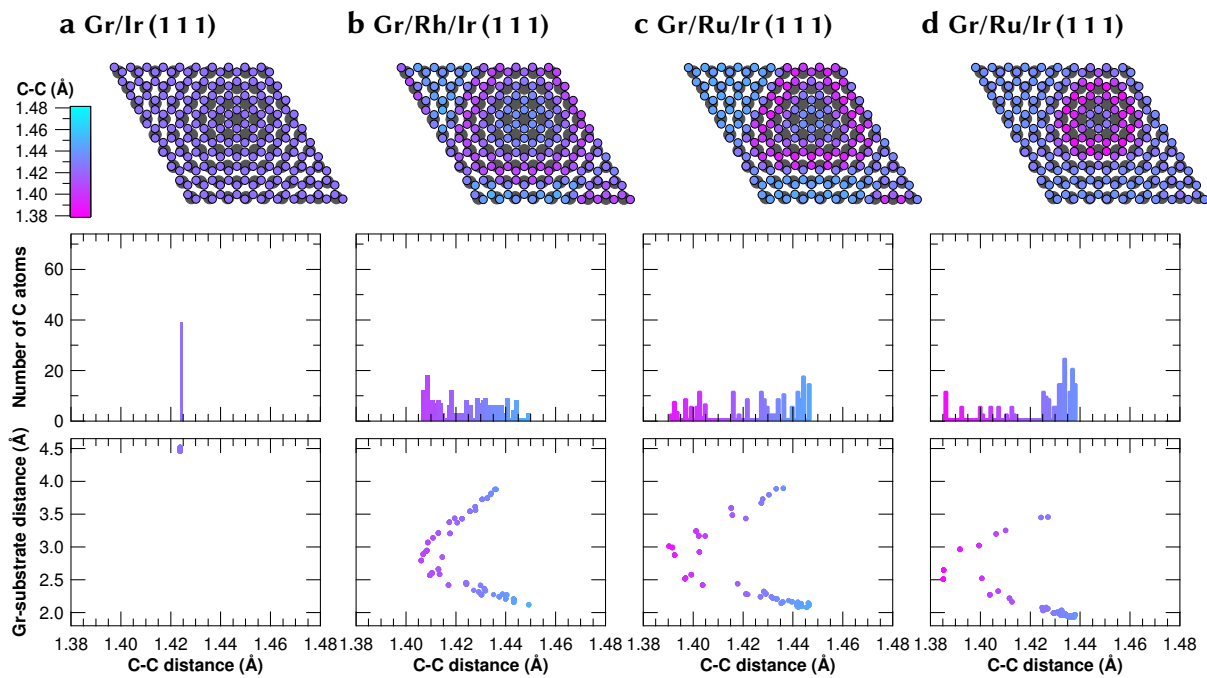


**Figure 2.17:** Theoretical results for Gr/Ir(111) before and after intercalation. Above: geometric configuration of the topmost metallic atoms (large, grey dots) and of the Gr atoms (smaller, coloured dots) inside the moiré cell: the colour scale of the latter indicates the average distance of each C atom from its three nearest neighbours. Middle: Distribution of C-C distances of all C atoms. Below: correlation between C-C distance and separation of each atom from the topmost metallic layer.

For this reason, in all systems modelled on the geometry of Ru(0001) the distribution of C-C distances is shifted towards higher values with respect to that of the systems modelled on Ir(111). For systems modelled on the geometry of Rh-terminated Ru(0001) (fig. 2.16b), the values of interatomic distance are



uniformly distributed between 1.43 and 1.48 Å; whereas for the Ru-terminated surface (fig. 2.16c) this distribution covers the range between 1.42 and 1.47 Å, with a peak towards higher values; finally for Gr above a Co-terminated Ru (0 0 0 1) (fig. 2.16d) the distribution has a sharp peak around 1.46 Å and a tail stretching towards lower values reaching 1.41 Å. For the systems modelled on the geometry of Ir (1 1 1), instead, the interatomic distances of Gr on Rh have a uniform distribution ranging between 1.41 and 1.45 Å (fig. 2.17b); their distribution above Ru ranges from 1.39 to 1.45 Å with a small peak towards higher values (fig. 2.17c); finally, the distribution of interatomic distances of Gr above Co (fig. 2.17d) has a sharp peak around 1.43 Å and a tail reaching 1.38 Å. The shape of the distributions, therefore, mostly depends on the chemical composition of the topmost layer, whereas the different geometry of the two systems causes a roughly rigid shift of the ranges.

By studying the behaviour of the C-C separation with respect to the position inside the moiré cell (Figure 2.16 and 2.17, above) and to the separation between Gr and the substrate (fig. 2.16 and 2.17, below), it can be noticed that the distance is usually minimum on the edges of the hills, whereas it is larger in the flat areas both on top of them and at the bottom of the valleys. This is one of the parameters influenced by geometry: since the moiré unit cell is preserved in the intercalation process, the average separation between C atoms is larger (by around 0.02 Å) in systems having the moiré unit cell of Gr/Ru (0 0 0 1) than in systems having the moiré unit cell of Gr/Ir (1 1 1).

### 2.3.4 Discussion

It is clear from the comparison of the data obtained in the different intercalation experiments that there are major differences in the geometric and electronic properties of the Gr layer between systems with a different chemical species at the interface. For example, the intercalation of Ir on Gr/Ru (0 0 0 1) leads to a very weakly interacting Gr layer, similar to the case of Gr/Ir (1 1 1), while the intercalation of the other species on Gr/Ir (1 1 1) leads to stronger interaction with the substrate, resulting in a significant buckling of the Gr layer. On the other hand, substrates having the same chemical termination show very similar properties regardless of the difference in the lattice parameter of the supporting substrate.

These results suggest that the key role in determining the strength of interaction is played by the chemical composition of the substrate. Geometry, on the other hand, mainly determines the periodicity of the moiré, which is preserved after intercalation. This is particularly obvious if we consider the case of Gr interacting with Co: it is flat and commensurate on Co (0 0 0 1)<sup>9</sup>, while it is buckled in the case of the Co intercalation.

A further proof of the important effects of the electronic structure and of the composition of the substrate on its interaction with Gr comes from the correlation between the position of C atoms with respect to the surface sites and their C 1s BE. As has been already mentioned, the BE — and therefore the interaction — is maximum for C atoms in on-top configuration and minimum for those in hollow sites, even among atoms located at the same distance from the substrate. This effect demonstrates that the interaction between Gr and metal surfaces depends on the hybridization between the  $\pi_z$  orbitals of Gr and the  $d$ -band of the substrate<sup>22</sup>.

In order to find the relationship between the C 1s core levels and the chemical properties of the supporting substrates we plotted (in Figure 2.18) the experimental and theoretical C 1s spectral barycentre versus the calculated  $d$ -band centre of the topmost metallic layers. The positions of the  $d$ -band centre  $E_d$  with respect to the Fermi energy  $E_F$  for the different Gr-free metal surfaces has been calculated as

$$E_d = \int_{-\infty}^{E_0} dE (E - E_F) \text{pd}(E)$$

Where  $\text{pd}(E)$  is the electronic density of states obtained by projecting the Kohn-Sham orbitals onto spherical harmonics of type  $d$  centred on the metal atoms, and  $E_0$  is a cut-off energy that was chosen to be 7 eV above the Fermi energy.

Indeed, as firstly pointed out by Wang *et al.*<sup>14</sup>, and more recently extensively described by Toyoda *et al.*<sup>23</sup>,  $d$ -band metals greatly influence the potential-energy surface of Gr on transition-metal surfaces and are largely responsible for the Gr/substrate interactions.

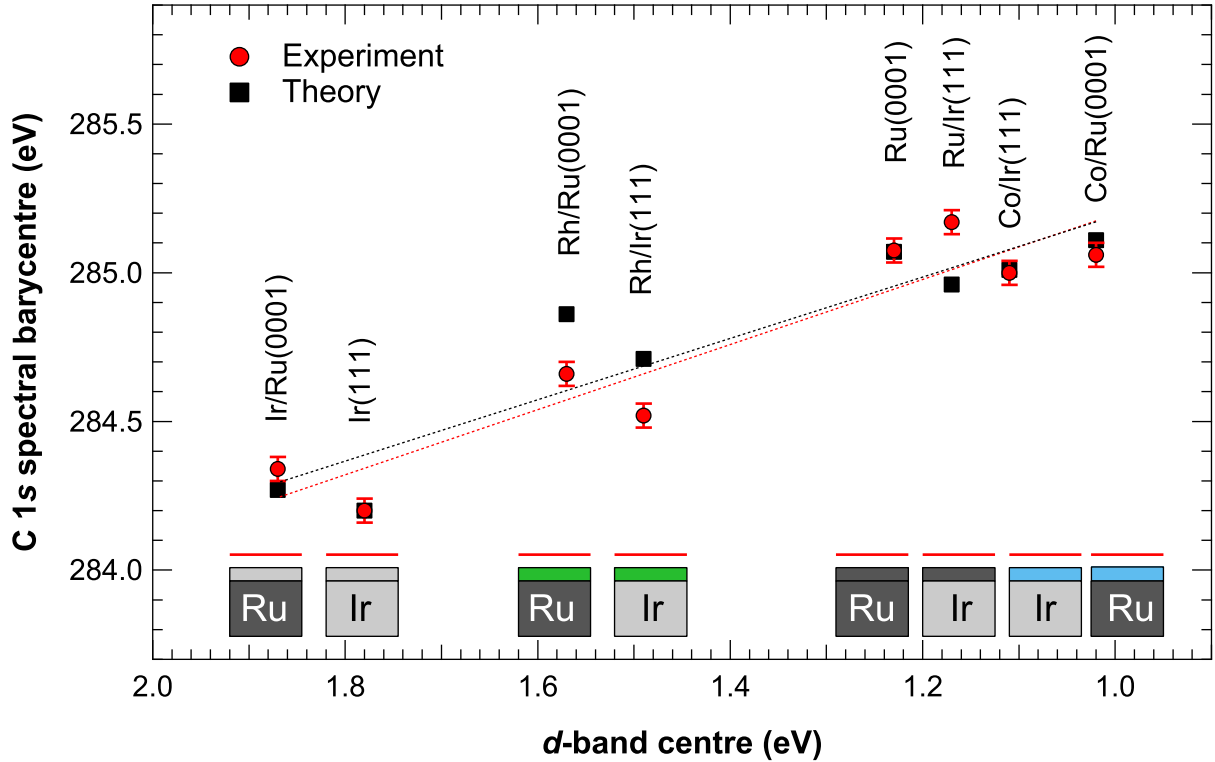


**Figure 2.18:** Theoretical (black squares) and experimental (red circles) values of the C 1s core-level BE distribution barycentre of all C atoms in the moiré unit cell for each system studied in this work versus calculated  $d$ -band centre of the underlying clean metal surface.

Besides the very good agreement between experimental (red markers) and theoretical (black markers) values, we found a strong linear relationship between the C 1s spectral centre of mass and the calculated  $d$ -band centres. This result can be interpreted as well in terms of Hammer and Nørskov’s model for molecular chemisorption, which predicts a linear dependence of the molecular adsorption energy on transition metal surfaces on their  $d$ -band centre<sup>22</sup>. According to this model, the linear relationship we found suggests that the C 1s core level BE of Gr provides a quantitative estimate of its degree of interaction with the underlying substrate. This offers a further proof that core level spectroscopy can be considered a useful experimental descriptor of the interaction strength of Gr with transition metal surfaces.

## Conclusions

In this chapter, I have described a combined experimental and theoretical study on systems in which Gr is supported on monocrystalline transition metal surfaces constrained to the periodicity of Ir (1 1 1) and Ru (0 0 1), yet with a different metallic species present at the interface below Gr. By measuring the core-level shifts of the C 1s level of carbon atoms, we have shown that the main factor determining the strength of interaction between Gr and its substrate is the chemical species of the topmost layer of the substrate.

In addition, these experiments have allowed us to shed light on the mechanisms driving this interaction. In fact, we have verified that the C 1s spectral barycentre has a linear relationship with the  $d$ -band centre position. This relationship indicates that the coupling between Gr and the metal surface can be attributed to the hybridization between those states and the bands of Gr.

This provides a powerful degree of freedom to tune the Gr-metal interaction, by choosing as a support for Gr a metal surface having the optimal electronic structure. Furthermore, the intercalation procedure allows to choose even metals where Gr cannot be grown directly using CVD, as we have shown that Gr can be grown on any other surface and subsequently its interaction be modified by the intercalation of the

chosen metal.

Finally, our measurements have allowed us to identify a reliable descriptor of the Gr-substrate interaction strength: in fact, we have shown that C 1s core-level spectroscopy can be employed as a reliable tool to investigate the interaction of Gr with its substrate.



## References

- [1] P. A. Khomyakov, G. Giovannetti, P. C. Rusu, G. Brocks, J. van den Brink, P. J. Kelly. First-principles study of the interaction and charge transfer between graphene and metals. *Phys. Rev. B* (2009) 79: 195425. doi:10.1103/physrevb.79.195425.
- [2] A. Varykhalov, M. Scholz, T. Kim, O. Rader. Effect of noble-metal contacts on doping and band gap of graphene. *Phys. Rev. B* (2010) 82: 121101. doi:10.1103/PhysRevB.82.121101.
- [3] A. La Torre, F. B. Romdhane, W. Baaziz, I. Janowska, C. Pham-Huu, S. Begin-Colin, G. Pourroy, F. Banhart. Formation and characterization of carbon–metal nano-contacts. *Carbon* (2014) 77: 906–911. doi:10.1016/j.carbon.2014.06.004.
- [4] S. Kim, M. Russell, D. D. Kulkarni, M. Henry, S. Kim, R. R. Naik, A. A. Voevodin, S. S. Jang, V. V. Tsukruk, A. G. Fedorov. Activating “invisible” glue: Using electron beam for enhancement of interfacial properties of graphene–metal contact. *ACS Nano* (2016) 10: 1042–1049. doi:10.1021/acs.nano.5b06342.
- [5] G. Giovannetti, P. Khomyakov, G. Brocks, V. Karpan, J. van den Brink, P. Kelly. Doping graphene with metal contacts. *Phys. Rev. Lett.* (2008) 101: 026803. doi:10.1103/PhysRevLett.101.026803.
- [6] B. J. Schultz, C. Jaye, P. S. Lysaght, D. A. Fischer, D. Prendergast, S. Banerjee. On chemical bonding and electronic structure of graphene-metal contacts. *Chem. Sci.* (2013) 4: 494–502. doi:10.1039/c2sc21018e.
- [7] L. Adamska, Y. Lin, A. J. Ross, M. Batzill, I. I. Oleynik. Atomic and electronic structure of simple metal/graphene and complex metal/graphene/metal interfaces. *Phys. Rev. B* (2012) 85: 195443. doi:10.1103/PhysRevB.85.195443.
- [8] A. B. Preobrajenski, M. L. Ng, A. S. Vinogradov, N. Mårtensson. Controlling graphene corrugation on lattice-mismatched substrates. *Phys. Rev. B* (2008) 78: 073401. doi:10.1103/PhysRevB.78.073401.
- [9] M. Batzill. The surface science of graphene: Metal interfaces, CVD synthesis, nanoribbons, chemical modifications, and defects. *Surf. Sci. Rep.* (2012) 67: 83–115. doi:10.1016/j.surfrep.2011.12.001.
- [10] C. Busse, P. Lazić, R. Djemour, J. Coraux, T. Gerber, N. Atodiresei, V. Caciuc, R. Brako, A. T. N’Diaye, S. Blügel, J. Zegenhagen, T. Michely. Graphene on Ir(1 1 1): Physisorption with chemical modulation. *Phys. Rev. Lett.* (2011) 107: 036101. doi:10.1103/PhysRevLett.107.036101.
- [11] P. Sutter, J. T. Sadowski, E. Sutter. Graphene on Pt(1 1 1): Growth and substrate interaction. *Phys. Rev. B* (2009) 80: 245411. doi:10.1103/PhysRevB.80.245411.
- [12] X. Li, W. Cai, J. An, S. Kim, J. Nah, D. Yang, R. Piner, A. Velamakanni, I. Jung, E. Tutuc, S. K. Banerjee, L. Colombo, R. S. Ruoff. Large-area synthesis of high-quality and uniform graphene films on copper foils. *Science* (2009) 324: 1312–1314. doi:10.1126/science.1171245.
- [13] S. Marchini, S. Günther, J. Wintterlin. Scanning tunneling microscopy of graphene on Ru(0 0 0 1). *Phys. Rev. B* (2007) 76: 075429. doi:10.1103/PhysRevB.76.075429.
- [14] B. Wang, M.-L. Bocquet, S. Marchini, S. Günther, J. Wintterlin. Chemical origin of a graphene moiré overlayer on Ru(0 0 0 1). *Phys. Chem. Chem. Phys.* (2008) 10: 3530–3534. doi:10.1039/b801785a.
- [15] D. Alfè, M. Pozzo, E. Miniussi, S. Günther, P. Lacovig, S. Lizzit, R. Larciprete, B. S. Burgos, T. O. Menteş, A. Locatelli, A. Baraldi. Fine tuning of graphene-metal adhesion by surface alloying. *Sci. Rep.* (2013) 3: 2430. doi:10.1038/srep02430.

- [16] E. Miniussi, M. Pozzo, A. Baraldi, E. Vesselli, R. R. Zhan, G. Comelli, T. O. Menteş, M. A. Niño, A. Locatelli, S. Lizzit, D. Alfè. Thermal stability of corrugated epitaxial graphene grown on Re (0 0 0 1). *Phys. Rev. Lett.* (2011) 106: 216101. doi:10.1103/PhysRevLett.106.216101.
- [17] E. Miniussi, M. Pozzo, T. O. Menteş, M. A. Niño, A. Locatelli, E. Vesselli, G. Comelli, S. Lizzit, D. Alfè, A. Baraldi. The competition for graphene formation on Re(0 0 0 1): A complex interplay between carbon segregation, dissolution and carburisation. *Carbon* (2014) 73: 389–402. doi:10.1016/j.carbon.2014.02.081.
- [18] J. Wintterlin, M.-L. Bocquet. Graphene on metal surfaces. *Surf. Sci.* (2009) 603: 1841–1852. doi:10.1016/j.susc.2008.08.037.
- [19] P. Merino, M. Švec, A. L. Pinardi, G. Otero, J. A. Martín-Gago. Strain-driven moiré superstructures of epitaxial graphene on transition metal surfaces. *ACS Nano* (2011) 5: 5627–5634. doi:10.1021/nn201200j.
- [20] A. Martín-Recio, C. Romero-Muñiz, A. J. Martínez-Galera, P. Pou, R. Pérez, J. M. Gómez-Rodríguez. Tug-of-war between corrugation and binding energy: revealing the formation of multiple moiré patterns on a strongly interacting graphene–metal system. *Nanoscale* (2015) 7: 11300–11309. doi:10.1039/c5nr00825e.
- [21] O. Frank, J. Vejpravova, V. Holy, L. Kavan, M. Kalbac. Interaction between graphene and copper substrate: The role of lattice orientation. *Carbon* (2014) 68: 440–451. doi:10.1016/j.carbon.2013.11.020.
- [22] B. Hammer, J. K. Nørskov. Theoretical surface science and catalysis-calculations and concepts. *Adv. Catal.* (2000) 45: 71–129. doi:10.1016/S0360-0564(02)45013-4.
- [23] K. Toyoda, K. Nozawa, N. Matsukawa, S. Yoshii. Density functional theoretical study of graphene on transition-metal surfaces: The role of metal d-band in the potential-energy surface. *J. Phys. Chem. C* (2013) 117: 8156–8160. doi:10.1021/jp311741h.
- [24] A. Dahal, R. Addou, H. Coy-Diaz, J. Lallo, M. Batzill. Charge doping of graphene in metal/graphene/dielectric sandwich structures evaluated by C-1s core level photoemission spectroscopy. *APL Mater.* (2013) 1: 042107. doi:10.1063/1.4824038.
- [25] A. V. Generalov, Y. S. Dedkov. EELS study of the epitaxial graphene/Ni(1 1 1) and graphene/Au/Ni(1 1 1) systems. *Carbon* (2012) 50: 183–191. doi:10.1016/j.carbon.2011.08.018.
- [26] H. Hattab, A. N'Diaye, D. Wall, G. Jnawali, J. Coraux, C. Busse, R. Van Gastel, B. Poelsema, T. Michely, F.-J. Meyer Zu Heringdorf, M. Horn-Von Hoegen. Growth temperature dependent graphene alignment on Ir(1 1 1). *Appl. Phys. Lett.* (2011) 98: 141903. doi:10.1063/1.3548546.
- [27] A. T. N'Diaye, J. Coraux, T. N. Plasa, C. Busse, T. Michely. Structure of epitaxial graphene on Ir(1 1 1). *New J. Phys.* (2008) 10: 043033. doi:10.1088/1367-2630/10/4/043033.
- [28] P. Lacovig, M. Pozzo, D. Alfè, P. Vilmercati, A. Baraldi, S. Lizzit. Growth of dome-shaped carbon nanoislands on Ir(1 1 1): The intermediate between carbidic clusters and quasi-free-standing graphene. *Phys. Rev. Lett.* (2009) 103: 166101. doi:10.1103/physrevlett.103.166101.
- [29] A. Locatelli, C. Wang, C. Africh, N. Stojić, T. O. Menteş, G. Comelli, N. Binggeli. Temperature-driven reversible rippling and bonding of a graphene superlattice. *ACS Nano* (2013) 7: 6955–6963. doi:10.1021/nn402178u.
- [30] M. Bianchi, D. Cassese, A. Cavallin, R. Comin, F. Orlando, L. Postregna, E. Golfetto, S. Lizzit, A. Baraldi. Surface core level shifts of clean and oxygen covered Ir(1 1 1). *New J. Phys.* (2009) 11: 063002. doi:10.1088/1367-2630/11/6/063002.

- [31] Y. Cui, Q. Fu, X. Bao. Dynamic observation of layer-by-layer growth and removal of graphene on Ru(0001). *Phys. Chem. Chem. Phys.* (2010) 12: 5053–5057. doi:10.1039/c000719f.
- [32] D. Martoccia, P. Willmott, T. Brugger, M. Björck, S. Günther, C. Schlepütz, A. Cervellino, S. Pauli, B. Patterson, S. Marchini, J. Wintterlin, W. Moritz, T. Greber. Graphene on Ru(0001): A  $25 \times 25$  supercell. *Phys. Rev. Lett.* (2008) 101: 126102. doi:10.1103/PhysRevLett.101.126102.
- [33] J. Yeh, I. Lindau. Atomic subshell photoionization cross sections and asymmetry parameters:  $1 \leq z \leq 103$ . *At. Data Nucl. Data Tables* (1985) 32: 1–155. doi:10.1016/0092-640x(85)90016-6.
- [34] E. Ferrari, L. Galli, E. Miniussi, M. Morri, M. Panighel, M. Ricci, P. Lacovig, S. Lizzit, A. Baraldi. Layer-dependent Debye temperature and thermal expansion of Ru(0001) by means of high-energy resolution core-level photoelectron spectroscopy. *Phys. Rev. B* (2010) 82: 195420. doi:10.1103/PhysRevB.82.195420.
- [35] S. Lizzit, R. Larciprete, P. Lacovig, M. Dalmiglio, F. Orlando, A. Baraldi, L. Gammelgaard, L. Barreto, M. Bianchi, E. Perkins, P. Hofmann. Transfer-free electrical insulation of epitaxial graphene from its metal substrate. *Nano Lett.* (2012) 12: 4503–4507. doi:10.1021/nl301614j.
- [36] C. Vo-Van, S. Schumacher, J. Coraux, V. Sessi, O. Fruchart, N. B. Brookes, P. Ohresser, T. Michely. Magnetism of cobalt nanoclusters on graphene on iridium. *Appl. Phys. Lett.* (2011) 99: 142504. doi:10.1063/1.3646480.
- [37] A. Cavallin, M. Pozzo, C. Africh, A. Baraldi, E. Vesselli, C. Dri, G. Comelli, R. Larciprete, P. Lacovig, S. Lizzit, D. Alfè. Local electronic structure and density of edge and facet atoms at Rh nanoclusters self-assembled on a graphene template. *ACS Nano* (2012) 6: 3034–3043. doi:10.1021/nn300651s.
- [38] Z. Zhou, B. F. Habenicht, Q. Guo, Z. Yan, Y. Xu, L. Liu, D. W. Goodman. Graphene moiré structure grown on a pseudomorphic metal overlayer supported on Ru(0001). *Surf. Sci.* (2013) 611: 67–73. doi:10.1016/j.susc.2013.01.016.
- [39] S. Vlaic, A. Kimouche, J. Coraux, B. Santos, A. Locatelli, N. Rougemaille. Cobalt intercalation at the graphene/iridium(111) interface: Influence of rotational domains, wrinkles, and atomic steps. *Appl. Phys. Lett.* (2014) 104: 101602. doi:10.1063/1.4868119.
- [40] B. Casarin, A. Cian, Z. Feng, E. Monachino, F. Randi, G. Zamborlini, M. Zonno, E. Miniussi, P. Lacovig, S. Lizzit, A. Baraldi. The thinnest carpet on the smallest staircase: The growth of graphene on Rh(533). *J. Phys. Chem. C* (2014) 118: 6242–6250. doi:10.1021/jp411582a.
- [41] K. Gotterbarm, W. Zhao, O. Höfert, C. Gleichweit, C. Papp, H.-P. Steinrück. Growth and oxidation of graphene on Rh(111). *Phys. Chem. Chem. Phys.* (2013) 15: 19625–19631. doi:10.1039/c3cp53802h.
- [42] K. Gotterbarm, C. Steiner, C. Bronnbauer, U. Bauer, H.-P. Steinrück, S. Maier, C. Papp. Graphene-templated growth of Pd nanoclusters. *J. Phys. Chem. C* (2014) 118: 15934–15939. doi:10.1021/jp5052563.
- [43] B. Wang, S. Günther, J. Wintterlin, M.-L. Bocquet. Periodicity, work function and reactivity of graphene on Ru(0001) from first principles. *New J. Phys.* (2010) 12: 043041. doi:10.1088/1367-2630/12/4/043041.
- [44] W. Moritz, B. Wang, M.-L. Bocquet, T. Brugger, T. Greber, J. Wintterlin, S. Günther. Structure determination of the coincidence phase of graphene on Ru(0001). *Phys. Rev. Lett.* (2010) 104: 136102. doi:10.1103/PhysRevLett.104.136102.
- [45] D. Pacilé, S. Lisi, I. Di Bernardo, M. Papagno, L. Ferrari, M. Pisarra, M. Caputo, S. K. Mahatha, P. M. Sheverdyayeva, P. Moras, P. Lacovig, S. Lizzit, A. Baraldi, M. G. Betti, C. Carbone. Electronic structure of graphene/Co interfaces. *Phys. Rev. B* (2014) 90: 195446. doi:10.1103/PhysRevB.90.195446.

- [46] D. Eom, D. Prezzi, K. T. Rim, H. Zhou, M. Lefenfeld, S. Xiao, C. Nuckolls, M. S. Hybertsen, T. F. Heinz, G. Flynn. Structure and electronic properties of graphene nanoislands on Co (0 0 0 1). *Nano Lett.* (2009) 9: 2844–2848. doi:10.1021/nl900927f.
- [47] E. Voloshina, Y. Dedkov. Graphene on metallic surfaces: Problems and perspectives. *Phys. Chem. Chem. Phys.* (2012) 14: 13502–13514. doi:10.1039/c2cp42171b.
- [48] I. Hamada, M. Otani. Comparative van der Waals density-functional study of graphene on metal surfaces. *Phys. Rev. B* (2010) 82: 153412. doi:10.1103/PhysRevB.82.153412.
- [49] B. Wang, M. Caffio, C. Bromley, H. Früchtl, R. Schaub. Coupling epitaxy, chemical bonding, and work function at the local scale in transition metal-supported graphene. *ACS Nano* (2010) 4: 5773–5782. doi:10.1021/nn101520k.

## Chapter 3

# Adsorption of atoms and molecules on Gr

In the previous chapter, I have shown that the interaction of Gr with metal substrates can significantly modify its properties, which can potentially affect most applications of Gr and must therefore be addressed before it can be successfully adopted. However, there are several other species, beside metal surfaces, to whom Gr could be exposed in its everyday use, and which are able to modify its properties when they interact with it. In fact, as I have already pointed out in the Introduction, also the adsorption of gas molecules on Gr can alter its band structure: for example, this is the case of gasses commonly found in the atmosphere such as water, and the effects of this interaction can have a negative impact on Gr-based devices when operated in atmosphere<sup>1-3</sup>. An in-depth understanding of the mechanisms of the adsorption of gasses on Gr is therefore needed in order to evaluate and address this issue. Furthermore, this knowledge can be beneficial to a much wider public, as it is at the base of several promising applications of Gr ranging from catalysis, where Gr could act either as a metal-free active phase<sup>4-6</sup> or as a co-catalyst in photocatalysis<sup>7,8</sup>, to gas sensing<sup>9</sup>. However, the understanding on the interactions between Gr and its adsorbates is not yet complete, as there is still on-going debate on some key aspects<sup>10</sup>.

In particular, one of the main issues which are still open is the way in which the substrate below Gr affects its interactions with adsorbates. In fact, it has been shown by several experimental techniques that the interaction of adsorbed molecules with Gr can vary significantly when Gr is supported on different substrates, such as metals having a higher or lower reactivity, semiconductors or metal-oxides. For example, temperature-programmed desorption experiments have shown that the adsorption energy of carbon monoxide on Gr strongly interacting with a Ni (1 1 1) surface is remarkably larger than in the case of CO on free-standing Gr<sup>11</sup>. Likewise, contact-angle measurements have shown a significant difference in the Gr-water interaction between oxide- (SiO<sub>2</sub>) and metal- (Cu) supported Gr leading to qualitative differences in the wettability of Gr, which is hydrophilic in the former case, yet hydrophobic in the latter<sup>12</sup>. These very remarkable results have lead to speculation that Gr might be even transparent to vdW forces, due to the combined effects of its extreme thinness and of the long range which characterizes this kind of interaction<sup>13</sup>. This has prompted a long-lasting debate which is still on-going<sup>10,14</sup>. On one hand, Rafiee *et al.*<sup>15</sup> from a study combining contact angle measurements with molecular dynamics simulations suggested that Gr could be fully transparent to vdW interactions. On the other hand, Shih *et al.*, on the basis of classical theory of vdW interactions, reported that the transparency is only partial – *i.e.* a layer of Gr does reduce the interaction with the underlying substrate, yet only to about 30% of its original value, and would then be more appropriately described as *translucent*.<sup>16</sup> Other studies have denied any effect of the substrate on the Gr-water interaction<sup>17</sup>. Up to now, no general consensus is found on this topic<sup>10</sup>, as further studies have even recently lead to incompatible results, either upholding<sup>12,18,19</sup> or rejecting<sup>20</sup> this transparency. This debate is of particular interest as chemically inert materials such as Gr, if proven transparent to electronic transfer and interaction, could be very promising for the development of passivating films allowing to employ electrocatalytically active materials in harsh environments while protecting them from corrosion<sup>21</sup>.

Another issue which is still hindering a full understanding on the interaction of Gr with atoms and molecules is related to the accuracy of the theoretical calculations of the adsorption energy and configurations of the molecules. In fact, as already mentioned in the Introduction, an accurate calculation of

the molecular adsorption energy on Gr requires a proper description of vdW interactions, and in particular dispersive forces<sup>22,23</sup>. Theoretical simulation methods such as Diffusion Monte Carlo (DMC) can provide reliable estimations of the vdW interactions between molecules and Gr, yet they are not suitable for large systems such as the moiré cells of Gr supported on metals due to their large computational cost<sup>24</sup>. On the other hand, different approaches have been developed to implement the description of dispersive forces into DFT, which is more affordable from the point of view of its computational cost. For example, a reasonable agreement with experimental data can be obtained by a semi-empirical method<sup>25,26</sup>, while a more recent implementation is based on a non-local correlation functional that approximately accounts for dispersion interactions<sup>27–29</sup>. However, these different implementations do not always lead to consistent results, and in some cases the choice between them can be essential to obtain accurate results from theoretical calculations. For example, this can be observed by studying the interaction of water molecules with Gr, as the use of potentials not implementing vdW interactions correctly can even predict that molecular adsorption is thermodynamically hindered, in contrast to experimental results<sup>24,30</sup>. For this reason, an extended set of experimental data is needed, to be able to perform a systematic benchmark of the different theoretical implementations of vdW forces and thereby identify the main issues affecting those methods and allow computational scientists to address them<sup>31,32</sup>.

In the research work I am describing in this Chapter, therefore, we have addressed these issues by characterising the adsorption configuration and energy of different atomic or molecular adsorbates on Gr and comparing the data to theoretical calculations. These experiments, moreover, represent a further step with respect to the previous Chapter towards a more comprehensive description of the properties of Gr in a real life environment. In order to deconvolute the different aspects of molecular adsorption, these experiments have been performed in a controlled manner, by studying the adsorption of a single substance at a time in UHV environment. There are, in fact, many effects which can contribute to make a correct experimental determination of the molecular adsorption energy challenging. For example, the density and the type of surface defects, such as mono- and di-vacancies, dislocations, disclinations and grain domain boundaries can locally affect the interaction strength<sup>33</sup>. Furthermore, on many Gr-substrate systems, multiple phases, characterized by different translational or rotational symmetry, can coexist, leading to a changeable degree of interaction with the substrate in different regions<sup>34</sup>. Finally, the superposition of the Gr unit cell to that of the substrate can induce a moiré-driven buckling of Gr, leading to a variable Gr-substrate distance on the nanometre scale<sup>35</sup>. This variable distance, besides affecting the electronic structure of Gr, could significantly influence the vdW interaction, due to its long-range dependence on the distance of the adsorbates from the substrate<sup>16</sup>: for example, it has been shown that hydrogen preferentially adsorbs on the convex regions of buckled Gr/SiC (0 0 1)<sup>36</sup>.

All these factors can affect the molecular adsorption properties on Gr on the local scale. This makes their experimental study challenging as the adsorption energy is typically probed using space-averaging experimental techniques such as Temperature Programmed Desorption (TPD). A powerful tool to address this issue is to use the Temperature Programmed XPS (TP-XPS) experimental technique available at the SuperESCA beamline, where photoemission spectra are acquired in real time while the sample temperature is increased with a linear rate. The technique, which is an improvement of TPD, exploits the core-level shifts induced by different adsorption configurations to provide the ability to distinguish the desorption rate and thereby the adsorption energy of non-equivalent adsorbates<sup>37</sup>. This technique was therefore fundamental in our measurements to be able to appreciate the effects of the Gr moiré and corrugation on the adsorption energy of molecules, as will be shown later in this chapter.

Another important aspect affecting the adsorption of molecules and atoms on Gr is the lateral interaction occurring between adsorbed molecules. The templating effect of Gr, due to the nature of the moiré structures, can even enhance the role of these intermolecular interactions, as the adsorption is preferred in some regions of the corrugated unit cell, where the density of adsorbates can locally increase<sup>38</sup>.

To reduce and control the degrees of freedom affecting the adsorption dynamics of molecules on Gr, in order to understand and quantify their different effects on the adsorption of molecules on epitaxial Gr, we have employed a strategy based on the comparison of the adsorption energy of molecules deposited in different concentrations on two different interfaces, namely Gr/Ir (1 1 1) – where Gr is considered almost

fully decoupled from this substrate, as shown in Chapter 2 – and Gr/Co/Ir (1 1 1). The great advantage of our approach is that the intercalation of cobalt atoms below an extended Gr monolayer results in the formation of a corrugated structure with regions of the carbon network close to (about 2.1 Å) and far from (about 3.2 Å) the metal substrate, while preserving the orientation and the lattice mismatch of Gr with respect to the substrate underneath and the resulting moiré, without significantly affecting the defects density, as described in Chapter 2.3.

### 3.1 Carbon monoxide adsorption on supported Gr: substrate-induced enhancement of the adsorption energy

The first species we have chosen for our studies is carbon monoxide. In fact, thanks to its polar nature and low reactivity, it is expected to interact with Gr exclusively through vdW forces, while the intermolecular interactions are expected to be weak as well, considering its very low sublimation point.

In addition, a few studies exist on a system similar to CO adsorption on Gr, namely on the adsorption of this gas on the (0 0 0 1) surface of graphite. In particular, X-ray<sup>39</sup> and low energy electron<sup>40</sup> diffraction studies and IR absorption experiments<sup>41</sup> on this system indicate that CO can form different commensurate structures depending both on temperature and coverage, characterized by relatively large unit cells and complex geometries. Theoretical calculations explain this complicated behaviour with the fact that the interaction between CO molecules not only depends on dipole-dipole interactions, but also higher moments (quadrupoles, octupoles) play an important role in this system<sup>40</sup>. Desorption of CO from graphite (0 0 0 1) starts above 40 K, indicating that the molecules are physisorbed on this surface<sup>40</sup>.

Finally, the study of the role of the substrate on the adsorption energy of CO on Gr is of particular interest following experimental<sup>11</sup> and theoretical<sup>42</sup> results showing that the adsorption energy of CO on Gr strongly interacting with a Ni (1 1 1) surface is remarkably larger than in the case of CO on free-standing Gr, which have suggested the application of this system as a promising metal-free catalyst<sup>43</sup>. However, the reason for this behaviour is still not clear. For example, it has been proposed that carbon monoxide forms dimers when adsorbed on Gr/Ni (1 1 1)<sup>42</sup>, but this has not yet been observed experimentally.

The aim of our experiment was therefore to understand and decouple the factors governing the adsorption energy and configuration of CO molecules on metal-supported Gr, by characterizing different coverages of CO adsorbed on Gr layers having a different interaction with the underlying substrate.

#### 3.1.1 Experimental details

As described above, we investigated and compared carbon monoxide adsorption on two different substrates. The first system was Gr directly grown on Ir (1 1 1), prepared and characterized as indicated in Chapter 2.1. The other was Gr on a cobalt-terminated Ir (1 1 1) surface, obtained by intercalation of a single Co layer below Gr, following the procedure described in Chapter 2.3.1.

The sample was cooled using a liquid-helium filled cryostat: the temperature was measured using two K-type thermocouples directly spot-welded to the crystal. We calibrated the temperature reading using two methods: by fitting the shape of the Fermi edge photoemission spectrum to the Fermi-Dirac function – convoluted with a Gaussian taking into account the experimental contribution – and by measuring the temperature of the desorption onset of Ar gas multilayers, which is known to start at 25 K<sup>44</sup>. The overall temperature calibration is affected by an error of  $\pm 1$  K. Carbon monoxide gas was dosed onto the sample from a leak valve at a constant pressure of  $5 \times 10^{-9}$  mbar, as obtained after correction for the base pressure and gauge-specific sensitivity factor.

In order to measure the CO desorption energy, a TP-XPS experiment was then performed for each CO exposure, by measuring in real time the C 1s photoemission spectrum during a linear temperature ramp (2.5 K/min). This technique allows to probe variations in the adsorption sites, configurations and adsorbate electronic properties as a function of the temperature and residual molecular coverage<sup>37</sup>. The desorption energy was obtained from the coverage curves thus obtained, by fitting the coverage curves to the Arrhenius equation. Due to the strong correlation between the parameters of this fit, the analysis

required a particular care to correctly evaluate the uncertainty on the fit parameters: the details of the fitting procedure are described below. It is important to underline that since there is no adsorption barrier in physisorbed systems, the measured desorption energy can be directly compared with the calculated adsorption energy<sup>45</sup>.

We investigated possible photon-beam induced desorption effects by moving the Ir crystal by a distance larger than the photon beam size at the sample (vertical dimension 5  $\mu\text{m}$ ) after dosing a full CO layer: even though such an effect could be detected (0.5 percent of ML undergoes photon-induced desorption after 1000 s x-ray exposure), it was only relevant on a time scale which was much larger than our data acquisition time per spectrum, which was about 20 seconds. Therefore, all photoemission spectra of CO were measured while moving the crystal in steps of 30  $\mu\text{m}$  perpendicularly to the beam every 30 s.

### Analysis of CO desorption curves

In order to obtain the desorption energy of CO from Gr, we performed a fit of our desorption curves based on the Arrhenius equation:

$$-\frac{d\theta}{dt} = \nu\theta^N e^{-E_{DES}/k_B T}$$

where  $\theta$  is the coverage,  $t$  is the time,  $\nu$  is the pre-exponential factor or desorption attempt frequency,  $N$  is the order of the desorption process,  $E_{DES}$  is the desorption energy and  $k_B$  is the Boltzmann constant. This relation can be integrated and the coverage can be then expressed explicitly as a function of the temperature:

$$\int_{\theta_0}^{\theta(T)} \frac{d\theta}{\theta^N} = -\nu \int_{T_0}^T e^{-E_{DES}/k_B T} \frac{dt}{dT} dT$$

where  $\frac{dt}{dT}$  is the reciprocal of the heating rate, which in our case was  $\frac{dt}{dT} = 24 \text{ s/K}$ . This equation can be integrated again to explicitly express the dependence of  $\theta$  on  $T$ . For  $N = 1$ , in particular, the equation above yields:

$$\theta = \theta_0 e^{-\nu \int_{T_0}^T \exp(-E_{DES}/k_B T) \frac{dt}{dT} dT}$$

while for other values of  $N$  it yields:

$$\theta = \left( \theta_0^{(1-N)} - (1-N) \nu \int_{T_0}^T e^{-E_{DES}/k_B T} \frac{dt}{dT} dT \right)^{1/(1-N)}$$

The fit was performed with  $\nu$  and  $E_{DES}$  as free fit parameters. Being these two parameters strongly correlated, in order to obtain a good estimate of their error bar we evaluated the presence of well-localized confidence regions for the fit in the space of these two parameters. In particular, we evaluated the normalized value of the fit's  $\chi^2$  in the space spanned by the parameters  $\nu$  and  $E_{DES}$ , while relaxing the other fit parameters one at a time. The confidence region was chosen as the one where the normalized chi square value is within 5% from its minimum value:  $\chi^2/\chi_{MIN}^2 \leq 1.05$ .

### 3.1.2 Experimental results

#### Characterisation of carbon monoxide adsorption on Gr/Ir (1 1 1)

Figure 3.1a shows the time evolution of C 1s core level spectra during the uptake of CO on Gr/Ir (1 1 1) at 38 K. We chose this deposition temperature as it is the highest at which CO can adsorb, in order to ensure that the molecules have some mobility to diffuse to their equilibrium adsorption configuration, and high enough to avoid a multilayer formation, which takes place below 30 K.

At the beginning of the uptake, the spectrum (shown in Figure 3.1c, below) shows a single component with a FWHM of 850 meV, centred at a BE value of 289.9 eV.



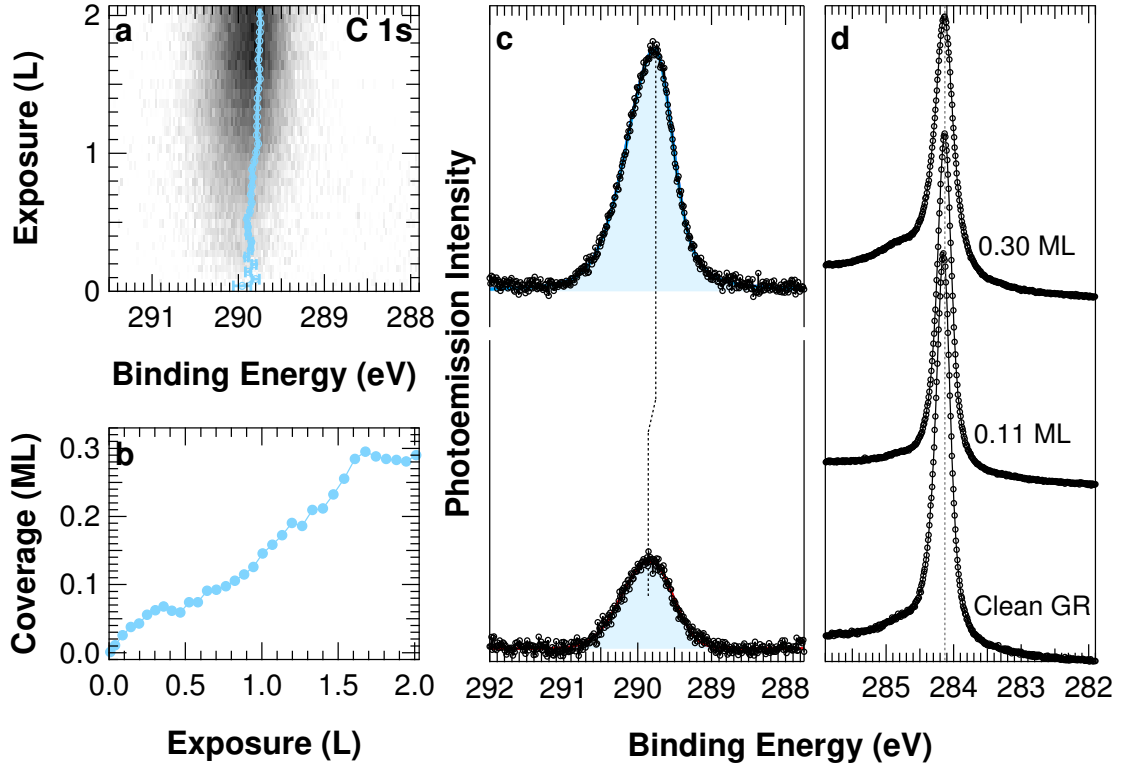


**Figure 3.1:** CO uptake on Gr/Ir (1 1 1) ( $h\nu = 325$  eV). a: Time resolved sequence of C 1s spectra acquired during exposure to  $p = 10^{-9}$  mbar CO at  $T=38$  K. The C 1s Binding Energy evolution of the different components is plotted as a function of the CO exposure. b: Evolution of CO coverage as a function of CO exposure (the photoemission intensity is in grey scale). c: Selected spectra of the uptake corresponding to a coverage of 0.08 ML (bottom) and to saturation, 0.3 ML (top). d: C 1s spectrum of GR as synthesized (below) and after adsorption of CO, for different coverages.

The C 1s photoemission intensity increases linearly with CO exposure, and then stops suddenly, showing that a saturation coverage has been reached for a coverage of about 0.3 ML (Fig. 3.1b). Throughout the uptake, the C 1s BE progressively shifts towards lower values by about 200 meV, reaching a value of 289.7 eV at saturation (Figure 3.1c, above).

The C 1s photoemission peak of about 0.3 ML CO/Gr/Ir (1 1 1) is shown in Figure 3.2a: it has a slightly asymmetric lineshape, which does not change appreciably with coverage. The reason for this asymmetry can be found in final-state vibrational excitation effects<sup>46,47</sup>. Indeed, vibrational splitting has been observed for CO in gas-phase<sup>48–50</sup> and adsorbed on metal surfaces<sup>47,51–53</sup>. If we consider the harmonic approximation of the molecular potential, the vibrational spectrum can be described by discrete levels separated by integer multiples of a vibrational quantum  $\hbar\omega_{VIB}$ . This corresponds to the vibrational quantum of the excited molecular ion  $\text{CO}^{+*}$  – *i.e.* characterized by a core hole in the C 1s level –, which in gas phase CO has been determined to be about 300 meV<sup>48–50</sup>. As happens for the vibrational modes of the neutral molecules, the quantum of these vibrations is reduced when CO is adsorbed on transition metal surfaces, with a C 1s vibrational splitting ranging from 210 meV in the case of Co (0 0 1)<sup>52</sup> to 235 meV in the case of Rh (1 1 1) (for CO sitting in on-top sites, on both surfaces)<sup>53</sup>. This reflects a weakening of the molecular bond strength due to the molecular orbitals being hybridized with the substrate and is a fingerprint of chemisorption<sup>47,51–53</sup>.

In order to describe the vibrationally resolved lineshape, a set of DS peaks was used (as shown in Figure 3.2a), each having the same lineshape, separated from the next one by an energy difference  $h\nu_{VIB}$  and having a relative intensity with respect to the adiabatic component equal to the Frank-Condon factor  $FC_N$ . Beside the adiabatic peak, two vibrational replicas could be resolved and were included in the description. The fit was performed in subsequent iterations, by relaxing the parameters one at a time until

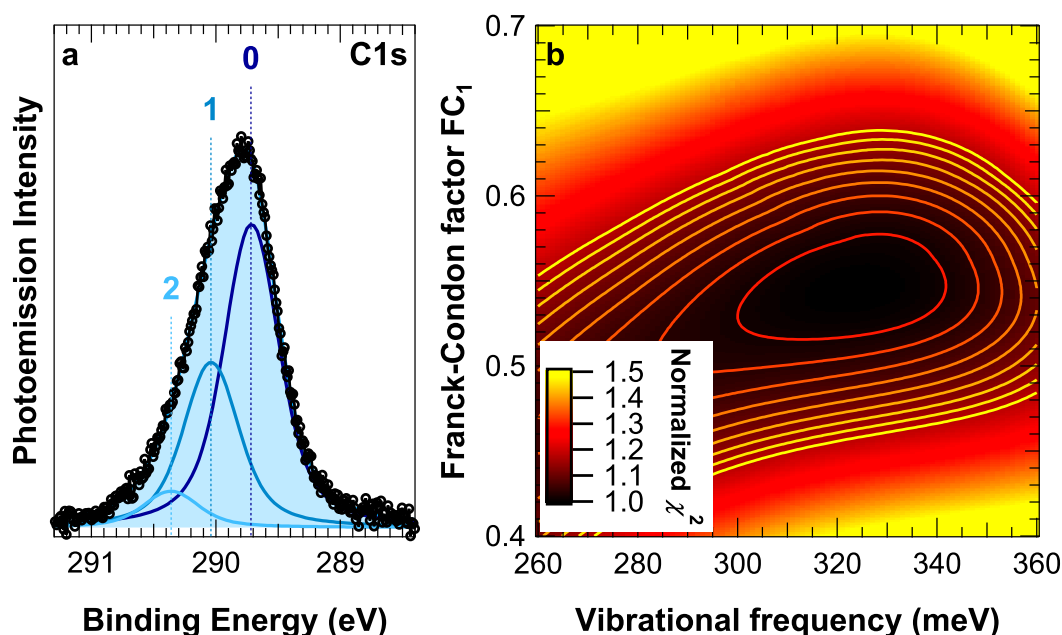


**Figure 3.2:** Vibrationally resolved high-resolution C 1s on Gr/Ir (1 1 1) ( $h\nu = 325$  eV). a: Deconvoluted vibrational components in the photoemission spectrum: component 0 corresponds to the adiabatic peak; the higher vibrational final states are progressively numbered. b: The dependence of the fit  $\chi^2$  value on two fit parameters – vibrational frequency of the final state of the photoemission process and Franck-Condon factor of the first excited state – is shown in color scale.

they converged. During the fit, a correlation was observed between the  $h\nu_{VIB}$  and  $FC_N$  parameters: in order to accurately estimate the uncertainty on these parameters, we evaluated the normalized value of the fit's  $\chi^2$  in the space spanned by the parameters  $h\nu_{VIB}$  and  $FC_1$ , using an analogous procedure to the one described in Section 3.1.1. The confidence region obtained from this fit is shown in figure 3.2b. The  $\chi^2$  displays a single, well defined minimum. The Franck-Condon coefficients found for the first two replicas were  $0.55 \pm 0.5$  and  $0.13 \pm 0.05$ , respectively. The vibrational frequency of the core-excited molecular state is  $320 \pm 25$  meV. This value, which is close to the values reported for CO in gas phase, *i.e.* 300 meV,<sup>49</sup> is a first indication of the weak interaction between CO and Gr.

The lineshape parameters which best fit the data correspond to a Lorentzian FWHM  $L$  of 285 meV, an asymmetry parameter  $\alpha$  of 0, and a Gaussian FWHM  $G$  of 340 meV.

To investigate the orientation of the CO adsorbates, we evaluated the linear dichroism in the NEXAFS absorption spectrum at the O K-edge. Fig. 3.3a shows the NEXAFS spectrum of CO/Gr/Ir (1 1 1). The absorption spectrum shows a sharp feature at  $533.5 \pm 0.1$  eV. This feature is attributed to the O 1s  $\rightarrow$  CO  $\pi^*$  transition<sup>54</sup>; this is a dipole transition which is only allowed when the polarization of the impinging radiation has a component perpendicular to the molecular axis<sup>55</sup>. It is clear already from a qualitative inspection of the spectra that this feature is not suppressed for either incidence angle; this indicates that the molecule is not standing upright on the surface. It is interesting to observe that the flat adsorption geometry was found also in the case of CO on graphite (0 0 0 1).<sup>39–41</sup>

At saturation coverage, we observed that the adsorbed CO generates a LEED pattern, which is shown in Figure 3.3b. This LEED pattern corresponds to a  $(\sqrt{3} \times \sqrt{3})R30^\circ$  structure, analogous to the one reported in literature for CO/graphite (0 0 0 1)<sup>40</sup>. However, the background in this pattern is stronger when compared to that of clean Gr, suggesting that the adsorbed layer is characterized by a higher degree of disorder. These extra diffraction spots also show additional second order spots, due to the superposition of the lattice formed by the CO molecules to the moiré supercell of Gr.

Actually, the theoretically predicted structure (see Theoretical Results) is more complex, as the calculated structure has the molecules' positions fixed on a  $(\sqrt{3} \times \sqrt{3})R30^\circ$  lattice, yet their orientation does not show long-range ordering. This can actually explain the fact that even though the diffraction spots from

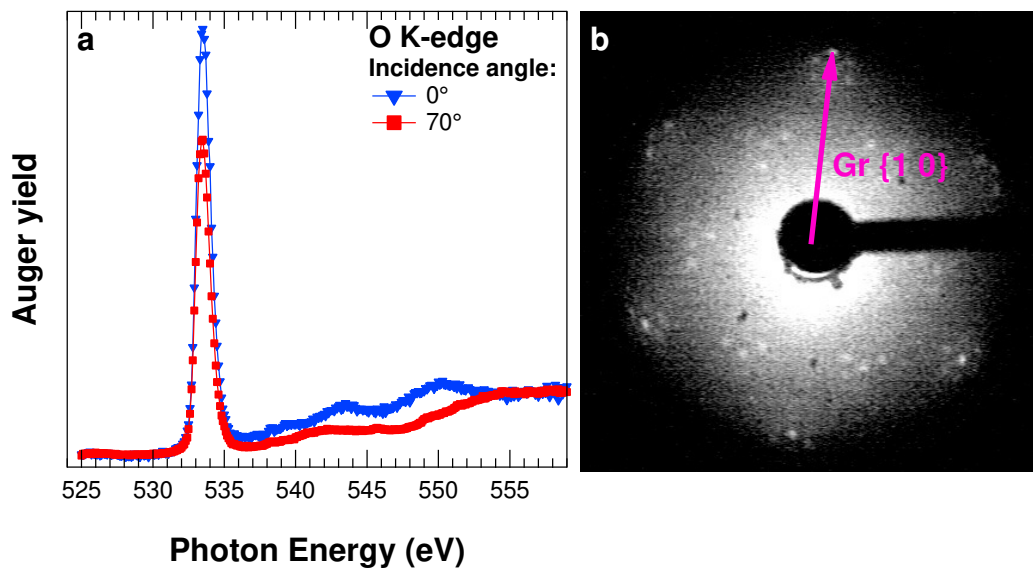


**Figure 3.3:** a: NEXAFS of 0.08 ML CO/Gr/Ir (1 1 1) measured in Auger yield at the O K-edge at normal incidence (*i.e.* incidence angle 0°) and at 70° incidence angle (grazing incidence). b: LEED pattern of a saturated layer of CO/Gr/Ir (1 1 1) ( $E = 76$  eV).

this structure are visible in LEED, they are faint while the background is relatively strong, indicating a high degree of disorder inside the system. This is a similar case to what occurs for CO/graphite (0 0 0 1), where an orientational disorder of the adsorbed molecules was observed in several studies<sup>40,41</sup>.

Finally, another interesting result comes from the analysis of the C 1s binding energy of Gr before and after CO adsorption. In fact, the lineshape and BE of the C 1s core level peak of Gr are not modified by the CO adsorption within our experimental accuracy (20 meV, as shown in Figure 3.1d). This indicates that the interaction with CO does not induce a significant charge transfer into Gr, whose doping remains instead entirely determined by the interaction with the Ir (1 1 1) substrate.

### Carbon monoxide desorption from Gr/Ir (1 1 1)

TP-XPS measurements were taken for different exposures of CO on Gr/Ir (1 1 1). Fig. 3.4a shows a selected TP-XPS experiment, corresponding to an initial CO coverage of  $\theta_i = 0.14$  ML: the C 1s photoemission intensity is plotted in grey scale, as a function of the annealing temperature. The evolution of coverage as a function of temperature during this experiment is shown in Fig. 3.4b.

As reported in Section 3.1.1, the free parameters in the fit were the desorption attempt frequency  $\nu$  and the desorption energy  $E_{des}$ . To evaluate the correlation between them, the analysis was performed by using the procedure described in Section 3.1.1. The results of this analysis of the parameter space, for a selected system (corresponding to 0.11 ML CO/Gr/Ir (1 1 1)), are shown as an example in Figure 3.5a. In this system, the parameters  $\nu$  and  $E_{DES}$  show a very strong anti-correlation: this is clearly visible from the shape of the confidence region, which has a highly eccentric elliptic shape, whose width is almost negligible with respect to its length. This demonstrates the need for a precise evaluation of the correlation between the parameters, to properly estimate the error bar associated to our fit results.

During our analysis, we verified that the order of the process is  $N = 1$ : this means that the desorption probability depends linearly from the coverage, and indicates that the desorption process does not involve any reaction between adsorbates<sup>45</sup>. However, if we compare the desorption curves measured for different exposure of CO (Fig. 3.4c), it is evident that the temperature at which desorption takes place is not the same, but clearly moves towards higher temperatures for increasing coverage. This cannot be described by a simple first order process, unless we assume that the desorption energy is dependent on coverage.

The analysis of all curves starting from different initial coverages yielded a  $\nu$  parameter of  $10^{17 \pm 3} \text{ s}^{-1}$ ;

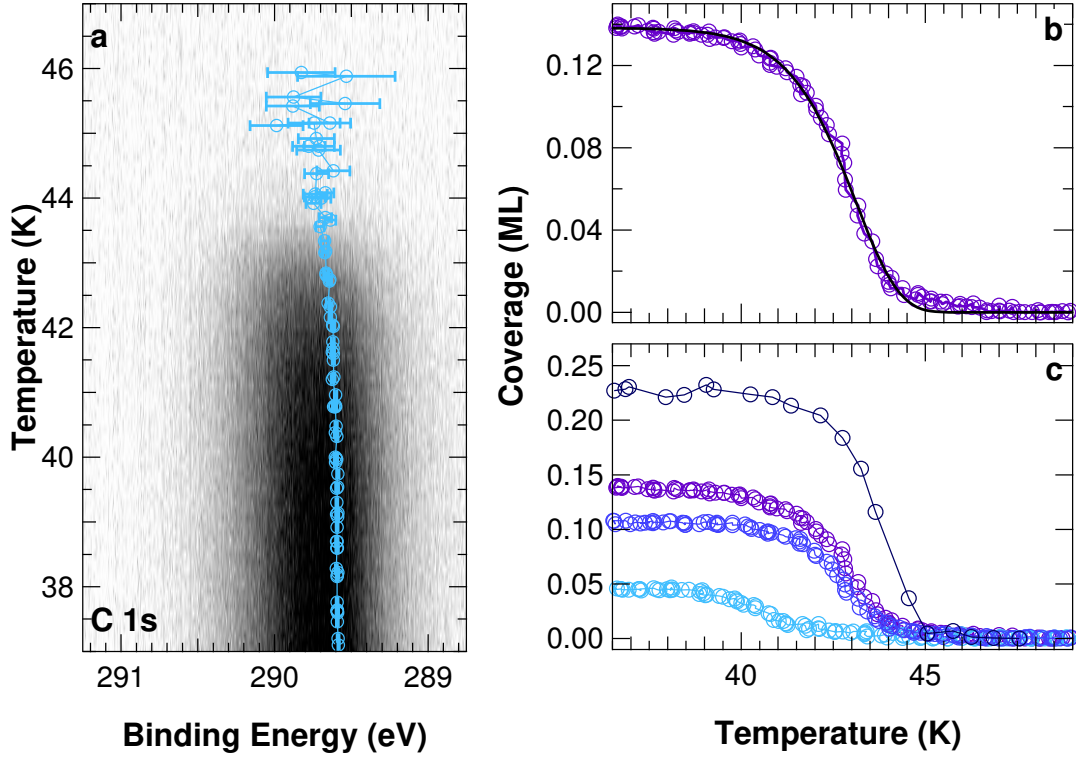


**Figure 3.4:** TP-XPS C 1s core level spectra measured during thermal desorption of CO from Gr/Ir (1 1 1) ( $h\nu = 325$  eV). a: Evolution of CO C 1s spectra acquired during a linear temperature ramp, and b: CO coverage curve evolution as a function of temperature (initial CO coverage is 0.14 ML). c: Comparison of CO desorption curves for different CO initial coverages.

$\theta_i$ (ML)	$E_{des}$ (meV)
0.03	$146 \pm 25$
0.05	$149 \pm 25$
0.11	$157 \pm 20$
0.23	$162 \pm 25$

**Table 3.1:** Desorption energy  $E_{des}$  obtained from the fit of the desorption curves of CO from Gr/Ir (1 1 1) for different initial CO coverage  $\theta_i$ .

however, the desorption energies were different depending on coverage and are reported in Table 3.1. While the uncertainty associated to each of the parameters is relatively large, about 25 meV for the desorption energy and more than 2 orders of magnitude for  $\nu$ , this error is over-estimated since it encloses a much wider area of the parameter space than the confidence region alone. In fact, as shown in Figure 3.5b, the confidence regions (*i.e.* those where  $\chi^2/\chi_{MIN}^2 \leq 1.05$ ) clearly don't overlap, even though the error bars of the single parameters do. Moreover, it can be noted that the shape and sizes of the different regions are very similar, yet they appear to be shifted along the  $E_{DES}$  coordinate. This allows us to calculate differences in the parameters' values between different desorption experiments with a significantly higher accuracy than we have for their absolute values, down to about 5 meV: this value has been calculated from the distance between the confidence regions along the  $E_{DES}$  axis of the graph, for different values of  $\nu$  within its error bar. This allows us to conclude that the desorption energy displays a significant dependence on coverage.

The value obtained for  $\nu$  is relatively high, as values typically used to fit the desorption curves are usually centred around  $10^{13} \text{ s}^{-1}$ . However, it has been shown that this value can vary by several orders of magnitude depending on the system, especially when the surface is not a metal - as is the case of Gr<sup>56</sup>.

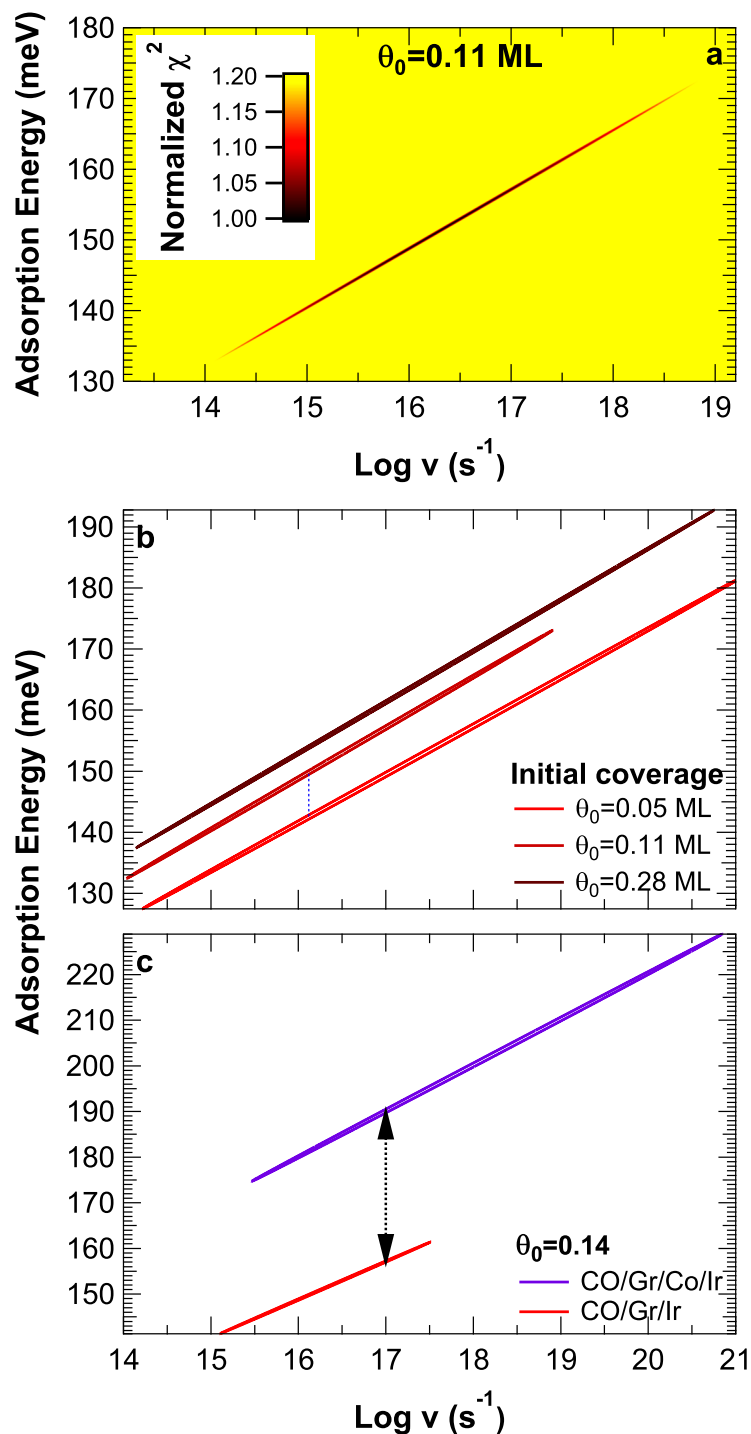


**Figure 3.5:** Confidence regions of the fit of the desorption curves. a: Dependence of the fit normalized  $\chi^2$  value of the desorption curve of 0.11 ML CO/Gr/Ir from two fit parameters: desorption energy  $E_{DES}$  and attempt frequency  $\nu$ . b: Confidence regions  $\chi^2/\chi_{MIN}^2 \leq 1.05$  for CO desorption from Gr/Ir, for different initial coverage. c: Confidence regions  $\chi^2/\chi_{MIN}^2 \leq 1.05$  for the desorption curve of 0.14 ML CO from Gr/Ir and Gr/Ir ML Co/Ir.

CO, besides, is characterized by a relatively high  $\nu$  (around  $10^{14}$  to  $10^{16}$   $s^{-1}$ ) when adsorbed on different metal surfaces<sup>57</sup>.

The value found for the adsorption energy, which is about 150 meV, is a clear indication that CO is very weakly interacting with the substrate. The adsorption energy increases with coverage by at least 20 meV, from the lowest coverage investigated (corresponding to 0.03 ML) to saturation (0.3 ML). This is

a fingerprint of the existence of an attractive interaction between the molecules, its average intensity per molecule being at least 20 meV at saturation, which corresponds to more than 10% of the adsorption energy of isolated molecules.

### Carbon monoxide adsorption on Gr/Cobalt/Ir (1 1 1)

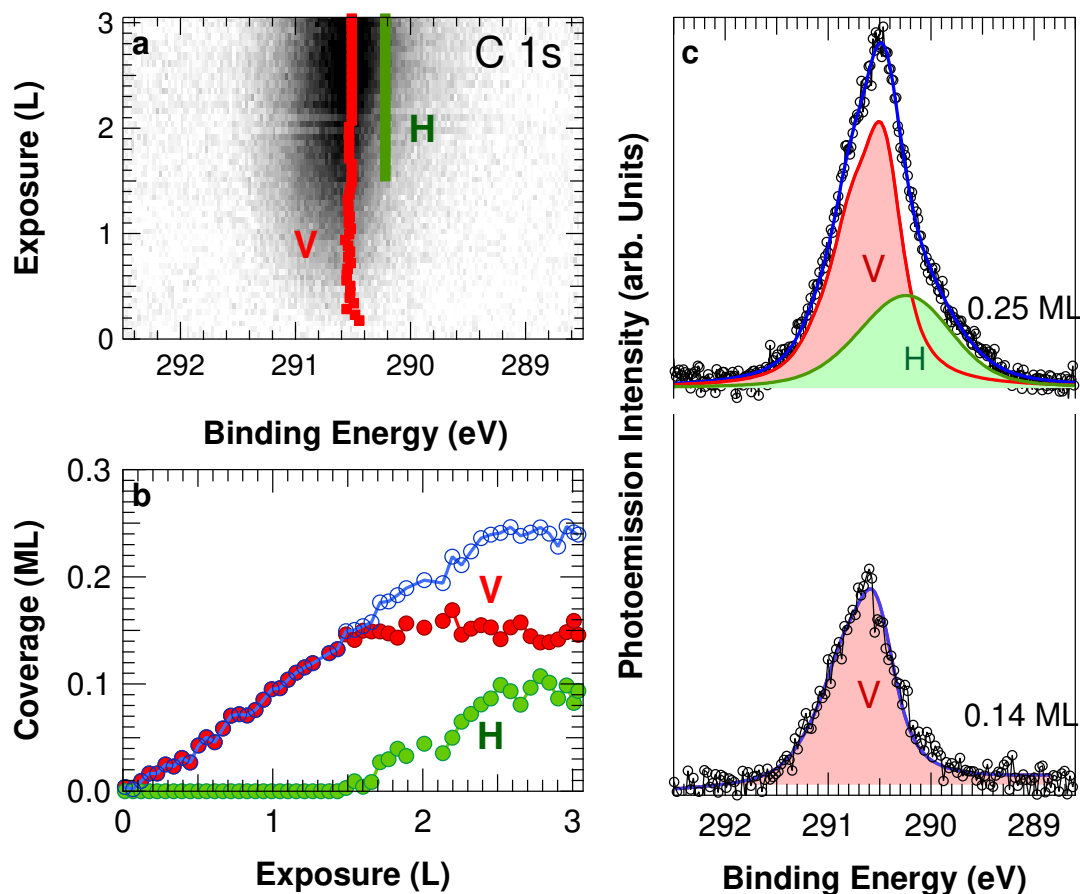


**Figure 3.6:** C 1s photoemission spectra during the uptake of CO on Gr/Co/Ir(1 1 1) ( $h\nu = 325$  eV). a: Time-lapsed sequence acquired during exposure to  $p=5 \times 10^{-9}$  mbar CO at  $T=41$  K. The C 1s Binding Energy evolution is plotted as a function of the CO exposure. b: Evolution of CO coverage as a function of CO exposure. c: Selected spectra of the uptake corresponding to a coverage of 0.08 ML (below) and to saturation (0.25 ML, above).

The sequence of C 1s spectra acquired during the uptake of CO at  $T=38$  K on Gr/Co/Ir (1 1 1) is shown in Figure 3.6a. Selected spectra are shown in Fig. 3.6c. At low coverage (Fig. 3.6c, below), a single component (V – red) is visible, which has an asymmetric shape due to the vibrational final state effects, as was the case for CO/Gr/Ir. Also in this case, the asymmetry can be described by taking into account vibrational final-state effects, using the vibrational frequency already found for CO/Gr/Ir (1 1 1) ( $320 \pm 25$  meV). The lineshape which best fits the low coverage data has a Lorentzian FWHM  $L = 310 \pm 20$  meV and a Gaussian FWHM  $G = 240 \pm 20$  meV, not significantly different from the Gr/Ir case; the Franck-Condon factors for the higher energy final states are 0.55 and 0.13, respectively.

As shown in Figure 3.6b, the coverage increases linearly with exposure. However, when the coverage becomes higher than 0.15 ML, the photoemission spectra can no longer be fitted with just a single component, but a second one (H – green) has to be included at lower BE. At this point, component V remains constant in intensity, while component H increases, so that the total coverage always increases with the same rate. The adsorption process ended at saturation for a coverage corresponding to slightly less than 0.3 ML, as was the case for CO/Gr/Ir (1 1 1).



The C 1s spectrum of a saturated CO monolayer is shown in Figure 3.6c (above). Component V has the same lineshape as in the low coverage spectrum. Component H can be fitted with the same vibrational quantum and Franck-Condon factor as component V, however the lineshape is characterized by a larger Gaussian broadening  $G = 0.76 \pm 0.12$  meV, indicating a higher degree of disorder in the system. The BE of the V component in the C 1s spectrum of CO at saturation coverage is 290.47 eV, which is significantly larger than for CO/Gr/Ir (1 1 1) (289.74 eV), by about 730 meV. The BE of component H is 290.12 eV, lower than V by about 350 meV. Still, both components V and H lie at a higher BE than those of CO/Gr/Ir (1 1 1). This C 1s BE shift is actually similar to that of the C 1s core level of Gr, which displays two photoemission components when it is supported on Co/Ir (1 1 1), both at higher BE with respect to Gr/Ir (1 1 1). At saturation, the photoemission intensity of component V is about 1.56 times that of component H, with the H coverage (0.095 ML) which corresponds to 39% of the overall CO populations.

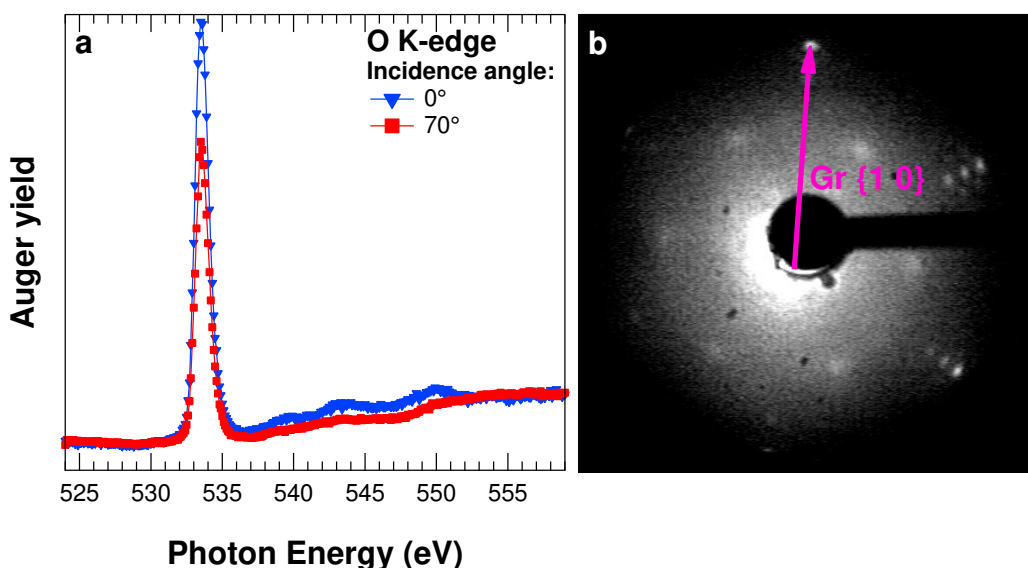


**Figure 3.7:** a: NEXAFS of 0.3 ML CO/Gr/Co/Ir (1 1 1) measured in Auger yield at the O K-edge at normal and grazing incidence. b: LEED pattern of a saturated layer of CO/Gr/Co/Ir (1 1 1) ( $E = 76$  eV).

The NEXAFS spectrum of CO/Gr/Co/Ir (1 1 1) at the O K-edge (Fig. 3.7a) shows a sharp feature at  $533.5 \pm 0.1$  eV, the same energy as for CO/Gr/Ir (1 1 1). This indicates that the difference in the C 1s core level BE is due to a different degree of charge transfer between the molecule and the substrate, while the electronic structure of the molecule is not perturbed, as is expected for physisorbed molecules. The dichroism in the O K-edge NEXAFS of CO/Gr/Co/Ir (1 1 1) shows a similar intensity at normal and grazing incidence, which shows that, also in this system, the molecules are not perpendicular to the surface.

The LEED pattern of a saturated monolayer (Fig. 3.7b) shows the same  $(\sqrt{3} \times \sqrt{3})R30^\circ$  structure as CO/Gr/Ir (1 1 1), thus indicating that the formation of long-range ordered structure is not influenced by the modified chemical composition of the interface. In this case, however, the additional spots of CO have a larger FWHM than for CO/Gr/Ir (1 1 1) and do not display any 2nd order spots around them; this could indicate that in this system the ordering of the CO molecules only occurs on a relatively short range, not larger than a few moiré cells of Gr.

### Carbon monoxide desorption from Gr/Cobalt/Ir (1 1 1)

Also for the Gr/Co/Ir (1 1 1) interface, TP-XPS measurements were taken for different initial coverages of CO. Fig. 3.8a shows a selected TP-XPS experiment, corresponding to a dose of 0.23 ML CO: the photoemission intensity is plotted in grey scale, as a function of the sample temperature. In this case, at the beginning of the temperature ramp, both the V and H photoemission components are present. The evo-

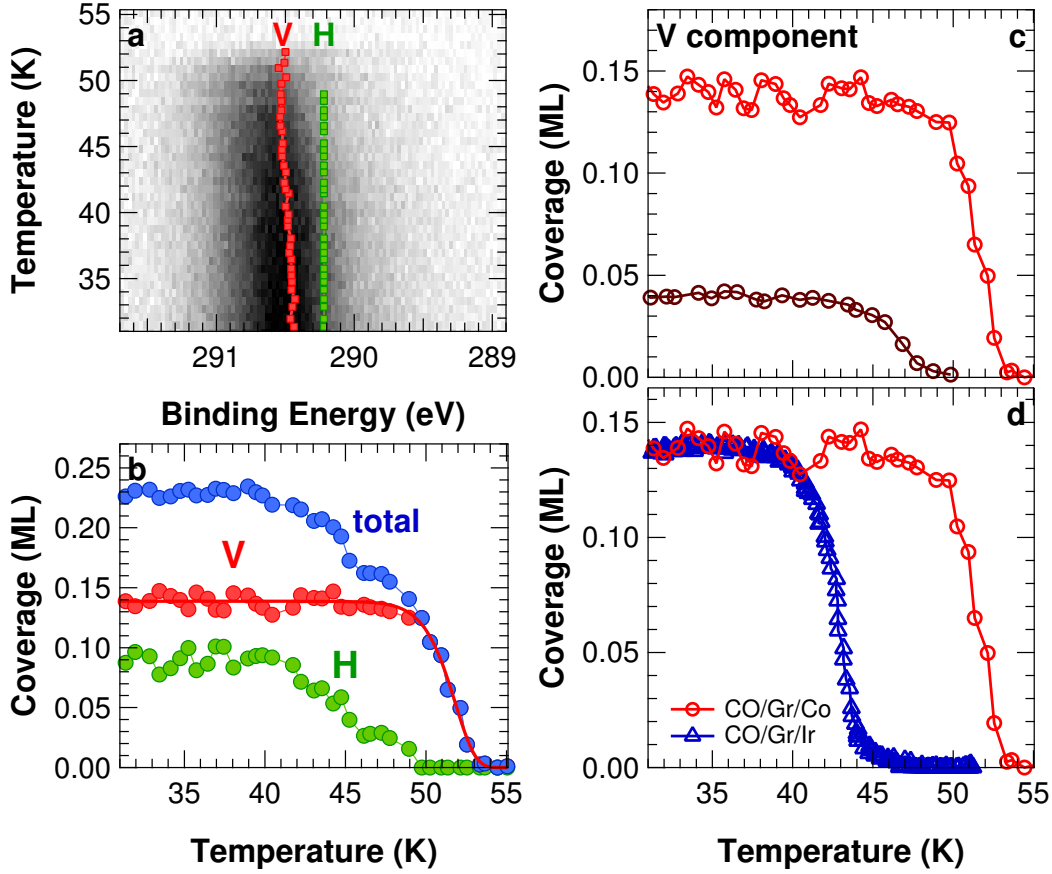


**Figure 3.8:** TP-XPS C 1s core level spectra measured during thermal desorption of CO from Gr/Co/Ir (1 1 1) ( $h\nu = 325$  eV). a: Evolution of CO C 1s spectra acquired during a linear temperature ramp (the photoemission intensity is in colour scale), and b: temperature behaviour of both photoemission components for a saturated CO layer as a function of temperature. c: Evolution of the V component for different CO initial coverages. d: Comparison of coverage curves for desorption from Gr/Ir (1 1 1) and Gr/Co/Ir (1 1 1)

lution of coverage of both components as a function of temperature during this experiment is shown in Fig. 3.8b. It is evident that the desorption dynamics as a function of temperature for the V and H components are quite different. The desorption of component H starts first, just above 40 K; however, this process is slow and this component only vanishes completely just below 50 K. The very wide temperature range over which component H desorbs cannot be described by parameters similar to those of component V. A factor that can account for the broad temperature range of the desorption process is a significant, decreasing dependence of the adsorption energy on coverage, which is the opposite behavior as observed for component V.

On the other hand, the V component follows a first order desorption process, starting at 48 K, when component H has almost completely disappeared. Also in this case, the desorption onset moves towards higher temperature for higher CO coverage (see Fig. 3.8c). Compared to the desorption from Gr/Ir, the temperature at which the desorption process occurs for component V is significantly higher, by about 8 K, as can be seen in Fig. 3.8d.

The fit of the desorption curves of component V yields a pre-exponential factor  $\nu = 10^{17\pm2} \text{ s}^{-1}$ , the same which was found for CO/Gr/Ir, yet the adsorption energy in this system is higher, as reported in Table 3.2. The comparison of the confidence regions in the parameter space between the CO/Gr/Ir and CO/Gr/Co systems, calculated with the procedure described in Section 3.1.1, is reported in Figure 3.5c.

This comparison shows that the adsorption energy of CO on Gr, at least up to a coverage of 0.15 ML, is increased by about 35 meV for the case of Gr on the Co-terminated Ir (1 1 1) surface. This substrate-



$\theta_i(\text{ML})$	$E_{\text{DES}}$ (meV)		$\Delta E_{\text{DES}}$ (meV)
	CO/Gr/Ir	CO/Gr/Co	CO/Gr/Co - CO/Gr/Ir
$0.04 \pm 0.01$	$146 \pm 25$	$180 \pm 20$	$34 \pm 5$
$0.13 \pm 0.02$	$157 \pm 20$	$190 \pm 20$	$33 \pm 5$

**Table 3.2:** CO desorption energy  $E_{\text{des}}$ , as obtained from the fit of the desorption curves of CO from Gr/Ir (1 1 1) and Gr/Co/Ir (1 1 1), for selected initial CO coverage  $\theta_i$  (for the case of CO on Gr/Co/Ir (1 1 1), only component V was present at these coverage values). The absolute values and the differences between the two systems are reported.

induced increase in adsorption energy accounts for 20% of the total adsorption energy of CO in this system, therefore demonstrating that the substrate below Gr plays an important role in determining the interaction strength of Gr with CO molecules. The different behaviour which is observed at higher coverages in this system could be instead attributed to the very different geometry (different Gr corrugation) between Gr on Co/Ir (1 1 1) and on Ir (1 1 1), as will be discussed in the next sections.

### 3.1.3 Theoretical results

In order to shed light on the experimental results, we have collaborated with the group headed by Eduardo Hernandez from CSIC, in Madrid, to perform theoretical calculations on a series of structural models of CO adsorbed on Gr/Ir(111) and Gr/Co/Ir(111).

The aim of these calculations was first of all to identify the most stable adsorption configurations for CO molecules on Gr, and to compare them with our experimental results (mainly LEED and NEXAFS). In addition, we wanted to fully decouple the different contributions to the adsorption energy of CO on Gr, namely the effect of vdW interactions with free-standing Gr, the role of the substrate, and the lateral interactions between molecules.

As explained above, particularly important for these calculations was the implementation of vdW forces. To this aim, exchange-correlation effects were incorporated with the revPBE generalized-gradient functional<sup>58,59</sup> and the vdW-DF functional developed by Langreth *et al.* was used.<sup>27–29</sup>

#### Gr on Ir(111) and on Co/Ir(111)

As the calculations described in Chapter 2.3.3 did not implement vdW forces, the first step in our theoretical calculations was to relax the Gr/Ir (1 1 1) and Gr/Co/Ir (1 1 1) to also include these interactions. The relaxation of the structure in the absence of any adsorbate results in a configuration that is characterized by an average separation between the Gr layer and the Ir top-most layer of 3.8 Å, somewhat larger than the interlayer separation in graphite (3.35 Å), and the reported average height determined by X-ray standing wave experiments reported by Busse *et al.*<sup>26</sup> of  $3.38 \pm 0.04$  Å. The Gr layer is observed to have a corrugation that ranges from a minimum separation of 3.7 Å to a maximum of 4.0 Å. As can be seen in Figure 3.9b, the highest separation occurs around a Gr hexagonal ring centered on top of a substrate Ir atom; in what follows we will refer to this region as the “hill” region. In contrast, the minimum separation occurs for a C atom located directly above an Ir one, in a region denoted as the “valley” region. Within the (10 × 10) Gr supercell there is one hill and one valley region (Figure 3.9a). Our relaxed structure is in good agreement with the observed moiré pattern characteristic of this system.

From our calculations we can obtain an average interaction between the Gr layer and the Ir substrate of 48 meV/C atom; this is in good agreement with the result obtained by Busse *et al.* using the semi-empirical vdW-DF method<sup>26</sup>.

We also studied the Gr structure when a layer of Co atoms is added on top of the Ir slab, to simulate the experimentally produced Gr/Co/Ir(111) interface, which is shown in Figure 3.12. In agreement with the findings described in Chapter 2.3, our new calculations (which also include vdW forces) show that the the moiré-driven corrugation is largely increased with respect to the Gr/Ir(111) case. The C to substrate distance amounts to 3.68 Å and 2.03 Å in the hills (H) and valley (V) configurations, respectively (see Fig. 3.12b). The Gr monolayer is more strongly bound to the substrate when Co is present; we calculate

an average Gr-substrate interaction of 73 meV/C atom, which is significantly larger than the one found for the pure Ir(111) substrate.

### Carbon monoxide on Gr/Ir(111): single molecule adsorption

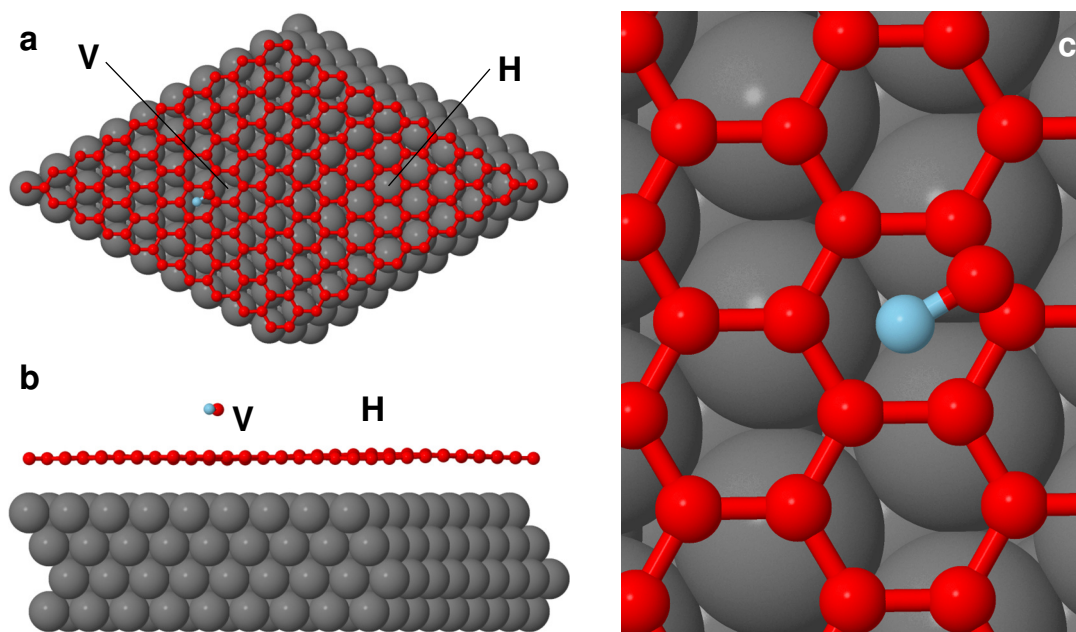


**Figure 3.9:** a: Top and b: side views of the of the most stable CO adsorption configuration as found in our DFT calculations. Grey atoms represent the Ir(111) substrate; carbon atoms are displayed in red, and the oxygen atom is shown in blue. Valley (V) and hill (H) regions are indicated. c: Local configuration of the molecule with the O atom sitting above the centre of a Gr hexagon and the C atom located in a bridge site.

We then proceeded to calculate the adsorption configuration of isolated CO molecules on the substrate: in particular, in order to find the most stable adsorption configuration, we have considered and relaxed more than twenty initial configurations of the adsorbate, distributed over the  $(10 \times 10)$  Gr supercell. Due to the corrugation of the Gr layer on the Ir substrate, there are small variations of the adsorption energy of CO in the hill and valley regions. In fact, we find that adsorption tends to be slightly stronger in the valley region, with an average adsorption energy of 190 meV, while in the hill region this reduces to 185 meV; even if small, this difference is systematic. Consequently, the most stable configuration occurs in the valley region, and is illustrated in Figure 3.9: the CO molecule lies approximately flat on the surface, with the oxygen atom located above the centre of a Gr hexagon, while the carbon atom is located over a bridge site of the Gr honeycomb. The center of the CO molecule is at a distance of 3.3 Å above the Gr layer. The adsorption energy we obtain for this configuration is 194 meV.

We also studied initial configurations in which the adsorbate was placed with its axis perpendicular to the surface, with either the oxygen or carbon atom pointing towards the surface: these initial configurations also resulted in stable relaxed structures retaining the verticality of the adsorbate, but they were less strongly bound to the substrate, typically by 40 meV.

In all the absorbed configurations, the CO bond distance is 1.145 Å, essentially unchanged from the gas-phase value, obtained by performing a calculation for the isolated CO molecule in the same simulation box, without the substrate. This is in agreement with the fact that the vibrational levels, as observed in the C 1s photoemission spectra described above, are not significantly different from the gas phase case.

### Carbon monoxide on Gr/Ir(111): high coverage configurations

Up to this point, we have considered the adsorption of single CO molecules, but as our experimental measurements show a significant dependence of the adsorption energy from the CO coverage, we have also investigated higher CO coverages.

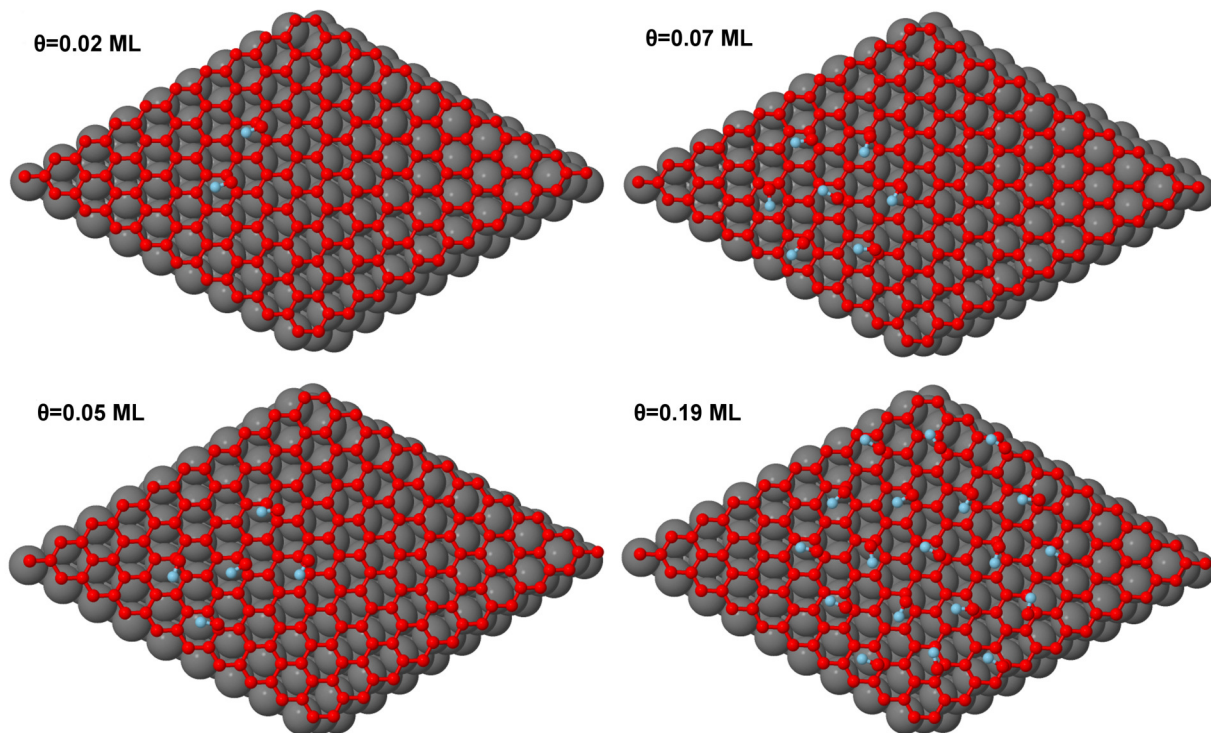


**Figure 3.10:** CO clusters adsorbed on Gr/Ir(111). Adsorption geometries and energetics of the CO clusters have been probed at different values of CO coverage  $\theta$ .

To explore this issue, we have performed relaxation calculations on clusters of CO molecules of various sizes adsorbed on Gr/Ir(111). Specifically, we have considered clusters of 2, 5, 7 and 19 CO molecules. We find that indeed the adsorption energy increases with coverage. In Figure 3.10 we show the relaxed configuration for different clusters, corresponding to CO coverages ranging from 0.02 to 0.19 ML. The molecules are arranged on a hexagonal lattice forming a  $(\sqrt{3} \times \sqrt{3})R30^\circ$  periodicity with respect to the Gr unit cell, by respecting the periodicity observed in LEED.

In Figure 3.11, we plot the adsorption energy as a function of coverage, as obtained from our calculations. As can be seen, the adsorption energy increases with coverage from the single adsorbate limit (194 meV) to 240 meV at the highest coverage considered here. The increase with coverage is initially rapid, although it shows a tendency towards reaching a limiting value in the range of highest coverage we were able to consider here. Our calculated adsorption energies are higher than those obtained from the fitting of experimental data, and also their predicted coverage dependence is more pronounced than observed in the experiments, but nevertheless the trends are correctly reproduced.

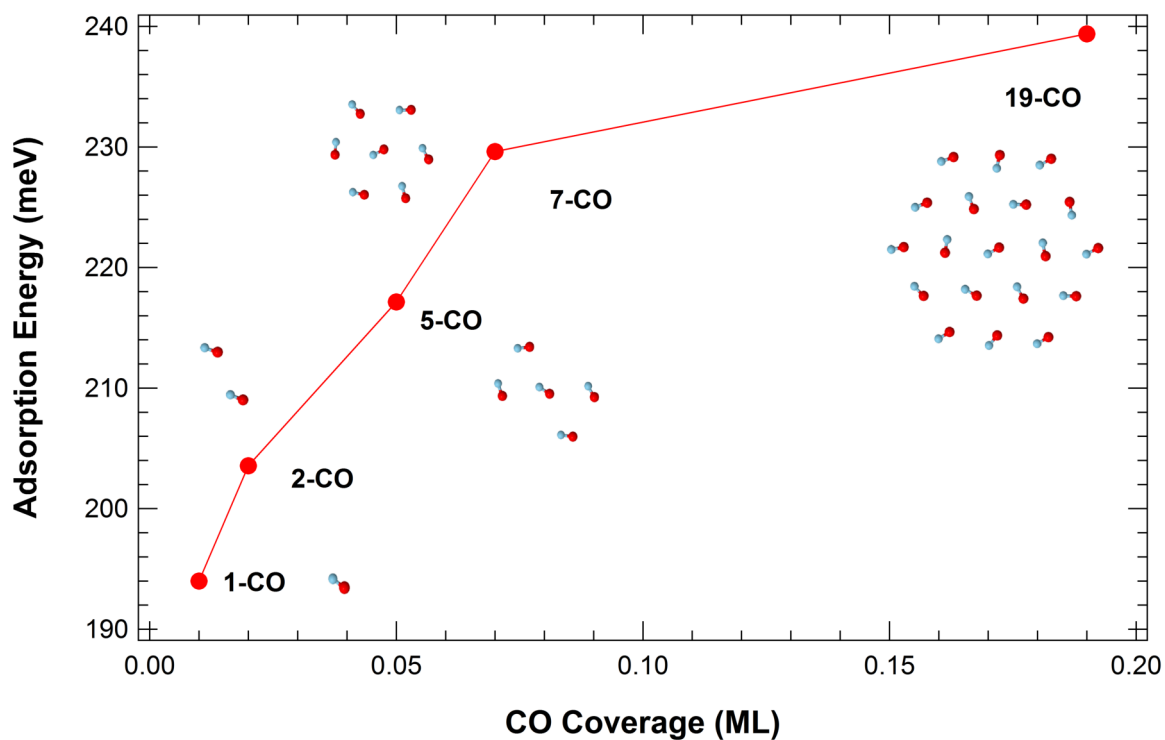


Figure 3.11: Coverage dependent CO adsorption energy on Gr/Ir(111)

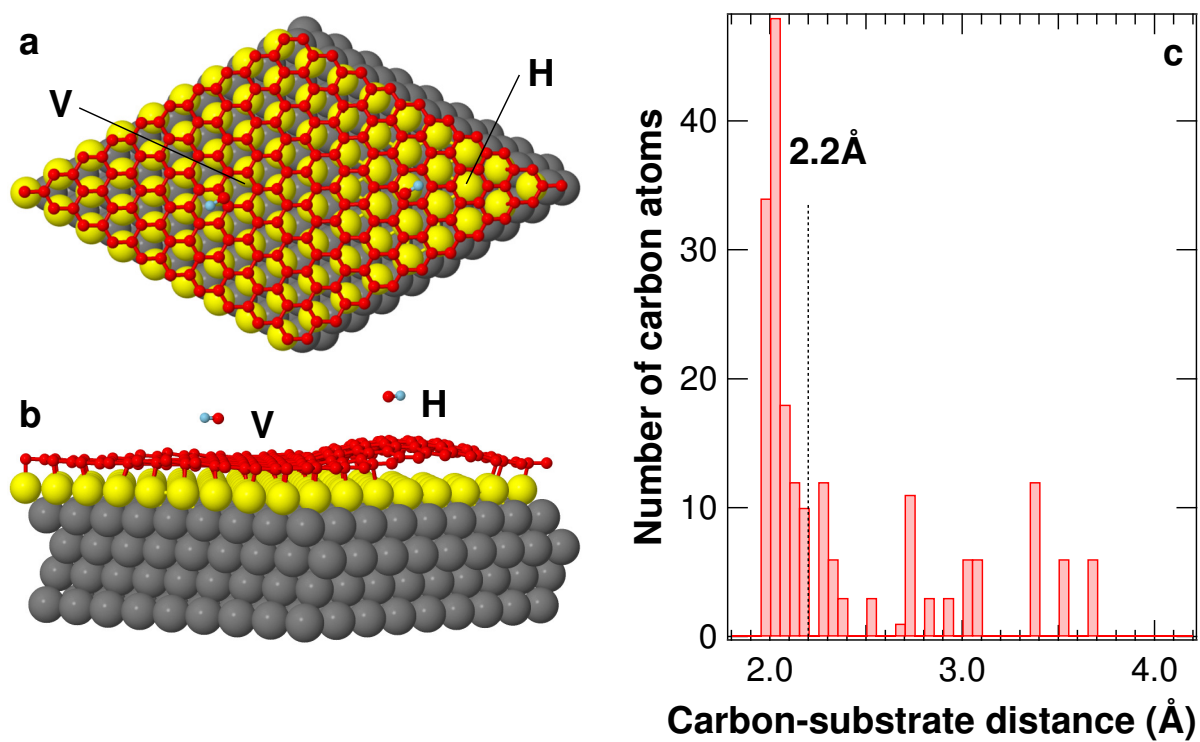


Figure 3.12: a: Top and b: side view of the minimum energy CO adsorption configurations on the hill (H) and valley (V) of the Gr moiré unit cell on Co/Ir(1 1 1). c: Histogram of the C-surface distance for the Gr/Co/Ir(1 1 1) interface.

### Carbon monoxide on Gr/Co/Ir(111)

Also for the Gr/Co/Ir(111) substrate, DFT was used to calculate the adsorption configuration and energy of CO molecules. As shown in Figure 3.12a, the preferred adsorption configuration is almost unaltered compared to the adsorption on Gr/Ir (1 1 1), with the CO molecular axis parallel to the surface, in a valley region, with a CO adsorption energy of 203 meV. This value is higher by about 10 meV with respect to that on Gr/Ir(111). On the other hand, the adsorption energy in the hills region is 169 meV, about 35 meV lower. This difference is clearly larger than the one between the hills and valleys of Gr/Ir(111), which was only about 5 meV. However it is interesting to note that the CO to Gr distance for the isolated molecules best adsorption configurations in the hills and in the valleys is almost the same and similar to the case of adsorption on Gr/Ir(111), being 3.46 Å (H) and 3.35 Å (V), as shown in Figure 3.12b.

#### 3.1.4 Discussion

The theoretically calculated models show that the preferred adsorption site for single CO molecules is in the valleys of the Gr supercell, while the hills are only populated at high coverage. In this respect, the presence of two C 1s photoemission components which have been observed during CO uptake on Gr/Co/Ir (Figure 3.6) can be attributed to molecules adsorbed in the valley (V component) and hills (H component) of the corrugation: the V component increases first, until it saturates, and only then the H component is populated. Furthermore, the higher C 1s BE of the V component with respect to the H component reflects the higher C 1s BE of the Gr atoms closest to the surface in Gr/Co/Ir(111), as described in Chapter 2. The presence of two distinct photoemission components, in fact, has been observed also for the case of noble gas atoms adsorbed on corrugated Gr<sup>60,61</sup>, as will be shown also in Section 3.2, and has been explained as due to the difference between the work function of Gr in the hills and valleys<sup>60</sup>. This similarly explains the overall higher C 1s BE of CO in the former system, where the C 1s BE of Gr is higher by more than 500 meV than in Gr/Ir(111). This difference is comparable to the one observed between the 2p<sub>3/2</sub> core level BE of Ar adsorbed on weakly interacting Gr/Pt and on corrugated Gr/Ru, as reported in literature<sup>61</sup> and as will be discussed later on, in Chapter 3.2.

It is also interesting to note that if we take as a threshold the value of 2.2 Å (maximum height of the C atoms in the flat region of the Gr layer on Co/Ir(111) interface), 61% of the Gr unit cell is in the flat region (the threshold is indicated in Figure 3.12c). This nicely compares with the populations of the CO molecules in the valleys as found by quantitative analysis for the CO saturated layer on Gr/Co/Ir(111) (see Fig. 3.6b).

Although the Gr layer displays valley and hill regions when deposited on both the Ir(111) and Co/Ir(111) substrates, it is obvious from Figures 3.9 and 3.12 that the level of Gr-corrugation is significantly larger in the latter case. This fact is reflected in the difference in adsorption energy values between valley and hill regions on both substrates: while the adsorption energy difference between the most stable valley and hill CO adsorption configurations on Gr/Ir(111) is only 5 meV, the same difference on the Gr/Co/Ir(111) substrate is 35 meV, *i.e.* seven times larger. This is consistent with the fact that only one component is observed in the C 1s core level spectra during uptake and desorption of CO on Gr/Ir(111) (Figure 3.1), even at high coverage, while two are observed in the case of CO on Gr/Co/Ir(111), once coverage is sufficiently high to fill the valley region (Figure 3.6b).

Following these considerations, the broad desorption edge of the H component can be well explained by the enhanced corrugation of Gr after Co intercalation, which leads to a wide distribution of adsorption sites on the hill regions, at variable distances from the substrate. This leads to the broad distribution in the adsorption energy of molecules in these non-equivalent sites observed in the desorption curve of the H component. This difference in the desorption energy between the hill and valley region is not limited to the case of molecular adsorption, and has also been observed for the case of noble gas atoms, such as for Xe adsorption on corrugated Gr<sup>60</sup>.

If we then compare our experimental and theoretical results, both show that the adsorption energy of CO/Gr is larger for Gr/Co/Ir (1 1 1), even though DFT overestimates the experimental results by about 50 meV. Moreover, DFT does correctly predict an increase in the adsorption energy by tens of meV due to the inter-molecular interactions, with an accuracy within 10 meV. This substrate-induced difference in



adsorption energy could be explained either by a direct interaction of CO with the metal below Gr (direct interaction), which would imply that Gr is translucent or transparent to vdW forces<sup>15,16</sup>, or to an indirect mechanism<sup>12</sup>. This, in turn, could be related either to the altered geometry and bond length of Gr when it is corrugated, or to the charge transfer and redistribution induced by the interaction with the substrate, as discussed in Chapter 2.

To decouple these different contributions and identify the mechanisms by which the substrate influences molecular adsorption of Gr, we have performed further theoretical calculations, as shown in Figure 3.13, in addition to the ones performed on the systems experimentally investigated (*i.e.* 1A, B and C). In particular, we investigated CO both on flat (A) and corrugated Gr (both in hill – B – and valley – C – configurations), both in absence of the metallic substrate (2) and with the metallic substrates swapped (3), *i.e.* with the corrugated Gr on Ir(111) and the flat Gr on Co/Ir(111). To further reduce the number of degrees of freedom, these calculations were performed by keeping all distances (CO-Gr and Gr-substrate) fixed to the value found for the corresponding real systems, *i.e.* the distance of flat Gr was fixed to the one it has from Ir(111) and that of corrugated Gr to the one it has from Co/Ir(111). For all these systems, we

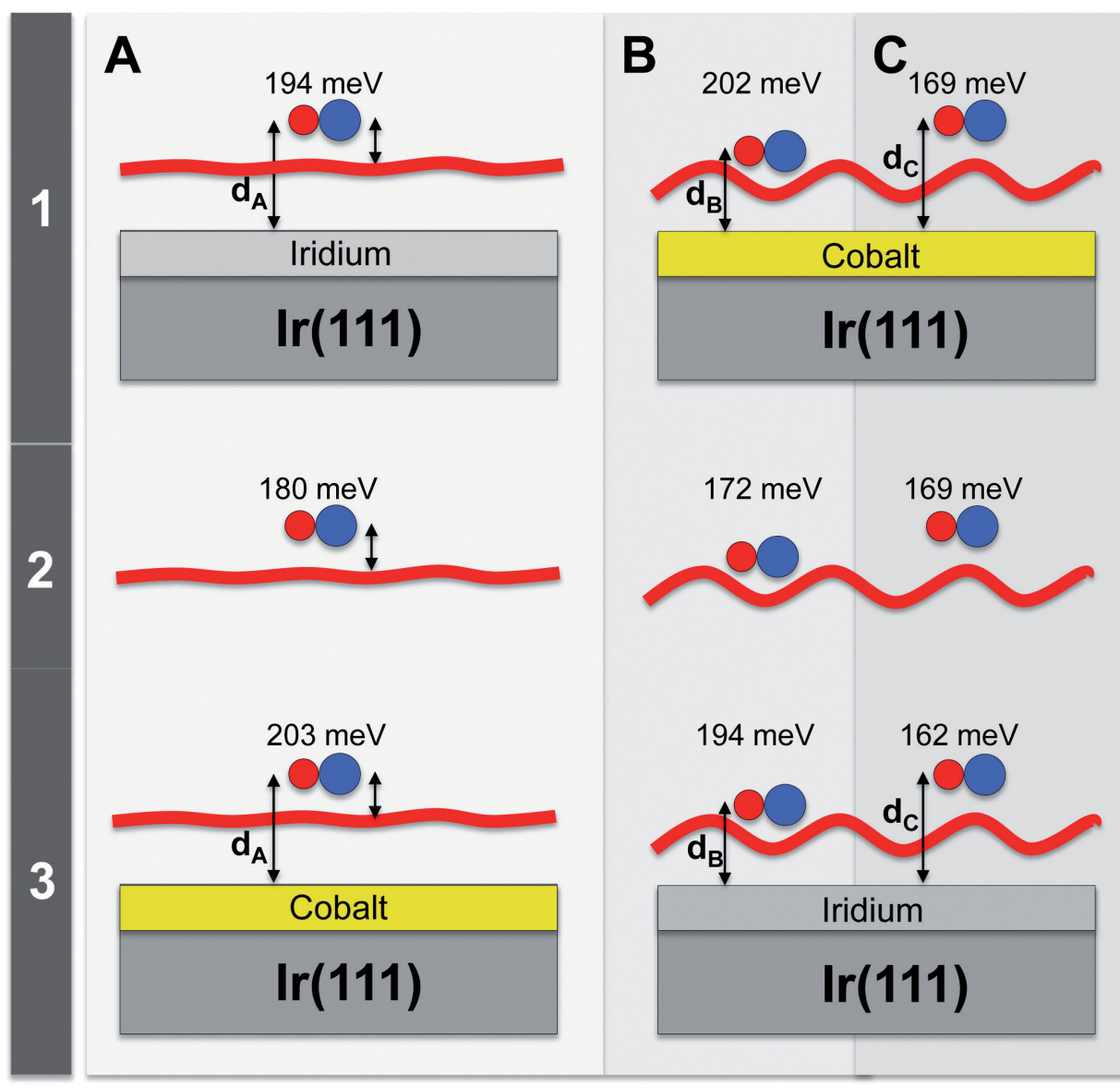


**Figure 3.13:** Calculated adsorption energy of carbon monoxide on different Gr and Gr/metal interfaces. 1: systems characterized experimentally, corresponding to CO adsorption on Gr/Ir(111) (A) and on the valleys (B) and hills (C) of Gr/Co/Ir(111). 2-3: systems obtained by removing (2) or inverting (3) the substrate below Gr while keeping the Gr and CO positions fixed.

calculated the CO adsorption energy, which is reported in Figure 3.13.

From the comparison of the results, it is clear that the effect of the geometry of the system, *i.e.* of the Gr corrugation, cannot explain the observed behaviour. In fact, with the substrate removed, there is no appreciable difference between adsorption on the hills and valleys of the corrugated layer (2B and 2C), which is instead clearly observed when any substrate is present. Furthermore, with the substrate removed, the adsorption energy is higher for flat Gr (2A), in contrast to what was observed and calculated for the two real systems (1 A, B and C). The most significant result from these calculations, however, is the fact that the adsorption energy of CO on flat Gr or in the valleys of the corrugation is the same when Gr is supported on the same substrate, *i.e.* the adsorption energy of 1A is the same as in 3C, and the one in 1C is the same as 3A. This means that the adsorption energy is not affected by the fact that the molecule lies at a different distance from the substrate on flat Gr with respect to the valleys of corrugated Gr, whereas it is significantly affected by the chemical identity of the topmost layer of the substrate.

Following these calculations, we can conclude that the effect of the substrate on the adsorption energy cannot be explained by direct vdW coupling, as such a coupling would have an inverse cubic dependence on the molecule-to-substrate distance and therefore lead to a lower adsorption energy on flat Gr with respect to the valley regions of corrugated Gr, which is not observed in our calculations<sup>62</sup>. The mechanism we propose is instead based on the charge transfer and redistribution which occurs on Gr due to the substrate, which is stronger by about one order of magnitude for the Gr/Co interface than for the Gr/Ir one, as shown in Chapter 2. Furthermore, in the case of corrugated Gr, this charge transfer is strongest in the valleys, while it is negligible in the hills: this very well explains why the adsorption energy of H and V regions, while almost degenerate for free-standing Gr, is instead very different when the substrate is present. In fact, the adsorption energy on the hills is not modified by the presence of a substrate, where the charge transfer obtained from our calculations is negligible. The mechanism which increases the adsorption energy of CO on Gr could therefore be explained by this increase in charge density leading to the presence of dipoles on the surface, interacting with that of the molecules: in particular, an additional positive charge accumulates in the bridge sites of Gr, which can couple to the negative charge at the C atom in the dipolar CO molecule. A further proof that the CO molecules are affected by the charge transfer between Gr and its substrates is the very different C 1s BE of the C 1s core level of CO, which moves to higher energies for increasing Gr/substrate interaction following the shift in the C 1s BE of Gr. This reflects an increased negative charge in the C atom, which is also observed by the DFT calculations and also contributes to an increased interaction with Gr.

Our results, highlighting the fundamental role of the interaction between the substrate and Gr on the molecular adsorption energy, can be linked to those reported in the study of charge transfer processes at the Gr surface<sup>61</sup>. Indeed, in the case of Ar atoms adsorbed on Gr, it was shown that the interaction strength between Gr and its substrate strongly affects the dynamics of the charge transfer of the adsorbed Ar.

## 3.2 Noble gas atomic adsorption on graphene: the case of argon

In our experiments on CO adsorption on Gr, we have seen that the effect of the substrate below Gr was not the only factor affecting the adsorption energy. In fact, we found that a comparable contribution was due to the lateral interactions between adsorbed CO molecules. Moreover, this effect was relevant already at low coverage, therefore making the unravelling of these two contributions and hence the determination of the single-molecule adsorption energy particularly challenging.

One possible way to address this issue is to study the adsorption behaviour of a less polar and more inert substance: in this respect, a good choice could be the adsorption of noble gasses of Gr. For this reason, we have performed an analogous experiment to the one described in the previous section, by studying the adsorption energy of argon on both the Gr/Ir (1 1 1) and Gr/Co/Ir (1 1 1) substrates.

### 3.2.1 Argon adsorption on Gr/Ir (1 1 1)

We characterized this system by adopting an approach similar to the one we used for CO. In particular, we started by analysing the uptake of Ar on Gr/Ir (1 1 1) by time-resolved XPS on the Ar  $2p_{3/2}$  core level:

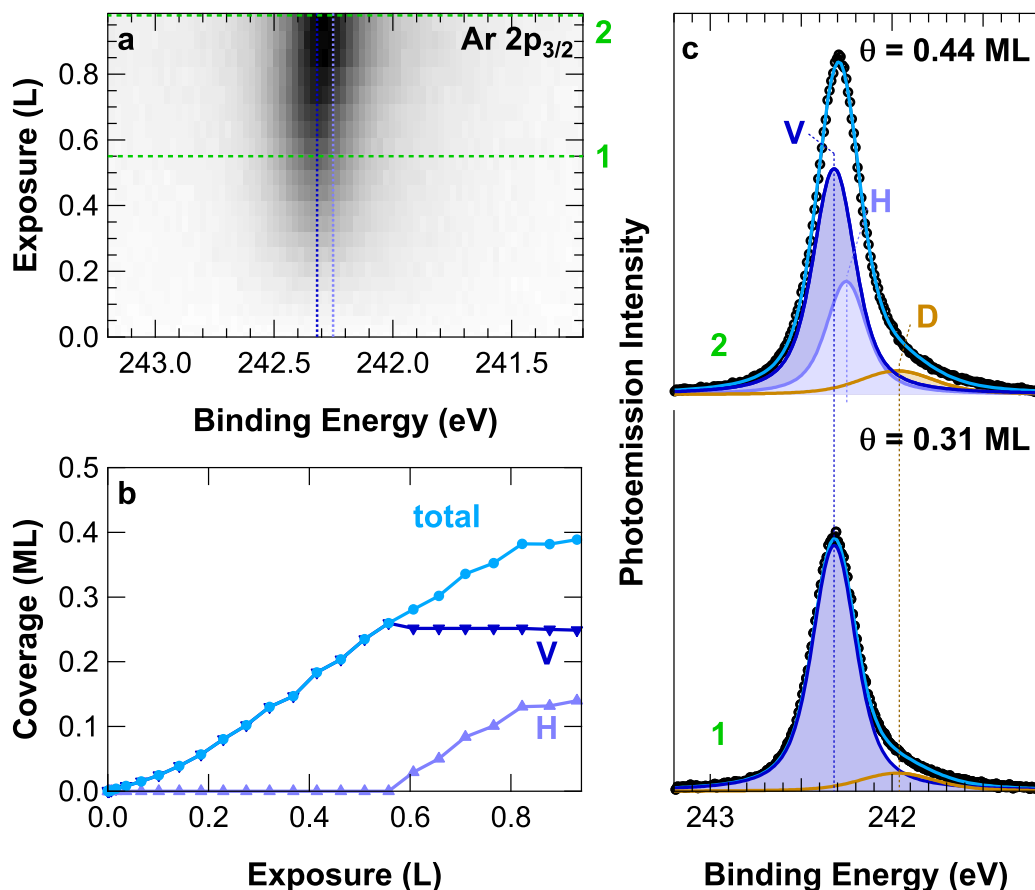


**Figure 3.14:** Ar  $2p_{3/2}$  photoemission spectra during uptake of Ar on Gr/Ir(1 1 1) ( $h\nu = 400$  eV). a: Time-lapsed sequence acquired during exposure to  $p=5 \times 10^{-9}$  mbar Ar at  $T=25$  K. The Ar  $2p_{3/2}$  Binding Energy of the two main components is indicated by dashed lines. b: Evolution of the total Ar coverage (circles) and of that of each component (triangles) as a function of Ar dose. c: Selected spectra of the uptake corresponding to a coverage of 0.31 ML (1, below) and to saturation (2, above) with deconvoluted components.

the results of this experiment are reported in Figure 3.14. In particular, Figure 3.14a shows the evolution of the photoemission spectrum (plotted in greyscale) as a function of Ar exposure (vertical axis), during the sample exposure to Ar gas at  $T=25$  K. This temperature was chosen to avoid the formation of bi- and multi-layers. At low coverage (a selected spectrum is shown in Figure 3.14c, below), two components must be included to correctly fit the data: a main component (V), at a BE of 242.32 eV, with a FWHM smaller than 300 meV, and a broader one (D), centred at about 242 eV, with a FWHM of about 500 meV. The latter component remains constant throughout the whole experiment and its spectral weight is significantly lower than that of V. Both components are characterised by a symmetric lineshape, as is expected for the case of non-metals such as noble gasses.

The behaviour of component V as a function of the Ar exposure is shown in Figure 3.14b. At the beginning of the uptake, it increases linearly with Ar exposure. When the Ar dose is larger than about 1.3 L, however, these two components are no longer sufficient to describe the photoemission spectrum, which clearly shows a broadening on the low BE side, as can be appreciated in Figure 3.14c, above. It is therefore necessary to add a further component to the spectrum (H), which has a BE of 242.25 eV, therefore shifted by 70 meV towards lower BE with respect to component V. This component has a FWHM of about 250 meV. After component H appears, it increases linearly with the Ar dose, while component V saturates, in such a way that the total Ar coverage continues to increase with the same rate up to an Ar exposure of about 2 L, after which it does no longer increase (see Figure 3.14b).

To calculate the factor relating the photoemission signal to the actual Ar coverage, we have studied the



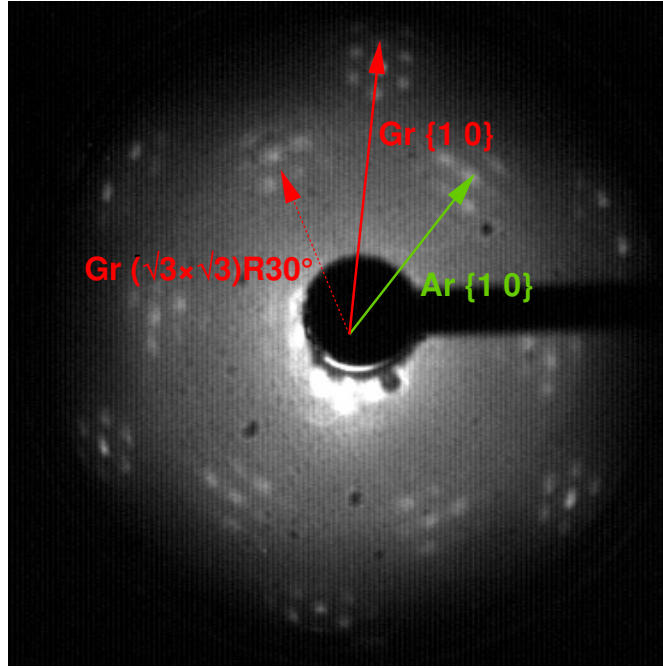


**Figure 3.15:** LEED pattern of Ar/Gr/Ir (1 1 1) ( $E = 83$  eV). The reciprocal lattice vector corresponding to a  $(\sqrt{3} \times \sqrt{3})R30^\circ$  supercell is indicated by the dashed arrow.

long-range ordering of Ar on Gr by acquiring the LEED pattern of a saturated Ar layer, which is reported in Figure 3.15. The pattern shows additional spots besides those of Gr, which are arranged to form a smaller hexagonal lattice inside that of Gr, rotated by  $30^\circ$  with respect to it. As for the case of CO/Gr, these spots are surrounded by satellites originated by multiple scattering processes.

While this pattern qualitatively resembles that of CO/Gr (see Section 3.1.2), which corresponded to a  $(\sqrt{3} \times \sqrt{3})R30^\circ$  superlattice, the spots of the Ar supercell are actually farther away from the centre, indicating that the actual periodicity of the structure is slightly smaller. In addition, the spots of the Ar supercell are characterised by a larger broadness in the tangential direction than in the radial one, indicating a certain degree of misalignment with respect to the  $R30^\circ$  direction. These results are in agreement with those reported for Ar adsorption on the graphite (0 0 0 1) surface, where a variable misalignment of the Ar diffraction spots with respect to the  $R30^\circ$  direction is observed as a function of temperature<sup>63</sup>. This misalignment has been attributed to the mismatch between the lattice parameter of Ar layers and that of the  $R30^\circ$  supercell of graphite, which leads to a rotation of the Ar lattice in order to form a commensurate structure<sup>64</sup>. The ratio between the radial distances of the Gr and Ar spots observed in our pattern amounts to  $1.5 \pm 0.1$ , where the error is mostly due to the deformation of the image arising from the curvature of the LEED screen. From this, we obtain a lattice parameter of the Ar lattice of  $3.7 \pm 0.2$  Å, in good agreement with the values reported in literature for a similar temperature range<sup>63</sup>.

From the geometry of the adsorbed layer, we were able to calculate the argon density per Gr unit cell. We thus estimated that the coverage reached by Ar at saturation is  $0.44 \pm 0.05$  ML: this value has been used to calibrate the uptake curves reported in Figure 3.14b and throughout all this experiment.

Our next step in the characterisation of this system was to understand the origin of the various components observed in the Ar  $2p_{3/2}$  spectrum. In particular, the two main components (V and H) have a behaviour which reminds of our results for CO adsorption on Gr/Co/Ir (1 1 1) (Section 3.1.2), as well as the behaviour reported in literature for Ar adsorption on Gr/Ru (0 0 0 1)<sup>61</sup>, and therefore we attribute them to atoms adsorbed in the valleys (component V) and on the hills (H) of the moiré formed by Gr on Ir (1 1 1). Actually, for the case of CO/Gr/Ir (1 1 1), we did not observe separate photoemission components for adsorption in the hills and valleys. However, as already mentioned there, the corrugation of Ir-supported Gr is signif-

icantly smaller than for Co and Ru-supported Gr; for this reason, the BE shift is much reduced, and we can only appreciate it in the case of Ar adsorption due to the smaller FWHM of the spectral components, which is only 2 meV for this system. At saturation, the H/V coverage ratio is about 50%.

Finally, the small spectral weight of component D (few percent of the saturated layer) and the fact that it remains constant throughout the uptake suggests that it could be originated by Ar adsorbed on Gr defect sites. For example, it could be attributed to an incomplete coverage of Ir by the Gr layer: as will be discussed in Chapter 5.3.3, single atoms can adsorb on small defects in the Gr lattice, which are instead left uncovered by the CVD growth process as these sites are not reachable by the gas precursors due to their larger steric encumbrance. Likewise, the larger encumbrance of the CO molecules could explain the reason why such a component was not observed, instead, during CO adsorption on Gr.

The last step in our characterisation of the Ar/Gr/Ir (1 1 1) system was the determination of the adsorption energy of Ar on this surface by measuring desorption curves for several initial coverages, using the TP-XPS technique. Figure 3.16a shows the desorption curves for the V and H component of a saturated Ar layer. The H component starts desorbing already at about 30 K, yet the desorption edge is quite broad, and this component completely vanishes only above 35 K. This broad desorption edge is similar to the one observed for the H component of CO/Gr/Co/Ir (1 1 1), and can be attributed to atoms adsorbed in non-equivalent sites on the slopes of the hill region. On the other hand, the desorption of component V starts just below 40 K and proceeds with a higher rate, and vanishes completely below 43 K.

The desorption curve of the V component can be described by a first order process, and its analysis yields a desorption energy  $E_{\text{DES}} = 134 \pm 4$  meV for Ar adsorbed in the valleys of Gr/Ir (1 1 1). The pre-exponential factor obtained from the fit is  $\nu = 10^{14.8 \pm 0.5} \text{s}^{-1}$ . On the other hand, due to the more complex desorption dynamics of the H component, it was not possible to obtain a quantitative estimate for its desorption energy; however, from a qualitative analysis based on the temperature at which desorption occurs, it is clear that it is significantly lower than for the V component.

The analysis was performed also for the desorption curves of the V component measured for dif-

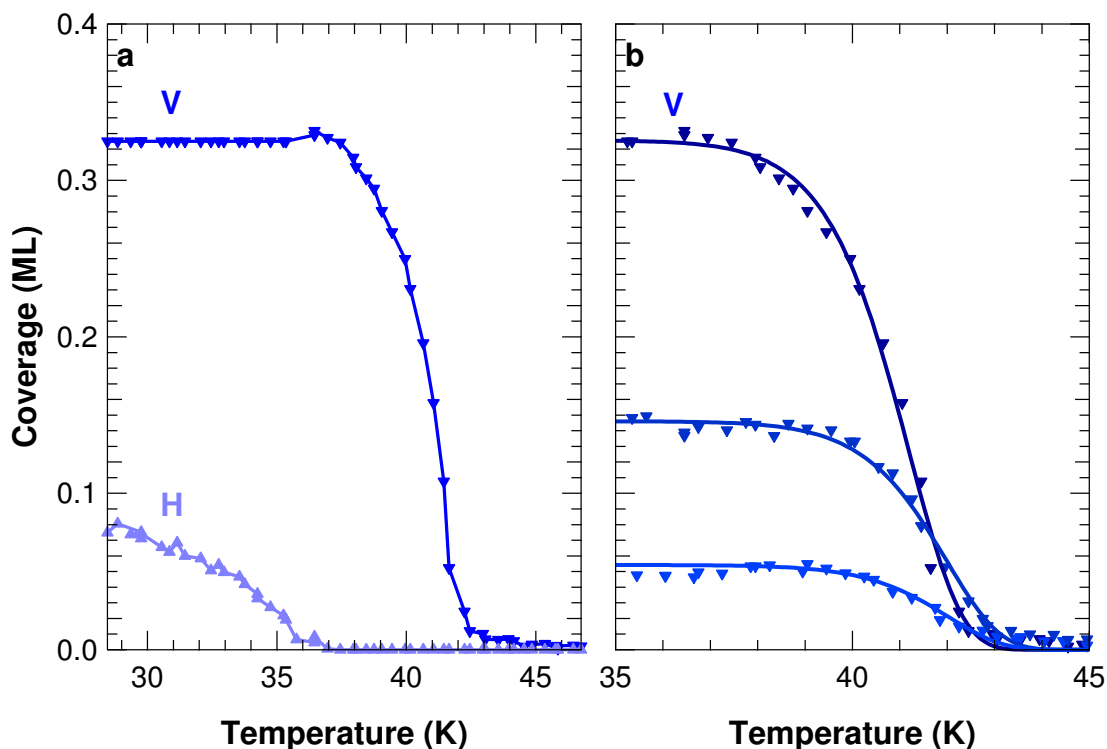


**Figure 3.16:** Coverage curves of Ar during thermal desorption from Gr/Ir (1 1 1), measured by TP-XPS. a: Evolution of the H and V components of a saturated Ar layer. b: Thermal evolution of the V component for different initial Ar coverage.

ferent initial Ar doses, namely 0.15 and 0.05 ML, which are shown in Figure 3.16b. The analysis yields the same value for both the pre-exponential factor,  $\nu = 10^{14.8 \pm 0.5} \text{s}^{-1}$ , and for the desorption energy  $E_{\text{DES}} = 136 \pm 4 \text{ meV}$ , indicating that the lateral inter-atomic interactions are negligible, unlike the case of CO. This also explains why the fit provides a significantly better description of the experimental data, which is also the reason why the errors associated to the parameters are significantly lower than for the case of CO adsorption.

### 3.2.2 Argon adsorption on Gr/Co/Ir (1 1 1)

The uptake of Ar on Gr supported on Co-terminated Ir (1 1 1) is shown in Figure 3.17a. Also in this case, two components are found at low coverage (Figure 3.17c, below), one behaving like the D component described above, at about 242.8 eV, the other behaving like the V component, increasing linearly with the Ar dose (Figure 3.17b). However, in this system, the BE of the V component is not constant, but decreases by about 100 meV for increasing coverage. At saturation, its core level BE is 243.14 eV. A third component (H) is present also in this system at high coverage (Figure 3.17c, above), with a BE of about 242.98 eV, shifted from the V component by 160 meV. This shift is larger than the one observed on the Gr/Ir substrate, which can be attributed to the larger corrugation of Gr on this system. This larger corrugation can also explain the coverage-dependent shift observed in the core-levels BEs as, for increasing coverage, regions of the moiré supercell at variable distance from the substrate are populated.

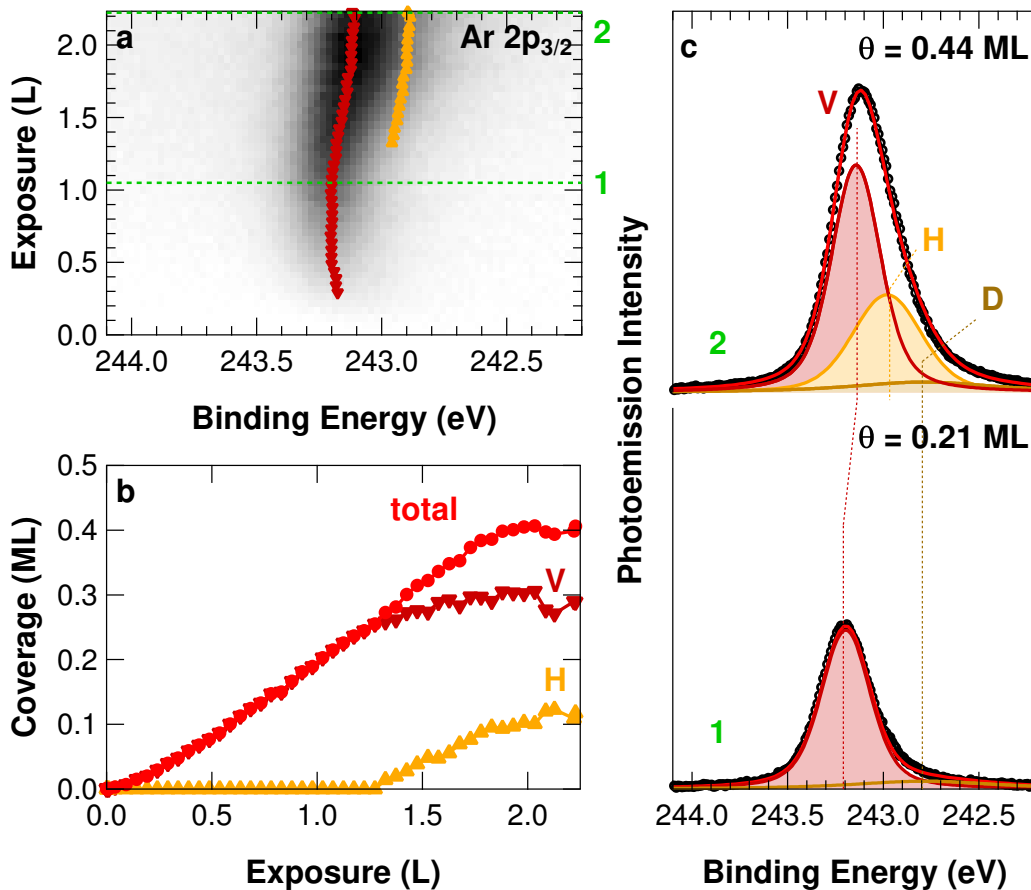


**Figure 3.17:** Ar  $2p_{3/2}$  photoemission spectra during uptake of Ar on Gr/Co/Ir (1 1 1) ( $h\nu = 400 \text{ eV}$ ). a: Time-lapsed sequence acquired during exposure to  $p = 5 \times 10^{-9} \text{ mbar}$  Ar at  $T = 35 \text{ K}$ . The Ar  $2p_{3/2}$  Binding Energy evolution of the two main components is plotted as a function of the Ar exposure. b: Evolution of the total Ar coverage (circles) and of that of each component (triangles) as a function of Ar dose. c: Selected spectra of the uptake corresponding to a coverage of 0.21 ML (1, below) and to saturation (2, above) with deconvoluted components.

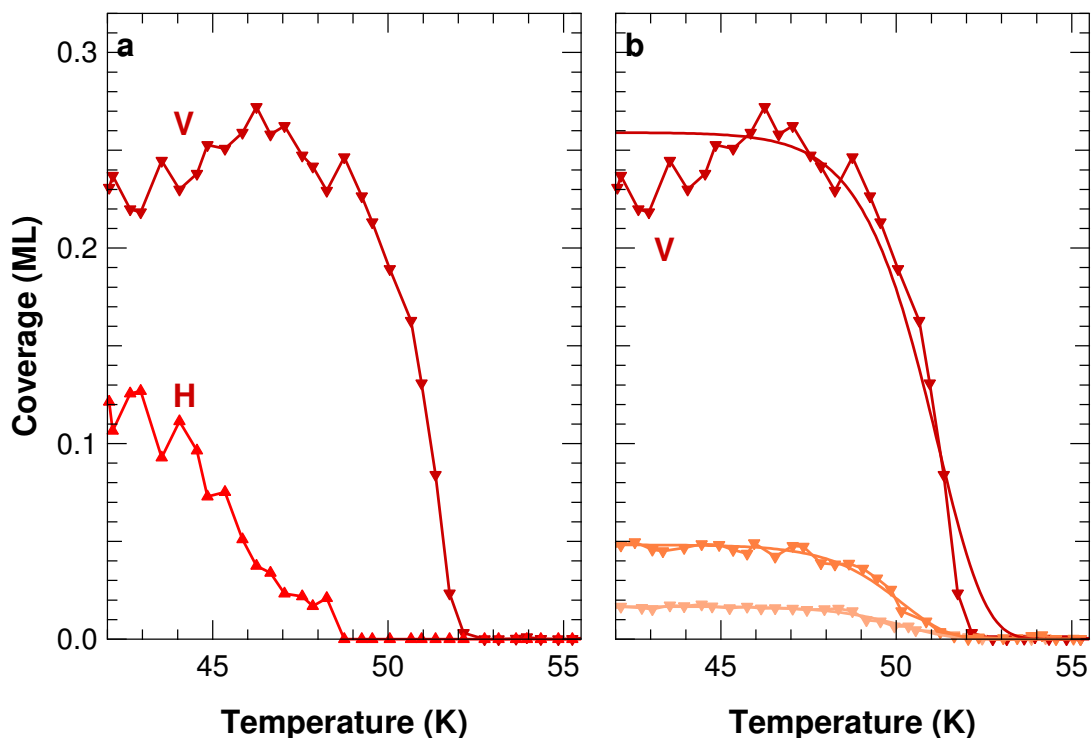


**Figure 3.18:** Coverage curves of Ar during thermal desorption from Gr/Co/Ir (1 1 1), measured by TP-XPS. a: Evolution of the H and V components of a saturated Ar layer. b: Thermal evolution of the V component for different initial Ar coverage.

It is interesting to compare these results to the adsorption of Ar on the Gr/Ru(0 0 1) surface<sup>61</sup>. In that case, the BE reported for the V and H components is 243.16 and 282.86 eV respectively. These values and the shift between them are very close to the ones obtained in our experiment, which shows that the effects of the interaction of Ru and Co on Gr are quite similar, in very good agreement to the results of the experiment described in Chapter 2.

Finally, desorption curves were measured for different initial coverages of Ar. The desorption curves of the H and V components for a saturated Ar layer are shown in Figure 3.18a. The H component desorbs first, with a broad edge starting at about 43 K, and completely desorbs at about 49 K; as for the case of Ar desorption from Gr/Ir, this curve cannot be analysed quantitatively. The desorption of the V component, on the other hand, starts just below 50 K and is complete just above 52 K. The fit yields a pre-exponential factor of  $\nu = 10^{14.8 \pm 0.5} \text{s}^{-1}$  and a desorption energy  $E_{\text{DES}} = 167 \pm 10 \text{ meV}$ .

As for the case of Ar/Gr/Ir, the temperature of the desorption process is independent of coverage, and also the low-coverage desorption curves (Figure 3.18b) yield an adsorption energy of  $164 \pm 5 \text{ meV}$ , comparable to the high-coverage case within our error bar.

### 3.2.3 Discussion

It is clear already from a qualitative comparison of the desorption curves for the Ar/Gr/Ir and Ar/Gr/Co systems (shown in Figure 3.19a) that the desorption temperature, and therefore the adsorption energy, is very different in the two systems, as was the case also for CO. In particular, the adsorption energy of Ar is larger by about 30 meV for Gr supported on the Co-terminated Ir(1 1 1) substrate. This difference is slightly lower than the one we measured between the adsorption energies of CO on the same two systems, barely appreciable with respect to our estimated error. This indicates that the substrate-induced increase in the interaction of Gr with adsorbates is not limited to the case of polar molecules such as CO, but is far more universal and also influences the even weaker, London-type interactions between Gr and apolar noble gasses to the same degree.

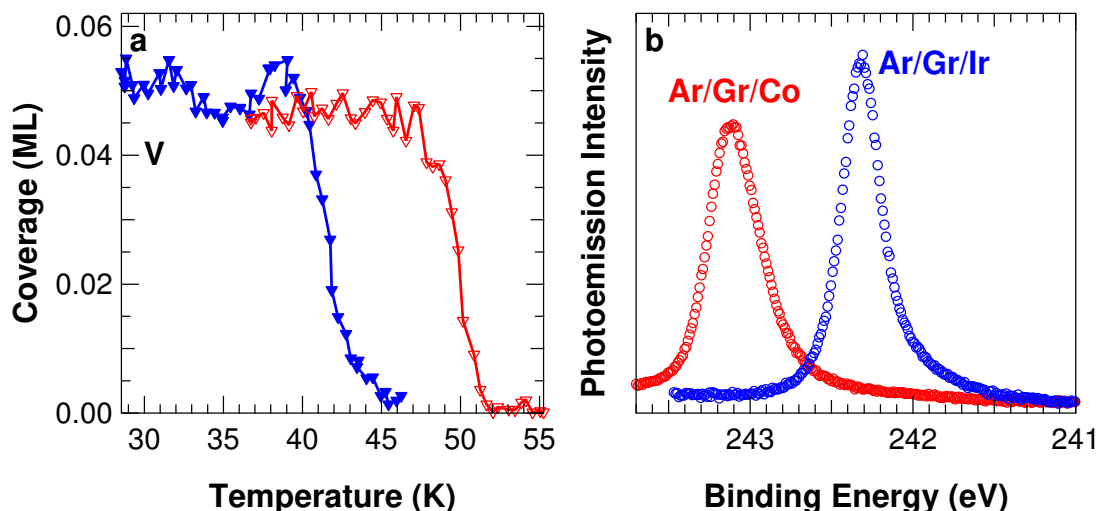


**Figure 3.19:** Comparison of the desorption curves (a) and Ar  $2p_{3/2}$  photoemission spectra (b) of Ar on Gr/Ir(111) and Gr/Co/Ir(111) ( $h\nu = 400$  eV).

Moreover, also in the case of Ar adsorption, as for the case of CO, we observe a shift in the adsorbates' core level BEs towards higher values for the case of the Gr/Co interface (Figure 3.19b). In particular, for the case of Ar, the difference between the Ar  $2p_{3/2}$  BE of the V components is about 800 meV, slightly higher than for the case of CO (about 500 meV).

In conclusion, we have shown that the Ar/Gr system is an ideal system to decouple the effects of the interactions between adsorbates and of their interaction with Gr. This experiment, therefore, shows that the substrate lying below Gr affects the adsorption energies of very different types of adsorbates, to a significant degree. Moreover, our results show that this effect is not appreciably influenced by the nature of the adsorbates, but is mainly determined by the degree of interaction between Gr and its substrate. This is a further proof that the increase of the adsorption energy is due to the modifications induced on Gr by the metallic substrate, and not on a direct interaction between the adsorbates and metal surface, which we would instead expect to be very different for two very different substrates.

### 3.3 Water adsorption on graphene: the role of inter-molecular forces

The experiments described up to now in this chapter have proven very effective in demonstrating the significant role played by the substrate on the adsorption of different molecules on Gr. However, from the point of view of the applications of Gr, another system which is very important to study is the adsorption of water on Gr. In fact, as already mentioned, Gr-based devices are likely to be exposed to water during their use, which can potentially impair their performance<sup>3</sup>.

In addition, the interaction of water with Gr controls its wettability, which plays a key role in many processes and applications involving Gr. For example, the hydrophobicity of Gr is a major drawback in several methods used for the synthesis of Gr, such as in its chemical exfoliation, as it requires the use of complex solvents to obtain a Gr suspension, which can contaminate and negatively affect the quality of the final product. Moreover, interfaces between Gr and water are a key element for biological applications of Gr. For these reasons, as already mentioned, the effect of different substrates on the Gr-water interfaces and on the wettability of Gr has been investigated with a variety of techniques such as contact angle measurements<sup>15</sup>, TPD<sup>12</sup>, NEXAFS<sup>65</sup>, as well as by theoretical calculations<sup>16</sup>. However, these experiments have often lead to contradictory results, either upholding or rejecting the transparency of Gr<sup>12,15</sup>, or even suggesting that water can form a chemical bond when adsorbed on metal-supported Gr<sup>65</sup>. For these reasons, we adopted once again the approach described in the previous Sections, to measure and compare the

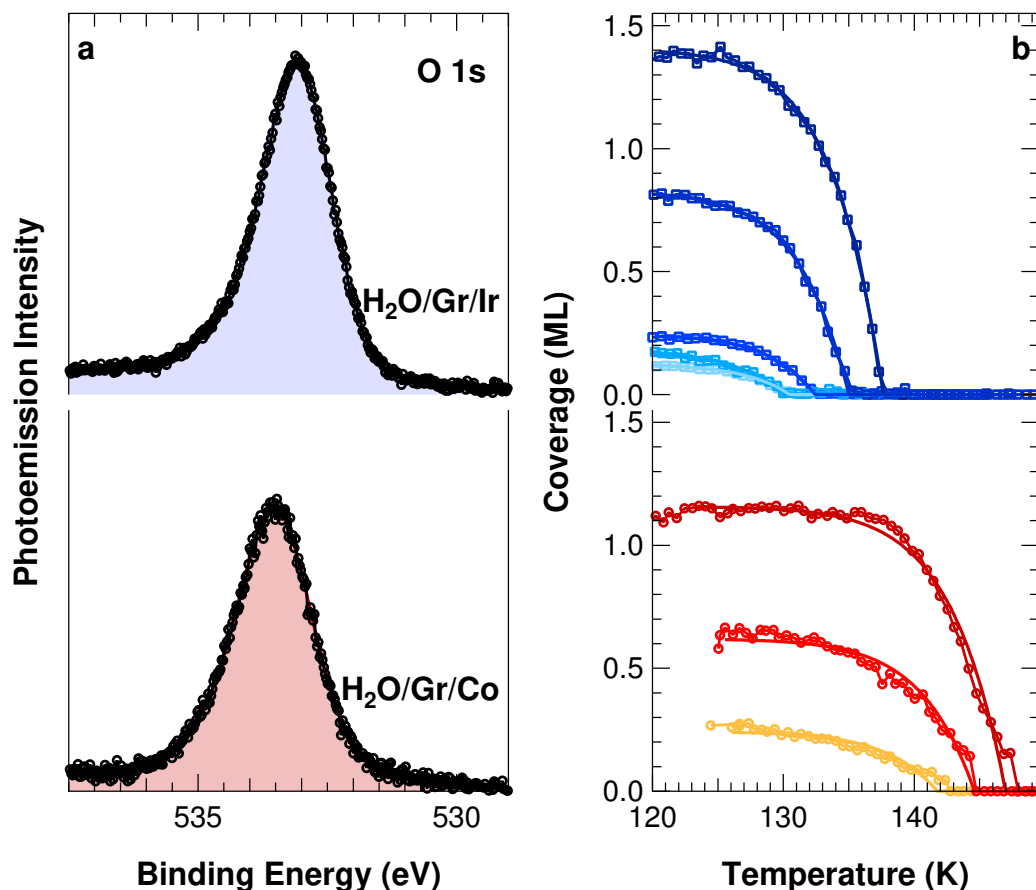


**Figure 3.20:** a: O 1s photoemission spectra of 1.2 ML water on Gr/Ir (1 1 1) (above) and Gr/Co/Ir (1 1 1) (below) ( $h\nu = 650$  eV). b: desorption curves of water from Ir- (above) and Co-supported (below) Gr.

adsorption energy of water on Ir- and Co- supported Gr.

The photoemission spectrum of the O 1s core-level of water supported on Gr/Ir(1 1 1) and Gr/Co/Ir(1 1 1) is shown in Figure 3.20a. In both cases, the spectrum displays a single, broad feature, with a FWHM of about 1.5 eV, about double as much as for the C 1s core level of CO. As is the case for CO, the shape is asymmetric, which can be attributed to the vibrational final state effects in the H<sub>2</sub>O<sup>+</sup> ion. However, due to the larger broadening, it is not possible to resolve the vibrational levels for this case. Therefore, the core level has been described by a single, asymmetric peak: it is important to stress, however, that this asymmetry does not have the usual physical meaning of the DS lineshape, as water does not have a metallic character, yet it is used to model the asymmetric lineshape of the peak arising from its vibrational fine structure. The O 1s BE of this peak is about 533.0 eV for water on Gr/Ir and 533.5 eV on Gr/Co: this increased core-level BE for the latter system is in good agreement with the behaviour already observed for CO and Ar adsorption.

Unlike the case of CO and Ar, saturation was never reached in our experiments during water uptake, for a dose comparable to those used for CO and Ar: this can be attributed to the growth occurring by islands, resulting in the formation of 2D water clusters and nanodroplets rather than a full water layer, as has been observed in STM studies<sup>66</sup>. Moreover, due to the large FWHM of the O 1s photoemission component observed in this system, it was not possible to distinguish the adsorption in different regions of the moiré, as no appreciable shifts could be observed in the core level BE, nor was it possible to verify the presence of multiple photoemission components.

Anyway, we were able to measure the desorption energy of water on the two systems by analysing the desorption curves obtained by TP-XPS on different initial doses of water, which are reported in Fig-



ure 3.20b. It is evident that also for the case of water, the desorption process occurs at higher temperature on the Gr/Co surface (below) than on Gr/Ir (above). Moreover, it is interesting to observe that on both substrates, the temperature at which desorption starts is independent on coverage, yet the process finishes at higher temperatures for increasing coverage. This is a fingerprint that this system undergoes a zero-order desorption process (as described in Section 3.1.1). This means that the desorption rate does not depend on coverage, and is usually found in the desorption of multi-layers. This behaviour has been already observed in TPD studies of water on Gr<sup>66,67</sup>, and has been attributed to the formation of a lattice of nanoclusters driven by the templating effect of the moiré<sup>66</sup>. As explained in Section 3.1.1, the Arrhenius equation for this system becomes therefore:

$$I = \alpha\theta = \alpha \left( \theta_0 - \nu \int_{T_0}^T e^{-E_{DES}/k_B T} \frac{dT}{T} \right)$$

where  $I$  is the photoemission intensity and  $\alpha$  is the normalization factor relating it to the coverage.

Due to the zero order of the desorption process, the coverage calibration of water could be carried out using a combination of two methods, to improve the accuracy of the results. One was by comparing the photoemission signal with that of a saturated layer of oxygen dosed on the Ir (1 1 1) surface at room temperature, which corresponds to a coverage of 0.5 oxygen atoms per Ir unit cell<sup>68</sup> – which, due to the lattice mismatch, corresponds to the same oxygen density as 0.4 ML water on our Gr layer. The other method used, which yielded comparable results, was obtained from the fit: in fact, as shown in the equation above, for a desorption order  $N \neq 1$ , the functional dependence on coverage is decoupled from the dependence on  $\theta_0$ , and therefore both can be obtained separately from the fit.

The fit was performed for all spectra at the same time, by constraining some of the fit parameters to be equal for all spectra (the multiplicative constant  $\alpha$  and the pre-exponential factor  $\nu$ ), while the desorption energy  $E_{DES}$  was let free for each curve. The pre-exponential factor obtained from the fit was  $\nu = 10^{12.5 \pm 1} \text{s}^{-1}$ , slightly lower than the one obtained by Standop *et al.* for the same system<sup>66</sup>. The desorption energy for the case of Gr/Ir was  $E_{DES} = 390 \pm 5 \text{ meV}$ , slightly lower than the values reported in the same work (420 meV), while for comparison an even larger value (490 meV) was found by Smith *et al.* for water on Pt-supported Gr<sup>67</sup>. The discrepancy with respect to the results by Standop *et al.* can be attributed to the difficulty of estimating the error due to the strong anti-correlation between the  $\nu$  and  $E_{DES}$  fit parameters, as was discussed in Section 3.1.1. For this reason, this comparison with the literature data for the Gr/Pt system is affected by a large uncertainty.

On the other hand, our results for the Gr/Co system yield  $E_{DES} = 420 \pm 5 \text{ meV}$ , while the value of  $\nu$  is the same. This corresponds to an increase in the adsorption energy of about 30 meV with respect to the Gr/Ir system, again very similar to our results for CO and Ar adsorption.

We can observe that this system behaves very differently with respect to those studied before, namely CO and Ar adsorption on Gr. First of all, the tendency to form islands instead of a full layer, and therefore the zero order of the desorption process, indicate that the inter-molecular forces play a major role in this system. This can partially explain also the fact that the adsorption energy is significantly higher, being almost three times as much as for CO. Besides enhancing the inter-molecular interactions, another effect of the strong polar nature of the water molecule is by adding a strong polar component to the vdW interaction with Gr, which in this case can become comparable to or exceeds the dispersion-type interactions. On the other hand, the relatively high adsorption energy, of about 0.5 eV, could be also attributed to the formation of a chemical bonding between water and Gr, as has been recently suggested by NEXAFS experiments<sup>65</sup>.

## Conclusion

To conclude, this chapter describes a systematic investigation of the adsorption energy of different species on two Gr-metal interfaces, characterised by a different degree of interaction with its substrate. In particular, the adsorbates studied have been chosen as they are characterised by a very different chemical reactivity and electronic structure, ranging from a noble gas (Ar) to the molecule of H<sub>2</sub>O, characterised

by a high dipole moment. Due to this variability, we measured differences up to a factor of three between the adsorption energy of each species; moreover, depending on the systems, other factors such as the lateral interactions between adsorbates had a very different magnitude. However, in all systems there was a common behaviour, *i.e.* a clear indication that the adsorbates had a higher adsorption energy on Gr strongly interacting with a cobalt layer beneath it than on the quasi free-standing Gr/Ir (1 1 1). This clearly demonstrates the importance of taking into account the role of the substrate supporting Gr to properly describe the interactions of graphene with other species in calculations.

By employing a combined experimental and theoretical investigation for the particular case of CO adsorption, we have investigated the mechanisms leading to this enhancement, by decoupling the different effects of the substrate. We have shown that there is no significant direct interaction between the adsorbates and the metallic substrate, in contrast with literature affirming that graphene might be partially or totally transparent to vdW forces due to its thinness<sup>15,16</sup>.

Finally, from a quantitative analysis, it is remarkable that despite the very different nature of the adsorbates studied in these experiments, the difference between the adsorption energy on Ir- and Co-supported Gr is almost the same for all three adsorbates, *i.e.* about 30 meV. This is a clear indication that this mechanism is not related to the polar interactions, which would lead for example to a completely different behaviour for water and Ar, but rather to the London dispersive interactions, which are independent on the reactivity and polarity of molecules.

We can think of a possible explanation for this behaviour by considering that the expression for the London forces contains a dependence on the polarizability of the species involved<sup>13</sup>. As already mentioned, the strong interaction of Gr with the cobalt substrate leads to a charge redistribution between them, due to a hybridization of its valence orbitals with those of the metal, as described in Chapter 2.3. This redistribution of the charge leads to strong perturbation to its band structure, which may in turn affect the polarizability of Gr, and therefore lead to an increase in the London forces without significantly affecting the other contributions to the vdW interactions. While this is a quite speculative conclusion, which will require further theoretical calculations to be verified, it could nevertheless justify at least qualitatively the fact that the similar modifications to the adsorption energy are observed for such different systems.



## References

- [1] T. O. Wehling, K. S. Novoselov, S. V. Morozov, E. E. Vdovin, M. I. Katsnelson, A. K. Geim, A. I. Lichtenstein. Molecular doping of graphene. *Nano Lett.* (2008) 8: 173–177. doi:10.1021/nl072364w.
- [2] R. Balog, B. Jørgensen, L. Nilsson, M. Andersen, E. Rienks, M. Bianchi, M. Fanetti, E. Lægsgaard, A. Baraldi, S. Lizzit, Z. Sljivancanin, F. Besenbacher, B. Hammer, T. G. Pedersen, P. Hofmann, L. Hornekær. Bandgap opening in graphene induced by patterned hydrogen adsorption. *Nat. Mater.* (2010) 9: 315–319. doi:10.1038/nmat2710.
- [3] Y. Yang, K. Brenner, R. Murali. The influence of atmosphere on electrical transport in graphene. *Carbon* (2012) 50: 1727–1733. doi:10.1016/j.carbon.2011.12.008.
- [4] A. Primo, V. Parvulescu, H. Garcia. Graphenes as metal-free catalysts with engineered active sites. *J. Phys. Chem. Lett.* (2017) 8: 264–278. doi:10.1021/acs.jpclett.6b01996.
- [5] Y. Liang, H. Wang, H. S. Casalongue, Z. Chen, H. Dai. TiO<sub>2</sub> nanocrystals grown on graphene as advanced photocatalytic hybrid materials. *Nano Res.* (2010) 3: 701–705. doi:10.1007/s12274-010-0033-5.
- [6] N. R. Khalid, E. Ahmed, Z. Hong, L. Sana., M. Ahmed. Enhanced photocatalytic activity of graphene–TiO<sub>2</sub> composite under visible light irradiation. *Curr. Appl Phys.* (2013) 13: 659–663. doi:10.1016/j.cap.2012.11.003.
- [7] X. Li, J. Yu, S. Wageh, A. A. Al-Ghamdi, J. Xie. Graphene in photocatalysis: A review. *Small* (2016) 12: 6640–6696. doi:10.1002/smll.201600382.
- [8] C. Fasciani, A. E. Lanterna, J. B. Giorgi, J. C. Scaiano. Visible light production of hydrogen by ablated graphene: Water splitting or carbon gasification? *J. Am. Chem. Soc.* (2017) 139: 11024–11027. doi:10.1021/jacs.7b06570.
- [9] F. Schedin, A. K. Geim, S. V. Morozov, E. W. Hill, P. Blake, M. I. Katsnelson, K. S. Novoselov. Detection of individual gas molecules adsorbed on graphene. *Nat. Mater.* (2007) 6: 652–655. doi:10.1038/nmat1967.
- [10] S. An, B. N. Joshi, J.-G. Lee, M. W. Lee, Y. I. Kim, M.-W. Kim, H. S. Jo, S. S. Yoon. A comprehensive review on wettability, desalination, and purification using graphene-based materials at water interfaces. *Catal. Today* (2017) 295: 14–25. doi:10.1016/j.cattod.2017.04.027.
- [11] M. Smerieri, E. Celasco, G. Carraro, A. Lusuan, J. Pal, G. Bracco, M. Rocca, L. Savio, L. Vattuone. Enhanced chemical reactivity of pristine graphene interacting strongly with a substrate: Chemisorbed carbon monoxide on graphene/nickel(111). *ChemCatChem* (2015) 7: 2328–2331. doi:10.1002/cctc.201500279.
- [12] A. Chakradhar, N. Sivapragasam, M. T. Nayakasinghe, U. Burghaus. Support effects in the adsorption of water on CVD graphene: an ultra-high vacuum adsorption study. *Chem. Commun.* (2015) 51: 11463–11466. doi:10.1039/c5cc03827h.
- [13] J. N. Israelachvili. Van der Waals forces. In *Intermolecular and Surface Forces* (Elsevier, 2011), Chapter 6. 107–132. doi:10.1016/b978-0-12-391927-4.10006-4.
- [14] Not so transparent. *Nat. Mater.* (2013) 12: 865–865. doi:10.1038/nmat3773. Editorial.
- [15] J. Rafiee, X. Mi, H. Gullapalli, A. V. Thomas, F. Yavari, Y. Shi, P. M. Ajayan, N. A. Koratkar. Wetting transparency of graphene. *Nat. Mater.* (2012) 11: 217–222. doi:10.1038/nmat3228.
- [16] C.-J. Shih, M. S. Strano, D. Blankschtein. Wetting translucency of graphene. *Nat. Mater.* (2013) 12: 866–869. doi:10.1038/nmat3760.

- [17] R. Raj, S. C. Maroo, E. N. Wang. Wettability of graphene. *Nano Lett.* (2013) 13: 1509–1515. doi:10.1021/nl304647t.
- [18] J. Driskill, D. Vanzo, D. Bratko, A. Luzar. Wetting transparency of graphene in water. *J. Chem. Phys.* (2014) 141: 18C517. doi:10.1063/1.4895541.
- [19] L. A. Belyaeva, P. M. G. van Deursen, K. I. Barbetseand, G. F. Schneider (2017). Submitted for publication.
- [20] C. A. Amadei, C.-Y. Lai, M. J. Esplandiu, F. Alzina, C. D. Vecitis, A. Verdaguer, M. Chiesa. Elucidation of the wettability of graphene through a multi-length-scale investigation approach. *RSC Adv.* (2015) 5: 39532–39538. doi:10.1039/c5ra04397b.
- [21] C. M. Hill, J. Kim, N. Bodappa, A. J. Bard. Electrochemical nonadiabatic electron transfer via tunneling to solution species through thin insulating films. *J. Am. Chem. Soc.* (2017) 139: 6114–6119. doi:10.1021/jacs.6b12104.
- [22] O. Leenaerts, B. Partoens, F. M. Peeters. Adsorption of H<sub>2</sub>O, NH<sub>3</sub>, CO, NO<sub>2</sub>, and NO on graphene: A first-principles study. *Phys. Rev. B* (2008) 77: 125416. doi:10.1103/physrevb.77.125416.
- [23] P. L. Silvestrelli, A. Ambrosetti. Including screening in van der Waals corrected density functional theory calculations: The case of atoms and small molecules physisorbed on graphene. *J. Chem. Phys.* (2014) 140: 124107. doi:10.1063/1.4869330.
- [24] J. Ma, A. Michaelides, D. Alfè, L. Schimka, G. Kresse, E. Wang. Adsorption and diffusion of water on graphene from first principles. *Phys. Rev. B* (2011) 84: 033402. doi:10.1103/physrevb.84.033402.
- [25] S. Grimme. Semiempirical GGA-type density functional constructed with a long-range dispersion correction. *J. Comput. Chem.* (2006) 27: 1787–1799. doi:10.1002/jcc.20495.
- [26] C. Busse, P. Lazić, R. Djemour, J. Coraux, T. Gerber, N. Atodiresei, V. Caciuc, R. Brako, A. T. N'Diaye, S. Blügel, J. Zegenhagen, T. Michely. Graphene on Ir (1 1 1): Physisorption with chemical modulation. *Phys. Rev. Lett.* (2011) 107: 036101. doi:10.1103/PhysRevLett.107.036101.
- [27] M. Dion, H. Rydberg, E. Schröder, D. C. Langreth, B. I. Lundqvist. Van der Waals density functional for general geometries. *Phys. Rev. Lett.* (2004) 92. doi:10.1103/physrevlett.92.246401.
- [28] G. Román-Pérez, J. M. Soler. Efficient implementation of a van der Waals density functional: Application to double-wall carbon nanotubes. *Phys. Rev. Lett.* (2009) 103. doi:10.1103/physrevlett.103.096102.
- [29] J. Klimeš, D. R. Bowler, A. Michaelides. Chemical accuracy for the van der Waals density functional. *J. Phys.: Condens. Matter* (2009) 22: 022201. doi:10.1088/0953-8984/22/2/022201.
- [30] J. P. Prates Ramalho, J. R. B. Gomes, F. Illas. Accounting for van der Waals interactions between adsorbates and surfaces in density functional theory based calculations: selected examples. *RSC Adv.* (2013) 3: 13085. doi:10.1039/c3ra40713f.
- [31] X. Lin, J. Ni, C. Fang. Adsorption capacity of H<sub>2</sub>O, NH<sub>3</sub>, CO, and NO<sub>2</sub> on the pristine graphene. *J. Appl. Phys.* (2013) 113: 034306. doi:10.1063/1.4776239.
- [32] M. Lorenz, B. Civalleri, L. Maschio, M. Sgroi, D. Pullini. Benchmarking dispersion and geometrical counterpoise corrections for cost-effective large-scale DFT calculations of water adsorption on graphene. *J. Comput. Chem.* (2014) 35: 1789–1800. doi:10.1002/jcc.23686.
- [33] P. Lacovig, M. Pozzo, D. Alfè, P. Vilmercati, A. Baraldi, S. Lizzit. Growth of dome-shaped carbon nanoislands on Ir (1 1 1): The intermediate between carbidic clusters and quasi-free-standing graphene. *Phys. Rev. Lett.* (2009) 103: 166101. doi:10.1103/physrevlett.103.166101.

- [34] E. Celasco, G. Carraro, M. Smerieri, L. Savio, M. Rocca, L. Vattuone. Influence of growing conditions on the reactivity of ni supported graphene towards co. *J. Chem. Phys.* (2017) 146: 104704. doi:10.1063/1.4978234.
- [35] M. Batzill. The surface science of graphene: Metal interfaces, CVD synthesis, nanoribbons, chemical modifications, and defects. *Surf. Sci. Rep.* (2012) 67: 83–115. doi:10.1016/j.surfrep.2011.12.001.
- [36] R. Balog, B. Jørgensen, J. Wells, E. Lægsgaard, P. Hofmann, F. Besenbacher, L. Hornekær. Atomic hydrogen adsorbate structures on graphene. *J. Am. Chem. Soc.* (2009) 131: 8744–8745. doi:10.1021/ja902714h.
- [37] A. Baraldi, G. Comelli, S. Lizzit, D. Cocco, G. Paolucci, R. Rosei. Temperature programmed x-ray photoelectron spectroscopy: a new technique for the study of surface kinetics. *Surf. Sci.* (1996) 367: L67–L72. doi:10.1016/s0039-6028(96)01126-0.
- [38] A. T. N'Diaye, S. Bleikamp, P. J. Feibelman, T. Michely. Two-dimensional Ir cluster lattice on a graphene moiré on Ir (1 1 1). *Phys. Rev. Lett.* (2006) 97: 215501. doi:10.1103/physrevlett.97.215501.
- [39] K. Morishige, C. Mowforth, R. K. Thomas. Orientational order in CO and N<sub>2</sub> monolayers on graphite studied by x-ray diffraction. *Surf. Sci. Lett.* (1985) 151: A80. doi:10.1016/0167-2584(85)90632-2.
- [40] H. You, S. C. Fain. Structure of carbon monoxide monolayers physisorbed on graphite. *Surf. Sci.* (1985) 151: 361–373. doi:10.1016/0039-6028(85)90381-4.
- [41] D. A. Boyd, F. M. Hess, G. B. Hess. Infrared absorption study of physisorbed carbon monoxide on graphite. *Surf. Sci.* (2002) 519: 125–138. doi:10.1016/s0039-6028(02)02207-0.
- [42] A. Ambrosetti, P. L. Silvestrelli. Communication: Enhanced chemical reactivity of graphene on a Ni (1 1 1) substrate. *J. Chem. Phys.* (2016) 144: 111101. doi:10.1063/1.4944090.
- [43] L. Zhu, W. Zhang, J. Zhu, D. Cheng. Ni (1 1 1)-supported graphene as a potential catalyst for high-efficient CO oxidation. *Carbon* (2017) 116: 201–209. doi:10.1016/j.carbon.2017.01.083.
- [44] H. Schlichting, D. Menzel. Techniques for attainment, control, and calibration of cryogenic temperatures at small single-crystal samples under ultrahigh vacuum. *Rev. Sci. Instrum.* (1993) 64: 2013–2022. doi:10.1063/1.1143992.
- [45] H. Lüth. Adsorption on solid surfaces. In *Solid Surfaces, Interfaces and Thin Films* (Springer-Verlag Berlin Heidelberg, 2010), Chapter 10. 5th edition, 517–543. doi:10.1007/978-3-319-10756-1\_10.
- [46] J. N. Andersen, A. Beutler, S. L. Sorensen, R. Nyholm, B. Setlik, D. Heskett. Vibrational fine structure in the C 1s core level photoemission of chemisorbed molecules: ethylene and ethynylidyne on Rh (1 1 1). *Chem. Phys. Lett.* (1997) 269: 371–377. doi:10.1016/s0009-2614(97)00288-1.
- [47] A. Föhlisch, N. Wassdahl, J. Hasselström, O. Karis, D. Menzel, N. Mårtensson, A. Nilsson. Beyond the chemical shift: Vibrationally resolved core-level photoelectron spectra of adsorbed CO. *Phys. Rev. Lett.* (1998) 81: 1730–1733. doi:10.1103/physrevlett.81.1730.
- [48] B. Kempgens, K. Maier, A. Kivimäki, H. M. Köppe, M. Neeb, M. N. Piancastelli, U. Hergenhausen, A. M. Bradshaw. Vibrational excitation in C 1s and O 1s photoionization of CO. *J. Phys. B* (1997) 30: L741–L747. doi:10.1088/0953-4075/30/21/005.
- [49] T. X. Carroll, K. J. Børve, L. J. Sæthre, J. D. Bozek, E. Kukk, J. A. Hahne, T. D. Thomas. Carbon 1s photoelectron spectroscopy of CF<sub>4</sub> and CO: Search for chemical effects on the carbon 1s hole-state lifetime. *J. Chem. Phys.* (2002) 116: 10221–10228. doi:10.1063/1.1476933.

- [50] E. Kukk, D. Ayuso, T. D. Thomas, P. Decleva, M. Patanen, L. Argenti, E. Plésiat, A. Palacios, K. Kooser, O. Travnikova, S. Mondal, M. Kimura, K. Sakai, C. Miron, F. Martín, K. Ueda. Effects of molecular potential and geometry on atomic core-level photoemission over an extended energy range: The case study of the CO molecule. *Phys. Rev. A* (2013) 88. doi:10.1103/physreva.88.033412.
- [51] A. Föhlisch, J. Hasselström, O. Karis, P. Väterlein, N. Mårtensson, A. Nilsson, C. Heske, M. Stichler, C. Keller, W. Wurth, D. Menzel. Franck–Condon breakdown in core-level photoelectron spectroscopy of chemisorbed CO. *Chem. Phys. Lett.* (1999) 315: 194–200. doi:10.1016/s0009-2614(99)01194-x.
- [52] T. Ramsvik, A. Borg, M. Kildemo, S. Raaen, A. Matsuura, A. Jaworowski, T. Worren, M. Leandersson. Molecular vibrations in core-ionised CO adsorbed on Co (0 0 0 1) and Rh (1 0 0). *Surf. Sci.* (2001) 492: 152–160. doi:10.1016/s0039-6028(01)01446-7.
- [53] M. Smedh, A. Beutler, T. Ramsvik, R. Nyholm, M. Borg, J. N. Andersen, R. Duschek, M. Sock, F. P. Netzer, M. G. Ramsey. Vibrationally resolved C 1s photoemission from CO absorbed on Rh (1 1 1): the investigation of a new chemically shifted C 1s component. *Surf. Sci.* (2001) 491: 99–114. doi:10.1016/s0039-6028(01)01357-7.
- [54] T. K. Sham, B. X. Yang, J. Kirz, J. S. Tse. K-edge near-edge x-ray-absorption fine structure of oxygen- and carbon-containing molecules in the gas phase. *Phys. Rev. A* (1989) 40: 652–669. doi:10.1103/physreva.40.652.
- [55] G. Hähner. Near edge X-ray absorption fine structure spectroscopy as a tool to probe electronic and structural properties of thin organic films and liquids. *Chem. Soc. Rev.* (2006) 35: 1244–1255. doi:10.1039/b509853j.
- [56] Z. Wang, E. G. Seebauer. Estimating pre-exponential factors for desorption from semiconductors: consequences for a priori process modeling. *Appl. Surf. Sci.* (2001) 181: 111–120. doi:10.1016/s0169-4332(01)00382-8.
- [57] C. T. Campbell, L. Árnadóttir, J. R. V. Sellers. Kinetic prefactors of reactions on solid surfaces. *Z. Phys. Chem.* (2013) 227. doi:10.1524/zpch.2013.0395.
- [58] J. P. Perdew, K. Burke, M. Ernzerhof. Generalized gradient approximation made simple. *Phys. Rev. Lett.* (1996) 77: 3865–3868. doi:10.1103/PhysRevLett.77.3865.
- [59] Y. Zhang, W. Yang. Comment on “Generalized gradient approximation made simple”. *Phys. Rev. Lett.* (1998) 80: 890–890. doi:10.1103/physrevlett.80.890.
- [60] T. Brugger, S. Günther, B. Wang, J. H. Dil, M.-L. Bocquet, J. Osterwalder, J. Wintterlin, T. Greber. Comparison of electronic structure and template function of single-layer graphene and a hexagonal boron nitride nanomesh on Ru(0 0 0 1). *Phys. Rev. B* (2009) 79: 045407. doi:10.1103/PhysRevB.79.045407.
- [61] S. Lizzit, R. Larciprete, P. Lacovig, K. L. Kostov, D. Menzel. Ultrafast charge transfer at monolayer graphene surfaces with varied substrate coupling. *ACS Nano* (2013) 7: 4359–4366. doi:10.1021/nn4008862.
- [62] J. N. Israelachvili. Contrasts between intermolecular, interparticle, and intersurface forces. In *Intermolecular and Surface Forces* (Elsevier, 2011), Chapter 11. 205–222. doi:10.1016/b978-0-12-391927-4.10011-8.
- [63] C. G. Shaw, S. C. Fain, M. D. Chinn. Observation of orientational ordering of incommensurate argon monolayers on graphite. *Phys. Rev. Lett.* (1978) 41: 955–957. doi:10.1103/physrevlett.41.955.
- [64] C. Fuselier, J. Raich, N. Gillis. Equilibrium configurations of commensurate adsorbed monolayers: Argon on graphite. *Surf. Sci.* (1980) 92: 667–680. doi:10.1016/0039-6028(80)90229-0.

- [65] S. Böttcher, H. Vita, M. Weser, F. Bisti, Y. S. Dedkov, K. Horn. Adsorption of water and ammonia on graphene: Evidence for chemisorption from X-ray absorption spectra. *J. Phys. Chem. Lett.* (2017) 8: 3668–3672. doi:10.1021/acs.jpcllett.7b01085.
- [66] S. Standop, T. Michely, C. Busse. H<sub>2</sub>O on graphene/Ir (1 1 1): A periodic array of frozen droplets. *J. Phys. Chem. C* (2015) 119: 1418–1423. doi:10.1021/jp510140a.
- [67] R. S. Smith, J. Matthiesen, B. D. Kay. Desorption kinetics of methanol, ethanol, and water from graphene. *J. Phys. Chem. A* (2014) 118: 8242–8250. doi:10.1021/jp501038z.
- [68] A. J. Martínez-Galera, U. A. Schröder, F. Huttmann, W. Jolie, F. Craes, C. Busse, V. Caciuc, N. Atodiresei, S. Blügel, T. Michely. Oxygen orders differently under graphene: new superstructures on Ir (1 1 1). *Nanoscale* (2016) 8: 1932–1943. doi:10.1039/c5nr04976h.



## Chapter 4

# Magnetic coupling between graphene-supported molecules and the substrate: the case of metal-phthalocyanines.

The experiments I have described in Chapter 3 are centred on the measurement of the interaction energy between Gr and different adsorbates. However, the interest in Gr-adsorbates interactions is not limited to a fundamental level, as the effects of this interaction on the electronic properties of Gr can be exploited for various applications.

One example is the possibility to employ Gr as a sensor for several species. For example, changes in the conductivity can be employed for the realization of gas sensors with unprecedented sensitivity<sup>1-4</sup>, while the covalent bonding which occurs between Gr and large, organic molecules makes it suitable as a sensor in biological applications<sup>2,5,6</sup>.

Another very interesting aspect of the interactions between Gr and adsorbates is the coupling which is introduced with magnetic adsorbates. In fact, the planar  $\pi_z$  band of Gr can couple with the  $d$  orbitals of nearby transition metal atoms, whose occupation is responsible for their magnetic properties, leading to a hybridisation between these states. This coupling is for example at the base of the strong interaction between Gr and some transition metal surfaces, as seen in Chapter 2. Likewise, the band structure of Gr can be perturbed when metal atoms or clusters are adsorbed on it<sup>7</sup>.

This coupling of the states of Gr with the partially filled  $d$  orbitals of transition metals has been shown to introduce magnetic properties into Gr<sup>8-11</sup>. On the other hand, also the properties of magnetic materials in contact with Gr can be altered. In fact, Gr has been shown to enhance the magnetic response of magnetic thin films over which it is supported: for example, it has been shown that thin cobalt films exhibit a significantly higher switching field on their out-of-plane easy axis when intercalated below Gr<sup>12</sup>. Moreover, cobalt films exhibit a perpendicular magnetic anisotropy characterised by a significantly higher critical thickness when intercalated at the Gr-support interface<sup>9,13</sup>.

These results make it an ideal support for low-dimensional magnetic systems composed of ordered spin networks of magnetic molecules or atomic clusters<sup>14,15</sup>. In fact, spin architectures composed by equally sized and evenly spaced molecular units are particularly promising for the engineering of materials with possible applications in spintronic devices, for information processing and information storage at the ultimate length-scale<sup>16,17</sup>.

However, a major issue to be solved before such systems can be successfully employed is their thermal stability. Beside the Curie temperature, a factor to take into account is the mobility of single molecules when adsorbed on surfaces, which allows them to diffuse close to each other and behave like a single magnetic material, rather than like single-molecule magnets<sup>18</sup>. A further issue of these networks arises when they are supported on a strongly interacting substrate: for example, the magnetic state of such molecules can be dramatically affected by molecule-substrate interaction upon adsorption on metal surfaces<sup>19</sup>. In this

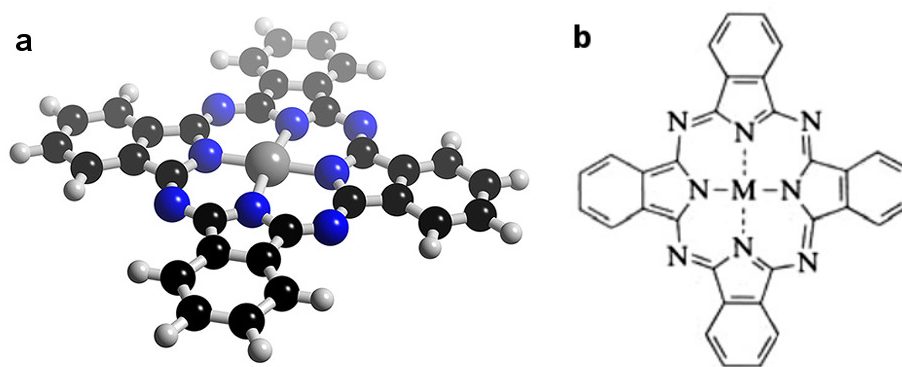


**Figure 4.1:** a: Ball and stick model<sup>25</sup>, and b: structure formula of a metal-phthalocyanine<sup>22</sup>.

context, metal-supported Gr can be considered an ideal substrate for spin networks, as it acts as a buffer layer decoupling the molecules from the metal surface<sup>20</sup>. In addition, it provides an ordering template for the self assembly of an extended layer of magnetic units thanks to the rippled moiré superstructure<sup>15,21</sup>.

Beside the substrate, also the choice of the units making up the network is fundamental to achieve adequate magnetic properties. In this respect, very promising candidates can be found among metal-phthalocyanines (MPcs), which are organic molecules composed of four outer benzene rings, bonded to an aza-porphyrine macrocycle, and with a metallic atom bonded to its pyrrole groups in the centre (tetrabenzotetraazaporphyrin)<sup>22</sup>. A model of these molecules is shown in Figure 4.1. Their outstanding magnetic properties, which can be easily tuned by the choice of the central metal ion, make them ideal for use as building blocks of 2D magnetic architectures<sup>23,24</sup>.

Following these considerations, the self-assembly of MPcs on a corrugated Gr layer has attracted considerable interest for the formation of magnetic spin networks characterised by a significant zero-field remanent magnetization stable up to and above room temperature, as required to be integrated in spintronic devices. In fact, it has been proved that FePc molecules adsorbed on Gr/Ir (1 1 1) lay flat on the surface, do not alter the periodicity of the superstructure and are electronically decoupled from the metal substrate<sup>20,26</sup>. Thanks to this decoupling and templating, they exhibit an enhanced magnetic anisotropy with easy axis parallel to the G layer, due to the adsorption-induced reduction of the molecular symmetry<sup>27</sup>.

The aim of the experiment described in this section was to introduce a further improvement to the magnetic properties of MPcs, by introducing a magnetic substrate below Gr. The Gr layer is a key component in this architecture, as it can mediate the magnetic interaction between the molecules and its substrate while preventing a direct electronic coupling. However, its precise role is still not clearly understood, as the mechanisms by which it mediates the magnetic coupling are still under debate. In fact, as the Gr prevents a direct coupling between the magnetic substrate below it and the metallic atom inside the molecule, a super-exchange interaction has been proposed, by which the magnetic coupling is mediated by non-magnetic atoms<sup>28,29</sup>. However, the details of this mechanism are not yet understood in detail, and the atoms which are responsible for mediating this interactions are yet to be identified.

In the experiment described in this Section, which has been performed in collaboration with the research group of Prof. M.-G. Betti from La Sapienza University of Rome, we have investigated the role of the nitrogen and carbon atoms on the super-exchange interaction between Gr on cobalt-terminated Ir (1 1 1) and different MPcs. In fact, the super-exchange interaction is strongly dependent on the symmetry of the orbitals involved, as it requires an overlap between the orbitals of the mediating and magnetic atoms. We exploited this fact to identify the orbitals involved in the super-exchange by comparing MPcs characterized by a different occupation of the *d* orbitals of the metallic atom. In fact, when MPcs are adsorbed on a surface, the degeneracy between the *d* orbitals of the metal atom having a different symmetry and orientation is removed, and therefore the symmetry of the partially occupied states responsible of the magnetic behaviour strongly depends on the *d*-band occupation. For example, copper has a *d*<sup>9</sup> occupation,



and therefore copper-PCs (CuPcs) have a partially occupied  $d_{x^2-y^2}$  orbital, which is parallel to the plane of the molecule, while iron- and manganese-PCs (FePcs and MnPcs) also have unpaired, magnetic states in an out-of-plane direction<sup>18</sup>.

Our experiment was therefore based on the comparison of the magnetic properties of two MPcs characterised by a different symmetry of the unpaired orbitals of the metallic atom, namely FePcs and CuPcs, to identify the symmetry of the orbitals involved in the super-exchange mechanism in the MPcs and in the Gr layer. To this aim, we employed a combined approach based on complementary experimental techniques, namely XPS and XMCD, in order to investigate the role of the molecule-substrate electronic interaction.

## 4.1 Experimental details

Two samples were prepared for this experiment by depositing two different MPcs (CuPcs and FePcs, respectively) on a Gr/Co/Ir (1 1 1) interface, which was obtained by using the procedure described in Chapter 2.3.1. The amount of MPcs deposited was relatively small, *i.e.* less than one molecule per Gr moiré cell, in order to benefit from the templating effect of Gr and ensure that only the valleys of the corrugated Gr layer were populated.

A combination of complementary experimental techniques was used to investigate our systems. In particular, the structural and electronic characterisation of the molecules was performed at the SuperESCA beamline: the NEXAFS linear dichroism was employed to probe the orientation of the molecules on Gr, while the electronic structure of the molecule, and the coupling of its states with those of Gr, were instead investigated by XPS.

Finally, the magnetic properties of the molecules were measured by XMCD, at the BOREAS beamline of the Alba synchrotron radiation facility in Barcelona. NEXAFS spectra were measured using alternatively right and left circularly polarized radiation, in total electron yield – by measuring the sample drain current – and normalized by the photon flux measured with a gold mesh placed in front of the sample. The background of the absorption spectra was acquired prior to MPc deposition, to correct the data for bulk-

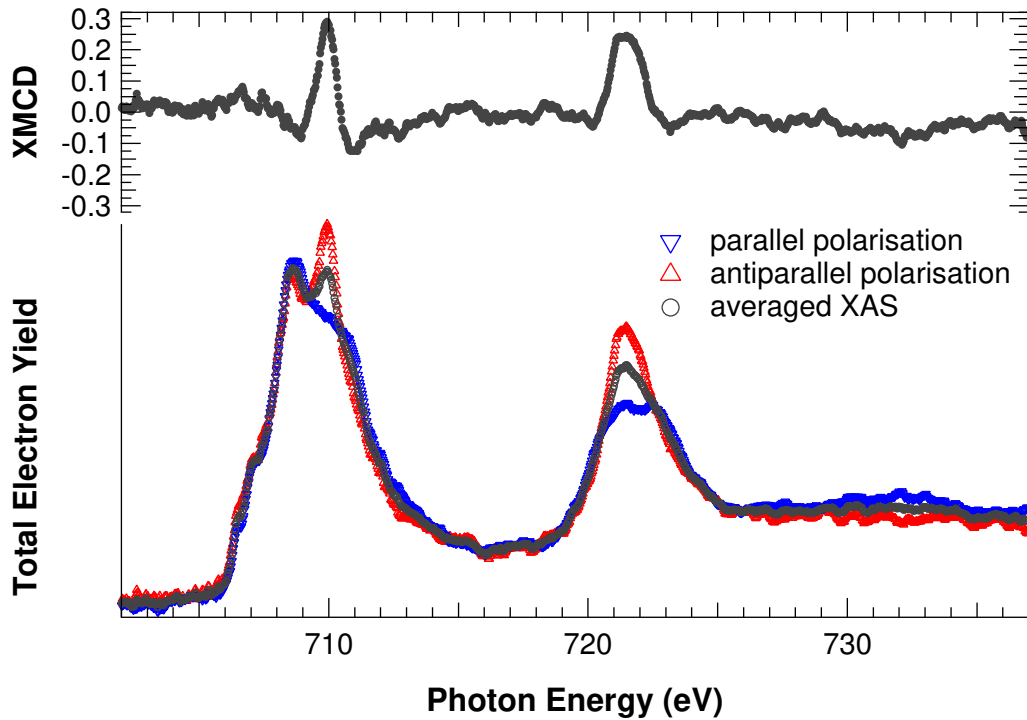


**Figure 4.2:** XMCD spectrum of a few-ML layer of cobalt intercalated below Gr, measured at 4 K under a magnetic field of 6 T. Below: NEXAFS spectrum measured with circularly polarized radiation, together with their average. Above: XMCD spectrum.

originated features. These spectra were acquired at a sample temperature of 4 K.

In order to investigate the magnetic properties of our system, we first measured the XMCD spectrum at fixed magnetic field, at the  $L_{23}$  edge of Fe and Cu, respectively, together with the  $L_{23}$  edge of the Co substrate. A sample XMCD spectrum, measured at the Co  $L_{23}$  edge, is shown in Figure 4.2. In particular, the NEXAFS spectrum for the two opposite polarizations is shown below, together with their average (which would correspond to the unpolarized absorption spectrum). The XMCD spectrum, which is plotted above in Figure 4.2, is defined as

$$XMCD = \frac{I_A - I_P}{\frac{I_A + I_P}{2}}$$

where  $I_A$  is the absorption spectrum for the antiparallel circular polarization (with respect to the X-ray photons' wavevector) and  $I_P$  for the parallel polarization.

This technique provides information on the density of states of the unbound states having opposite spin polarization, and therefore on the differences in the occupancy of the metal  $d$ -band states of opposite spin<sup>30</sup>. As this quantity is the source of the magnetisation of the atoms, this technique allows to quantitatively measure the magnetisation of a system, which is proportional to the integral of the XMCD spectrum on the energy range. A very important application of XMCD is the measurement of the magnetic hysteresis loop, which is obtained by measuring this integral of the XMCD spectrum as a function of the magnetic field applied to the sample as the field is linearly ramped up to a maximum value, then back to zero, to an opposite value and finally back to zero.

## 4.2 Experimental results

### Core-level photoemission spectra

The photoemission spectra acquired on the FePc layer are shown in Figure 4.3. In particular, the N 1s core level region (Figure 4.3a) shows a broad feature with a FWHM of about 1 eV, which is originated by the two non-equivalent species of nitrogen which are present in equal number in the molecule, as can be seen in Figure 4.1b. In particular, the four nitrogen atoms adjacent to the metal atoms are in a pyrrole configuration, while four others, located on the outside in bridge positions, form an azomethine configuration. Due to the non-equivalence of these two species, the N 1s spectrum can be fitted with two components, separated by about 300 meV<sup>20</sup>: the core level of the pyrrole species lies at a BE of 398.2 eV, while the one of the azomethine species lies at a higher BE of 398.5 eV. It is interesting to compare these values to those found for the adsorption of the same molecules on Ir-supported Gr. In fact, in that system, the N 1s BE of the two non-equivalent nitrogen species is 398.8 and 399.1 eV, respectively. This corresponds to a shift of about 600 meV towards lower core-level BEs for FePcs adsorbed on Co-supported Gr.

Figure 4.3b shows the C 1s core level of the same system. The deconvolution of this spectrum is complicated by the overlap of the signal from the carbon atoms in the FePcs with those of the Gr below. In fact, the two most prominent features, indicated in the figure by the letters V and H, are those originated by Gr, in good agreement with the results discussed in Chapter 2. The additional components which appear in the spectrum can be attributed to the non-equivalent carbon atoms in the molecule, characterised by a different number (or chemical identity) of nearest neighbours. Due to the overlap of these components, it is not possible to perform a reliable deconvolution of the spectrum: for this reason, the results of this fit are only meant to provide a generic description of the spectrum, while an accurate attribution of these components to specific C atoms in the molecule is beyond the scope of this work.

Finally, the Fe  $2p_{3/2}$  core level has a very broad line-shape which requires several components to be properly described. This structured lineshape, which has been observed in the Fe  $2p_{3/2}$  core level of several iron-core organic molecules, has been attributed to final state effects related to the spin degeneracy<sup>31–33</sup>.

The difference observed in the N 1s BE with respect to the FePcs adsorbed on Ir-supported Gr indicates a different degree of charge transfer between Gr and the adsorbed molecules. However, this behaviour is opposite to the one observed for the case of small molecules such as CO on Gr, described in Chapter 3: in that case, in fact, the core level BE was higher for the case of Co-supported Gr. The reason for this different

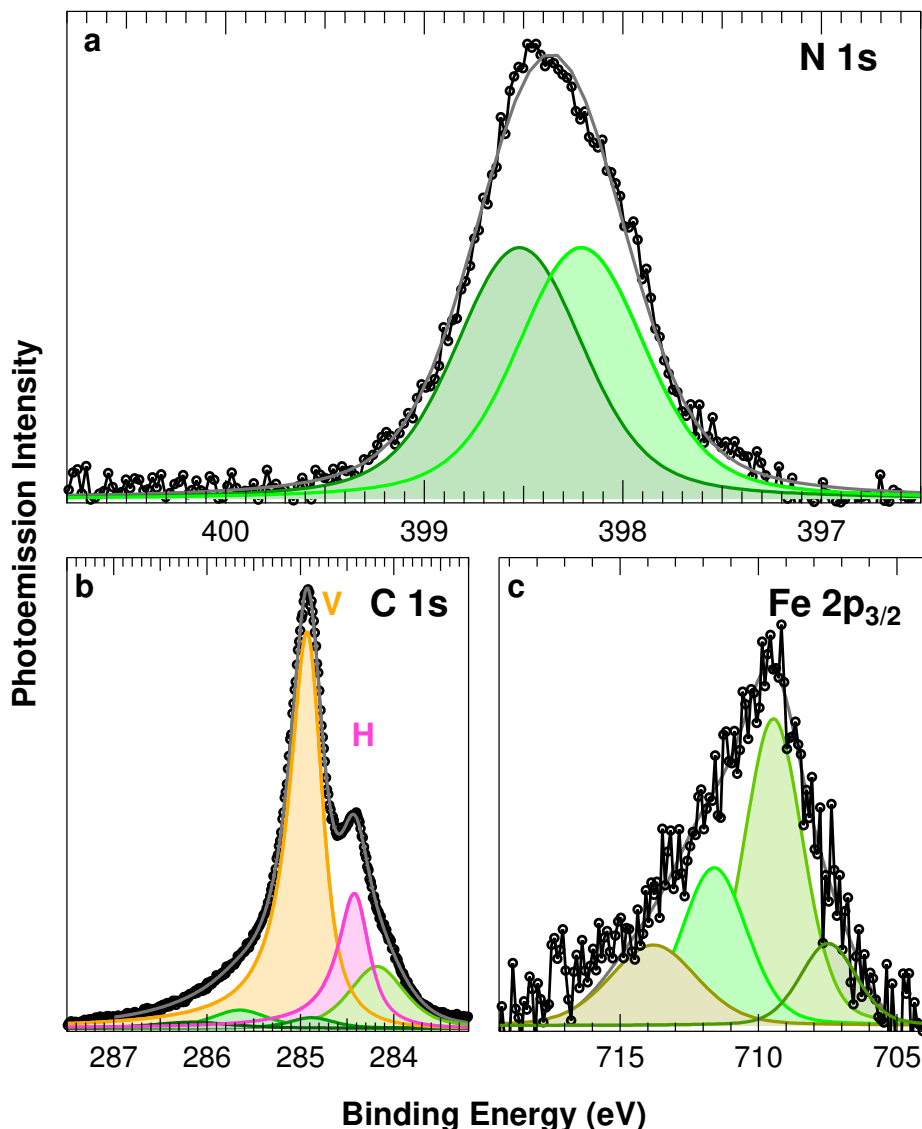


**Figure 4.3:** Photoemission spectra measured on Gr/Co/Ir(111) partially covered by FePc. a: N 1s spectrum ( $h\nu = 500$  eV) with deconvoluted components. b: C 1s spectrum ( $h\nu = 400$  eV) with deconvoluted components. The components originating from Gr are denoted with the letters V (atoms in the valleys of the corrugation) and H (atoms in the hills), according to the results discussed in Chapter 2. c: Fe 2p<sub>3/2</sub> spectrum ( $h\nu = 800$  eV) with deconvoluted components.

behaviour can be attributed to the fact that the interaction of MPCs with Gr is based on a hybridisation of the molecular orbitals with the  $\pi$  states of Gr, leading to a significant disruption in the molecular orbitals.

Figure 4.4 shows the photoemission spectra acquired on the CuPc layer. The N 1s spectrum, shown in Figure 4.4a, has an analogous lineshape to that of FePcs (Figure 4.3a), originated by two components separated from each other by about 300 meV, yet both are shifted towards higher BE by about 700 meV, being found respectively at 398.9 and 399.2 eV. The reason for this shift can be attributed to the higher electronegativity of the Cu central atom with respect to Fe, leading to a different chemical state and consequently a different degree of core-hole screening in each atom of the molecule.

The same trend is observed in the C 1s spectrum, where a qualitative analysis shows a shift towards higher BEs in those components originated by the C atoms of the MPC. However, due to the overlap with the Gr spectrum, the single components are not easily resolved from each other, nor from those of Gr, as was also the case for the FePcs.

Finally, the Cu 2p<sub>3/2</sub> spectrum shows a single component centred at about 935.5 eV, which is significantly

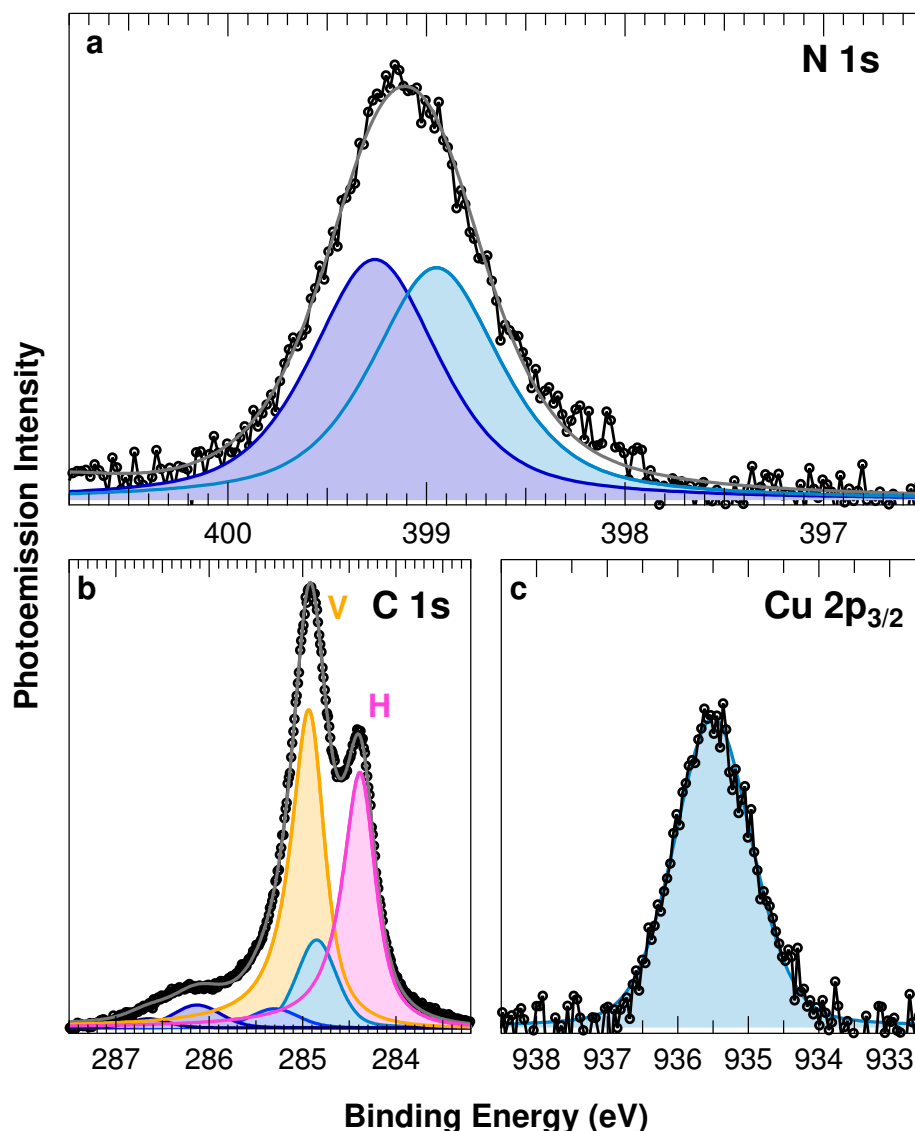


**Figure 4.4:** Photoemission spectra measured on Gr/Co/Ir (1 1 1) partially covered by CuPc. a: N 1s spectrum ( $h\nu = 500$  eV) with deconvoluted components. b: C 1s spectrum ( $h\nu = 400$  eV) with deconvoluted components. The components originating from Gr are denoted with the letters V (atoms in the valleys of the corrugation) and H (atoms in the hills), according to the results reported in Chapter 2. c: Cu 2p<sub>3/2</sub> spectrum ( $h\nu = 1050$  eV) with deconvoluted components.

higher than that of metallic Cu (about 932.6 eV) and compatible with an oxidation state of +2<sup>34</sup>. The FWHM of this component is just above 1 eV, due to the large intrinsic lineshape and lower experimental resolution at the high photon energies required to measure this spectrum.

### X-ray absorption spectra and dichroism

NEXAFS measurements were performed with linearly polarized radiation at different incidence angles, to investigate the orientation of the adsorbed molecules, using the same approach shown in Chapter 3.1.2. In particular, we performed these measurements at the N K-edge, in order to avoid features originated by the overlap of other species (such as the adsorption edge of Gr, which contributes to the C K-edge spectral region). These spectra are shown in Figure 4.5.

In particular, the N K-edge of the FePc layer (Figure 4.5a) shows a strong dichroism between normal- and grazing-incidence measurements. In fact, at grazing incidence, a sharp absorption feature is found

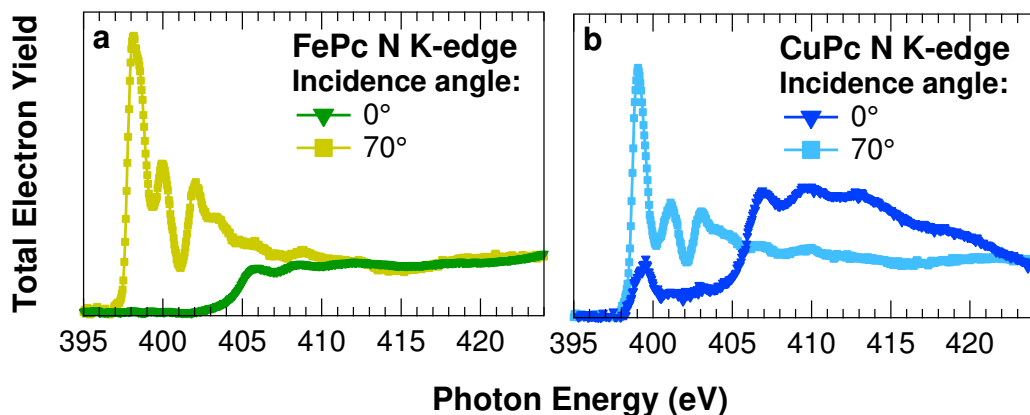


**Figure 4.5:** NEXAFS of Gr/Co/Ir(111) partially covered by FePc (a) and CuPc (b), at the N K-edge, measured with linearly polarized radiation at normal and grazing incidence.

at about 398 eV, which is originated by two unresolved pre-edge features associated to a transition to the LUMO, which has a  $\pi^*$  symmetry<sup>20</sup>. Further features at higher energies are due to transitions to higher-lying unoccupied states. The fact that these features are only visible at grazing incidence indicates that the molecules lie flat on the surface, as the  $\pi^*$  orbitals are oriented perpendicularly to the plane of the molecules.

A similar behaviour is observed for the case of the CuPc layer (Figure 4.5a), where however both the feature due to the transition to the LUMO and the edge are moved towards higher energies: this, together with the observed shift in the N 1s core level BE, is an indication that the higher electronegativity of the Cu atom leads to a higher oxidation state of all other atoms in the molecule. Furthermore, in the case of the CuPc layer, the feature due to the transition to the LUMO is also observed at normal incidence, even though strongly suppressed in intensity with respect to the one at grazing incidence, indicating a small tilting of some molecules.

To evaluate the magnetic properties of the molecules, the XMCD of their metal atom was measured during a hysteresis loop and compared to that of the underlying Co layer, following the procedure described in Section 4.1. The loops thus obtained are shown in Figure 4.6.

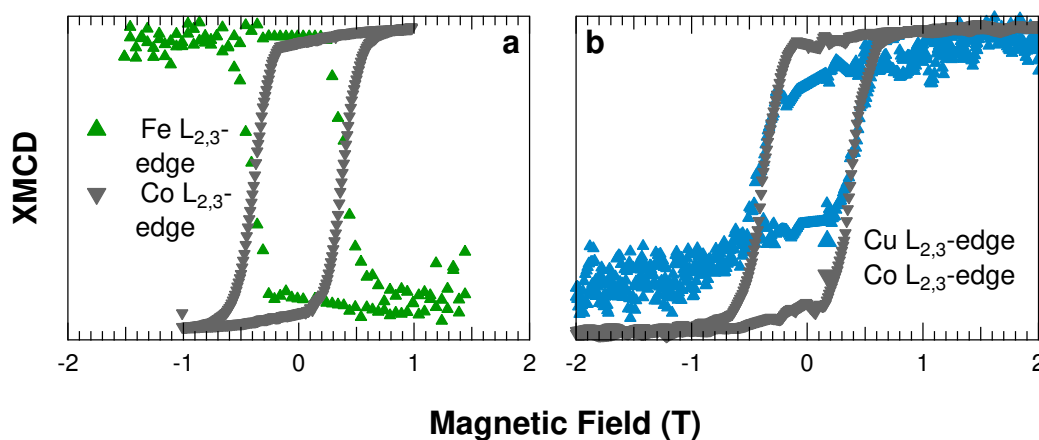


**Figure 4.6:** Hysteresis loop of Gr/Co/Ir(111) partially covered by MPcs, measured at 4 K. a: hysteresis loop of FePcs, measured from XMCD at the Fe and Co L<sub>2,3</sub>-edge. b: hysteresis loop of the CuPc layer, investigated by XMCD at the Cu and Co L<sub>2,3</sub>-edge. The curves are not to scale.

In particular, the XMCD hysteresis loop was measured on the  $L_{2,3}$ -edge of Co for the substrate, and of Fe and Cu for the FePc and CuPc respectively. As can be seen in Figure 4.6b, the CuPc layer shows a hysteresis for fields ranging between  $-1$  and  $+1$  T, which is similar to that of the underlying Co layer. This is what is expected for the case of a direct magnetic coupling of the molecules with the substrate, leading to them showing a similar magnetic behaviour.

For the case of FePcs (Figure 4.5a), instead, the situation is very different. In fact, the magnetisation of the molecules (as obtained from the XMCD at the Fe  $L_{2,3}$ -edge) is oriented in the opposite direction with respect to the magnetic field. This is a clear indication that in this system the behaviour of the Co layer is ferromagnetic, yet that of the molecules is antiferromagnetic.

### 4.3 Discussion

The antiferromagnetic character of the FePcs when adsorbed on Gr on a magnetic substrate is a striking result, as it sheds light on the role of Gr in mediating the interaction between this magnetic adsorbate and the magnetic substrate. In particular, an antiferromagnetic behaviour cannot be explained in terms of a direct magnetic coupling between the molecules and the substrate. On the contrary, it is a clear fingerprint that the coupling occurs through a super-exchange process: in fact, antiferromagnetism has been long associated with super-exchange processes<sup>35</sup>. In this particular case, therefore, these results pinpoint the role played by Gr on the magnetism of the molecules. As already mentioned, this super-exchange is based on the fact that the electronic states of Gr, which are non-magnetic when isolated, couple with those of both the magnetic substrate and adsorbates, and this hybridisation introduces a magnetic character into them, by breaking the degeneracy of opposite spin bands.

The comparison between the behaviour of the FePcs and CuPcs allows to further expand our knowledge on this process. In fact, the ferromagnetic character observed in the FePcs is not found instead in the CuPcs, which suggests that the super-exchange is not present in this latter system. As pointed out before, this comparison allows us to identify the orbitals involved in the super-exchange, by exploiting the fact that the occupancy of the in-plane and out-of-plane molecular orbitals at the base of the magnetism of the molecules depend on the identity of the metal atom. In particular, in CuPcs the unoccupied states determining the magnetic properties are all oriented parallel to the plane of the molecule, and therefore they cannot couple with the  $\pi$  band of Gr. FePcs, instead, also have unoccupied magnetic states perpendicular to the plane: these states are able to couple with those of cobalt, and this coupling is what transmits the magnetic super-exchange with the Co substrate. These results, therefore, prove that the super-exchange is based on the hybridisation between the  $\pi$  band of Gr, which is further hybridised with the  $d$ -band of the cobalt layer below, and the  $d$  orbitals of the metal atom in the MPc molecule having a component along  $z$  i.e., the  $d_{z^2}$ ,  $d_{xz}$  and  $d_{yz}$  states. This is therefore at the base of the antiferromagnetic behaviour which is observed only in those molecules where these orbitals are partially occupied, when adsorbed on Co-supported Gr.

### Conclusion

In this chapter, I have described one example of the effect of the interaction of Gr with the substrate on the properties of adsorbed molecules. In particular, I have studied a magnetic system based on magnetic organic molecules, adsorbed on a Gr layer supported on a magnetic interface.

By employing a combination of experimental techniques, and in particular using XMCD, we have shown that Gr can mediate the magnetic coupling between the molecules and the substrate by a super-exchange mechanism.

This super-exchange process is very promising for several applications, as it allows a very efficient coupling between two magnetic systems, thereby enhancing their magnetic properties, while preventing a direct electronic coupling, which would instead negatively affect them, as pointed out earlier in this chapter.

This system represents therefore a very meaningful example of how the reciprocal interaction between Gr, its substrate and its adsorbates can dramatically affect the properties of the system with respect to those of the single components, and can be exploited for the development of stable and efficient magnetic systems at the nanometre scale.

## References

- [1] F. Schedin, A. K. Geim, S. V. Morozov, E. W. Hill, P. Blake, M. I. Katsnelson, K. S. Novoselov. Detection of individual gas molecules adsorbed on graphene. *Nat. Mater.* (2007) 6: 652–655. doi:10.1038/nmat1967.
- [2] Y. Shao, J. Wang, H. Wu, J. Liu, I. A. Aksay, Y. Lin. Graphene based electrochemical sensors and biosensors: A review. *Electroanalysis* (2010) 22: 1027–1036. doi:10.1002/elan.200900571.
- [3] H. J. Yoon, D. H. Jun, J. H. Yang, Z. Zhou, S. S. Yang, M. M.-C. Cheng. Carbon dioxide gas sensor using a graphene sheet. *Sens. Actuators, B* (2011) 157: 310–313. doi:10.1016/j.snb.2011.03.035.
- [4] A. C. Ferrari, F. Bonaccorso, V. Fal'ko, K. S. Novoselov, S. Roche, P. Bøggild, S. Borini, F. H. L. Koppens, V. Palermo, N. Pugno, J. A. Garrido, R. Sordan, A. Bianco, L. Ballerini, M. Prato, E. Lidorikis, J. Kivioja, C. Marinelli, T. Ryhänen, A. Morpurgo, J. N. Coleman, V. Nicolosi, L. Colombo, A. Fert, M. Garcia-Hernandez, A. Bachtold, G. F. Schneider, F. Guinea, C. Dekker, M. Barbone, Z. Sun, C. Galiotis, A. N. Grigorenko, G. Konstantatos, A. Kis, M. Katsnelson, L. Vandersypen, A. Loiseau, V. Morandi, D. Neumaier, E. Treossi, V. Pellegrini, M. Polini, A. Tredicucci, G. M. Williams, B. H. Hong, J.-H. Ahn, J. M. Kim, H. Zirath, B. J. van Wees, H. van der Zant, L. Occhipinti, A. D. Matteo, I. A. Kinloch, T. Seyller, E. Quesnel, X. Feng, K. Teo, N. Rupasinghe, P. Hakonen, S. R. T. Neil, Q. Tannock, T. Löfwander, J. Kinaret. Science and technology roadmap for graphene, related two-dimensional crystals, and hybrid systems. *Nanoscale* (2015) 7: 4598–4810. doi:10.1039/c4nr01600a.
- [5] P. Li, B. Zhang, T. Cui. Towards intrinsic graphene biosensor: A label-free, suspended single crystalline graphene sensor for multiplex lung cancer tumor markers detection. *Biosens. Bioelectron.* (2015) 72: 168–174. doi:10.1016/j.bios.2015.05.007.
- [6] H. Arjmandi-Tash, L. A. Belyaeva, G. F. Schneider. Single molecule detection with graphene and other two-dimensional materials: nanopores and beyond. *Chem. Soc. Rev.* (2016) 45: 476–493. doi:10.1039/c5cs00512d.
- [7] A. Cavallin, M. Pozzo, C. Africh, A. Baraldi, E. Vesselli, C. Dri, G. Comelli, R. Larciprete, P. Lacovig, S. Lizzit, D. Alfè. Local electronic structure and density of edge and facet atoms at Rh nanoclusters self-assembled on a graphene template. *ACS Nano* (2012) 6: 3034–3043. doi:10.1021/nn300651s.
- [8] M. Weser, E. N. Voloshina, K. Horn, Y. S. Dedkov. Electronic structure and magnetic properties of the graphene/Fe/Ni (1 1 1) intercalation-like system. *Phys. Chem. Chem. Phys.* (2011) 13: 7534–7539. doi:10.1039/c1cp00014d.
- [9] N. Rougemaille, A. T. N'Diaye, J. Coraux, C. Vo-Van, O. Fruchart, A. K. Schmid. Perpendicular magnetic anisotropy of cobalt films intercalated under graphene. *Appl. Phys. Lett.* (2012) 101: 142403. doi:10.1063/1.4749818.
- [10] T. Abtew, B.-C. Shih, S. Banerjee, P. Zhang. Graphene-ferromagnet interfaces: Hybridization, magnetization and charge transfer. *Nanoscale* (2013) 5: 1902–1909. doi:10.1039/c2nr32972g.
- [11] H. Vita, S. Böttcher, P. Leicht, K. Horn, A. B. Shick, F. Máca. Electronic structure and magnetic properties of cobalt intercalated in graphene on Ir(1 1 1). *Phys. Rev. B* (2014) 90. doi:10.1103/physrevb.90.165432.
- [12] R. Decker, J. Brede, N. Atodiresei, V. Caciuc, S. Blügel, R. Wiesendanger. Atomic-scale magnetism of cobalt-intercalated graphene. *Phys. Rev. B* (2013) 87: 041403. doi:10.1103/physrevb.87.041403.
- [13] S. Yang, M. R. Lohe, K. Müllen, X. Feng. New-generation graphene from electrochemical approaches: Production and applications. *Adv. Mater.* (2016) 28: 6213–6221. doi:10.1002/adma.201505326.



- [14] C. Vo-Van, S. Schumacher, J. Coraux, V. Sessi, O. Fruchart, N. B. Brookes, P. Ohresser, T. Michely. Magnetism of cobalt nanoclusters on graphene on iridium. *Appl. Phys. Lett.* (2011) 99: 142504. doi:10.1063/1.3646480.
- [15] M. Bazarnik, J. Brede, R. Decker, R. Wiesendanger. Tailoring molecular self-assembly of magnetic phthalocyanine molecules on Fe- and Co-intercalated graphene. *ACS Nano* (2013) 7: 11341–11349. doi:10.1021/nn405172q.
- [16] A. R. Rocha, V. M. García-suárez, S. W. Bailey, C. J. Lambert, J. Ferrer, S. Sanvito. Towards molecular spintronics. *Nat. Mater.* (2005) 4: 335–339. doi:10.1038/nmat1349.
- [17] L. Bogani, W. Wernsdorfer. Molecular spintronics using single-molecule magnets. *Nat. Mater.* (2008) 7: 179–186. doi:10.1038/nmat2133.
- [18] J. Bartolomé, C. Monton, I. K. Schuller. Magnetism of metal phthalocyanines. In J. Bartolomé, F. Luis, J. Fernández, (eds.) *NanoScience and Technology* (Springer-Verlag Berlin Heidelberg, 2014). 221–245. doi:10.1007/978-3-642-40609-6\_9.
- [19] P. Gargiani, G. Rossi, R. Biagi, V. Corradini, M. Pedio, S. Fortuna, A. Calzolari, S. Fabris, J. Criginski Cezar, N. B. Brookes, M. G. Betti. Spin and orbital configuration of metal phthalocyanine chains assembled on the Au(110) surface. *Phys. Rev. B* (2013) 87: 165407. doi:10.1103/physrevb.87.165407.
- [20] M. Scardamaglia, S. Lisi, S. Lizzit, A. Baraldi, R. Larciprete, C. Mariani, M. G. Betti. Graphene-induced substrate decoupling and ideal doping of a self-assembled iron-phthalocyanine single layer. *J. Phys. Chem. C* (2013) 117: 3019–3027. doi:10.1021/jp308861b.
- [21] J. Mao, H. Zhang, Y. Jiang, Y. Pan, M. Gao, W. Xiao, H.-J. Gao. Tunability of supramolecular Kagome lattices of magnetic phthalocyanines using graphene-based moiré patterns as templates. *J. Am. Chem. Soc.* (2009) 131: 14136–14137. doi:10.1021/ja904907z.
- [22] G. Löbbert. *Phthalocyanines* (Wiley-VCH Verlag GmbH & Co. KGaA, 2000). doi:10.1002/14356007.a20\_213.
- [23] C. G. Barraclough, R. L. Martin, S. Mitra, R. C. Sherwood. Paramagnetic anisotropy, electronic structure, and ferromagnetism in spin  $s = 3/2$  manganese(II) phthalocyanine. *J. Chem. Phys.* (1970) 53: 1638–1642. doi:10.1063/1.1674236.
- [24] C. G. Barraclough, R. L. Martin, S. Mitra. Diamagnetic anisotropies of metal-free, nickel(II), and zinc(II) phthalocyanines. *J. Chem. Phys.* (1971) 55: 1426–1429. doi:10.1063/1.1676238.
- [25] <http://www.chemtube3d.com/gallery/structurepages/fephthalocyanine.html>. Web Site. ChemTube3D Team, The University of Liverpool.
- [26] S. K. Hämäläinen, M. Stepanova, R. Drost, P. Liljeroth, J. Lahtinen, J. Sainio. Self-assembly of cobalt-phthalocyanine molecules on epitaxial graphene on Ir(111). *J. Phys. Chem. C* (2012) 116: 20433–20437. doi:10.1021/jp306439h.
- [27] S. Lisi, P. Gargiani, M. Scardamaglia, N. B. Brookes, V. Sessi, C. Mariani, M. G. Betti. Graphene-induced magnetic anisotropy of a two-dimensional iron phthalocyanine network. *J. Phys. Chem. Lett.* (2015) 6: 1690–1695. doi:10.1021/acs.jpcclett.5b00260.
- [28] C. F. Hermanns, K. Tarafder, M. Bernien, A. Krüger, Y.-M. Chang, P. M. Oppeneer, W. Kuch. Magnetic coupling of porphyrin molecules through graphene. *Adv. Mater.* (2013) 25: 3473–3477. doi:10.1002/adma.201205275.
- [29] H. Yang, A. D. Vu, A. Hallal, N. Rougemaille, J. Coraux, G. Chen, A. K. Schmid, M. Chshiev. Anatomy and giant enhancement of the perpendicular magnetic anisotropy of cobalt-graphene heterostructures. *Nano Lett.* (2016) 16: 145–151. doi:10.1021/acs.nanolett.5b03392.

- [30] G. Rossi. Spin polarization of the photoelectrons and photon polarization of X-ray absorption: Spectroscopy and magnetometry. In S. Mobilio, F. Boscherini, C. Meneghini, (eds.) *Synchrotron Radiation* (Springer-Verlag Berlin Heidelberg, **2014**), volume 20. 539–570. doi:10.1007/978-3-642-55315-8\_20.
- [31] C. Isvoranu, B. Wang, E. Ataman, J. Knudsen, K. Schulte, J. N. Andersen, M.-L. Bocquet, J. Schnadt. Comparison of the carbonyl and nitrosyl complexes formed by adsorption of CO and NO on monolayers of iron phthalocyanine on Au(111). *J. Phys. Chem. C* (**2011**) 115: 24718–24727. doi:10.1021/jp204461k.
- [32] M. Schmid, J. Zirzmeier, H.-P. Steinrück, J. M. Gottfried. Interfacial interactions of iron(II) tetrapyrrole complexes on Au(111). *J. Phys. Chem. C* (**2011**) 115: 17028–17035. doi:10.1021/jp204524s.
- [33] G. Avvisati, S. Lisi, P. Gargiani, A. Della Pia, O. De Luca, D. Pacilé, C. Cardoso, D. Varsano, D. Prezzi, A. Ferretti, M. G. Betti. FePc adsorption on the moiré superstructure of graphene intercalated with a cobalt layer. *J. Phys. Chem. C* (**2017**) 121: 1639–1647. doi:10.1021/acs.jpcc.6b09875.
- [34] M. C. Biesinger, L. W. Lau, A. R. Gerson, R. S. C. Smart. Resolving surface chemical states in XPS analysis of first row transition metals, oxides and hydroxides: Sc, Ti, V, Cu and Zn. *Appl. Surf. Sci.* (**2010**) 257: 887–898. doi:10.1016/j.apsusc.2010.07.086.
- [35] P. W. Anderson. Antiferromagnetism. Theory of superexchange interaction. *Phys. Rev.* (**1950**) 79: 350–356. doi:10.1103/physrev.79.350.

## Chapter 5

# Dynamics of single- and multi-layer graphene growth on Ir (1 1 1) using Molecular Beam Epitaxy

The next step in my research has been oriented towards another issue which is still open in the research on Gr, *i.e.* the direct growth of Gr on arbitrary surfaces. In fact, while it is possible to synthesize Gr on a metallic surface first and transfer it onto its final one afterwards<sup>1</sup>, this technique has several drawbacks: mainly, the transfer process introduces defects and contaminants into the honeycomb carbon network, leading to a degradation of its performance and to difficulties in its integration with the technologies used in semiconductors industry<sup>2,3</sup>.

For industrial-scale production of Gr, the technique which currently yields the best compromise between cost and quality is CVD. For example, it is possible to directly grow monolayer Gr via CVD on some transition or noble metal surfaces, such as Ni (1 1 1)<sup>4</sup>, Co (0 0 0 1)<sup>5</sup>, Ru (0 0 0 1)<sup>6</sup>, Rh (1 1 1)<sup>7</sup>, Re (0 0 0 1)<sup>8</sup>, Cu (1 1 1)<sup>9</sup>, Ir (1 1 1)<sup>10</sup> and Ir (1 0 0)<sup>11</sup>, and even on some polycrystalline surfaces, such as nickel<sup>12</sup> or copper<sup>13</sup>, with a very high crystalline quality<sup>14</sup>. However, the number of surfaces where this process is successful is quite limited, and not sufficient to cover the requirements of Gr-based nanoelectronics. In fact, Gr-based devices often need to be electrically insulated from their substrate, for example Gr-based Field Effect Transistors, where Gr is used for the channel connecting source and drain and therefore has to be insulated from the gate and from its support<sup>15</sup>. Moreover, in order to integrate Gr-based and traditional electronics, Gr-semiconductor interfaces must be provided<sup>16</sup>.

There are, in particular, several metals or metal surfaces over which CVD growth of Gr has not been successful up to now, such as aluminium<sup>14</sup>. Moreover, CVD growth is possible only at high temperature and with poor yield on noble metals such as Cu and Au, due to the low efficiency these metals have in the catalytic decomposition of the molecular precursors<sup>17</sup>. For this reason, even worse is the situation for semiconductors or insulators: few attempts to grow Gr on such surfaces via CVD have been successful, for example on Ge (1 0 0), yet even there the product has a poor yield and quality and the process requires very high temperature and a long time, which negatively affects the production costs<sup>18,19</sup>. In fact, in order to obtain the decomposition of the gas precursor, the temperature must be high enough to activate the non-catalytic, thermal cracking of the precursor<sup>20</sup>.

On the other hand, an effective technique to grow Gr on such surfaces where CVD cannot be used effectively is Molecular Beam Epitaxy (MBE) from solid carbon sources<sup>21,22</sup>. This process is similar to CVD, yet the origin of the carbon feedstock is different, as carbon is evaporated from an annealed high-purity graphite rod and deposited on the substrate. The two methods are schematically compared in Figure 5.1.

The effectiveness of this technique on surfaces where CVD is not possible can be attributed to several factors within the atomic mechanism of the Gr flakes' nucleation and accretion process: for example, to the fact that it does not involve any hydrocarbon decomposition reaction, or to the different carbon species which are deposited on the surface and which feed the nucleation and growth of Gr. This technique, therefore, has been successfully used to directly grow Gr on several semiconductor or insulator

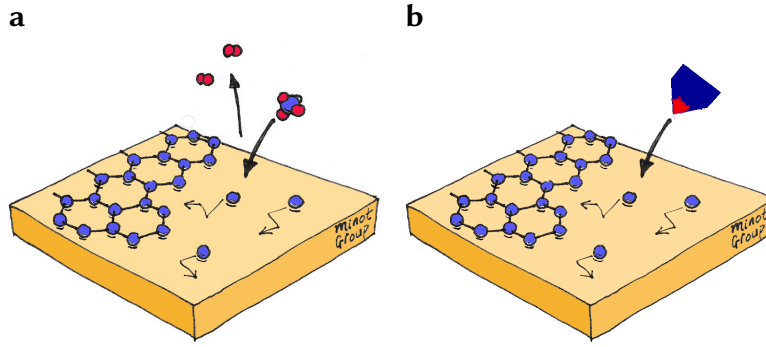


**Figure 5.1:** Schematic comparison of the CVD (a) and MBE (b) Gr growth process<sup>23</sup>.

surfaces<sup>3,24</sup>, allowing it to be used in nanoelectronic applications, where transferred CVD Gr cannot yet be used effectively<sup>25,26</sup>. However, this technique is not yet able to produce very high quality Gr. For example, MBE-grown Gr on Ge(001) is characterized by translational and rotational domains at most as wide as 1  $\mu\text{m}$ , which is not sufficient for high-tech applications<sup>19</sup>. Furthermore, unlike CVD, MBE is not self-terminating and therefore regions of bi- and multi-layer Gr can be found<sup>27</sup>.

As part of my PhD research project, I investigated the dynamics of MBE Gr growth, in order to identify the degrees of freedom which could be most effectively exploited to improve the MBE growth of Gr. Therefore, my work has been divided in different phases: in the first one, I have identified the elementary building blocks feeding the growth of Gr, following which I have studied the dynamics of the flakes' nucleation and growth. In fact, these are both key factors influencing the growth process and their understanding is a key step towards the optimization of the growth conditions for Gr on different substrates<sup>28,29</sup>. In order to highlight the most relevant differences between this technique and CVD, I have chosen as a substrate for my experiments the Ir(1 1 1) surface, where the individual phases of the CVD growth process are already well known<sup>30</sup>.

## 5.1 Characterisation of the feedstock delivered by the solid state carbon source

The first step in my investigation of the MBE growth of Gr has been the identification of the building blocks which participate in the nucleation and accretion of the Gr flakes. In fact, different species of carbon clusters formed by a small number of atoms are known to play an important role in determining the atomistic mechanisms for the CVD growth of Gr on different surfaces<sup>29</sup>. In particular, theoretical calculations have identified three main groups of metal surfaces, characterized by a different degree of reactivity towards carbon, where the most stable species formed by deposited C atoms can be either monomers ( $\text{C}_1$ ) or dimers ( $\text{C}_2$ ) adsorbed on the surface, or subsurface species<sup>31</sup>. For example, C monomers are predicted to be essential for the growth of the Gr islands on Ir(1 1 1) both through direct attachment to the Gr edges and through the formation and attachment of larger C clusters<sup>32</sup>. Indeed, C monomers have been identified as the final product of the dehydrogenation of gas precursors such as ethylene, commonly used in the CVD growth of Gr on Ir(1 1 1)<sup>30</sup>. On the other hand, dimers can also play an important role in the synthesis of Gr monolayers characterized by high crystalline quality, *i.e.* by a low density of defects<sup>33</sup>. While calculations have shown that the concentration and diffusion of dimers control the growth of Gr flakes on noble metals such as Cu<sup>34,35</sup>, it has been predicted that the formation of dimers is thermodynamically hindered on flat surfaces of transition metals characterized by a large C-metal bond strength, such as Ir and Ru<sup>32</sup>. Nevertheless, an important role played by dimers has been experimentally observed also in the case of Gr growth on stepped Ru(0 0 1)<sup>36,37</sup>, Ni(1 1 1)<sup>38,39</sup>, Co(0 0 1)<sup>40,41</sup> and even for CuNi surface alloys<sup>42</sup>, despite their formation being thermodynamically unfavourable on flat terraces.

While most of these studies on the role of C monomers and dimers were performed during CVD growth,

for the case of MBE the fundamental processes leading to the formation of Gr from carbon monomers and dimers does not significantly differ from the former case: however, being the origin of the carbon feedstock different, its composition may significantly vary from that observed during CVD. In particular, the species deposited on the surface depend on the characteristics of the molecular beam, such as the conditions used for the evaporation of carbon from the solid state target. Moreover, in addition to the species which are directly deposited on the surface by the molecular beam, different types of clusters can be generated on the surface by associative or dissociative reactions between those, which are known to occur in particular in defective sites such as step edges<sup>32,36</sup>.

One of the main issues when studying the composition of the adsorbed precursors of Gr is that the detection of carbon monomers using spectroscopy techniques is rather challenging due to their low concentration, while their direct observation with microscopy-based techniques is complicated by their high mobility: for this reason, their concentration has often been indirectly studied by low energy electron microscopy, by evaluating changes in the electron reflectivity of the substrate<sup>28</sup>. Moreover, as their diffusion barrier is quite low<sup>36</sup>, they can rapidly diffuse and attach to step edges at the temperatures typically employed for high-quality Gr growth. For the same reason, their concentration is typically of the order of few percent of monolayer, so a high sensitivity towards carbon is needed. In order to overcome these problems and produce a high density of C monomers and dimers in a stable configuration on the Ir (1 1 1) surface, we made the first carbon depositions at low temperature ( $T = 80$  K). As discussed below, this method allowed us to characterize the carbon source by producing several C species that we could reveal and characterize by means of high energy-resolution core level photoelectron spectroscopy. The identification of these species based on their C 1s core level BE was assisted by DFT calculations, performed by the group of Prof. Kantorovich at King's College London.

### 5.1.1 Experimental details and data analysis procedure

The experiment was performed by evaporating different amounts of carbon on the Ir (1 1 1) surface at  $T = 80$  K, by employing electron-beam bombardment on a high-purity graphite rod placed 80 mm from the sample surface. The carbon flux at the sample was estimated to be about 0.007 ML/s. The sample was kept at this temperature during all measurements, in order to reduce the vibrational broadening, enhancing the possibility of distinguishing different components, as well as to ensure that the C species were immobile during the whole experiment due to their thermal energy being low with respect to their diffusion and reaction barriers.

In order to reduce as much as possible the lateral interaction between nearby C clusters, we chose to deposit an amount of carbon well below the monolayer, therefore the deposition times ranged between tens of seconds and a few minutes. The carbon coverage was calculated by comparing the C 1s photoemission intensity with the one measured for a single layer of Gr on Ir (1 1 1) ( $3.87 \times 10^{15}$  atoms/cm<sup>2</sup> = 2.47 ML). C 1s and Ir 4f<sub>7/2</sub> core level spectra were acquired after each C deposition at a photon energy  $h\nu = 400$  eV and 200 eV, respectively, and at normal emission.

Due to the complex structure of the measured C 1s spectra, which require several photoemission components for fitting (a representative example is shown in Figure 5.6), the data analysis was performed in several steps, by releasing the fit parameters one at a time after an initial guess. As some of the fit parameters are correlated (such as the parameters describing the line-shape of each component), in order to estimate the confidence region for each parameter, the fit was repeated several times, each by releasing a different parameter, by sampling an area in the parameter space, and evaluating the presence of localized minima of the fit's  $\chi^2$  parameter, following the approach described in Chapter 3.1.1.

The number and C 1s core level BEs of the different components were initially obtained from DFT calculations, where the preferred adsorption configurations and formation energies of carbon clusters of different sizes were calculated. In particular, we analysed clusters ranging from monomers (C<sub>1</sub>) to pentamers (C<sub>5</sub>) (Figure 5.3): for all the stable structures thus identified, also the C 1s core level BEs were calculated (as reported in Table 5.1). It is important to point out that these calculations, which include final state effects, do not provide an absolute value for the core level BEs, but only relative shifts. For this reason, the fit was initially performed by keeping the BE shifts between the different components fixed,

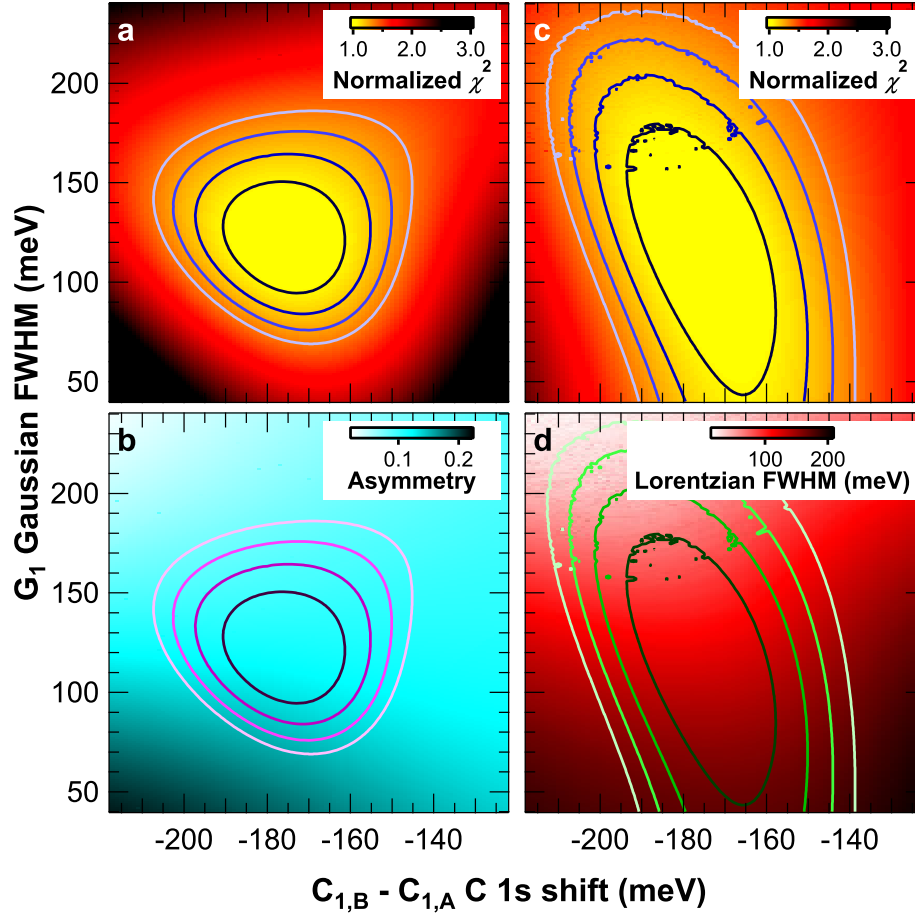


**Figure 5.2:** Data analysis of the M region of the C 1s spectrum corresponding to 0.11 ML carbon on Ir(1 1 1), shown in Figure 5.6b. a-b: Confidence region (a) and best fit of the asymmetry parameter  $\alpha$  (b) sampled in the space of parameters spanned by  $G$  and the shift  $\Delta E_{C_1}$  between the C 1s BEs of  $C_{1,B}$  and  $C_{1,A}$ , for parameter  $L$  fixed. c-d: Confidence region (c) and best fit of the Lorentzian FWHM parameter  $L$  (d) sampled in the space of parameters spanned by the  $C_1$  Gaussian FWHM  $G_1$  and  $\Delta E_{C_1}$ , for fixed  $\alpha$ .

while the energy scale was allowed to rigidly translate. In particular, we expressed the C 1s BEs of all other components in terms of their shift from that of the configuration which was predicted to be most stable in our system, *i.e.* monomers in an HCP adsorption site (denoted in Figure 5.3 as  $C_{1,A}$ ).

Furthermore, due to the number of components used in the fit, it was not possible to reliably obtain the line-shape for each component from the fit. Therefore, we made some assumptions on the parameters, based on their physical meaning. In particular, we imposed the  $L$  parameter controlling the Lorentzian broadening of the line-shape to be the same for all components, as it depends on the relaxation time of the core-hole of the photoemission process, which is not expected to be significantly different for the various carbon species. Likewise, we do not expect the Gaussian broadening to be significantly affected by the adsorption site, so we kept  $G_1$  equal for monomers adsorbed in different sites. However, the Gaussian broadening does depend on low-energy excitations such as vibrational modes<sup>43</sup>, therefore the larger C clusters can have a larger Gaussian broadening than monomers. For this reason, we allowed the components assigned by theory to  $C_2$  and larger clusters to have a  $G$  parameter different from monomers. Due to the wider line-shape and smaller BE differences affecting the components originated by dimers and trimers, these were constrained to all have the same  $G$  parameter, even though different from the compo-

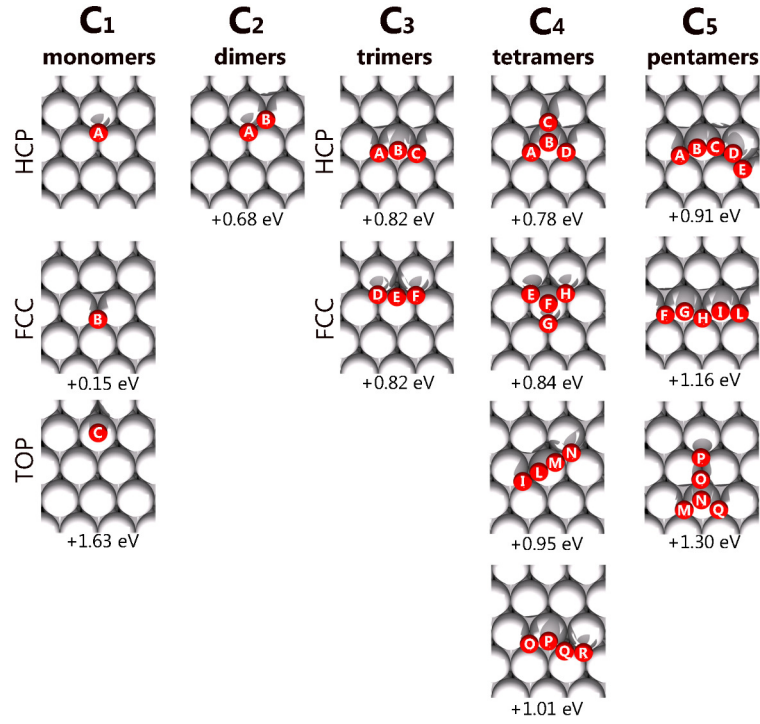


**Figure 5.3:** Theoretically calculated stable adsorption configurations for carbon monomers and clusters, up to 5 atoms in size. The formation energy, relative to the most stable configuration, *i.e.* C<sub>1,A</sub>, is reported for each species.

	C <sub>1</sub>	C <sub>2</sub>	C <sub>3</sub>	C <sub>4</sub>	C <sub>5</sub>
A	0	+0.650	+0.920	+0.727	+0.745
B	-0.120	+0.510	+0.370	+0.152	+0.351
C	+0.110		+0.920	+1.022	+1.486
D			+0.780	+0.543	+0.310
E			+0.190	+0.609	+0.559
F			+0.780	+1.514	+0.680
G				+0.614	+1.908
H				+0.614	+1.270
I				+0.773	+0.675
L				+1.488	+0.681
M				+0.773	+0.828
N				+0.773	+0.366
O				+0.890	+0.343
P				+0.679	+0.164
Q				+0.651	+0.797
R				+0.972	

**Table 5.1:** Theoretically calculated C 1s core level shifts for the C monomers (C<sub>1</sub>) and small clusters (C<sub>2-5</sub>) shown in Figure 5.3

nents associated to C<sub>1</sub> species. Finally, the asymmetry parameter was kept equal for all parameters, as the correlation between the asymmetry parameter of the different components did not allow to reliably obtain one individual value for each species.

The next step in our data analysis was to verify the compatibility of the core level BE shifts provided by theory with the experimental results. To this aim, we started our analysis on the data acquired for the lowest coverage (see Figure 5.6b), where we expected to find only a few C species on the surface, namely single C<sub>1</sub> adatoms or very small clusters, such as C<sub>2</sub> dimers and C<sub>3</sub> trimers. In the first step of our analysis, we determined the line-shape of the components within the M double peak and therefore the BE

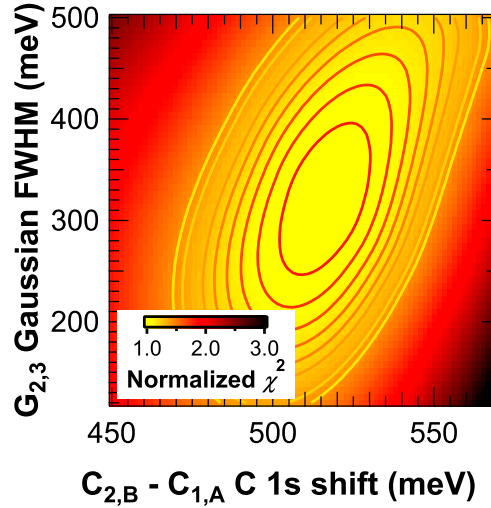


**Figure 5.4:** Data analysis of the C 1s spectrum corresponding to 0.11 ML carbon on Ir(1 1 1), shown in Figure 5.6b: confidence region sampled in the space of parameters spanned by the Gaussian of the C<sub>2</sub> and C<sub>3</sub> species,  $G_{2,3}$ , and the core level shift  $\Delta E_{C_{2,3},C_1}$  between  $C_{2,B}$  and  $C_{1,A}$ .

shift between monomers adsorbed in FCC and HCP sites  $\Delta E_{C_1}$ . This was done by analysing the region of minimum  $\chi^2$  of the fit while ranging step by step the Gaussian parameter  $G_1$  around an initial guess and the CLS around the theoretically calculated value. We repeated this procedure twice, allowing first the asymmetry parameter  $\alpha$  (Figures 5.2a and b) and then the Lorentzian FWHM  $L$  (Figures 5.2c and d), one at a time, to relax for each point in the parameter space explored.

Following this, we repeated this procedure to determine the line-shape and CLS for the D region of the spectrum where, according to the theoretical results (Table 5.1), the spectral intensity is originated by the dimers and trimers. A further constraint was used by fixing the intensity of those components arising from different atoms belonging to the same structure to be the same, such as the two components generated by each atom in the dimer. Moreover, since the deconvolution of these components cannot be easily performed due to their small CLSs (as pointed out in the calculations), we decided to fix their relative shifts to the theoretically calculated values, only refining the BE shift between all of them and our reference (the monomers in HCP sites),  $\Delta E_{C_{2,3},C_1}$ . The deconvoluted components originated by each atom in each structure are shown in Figure 5.6b. We then monitored the evolution of the  $\chi^2$  as a function of this Gaussian FWHM  $G_{2,3}$  and of  $\Delta E_{C_{2,3},C_1}$ . The image plot of the  $\chi^2$  minimum is reported in Figure 5.4.

Finally, for the spectra acquired at higher C coverage, it was necessary to take into account also larger clusters, namely tetramers and pentamers, to correctly describe the experimental data. The first step in the analysis of these spectra was to introduce only one type of tetramer or pentamer, with a free Gaussian component  $G_{4,5}$ , still keeping  $L$  and  $\alpha$  at the value found for the lower coverage spectrum. Only then we added new species in order to minimize the  $\chi^2$ , one at a time, until the fit residual was no longer showing an appreciable modulation.

### 5.1.2 Theoretical results

The stable structures formed by C on Ir(1 1 1) are reported in Figure 5.3. In particular, carbon adatoms ( $C_1$ ) can adsorb in three configurations: top and three-fold hollow, which can be either FCC or HCP; the bridge site, instead, is energetically unstable and relaxes to the hollow sites. The most favourable adsorption site is HCP, with an energy gain of 0.15 eV with respect to the FCC, while the top site is considerably less stable. Carbon dimers ( $C_2$ ) are only stable when their two C atoms (which have a C-C bond length of 1.38 Å) are placed in FCC and HCP adsorption sites respectively ( $C_{2,A}$  and  $C_{2,B}$ ). Finally, the most stable adsorption sites for C trimers ( $C_3$ ) are those with an almost linear atomic arrangement, whose central atoms are placed close to either FCC ( $C_{3,B}$ ) or HCP ( $C_{3,E}$ ) sites, but slightly out of axis, being



displaced toward the nearest-neighbour first layer Ir atom. The two C atoms placed at the edges in each trimer are instead both in HCP ( $C_{3,A}$  and  $C_{3,C}$ ) or FCC sites ( $C_{3,D}$  and  $C_{3,F}$ ), respectively.

### 5.1.3 Experimental results

#### Analysis of the Ir $4f_{7/2}$ spectra

In order to obtain a preliminary information of the local carbon atom configuration on the Ir (1 1 1) surface, we decided to start our data analysis from the Ir  $4f_{7/2}$  spectra, by examining the variations of the electronic structure of substrate Ir atoms induced by adsorbed C atoms. The Ir  $4f_{7/2}$  spectra of the sample as cleaned (a) and after deposition of different doses of carbon at 80 K (b-d) are displayed in Figure 5.5. The spectrum corresponding to the clean Ir (1 1 1) surface (Figure 5.5a) can be fitted with two components, as reported in literature<sup>44</sup>: the higher BE component, at 60.85 eV, originates from subsurface and deeper layers, while the lower BE peak S0, shifted by  $-550 \pm 10$  meV with respect to the bulk peak, originates from the topmost Ir atoms. A two component analysis gives best fit values for  $L$ ,  $\alpha$  and  $G$  parameters respectively

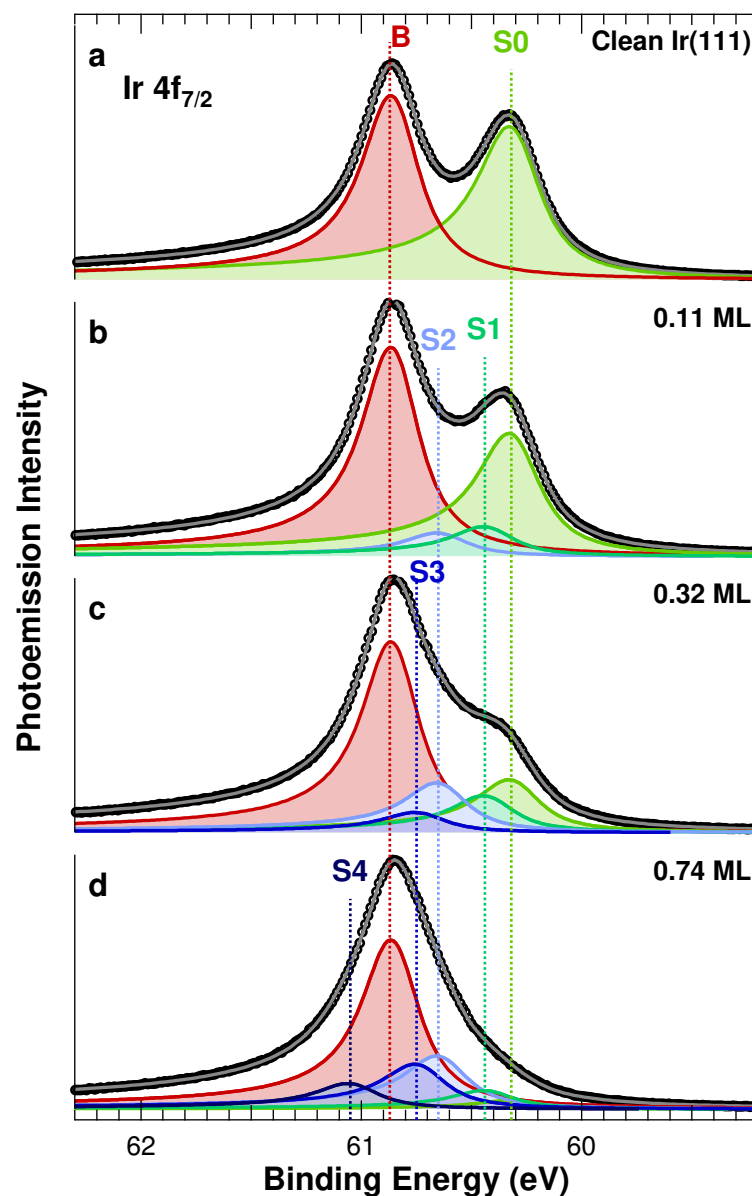


**Figure 5.5:** Ir  $4f_{7/2}$  photoemission spectra ( $h\nu = 200$  eV) of clean Ir (1 1 1) (a) and after deposition of 0.11 ML (b), 0.32 ML (c) and 0.74 ML (d) of carbon at 80 K.

of 0.25 eV, 0.10, and 0.10 eV for the bulk, and 0.25 eV, 0.17, and 0.12 eV for the surface component.

To describe the effect of the adsorbates on the surface Ir atoms, we employed a model which has proved effective in several works studying atomic adsorbates on transition metal surfaces with photoemission spectroscopy. In this model, additional components are used each to describe surface atoms bonded to a different number of adsorbate atoms: so there will be one component originated by surface atoms bonded to a single adsorbate, one for atoms bonded to two adsorbate atoms, and so on<sup>45–48</sup>. These components will be shifted from the one generated by the clean surface by a shift increasing with the number of adsorbates, and this increase often shows an approximately linear behaviour<sup>45,46</sup>. Clearly, this is a naïve model and for our system it is oversimplified, as it only considers the number of C atoms coordinated with Ir atoms, while possible differences in the local geometry are not taken into account. For example, within this approach, the adsorption of two C monomers next to each other would result in the same surface CLS as a single carbon dimer. Besides coordination, C atoms can occupy a large variety of slightly different positions relative to the Ir surface, resulting in a broader distribution of BEs. For these reasons, it is not possible to identify in an unambiguous way a relationship between surface core level shifted components and non-equivalent Ir atoms. Nevertheless, we believe that this approach can provide, at least qualitatively, a good starting point to understand the types of carbon structures present on the surface, which will be better understood by the subsequent analysis of the C 1s core level.

The low carbon coverage of 0.11 ML (Figure 5.5b) leads to the appearance of two additional core level shifted components, S1 and S2, shifted by  $-430 \pm 20$  meV and  $-220 \pm 20$  meV with respect to the bulk component, while the original S0 surface peak intensity decreases. Upon increasing the C coverage (0.32 ML spectrum, Figure 5.5c), we observe a further decrease of S0, accompanied by the growth of a third carbon-induced surface component, S3, at a BE close to that of the bulk component ( $-120 \pm 20$  meV). Finally, in order to properly fit the 0.74 ML spectrum (Figure 5.5d), a new component, with a positive surface CLSs ( $180 \pm 20$  meV), needs to be included. Although the different components cannot be unambiguously assigned to specific cluster configurations, the trend observed, according to our model, shows a progressive increase in the coordination of the first-layer Ir atoms with C atoms. This indicates that at the highest coverage the system is formed by a large number of different and contiguous C clusters placed in non-equivalent configurations. On the basis of these results we decided to focus the C 1s core level analysis only on the two low coverage systems we have prepared, namely 0.11 and 0.32 ML.

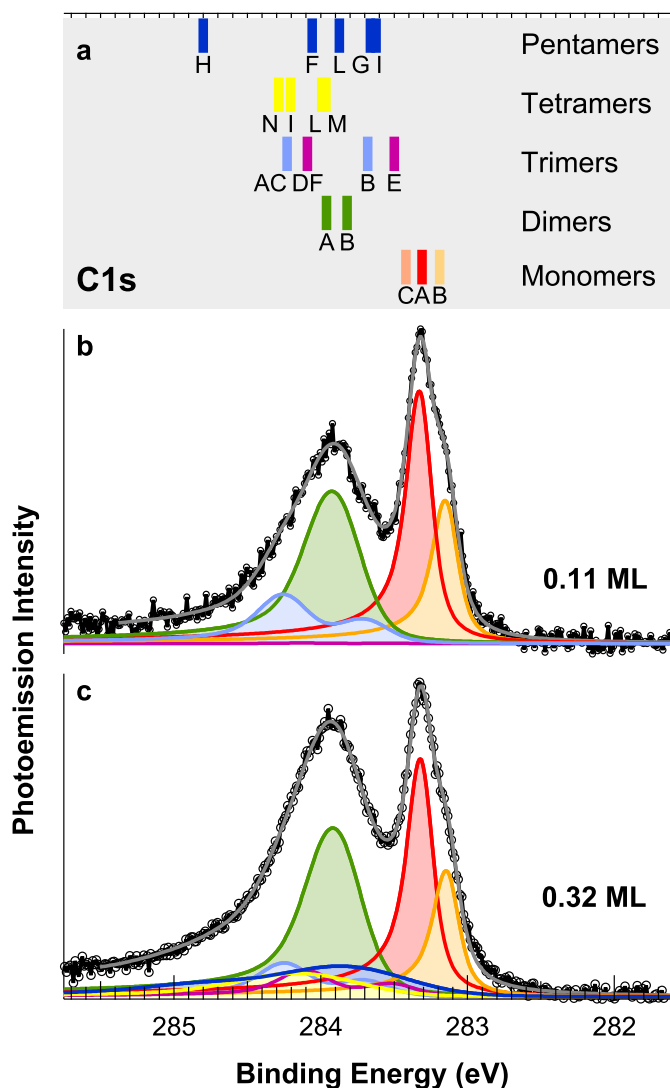
### Analysis of the C 1s spectra

Figure 5.6b shows the C 1s data acquired for the lowest coverage, where we expected to find only a few C species on the surface, namely single C<sub>1</sub> adatoms or very small clusters, such as C<sub>2</sub> dimers and C<sub>3</sub> trimers. The calculated C 1s CLSs suggest that the C monomers are the surface species with the lowest C 1s BEs, and therefore could originate the narrow spectral components in the range between 283.5 and 283 eV, as indicated in Figure 5.6a. Using the procedure described in section 5.1.1, we found a CLS of  $-170 \pm 20$  meV between monomers adsorbed in HCP and FCC (see Figure 5.2d), which is in quite good agreement with the theoretically calculated value of  $-120$  meV. Likewise, the analysis of the confidence region for the BE shift of the larger clusters (see Figure 5.4) reveals that the CLS experimental results are consistent with the theoretically calculated values to within 50 meV. The best line-shape parameters we found are  $L = 120$  meV,  $\alpha = 0.117$ , while the Gaussian values were  $G_1 = 120$  meV and  $G_{2,3} = 316$  meV for monomers and dimers/trimers, respectively.

The fitting residual, which shows no appreciable modulations, suggests that this system is composed by clusters formed by at most three atoms. The intensity of the different components provides the coverage of monomers (in HCP and FCC adsorption sites), dimers and trimers (see Table 5.2).

The same procedure was applied to the C 1s spectrum acquired at higher coverage (0.32 ML), shown in Figure 5.6c. However, in this spectrum, a high BE shoulder can be seen at about 284.7 eV: according to the DFT calculations, this can only be justified by assuming that C<sub>4</sub> and C<sub>5</sub> species are present on the surface.

Following the procedure previously described, the best agreement was achieved by including tetramers formed by C<sub>4,I</sub>, C<sub>4,L</sub>, C<sub>4,M</sub> and C<sub>4,N</sub> (as labelled in Figure 5.3). The further addition of pentamers with C atoms arranged in a linear fashion allowed to properly reproduce the experimental data. While it is not



**Figure 5.6:** Deconvoluted C 1s spectra of b: 0.11 ML and c: 0.32 ML carbon deposited at 80 K on Ir(111) ( $h\nu = 400$  eV). a: Theoretically calculated C 1s core level BEs of different  $C_N$  species (as labelled in Figure 5.3).

possible to draw a clear-cut picture about the concentration of the different  $C_4$  and  $C_5$  species, our results unambiguously show that the 0.32 ML coverage structure cannot be described by including just monomers, dimers and trimers, as was the case for the lowest coverage spectrum. Owing to this behaviour and to the results of the Ir  $4f_{7/2}$  analysis described above, we did not make any fitting of the 0.74 ML spectrum, shown in Figure 5.8c. Nevertheless, this spectrum is consistent with our findings, as it displays an increased spectral intensity toward higher BEs, where we expect to have, besides the C dimers at 284.8 eV, also larger C clusters.

#### 5.1.4 Discussion

The analysis of the coverage of the different species obtained after low temperature deposition provides an interesting information about the building blocks of Gr in MBE. As reported in Table 5.2 the deposition of 0.11 ML at  $T = 80$  K results in the formation of 0.037 ML, 0.021 ML, and 0.040 ML of monomers HCP, monomers FCC and dimers, respectively, and with 0.016 ML of trimers.

We compared these results with those obtained using a random deposition model, in which C atoms are randomly distributed on the (111) surface, with the possibility of occupying with equal probability HCP and FCC three-fold sites and with the assumption that, when sitting in neighbouring three-fold sites, they form a dimer. Besides the experimentally observed strong preference for the occupation of HCP

	C <sub>1</sub> -HCP	C <sub>1</sub> -FCC	C <sub>2</sub>	C <sub>3</sub> -HCP	C <sub>3</sub> -FCC	others	total
experiment	0.037 (32.5%)	0.021 (18.5%)	0.040 (35%)	0.016 (14%)	0	0	0.114
random deposition model	0.0478 (42%)	0.0478 (42%)	0.0154 (13.5%)	0.0012 (1%)	0.0012 (1%)	0.0006 (0.5%)	0.114

**Table 5.2:** Coverage (ML) of carbon monomers and clusters measured on the surface and obtained from a random deposition model. The relative amount of each species with respect to the total C coverage is also reported.

sites in comparison with that for FCC sites, which is in agreement with our theoretical findings, the main difference between experimental and theoretical results is found in the relative populations of dimers and monomers. In fact, the experimental occupation of C atoms in the dimer configuration (35%) is much larger than the value obtained with the random deposition model calculation (13.5%).

This discrepancy could be explained as due to:

1. thermal diffusion of C adatoms on the surface (that effect was not included in our random deposition model) with subsequent formation of dimers already at low temperature, or
2. deposition of C dimers on the surface originating directly from the graphite rod in the sublimation process.

However, the first hypothesis can be disregarded since C dimers are energetically unfavourable with respect to C monomers by 0.68 eV (Figure 5.3 and ref<sup>30</sup>).

In order to support the second hypothesis about the formation of different C species, we have performed Nudged Elastic Band (NEB) monomer and dimer detachment calculations on graphite with different initial state geometries. In particular, we considered a graphite surface showing zigzag (Figure 5.7a) or armchair monoatomic step edges (Figure 5.7b), both of which have been experimentally found in Scanning Tunnelling Microscopy measurements on highly oriented pyrolytic graphite<sup>49</sup>. In these defective sites the C atoms have to break a smaller number of bonds with respect to the  $sp^2$  inner C atoms configuration. For both edge configurations we calculated the energy barrier of the processes in which either a monomer or dimer was removed. It is clear that the detachment mechanism showing the lowest barrier ( $E_{\text{barrier}} = 8.36$  eV) is the removal of a dimer from a zigzag edge.

These results are in agreement with what was observed experimentally, for instance in high temperature transmission electron microscopy measurements<sup>50</sup>. While we believe that several others local defective configurations can be present on the graphite rod surface, our results suggest that the sublimation process in our carbon source produces dimers which are directly deposited on the surface and, at low temperature, do not decompose to the most stable configuration, *i.e.* monomers.

The presence of this metastable species on the surface is a difference with respect to what is observed in the CVD growth of Gr<sup>30</sup>. My next step in the investigation of the MBE growth of Gr was therefore to verify the evolution of the species obtained from the low temperature deposition, in order to understand whether the dimers play an active role in the nucleation and growth of Gr or whether at higher temperature

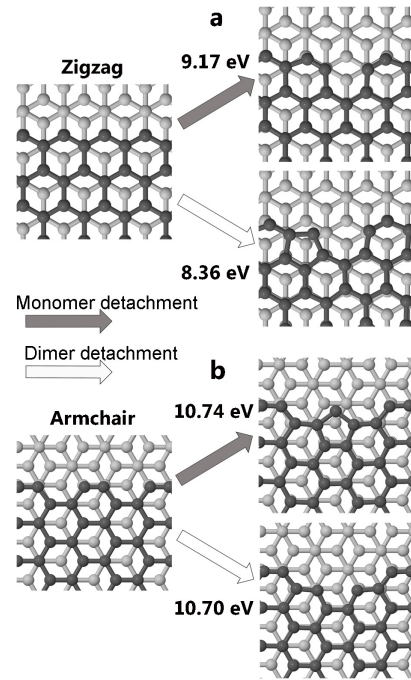


**Figure 5.7:** Initial (left) and final (right) geometrical configurations in NEB calculations for the sublimation of carbon monomers (dark arrow) and dimers (white arrow) from zigzag (a) and armchair (b) graphite edges. Corresponding energy barriers are also reported.

they are decomposed to monomers, leading to the same situation found in CVD after the precursor's dehydrogenation.

## 5.2 Dynamics of temperature-programmed MBE graphene growth

Following the characterisation of the carbon species deposited on the Ir (1 1 1) surface at low temperature, which indicated that both monomers and small C clusters (in particular, dimers) were produced by the C source, our next step in the investigation of the mechanisms leading to Gr growth by MBE was to study the effect of temperature on the species adsorbed on the surface. To this purpose, after each C deposition, we annealed the sample to increasing temperatures. The spectra measured after each annealing step are reported in Figure 5.8.

For the analysis of these data, a quantitative analysis like the one performed for the low temperature spectra was not possible, due to the presence of a large number of overlapping components. However, a qualitative analysis can still provide valuable information about the type of processes involved and the temperature range at which they are occurring.

In the two low-coverage systems (Figures 5.8a and b), the first phase of the evolution of the system occurs after annealing to about 300 K, and is characterized by an increase in the spectral weight of the M component with respect of the D component. According to the results obtained in Section 5.1, this indicates an increase in the density of C monomers with respect to that of small  $C_N$  clusters, which is in agreement with the fact that on Ir (1 1 1) monomers are thermodynamically more stable than small clusters.

However, the situation changes again when the temperature is increased to about 370 K: at this point,

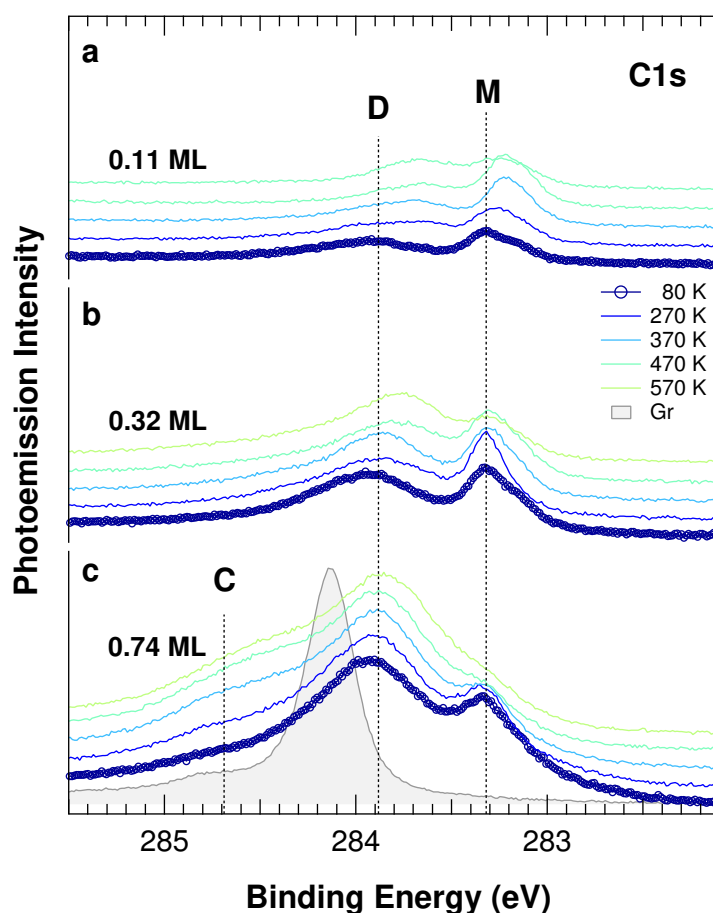


**Figure 5.8:** C1s spectra ( $h\nu = 400$  eV) acquired after deposition of: c – 0.74 ML, b – 0.32 ML and a – 0.11 ML carbon at 80 K on Ir (1 1 1) and subsequent annealing to higher temperatures. For the highest coverage deposition (c), the spectrum obtained after an annealing to 1400 K, leading to Gr formation, is also shown.

the intensity of the M component in the spectrum begins instead to decrease, while new components appear close to the D component. For increasing temperature, the D component moves towards lower BE, while the M component progressively vanishes, a process which is completed around 600 K.

Slightly different is the case of the high-coverage deposition (Figure 5.8c), where the initial increase in the monomer's density is not observed. This can be attributed to the fact that at such a high coverage, at least in some regions, most surface sites are occupied, in such a way that the adsorption dynamics are no longer those of isolated adsorbates, but must also take into account the lateral interactions and the formation of larger clusters.

These results show that, for all the coverages investigated, a full conversion of dimers to monomers, even though thermodynamically favoured, is never achieved. Therefore, both monomers and carbon clusters such as dimers compose the carbon feedstock from which Gr grows, and the growth dynamics will be in general different from those of CVD growth, where the feedstock only consists of monomers<sup>30</sup>.

### 5.3 Dynamics of high-temperature MBE graphene growth

The experiments performed up to now correspond to a Temperature Programmed Growth approach for Gr synthesis, where the precursor is first deposited at lower temperature, and then annealed at higher temperature to promote Gr growth (this process often consists of repeated cycles, as described in Section 2.1). However, another option for both the CVD and MBE process is High Temperature Growth, where the surface is exposed to the precursor at a temperature which is already sufficient for Gr growth. Depending on the substrate, either of these techniques can lead to the highest quality product<sup>51–54</sup>. CVD growth of Gr on Ir(1 1 1) is commonly carried out with both techniques, with the former usually leading to a single crystalline orientation, yet with a higher density of defects, while the latter leads to domains larger on average, yet leads to rotational domains not aligned to the substrate unless very high growth temperatures are employed<sup>52,55</sup>.

We have therefore extended our study on the MBE growth of Gr to the Constant Temperature Growth: this approach also has the advantage that it allows to study the dynamics of the flakes' accretion process in real time, in particular at the high-coverage limit. This is a very important step in the growth process, because at the end the metal surface directly exposed to the precursor is very limited, often consisting of 0D or 1D defects, which might not provide sufficient suitable adsorption sites for the precursor to adsorb. This issue can lead to an incomplete Gr coverage, and the resulting uncovered areas and vacancies, besides lowering the electron mobility, represent a weak point from which Gr can be attacked by reactive species<sup>56</sup>. On the other hand, on several substrate including Ir(1 1 1), a second layer may form in some regions, especially at high precursor flux<sup>27,57</sup>. For these reasons, a good understanding of the dynamics of the last phases of the growth process is needed to ensure that the growth conditions lead to Gr with a controlled number of layers and a low density of defects.

To improve our understanding on the growth dynamics of MBE, I have compared the growth rate of Gr during an MBE and constant temperature CVD growth performed on Ir(1 1 1) at the same temperature, as a function of the carbon coverage. My experiments show that while CVD growth is self-terminating as its growth rate is proportional to the uncovered metal surface, the MBE growth rate has a more complex dependence on coverage which is controlled by the interaction between the carbon feedstock and the growing Gr flakes. This more complex kind of interaction can be exploited to obtain a multilayer growth of Gr on this surface. These results show that the interaction of Gr with atomic and molecular adsorbates, which I have described in Chapter 3, plays an important role already in determining the growth process of Gr on metallic surfaces.

#### 5.3.1 Experimental details and data analysis procedure

Both the CVD and MBE growth were performed at a temperature of 1200 K, which is known to result in the formation of a high-quality Gr layer<sup>29</sup>. For the CVD growth, we performed several experiments by exposing the sample to different pressures of C<sub>2</sub>H<sub>4</sub>, ranging from  $1 \times 10^{-9}$  mbar to  $1 \times 10^{-7}$  mbar. The MBE

growth was carried out with the same graphite rod evaporation conditions used for the low-temperature characterisation previously described. In order to be able to compare the two different methods, it was necessary to correctly align the reaction coordinate for the two experiments, namely the atomic C flux on the sample and the exposure of the surface to the gas precursor, respectively. This was achieved by calculating an effective exposure coordinate for the carbon deposition experiment, obtained by multiplying the deposition time of the MBE experiment by a factor such as to obtain an overlap of the C 1s photoemission signal at the early stage of the Gr growth with that of the CVD growth. In particular, this factor was calculated by imposing a matching of the first derivatives of the photoemission intensity curves with respect to the exposure coordinate. This strategy is based on the approximation that at the early stage of Gr nucleation (i.e. in the very low coverage regime, below 0.1 ML) the change in the coverage depends mainly on the C supply rate (either from  $C_2H_4$  molecules or from monomers/dimers originated by the source) and not by the specific structures present on the surface<sup>28,29</sup>.

The growth process was followed by real-time C 1s core level spectroscopy; this was performed in sweep mode with a sampling rate of about 25 s/spectrum. After each growth, both the Ir  $4f_{7/2}$  and C 1s core levels were acquired at both 1200 K and room temperature. These high resolution spectra were used for calculating the total coverage of Gr.

In order to quantitatively determine the evolution of the different species at different C coverages we

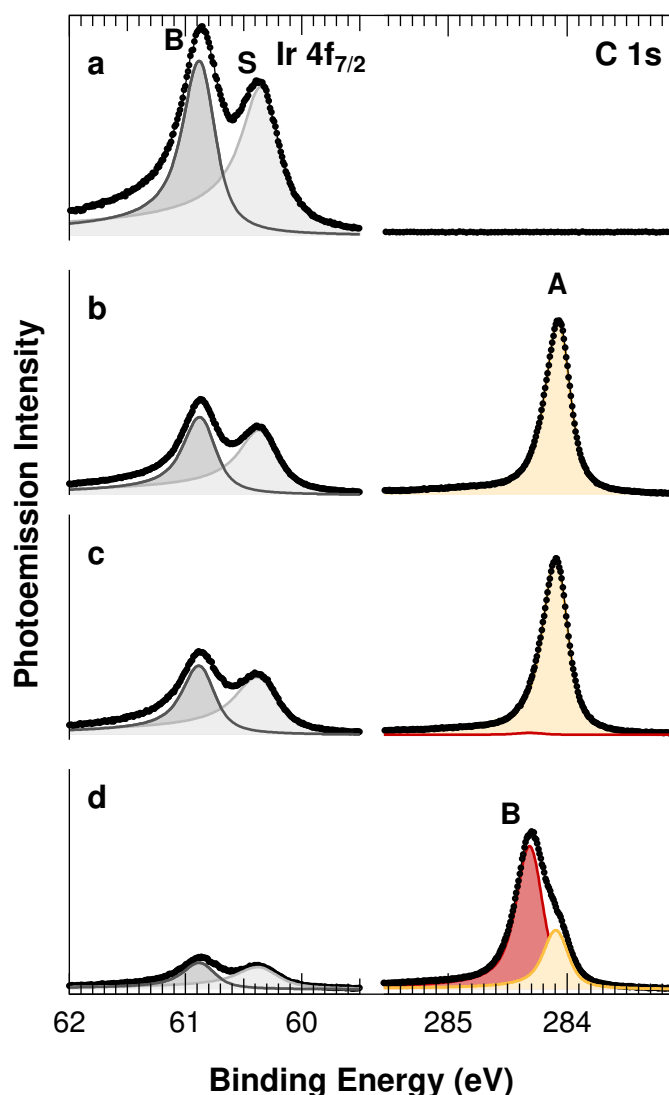


**Figure 5.9:** Ir  $4f_{7/2}$  (left;  $h\nu = 200$  eV) and C 1s (right;  $h\nu = 400$  eV) spectra acquired a: on clean Ir (1 1 1), and after b: CVD growth of a full monolayer Gr, c: MBE growth of a single monolayer Gr, and d: growth of multilayer Gr.



have fitted the C 1s spectra in two steps. The low-coverage spectra (Figure 5.9c) were analysed first, using a single component (A – orange peak) at a BE of 284.15 eV: a good fit was obtained using a DS line-shape similar to that of a complete Gr layer on Ir(1 1 1), described in Section 2.1 ( $L = 201$  meV,  $G = 182$  meV,  $\alpha = 0.156$ ). A new component B (red peak) was included at a higher BE of 284.35 eV, in order to properly fit the high-coverage spectra (Figure 5.9d). This peak has a line-shape characterised by  $L = 213$  meV,  $G = 150$  meV and  $\alpha = 0.046$ .

To achieve a quantitative assessment of the total carbon coverage of multilayer Gr, we evaluated the attenuation of the photoemission signal of both the Ir  $4f_{7/2}$  and C 1s levels due to the limited mean free path of photoelectrons at the kinetic energies employed (115 eV). In particular, for the case of the C 1s (see Figure 5.9d), it is important to consider that not only the A component (which is attributed to the bottom layer of Gr, *i.e.* the one directly in contact with the Ir(1 1 1) substrate, as will be described later) will be screened by the 2<sup>nd</sup> and further layers, but also the total intensity of component B will be given by the sum of the contribution by each layer, each screened by all the layers lying above it. This contribution, however, cannot be simply modelled since it requires the knowledge of the growth method of the extra layers (layer-by-layer or by islands) and the average size of these islands. For this reason, an average number  $m$  of the further layers was calculated by evaluating their attenuation on the first layer, which can be modelled as:

$$\frac{I_A}{I_{A,MAX}} = a^m$$

where  $a$  is the attenuation by a single C layer and  $m$  is the number of layers not in contact with the metallic surface (2<sup>nd</sup> and further). As a full layer of Gr has 2.47 carbon atoms/unit cell of Ir(1 1 1) (as described in Section 2.1),  $m$  can be calculated by the relation

$$m = \frac{\theta_B}{2.47}$$

In order to quantify  $a$ , we measured the attenuation by a full monolayer of Gr (as obtained by CVD) on the Ir  $4f_{7/2}$  core level, by tuning the photon energy in such a way that the photoelectron kinetic energy was the same as in the excitation of the C 1s core electrons. In fact, as described in Section 1.4, the mean free path of electrons through a solid depends strongly on its kinetic energy<sup>58</sup>. The total number of Gr layers  $n = m + 1$  was then obtained from the formula above. In particular, we evaluated the attenuation of the Ir  $4f_{7/2}$  signal by single and multi-layer Gr, as shown on the left of Figure 5.9. We obtained that, in our experimental conditions, the signal after the growth of a full ML of Gr via CVD (Figure 5.9b) is attenuated with respect to the signal of the clean surface (Figure 5.9a) by a factor 0.43, which, for this specific case where  $n = 1$ , corresponds to the value of  $a$ :

$$\frac{I_{Ir}}{I_{Ir,0}} = a^n$$

It is interesting to notice that this is the same attenuation which is obtained from the growth using the C source, at the moment when the second component starts to appear (Figure 5.9c). Finally, the attenuation of the Ir  $4f_{7/2}$  signal at the end of the experiment is 0.16: by applying the same formula, this yields a total number of layers  $n = 2.23$ , corresponding to a C coverage of 5.50 ML.

The right part of Figure 5.9 shows instead the photoemission intensities of C 1s components A and B in the same systems. In Figure 5.9c, component A has the same intensity as the one obtained in the CVD experiment (Figure 5.9b), whereas component B is just 0.01 times as intense. On the other hand, in Figure 5.9d, corresponding to multilayer Gr, component A has decreased to 0.35 times its original intensity, while the intensity of B is 0.86 times that of the full monolayer Gr in Figure 5.9b.

An important observation is that the ratio between the A and B components of C 1s in the spectra taken at high temperature (as will be shown in Figure 5.11) does not correspond to the one obtained from measurements at room temperature (Figure 5.9). This can be explained in terms of a reduced mean free path which could be originated for instance by an increased scattering by Gr phonons. Therefore, in order to calculate the real C coverage for the uptake experiment described in the next Section, the following procedure has been applied: as long as a single component was present, the coverage was considered proportional to the photoemission intensity. For the part of the experiment where the second component was

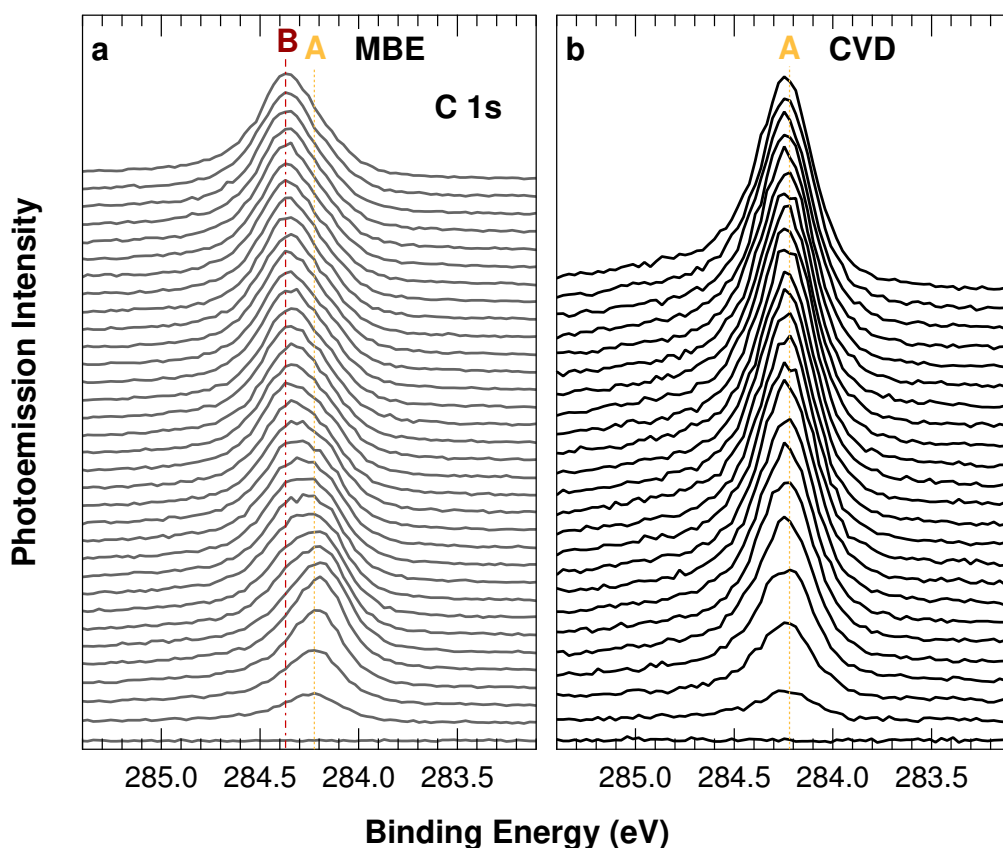


present, the coverage of the first component was fixed to the maximum value it had reached. We calculated a new attenuation parameter  $a_{1200\text{K}}$ , *i.e.* the value of the attenuation by one layer Gr at  $T = 1200\text{ K}$ , which was obtained from the intensity ratio of the A component of the C 1s spectrum between the last points and its maximum value, by employing the coverage value obtained from the room temperature measurements. Finally, the ratio of the intensity of A with respect to its real coverage was used to quantify the number  $m$  of C layers covering the interface layer.

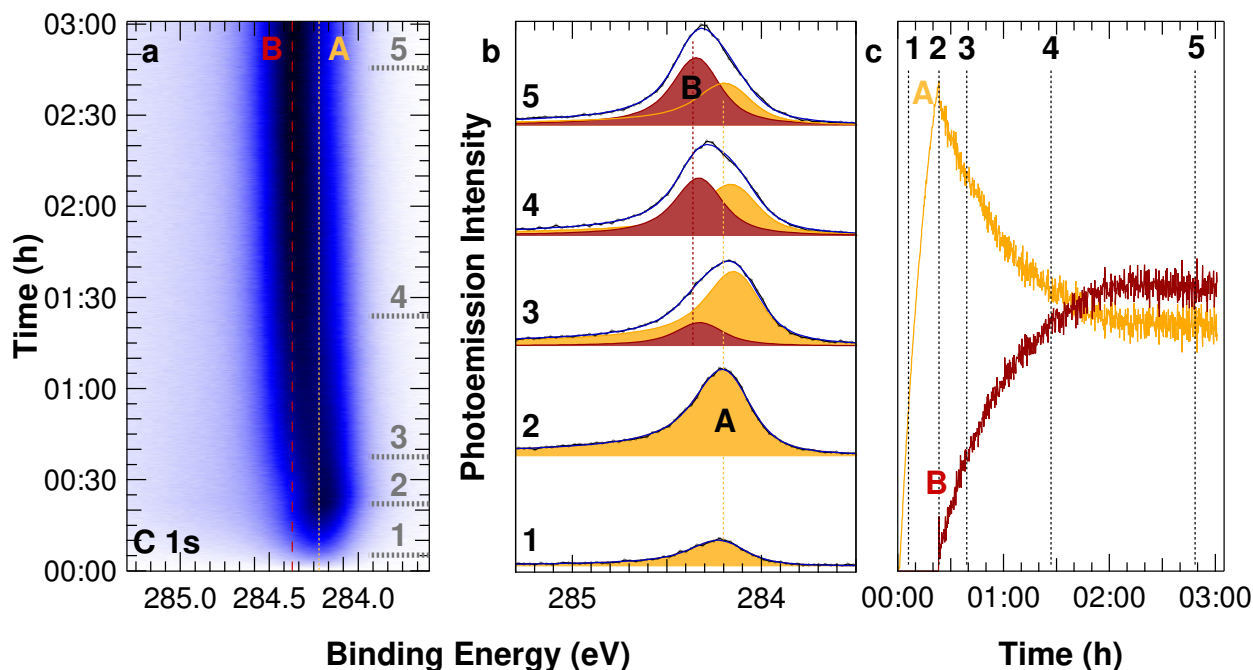
### 5.3.2 Experimental results

Figure 5.10a shows the sequence of high resolution C 1s core level spectra measured *in situ* during C deposition from the carbon source. As mentioned in the previous Section, at the beginning of the uptake a single component, A, is detected at 284.15 eV BE. With increasing C coverage, we observe a second component appearing at higher BE (284.35 eV), while the spectral weight of the low BE component decreases. This spectral series can be compared with the one measured during Gr CVD growth at the same temperature, which is shown in Figure 5.10b. In the latter case, only a single component can be detected throughout the whole experiment, having the same BE of the A peak observed at the beginning of the MBE growth (a). This trend suggests that, while in the first stages of the growth the two methods produce the same C species, another non-equivalent C species appears at higher coverages only when depositing carbon from a solid target. The modification in the spectral line-shape can be also appreciated in Figure 5.11a, where the time-lapsed C 1s spectra is reported as a two-dimensional plot in which the photoemission intensity is represented in colour scale, ranging from low (white) to high (dark).

Representative spectra are shown in Figure 5.11b with their deconvoluted spectral components A and B (as described above). A single component A was sufficient to properly describe the spectrum up to a



**Figure 5.10:** Time-resolved C 1s spectra ( $h\nu = 400\text{ eV}$ ) acquired during Gr growth on Ir (1 1 1) at 1200 K using MBE (a) and CVD at  $1 \times 10^{-8}$  mbar  $\text{C}_2\text{H}_4$  (b) technique. The two graphs are not to scale.



**Figure 5.11:** a: Time-resolved C 1s spectrum ( $h\nu = 400$  eV) acquired during MBE growth at 1200 K. Selected spectra are plotted in b, with their deconvoluted components. c: Evolution of the photoemission intensity of each component.

coverage of 2.4 ML, corresponding to the coverage of a full ML of Gr on Ir(1 1 1), as demonstrated by low fitting residuals without an appreciable modulation. For higher coverage, instead, component B also had to be included.

It is clear from Figure 5.11c, where the intensities of the A and B components are plotted as a function of exposure to the C source, that the intensity of component A decreases as component B increases. The evolution of the two components suggests that the new B species could originate from a second and further layers of Gr located above the first monolayer Gr: the photoemission intensity decrease of the A components is indeed explained as due to the increasing attenuation of the photoemission signal of the interface carbon layer – the one directly above the surface – exerted by the layers of carbon atoms lying above it.

The growth was further characterised by acquiring low energy diffraction images corresponding to the different systems, as reported in Figure 5.12. The Gr monolayer prepared by CVD shows the typical diffraction pattern described in Section 2.3.2, with the presence of several spots due to the formation of the

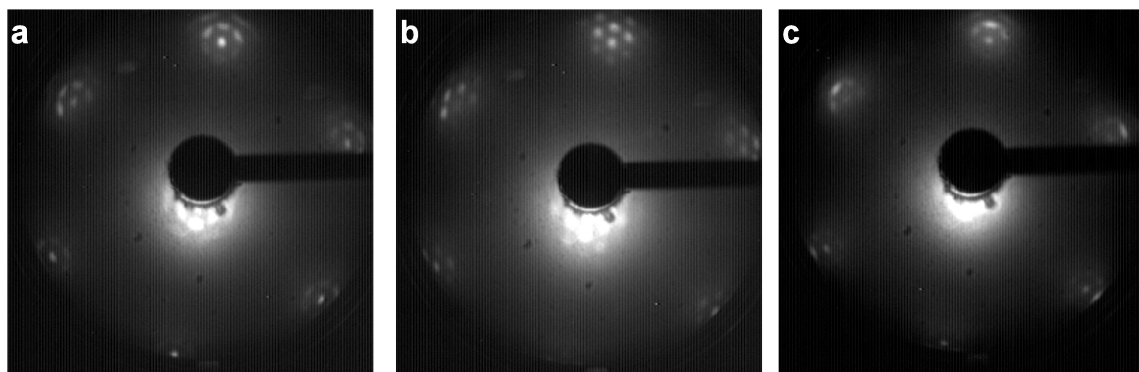


**Figure 5.12:** LEED of single-layer Gr grown on Ir(1 1 1) at 1200 K via CVD (a) and MBE (b) and after multi-layer Gr growth by MBE (c).

long-range order periodicity of the moiré superlattice, which are aligned with those of the Ir (1 1 1) surface (Figure 5.12a). This spots, however, are much broader along a tangential than along a radial direction: this indicates that Gr is not completely aligned with the substrate's crystallographic directions, but has several rotational domains narrowly distributed around this direction. The presence of rotational domains in High-Temperature CVD-grown Gr on Ir (1 1 1) is indeed one of the main drawbacks when using this growth method on this surface<sup>55</sup>. On the other hand, the MBE growth leads to significantly narrower spots, which do not display any angular broadening; moreover, a higher number of diffraction orders can be seen. This indicates that for similar growth conditions at constant temperature, MBE Gr growth of single-layer Gr on Ir (1 1 1) leads to a higher crystallographic quality of the product. Finally, the image corresponding to the multilayer formation (Figure 5.12c) still shows the same moiré spots, even though the background intensity has increased, indicating an overall poorer ordering in the multilayer Gr.

Another interesting result obtained in the carbon MBE experiment can be appreciated in Figure 5.13a, where the C 1s spectra of the A and B components measured at the end of the uptake at high temperature ( $T=1200$  K) and at room temperature ( $T=300$  K) are reported. At the end of the uptake, when 2.23 layers (*i.e.* 5.50 ML) are present, the BE difference results to be about 150 meV, as shown in the top spectrum of Figure 5.13a. However, if we cool the Ir (1 1 1) crystal to room temperature, the two components, while keeping a similar spectral weight ratio, are characterized by a quite different core level shift, which amounts to 210 meV (Figure 5.13a, below). We explain this change as due to the different thermal expansion of monolayer and free-standing Gr. Because of the weak vdW coupling between the C layers, we can consider the topmost Gr layers as free-standing, while the first C layer is directly interacting with the Gr substrate. Therefore, its thermal expansion is driven by the positive thermal expansion of the Ir substrate underneath, while for the upper and decoupled layers the thermal expansion is expected to be negative, as for free-standing Gr. For a quantitative evaluation we compared our experimental findings with the expected C 1s core level shift for epitaxial and free-standing Gr, calculated by means of DFT and molecular dynamics simulations<sup>59</sup>. By increasing the temperature from 300 K to 1000 K, the differences between the calculated C 1s core level shifts of free-standing and supported Gr decreases by 90 meV, which is in quite good agreement with the decrease we observe in our data (150 meV). Small discrepancies can be explained as due to the coupling of the first Gr layer with the new carbon layers above it.

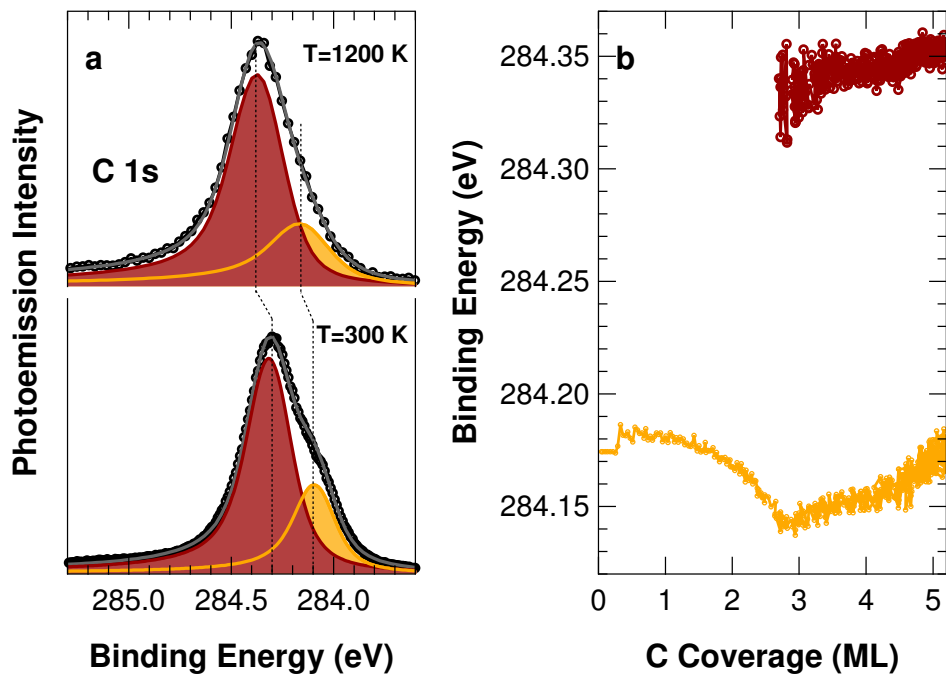


**Figure 5.13:** a: Comparison of C 1s core-level spectra of multilayer Gr at growth temperature (above) and room temperature (below) ( $h\nu = 400$  eV). b: C 1s core-level Binding Energy evolution during MBE Gr growth at 1200 K.

Furthermore, as shown in Figure 5.13b, the C 1s BE of both components A and B shifts during the whole growth. In particular, before a full monolayer is formed, the BE of the only component (A) decreases progressively. The minimum BE of the interface Gr layer, corresponding to the minimum degree of  $n$ -doping, is achieved when a full monolayer Gr is present. The C 1s BE of both components, instead, increases when the multilayers start forming, with a roughly linear dependence from coverage. In particular, for increasing number of layers, the C 1s BE moves closer to the value found in bulk graphite, which is 284.0 eV<sup>60</sup>.

### 5.3.3 Discussion

The comparison between the evolution of the C coverage in the uptakes performed at the same temperature, using either the carbon source or ethylene CVD, is shown in Figure 5.14. The two curves corresponding respectively to the A peak in MBE (red) and the corresponding single component in CVD (green) reach approximately the same maximum intensity, which corresponds to about 2.47 ML. However, the rate at which this maximum is reached is very different: while the speed of the CVD process gradually decreases and the approach to the 2.47 ML limit is asymptotic with coverage, the growth rate for MBE is still close to its initial value when the coverage reaches that value. This difference can be appreciated in particular starting from a coverage of 1 ML, where the slope of the curve corresponding to the CVD growth experiment is clearly decreasing with respect to the C-source experiment, as highlighted in the zoom shown in Figure 5.14b.

The asymptotic behaviour is a clear fingerprint that in the CVD process, the growth rate depends on the portion of the surface which is still free from Gr. This can be attributed to the very weak interaction between the regions already covered by Gr and the precursor C<sub>2</sub>H<sub>4</sub> molecules, which causes the molecules adsorbing there to immediately desorb, without generating carbon feedstock. This fact can be attributed to two main reasons: Gr cannot catalyse the hydrocarbon breaking, and at the temperature used for Gr growth the precursor cannot adsorb on the Gr flakes for sufficient time to undergo thermal decomposition anyway. This is at the basis of the well-known self-terminating behaviour of CVD-grown Gr on Ir(1 1 1), which allows to obtain single-layer Gr with 100% selectivity on this surface.

In addition, it is interesting to notice that the maximum intensity reached in the CVD growth is smaller by a few percent than the one obtained by MBE for the first Gr layer. A possible explanation for this fact is that in order to dissociate, the gas precursor molecules must be able to reach the metal surface to dissociate, yet their steric encumbrance does not allow them to adsorb on the bare Ir which is still exposed within the smallest defects, such as vacancies or grain boundaries. Instead, single atoms, having a

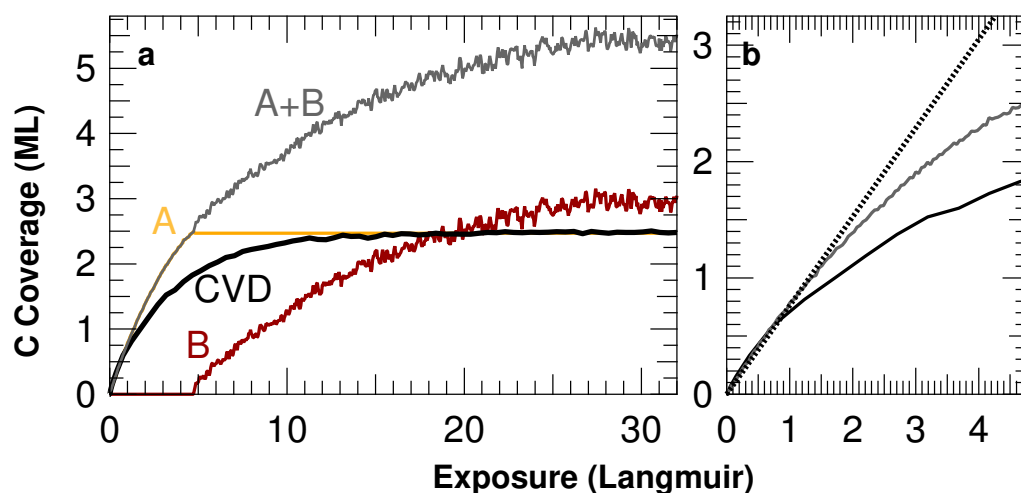


**Figure 5.14:** Comparison of the growth rate of Gr during MBE and CVD rate. In a, the total coverage of CVD- and MBE-grown Gr are shown, together with the individual coverage of the first and upper layers. b: zoom on the initial growth rate and comparison with linear behaviour (dashed).

smaller encumbrance, are more effective in attaching to the edges and close even the defects with smallest dimensionalities, allowing to obtain a larger coverage.

On the other hand, the Gr growth rate with MBE does not vanish at a coverage of a full layer Gr, and the total coverage increases further, as the new photoemission component B grows. It is interesting to point out that the growth of the B peak starts exactly after the A component has reached its maximum. This indicates that while the MBE growth is not self-terminating and causes multi-layer growth, it is still possible to employ this technique to reproducibly achieve either a full single-layer Gr coverage or Gr of different thickness, by carefully monitoring the deposition.

However, there is a limit to this, as the total C coverage during the growth of the further layers, shown in Figure 5.14, eventually does eventually reach saturation, for an exposure of about 6 times the one needed to complete the first layer. The saturation was observed to occur for a total carbon coverage corresponding to  $n = 2.23$  layers of Gr. We can exclude that this saturation is only apparent, *i.e.* that what we are observing is just a plateau reached in the photoemission signal due to the limited mean free path of photoelectrons, thanks to the possibility to distinguish the signal of the bottom (A) and top layers (B): as not only their total intensity, but also their spectral weight does not vary any longer (as can be seen in Figure 5.11c), we can conclude that the growth has really stopped. This is quite surprising, as one would expect the sticking probability not to vary significantly any more once the whole surface is covered by Gr.

Another remarkable fact can be observed in the LEED pattern generated by the Gr multilayer, shown in Figure 5.12c, which still shows that the Gr layer is well aligned to the Ir (1 1 1) substrate. A high degree of orientational ordering between CVD- or MBE-grown Gr and its substrate is usually only observed when there is a high degree of interaction between the C feedstock and the substrate. For example, Gr has very few preferential orientations on strongly interacting surfaces such as Re (0 0 1)<sup>53</sup> and Ru (0 0 1)<sup>61</sup>, can display several rotational domains on surfaces such as Ir (1 1 1)<sup>55</sup> and Rh (1 1 1)<sup>62</sup>, and often shows no preferred orientation on very weakly interacting ones such as Pt (1 1 1)<sup>63,64</sup> and Au (1 1 1)<sup>22</sup>. According to this, Gr is expected to show very poor rotational alignment when growing on top of another Gr layer<sup>57</sup>, and therefore the appearance of ring-like diffraction features in the LEED pattern would be likely, as in the case of highly oriented pyrolytic graphite<sup>65,66</sup>.

These two issues can both be explained if the growth of the new C layers takes place not on top of the already grown layers, but on the buried Ir (1 1 1) surface, by intercalation of C monomers/dimers at the interface between the monolayer Gr and the Ir substrate. This behaviour has been already observed in previous LEEM experiments on the Ir (1 1 1) surface<sup>27</sup> and on other surfaces such as Cu (1 1 1)<sup>57</sup>. In particular, according to this model, the progressive reduction in the rate of multilayer growth can be attributed to the fact that as further layers grow, it becomes increasingly difficult for the C atoms to intercalate and reach the surface, which is required to continue the growth. Moreover, the growth of the new layers, since it occurs on the Ir (1 1 1) surface, is still driven in its crystallographic direction by the interaction of the precursors with it.

Finally, it is evident from Figure 5.14b that the growth rate of the first Gr layer by MBE is still influenced by the amount of free metal surface, even though not as dramatically as in CVD. In fact, while the growth rate remains relatively large, it is nevertheless decreasing at high coverage (starting slightly below 1 ML), reaching about 80% of its initial value when the coverage approaches that of a full Gr layer. As the evaporation rate of the C source was verified to be constant, this decrease must be related to some process occurring on the surface, similar to the self-terminating behaviour occurring in the CVD growth yet less dramatic. For the case of CVD, in fact, the reduction in growth rate is due to the very low residence time of the gaseous precursors on the Gr flakes, which causes them to desorb before they can participate to the growth. The MBE behaviour, instead, can be explained if the carbon monomers and dimers have an adsorption energy on Gr which is large enough to allow them to adsorb on the surface and diffuse for a certain distance across the Gr flakes, yet the desorption probability is still not negligible. This leads to an interplay between the two processes of diffusion and desorption: more specifically, the carbon species adsorbed close enough to the flakes' edges can diffuse and reach the edge in a time smaller than their average residence time on the surface, while those farthest from the edges will desorb with high probability before they reach it. Once the carbon precursor has reached the edge, it can either attach directly there or dif-



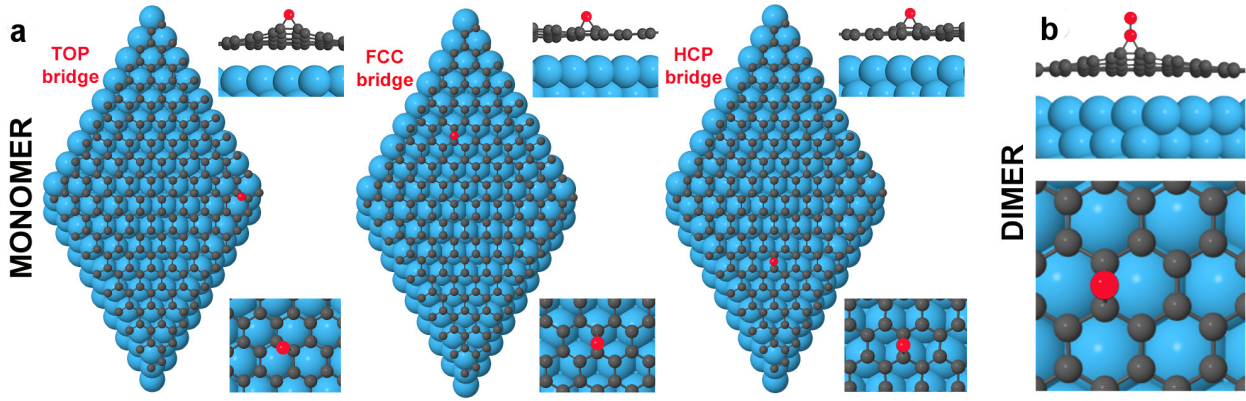


**Figure 5.15:** Preferred adsorption configurations for a: C<sub>1</sub> and b: C<sub>2</sub> species on Gr supported on Ir(1 1 1). For the case of the monomers (a), the adsorption energy in non-equivalent regions of the Gr moiré supercell is shown.

fuse on the Ir surface, but then its adsorption energy becomes high enough that its desorption probability becomes negligible. A proof of this behaviour is that, up to a coverage of 1 ML, the growth rate is linear, since the islands are so small that wherever the C species are deposited, the time they take to reach an edge is not sufficient to allow them to desorb; whereas only at high coverages, when extended regions of the surface are covered by Gr, a decrease in the growth rate is observed.

To verify this hypothesis, we have once again resorted to DFT calculations performed by our collaborators, where the adsorption energy of C monomers and dimers on graphene has been calculated. The results are shown in Table 5.3.

	C <sub>1</sub>	C <sub>2</sub>
$E_{\text{DES}}$ (eV)	2.48	2.60
$E_{\text{DIFF}}$ (eV)	0.60	0.28

**Table 5.3:** Adsorption ( $E_{\text{DES}}$ ) and diffusion ( $E_{\text{DIFF}}$ ) energies for carbon monomers and dimers adsorbed on Ir(1 1 1).

In particular, the C monomer is found to be unstable in the hollow and atop positions in the Gr unit cell, and will tend to relax to the bridge position. We calculated the adsorption energy for C monomers sitting in this site in different regions (TOP, HCP and FCC) of the Gr (10 × 10) unit cell, as shown in Figure 5.15a. While the HCP-bridge and FCC-bridge configurations show quite similar adsorption energy values, the TOP-bridge site is slightly preferred, with an adsorption energy of 2.48 eV. Also C dimers preferentially adsorb in TOP-bridge sites (Figure 5.15b), with an adsorption energy slightly larger than 2.60 eV. It is interesting to note that the dimer axis is vertical with respect to the Ir surface and induces a considerable local deformation in the Gr lattice, by lifting up the nearest- and next-nearest-neighbour C atoms.

By comparing the two systems, it is clear that the adsorption energy of a C monomer or dimer is quite similar. Moreover, it is higher by an order of magnitude than the values found for the systems studied in Chapter 3, indicating that in this case the C species are chemisorbed.

In addition, our collaborators calculated the diffusion barrier ( $E_{\text{DIFF}}$ ) of C monomer and dimers. The pathway and energetics of the diffusion process are shown for both species, in Figure 5.16. The most interesting finding is the much larger barrier for the diffusion of C<sub>1</sub> monomers from TOP-bridge to TOP-bridge sites with respect to the case of C<sub>2</sub> dimers, as reported in Table 5.3.

As discussed in Chapter 3, since the adsorption process is non-dissociative and therefore has no activation barrier, the desorption energy corresponds to the adsorption energy  $E_{\text{DES}}$ . Being the diffusion barriers smaller than the desorption ones by one order of magnitude, the time required for the adsorbed carbon to desorb from Gr will be significantly larger than the one required to move to an adjacent cell.

In particular, the probability for an individual diffusion event per unit of time will be:

$$P_1(T) = \nu e^{-E_{\text{DIFF}}/k_B T}$$

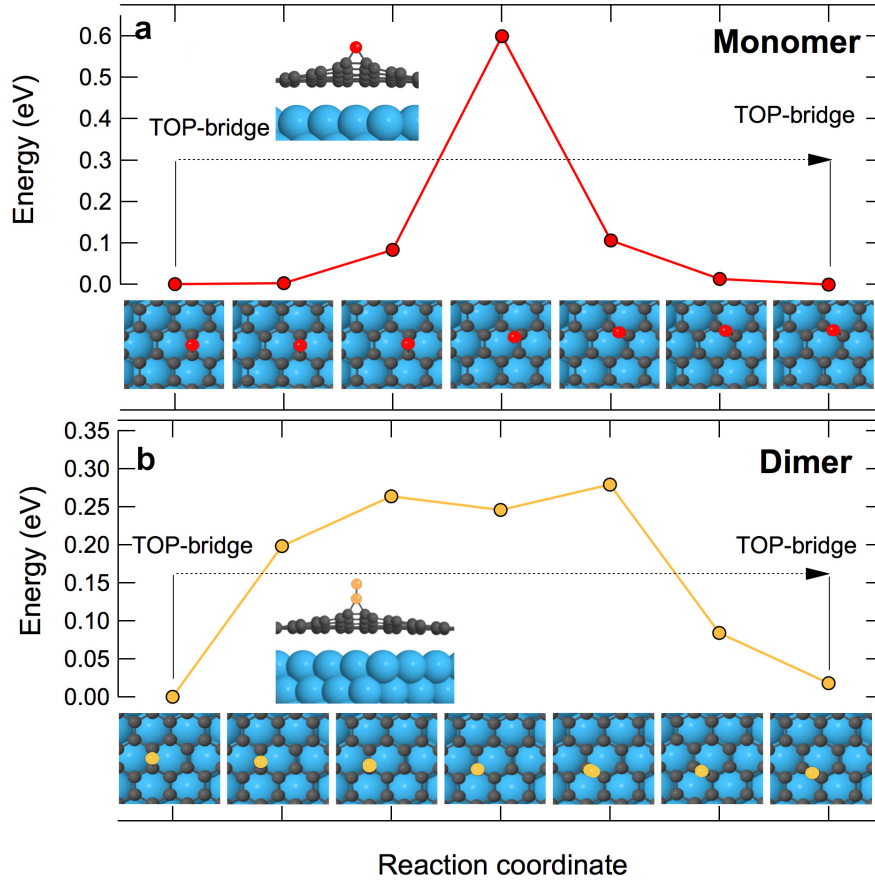


**Figure 5.16:** Calculated pathway for a: C<sub>1</sub> and b: C<sub>2</sub> species diffusion between adjacent unit cells on Gr supported on Ir(111). The energy variation of each system is plotted as a function of the reaction coordinate; the intermediate steps of the process are shown below.

where  $\nu$  is the pre-exponential factor, which can be assumed in a first approximation equal for diffusion and desorption;  $k_B$  is the Boltzmann constant and  $T$  is the temperature. We can therefore express the average time it takes for one adsorbed species to diffuse to a nearby cell as:

$$\tau_1 \propto \frac{1}{P_1(T)} \propto e^{E_{\text{DIFF}}/k_B T}$$

and the time required to cross several ( $N$ ) unit cells will be:

$$\tau_N \propto N e^{E_{\text{DIFF}}/k_B T}$$

Likewise, the desorption process will have an associated lifetime, corresponding to the average time the adsorbate remains on Gr before desorbing:

$$\tau_{\text{DES}} \propto e^{E_{\text{DES}}/k_B T}$$

The number  $N_{\text{MAX}}$  of Gr unit cells the adsorbate crosses before desorbing is the value for which  $\tau_{N_{\text{MAX}}} = \tau_{\text{DES}}$ :

$$N_{\text{MAX}} e^{E_{\text{DIFF}}/k_B T} = e^{E_{\text{DES}}/k_B T}$$

Finally, as the adsorbates move in random directions, the unit cells they cross will typically be diffused over an approximately circular region centred on their landing site, rather than aligned; the average radius of this region can be estimated as:

$$r_{\text{MAX}} = a_{\text{Gr}} \sqrt{N_{\text{MAX}}}$$

where  $a_{\text{Gr}}$  is the lattice parameter of Gr.

Using these formulas, I calculated  $r_{\text{MAX}}$  for both monomers and dimers adsorbed on Gr/Ir(1 1 1), which yields respectively  $r_{\text{MAX},M} = 2.4 \mu\text{m}$  and  $r_{\text{MAX},D} = 18.3 \mu\text{m}$ .

For each carbon species, this value defines two zones inside the Gr islands growing on the Ir(1 1 1) surface. In particular, for the case of monomers, those flakes whose radius is larger than the  $r_{\text{MAX},M}$  have an inner and an outer region, separated by a boundary located at a distance  $r_{\text{MAX},M}$  from the edge, such that carbon monomers deposited in the outside region participate to the flakes' growth, as they manage to diffuse until the edge of the flake, while those deposited in the inside region desorb before they can reach an edge. Likewise, a different boundary, at a distance of  $r_{\text{MAX},D}$  from the islands' edge, separates the region where deposited dimers can participate to growth or not. Due to the different values of  $r_{\text{MAX},M}$  and  $r_{\text{MAX},D}$ , the islands of intermediate size (between 2 and 20  $\mu\text{m}$  only have two regions: the outer, where both monomers and dimers can reach the edge, and the inner region, where only dimers can migrate to the edges. For even larger islands, a third, innermost region is present, where no deposited species is able to participate in the growth.

This mechanism very well explains the observed curve of the growth rate. In fact, for low carbon coverage, the islands size is smaller than the diffusion limit of both carbon species, and the growth rate is constant as all adsorbed C species participate to the growth, regardless whether they are deposited on an already nucleated Gr flake or on a bare region of the surface. As the coverage increases, some islands reach the size for which desorption starts to occur, and only then is a decrease in the growth rate observed. For example, in an island characterized by a radius twice  $r_{\text{MAX},M}$ , 25% of the area will not allow monomers deposited there to contribute to the growth; while in an island 10 times larger than  $r_{\text{MAX},M}$  only 20% of the adsorbed monomers will contribute to the growth. It is interesting to notice that in the latter case, a region where even deposited dimers cannot diffuse to the edge is present, yet still represents a negligible part of the total area.

As we know, from the experiments described in the previous sections, that in our system the growth is fed by monomers and dimers in a fairly similar ratio and as the reduction we observe in the growth rate is about 20%, we can conclude that this decrease is almost exclusively due to the monomers and that the average size of the Gr islands, at a coverage approaching that of a full Gr layer, is between 5 and 10  $\mu\text{m}$ . Indeed, the LEED pattern of the single layer MBE-grown Gr, which is reported in Figure 5.12b, shows very sharp spots, compatible with a large domain size. However, the transfer width of the instrument only allows us to conclude that the coherent domains in Gr are at least as large as 100 Å. It is important to observe, finally, that the size of the islands obtained from these considerations might be larger than that of the coherent domains of graphene, as a single island could be formed by several domains separated by grain boundaries, as long as there is no free iridium surface in between.

## Conclusion

In this chapter, I have described an investigation of the individual steps in the MBE growth of Gr by means of carbon deposition from a solid evaporator. In particular, in the first part of this experiment I have shown how high energy-resolution core-level photoemission spectroscopy can be employed to identify carbon species, such as monomers and small clusters, having different number of atoms or in different adsorption sites. Using this technique, I have shown that the carbon feedstock in MBE Gr growth from a solid carbon evaporator is composed of both carbon monomers and dimers, unlike the case of CVD where only dimers are present. Following this study, I have shown that high quality Gr can be formed by deposition of carbon monomers and dimers on the Ir(1 1 1) surface at high temperature (1200 K). Furthermore, this technique allows to obtain both single- and multi-layer Gr; however, a careful monitoring of the growth rate is needed to precisely control this parameter. Moreover, by analysing the growth rate, I have shown how the growth kinetics are controlled by a complex interplay between the diffusion of the C precursors on the growing Gr islands and their desorption. This interplay is controlled by the size of the islands and differs among the chemical species composing the carbon feedstock: this fact provides an additional degree of freedom, besides temperature, to tune both the quality of the Gr and the number of



layers grown, by modifying the composition of the carbon feedstock delivered. This could be achieved for instance by tuning the evaporation conditions of the carbon evaporator, or by using a different type of carbon source; for example, the Mass Selected Nanoclusters Source described in Chapter 7 could be employed to this aim.

I have therefore shown that even during the growth process, when Gr is only covering part of the surface, its interaction with the adsorbed precursor atoms and molecules can affect the islands' accretion process and thereby the quality of the final product. This is a further indication of the importance of a correct understanding of the interactions occurring on supported Gr, as the interplay between diffusion and desorption, which influences the size of the Gr islands, will be in general different depending on the substrate over which Gr is being grown. For this reason, a careful evaluation of the energy barriers ruling these two processes can provide a tool to significantly improve the growth of Gr on new substrates using Molecular Beam Epitaxy.

Finally, this technique is not limited to Gr growth, as it can be also employed for the growth of other 2D materials. For example, MBE from a solid evaporator is up to now the only successful technique in the synthesis of different phases of 2D allotropes of boron, known as borophenes<sup>67,68</sup>.

The simple working principles of this technique, which unlike CVD does not require any catalytic reactions, make it therefore an ideal tool for the growth of diverse 2D materials on a wide variety of substrates.

## References

- [1] X. Li, Y. Zhu, W. Cai, M. Borysiak, B. Han, D. Chen, R. D. Piner, L. Colombo, R. S. Ruoff. Transfer of large-area graphene films for high-performance transparent conductive electrodes. *Nano Lett.* (2009) 9: 4359–4363. doi:10.1021/nl902623y.
- [2] J. Kang, D. Shin, S. Bae, B. H. Hong. Graphene transfer: key for applications. *Nanoscale* (2012) 4: 5527. doi:10.1039/c2nr31317k.
- [3] G. Lupina, J. Kitzmann, I. Costina, M. Lukosius, C. Wenger, A. Wolff, S. Vaziri, M. Östling, I. Pasternak, A. Krajewska, W. Strupinski, S. Kataria, A. Gahoi, M. C. Lemme, G. Ruhl, G. Zoth, O. Luxenhofer, W. Mehr. Residual metallic contamination of transferred Chemical Vapor Deposited graphene. *ACS Nano* (2015) 9: 4776–4785. doi:10.1021/acsnano.5b01261.
- [4] R. Addou, A. Dahal, P. Sutter, M. Batzill. Monolayer graphene growth on Ni (1 1 1) by low temperature chemical vapor deposition. *Appl. Phys. Lett.* (2012) 100: 021601. doi:10.1063/1.3675481.
- [5] A. Varykhalov, O. Rader. Graphene grown on Co (0 0 1) films and islands: Electronic structure and its precise magnetization dependence. *Phys. Rev. B* (2009) 80: 035437. doi:10.1103/PhysRevB.80.035437.
- [6] A. L. Vázquez de Parga, F. Calleja, B. Borca, M. C. G. Passeggi, J. J. Hinarejos, F. Guinea, R. Miranda. Periodically rippled graphene: Growth and spatially resolved electronic structure. *Phys. Rev. Lett.* (2008) 100: 056807. doi:10.1103/physrevlett.100.056807.
- [7] A. B. Preobrajenski, M. L. Ng, A. S. Vinogradov, N. Mårtensson. Controlling graphene corrugation on lattice-mismatched substrates. *Phys. Rev. B* (2008) 78: 073401. doi:10.1103/PhysRevB.78.073401.
- [8] E. Miniussi, M. Pozzo, A. Baraldi, E. Vesselli, R. R. Zhan, G. Comelli, T. O. Menteş, M. A. Niño, A. Locatelli, S. Lizzit, D. Alfè. Thermal stability of corrugated epitaxial graphene grown on Re (0 0 1). *Phys. Rev. Lett.* (2011) 106: 216101. doi:10.1103/PhysRevLett.106.216101.
- [9] L. Gao, J. R. Guest, N. P. Guisinger. Epitaxial graphene on Cu (1 1 1). *Nano Lett.* (2010) 10: 3512–3516. doi:10.1021/nl1016706.
- [10] C. Busse, P. Lazić, R. Djemour, J. Coraux, T. Gerber, N. Atodiresei, V. Caciuc, R. Brako, A. T. N'Diaye, S. Blügel, J. Zegenhagen, T. Michely. Graphene on Ir (1 1 1): Physisorption with chemical modulation. *Phys. Rev. Lett.* (2011) 107: 036101. doi:10.1103/PhysRevLett.107.036101.
- [11] A. Locatelli, G. Zamborlini, T. O. Menteş. Growth of single and multi-layer graphene on Ir (1 0 0). *Carbon* (2014) 74: 237–248. doi:10.1016/j.carbon.2014.03.028.
- [12] A. Reina, S. Thiele, X. Jia, S. Bhaviripudi, M. S. Dresselhaus, J. A. Schaefer, J. Kong. Growth of large-area single- and bi-layer graphene by controlled carbon precipitation on polycrystalline Ni surfaces. *Nano Res.* (2009) 2: 509–516. doi:10.1007/s12274-009-9059-y.
- [13] X. Li, W. Cai, J. An, S. Kim, J. Nah, D. Yang, R. Piner, A. Velamakanni, I. Jung, E. Tutuc, S. K. Banerjee, L. Colombo, R. S. Ruoff. Large-area synthesis of high-quality and uniform graphene films on copper foils. *Science* (2009) 324: 1312–1314. doi:10.1126/science.1171245.
- [14] M. Batzill. The surface science of graphene: Metal interfaces, CVD synthesis, nanoribbons, chemical modifications, and defects. *Surf. Sci. Rep.* (2012) 67: 83–115. doi:10.1016/j.surfrep.2011.12.001.
- [15] F. Xia, D. B. Farmer, Y.-M. Lin, P. Avouris. Graphene field-effect transistors with high on/off current ratio and large transport band gap at room temperature. *Nano Lett.* (2010) 10: 715–718. doi:10.1021/nl9039636.

- [16] S. Hertel, D. Waldmann, J. Jobst, A. Albert, M. Albrecht, S. Reshanov, A. Schöner, M. Krieger, H. Weber. Tailoring the graphene/silicon carbide interface for monolithic wafer-scale electronics. *Nat. Commun.* (2012) 3: 957. doi:10.1038/ncomms1955.
- [17] X. Wang, Q. Yuan, J. Li, F. Ding. The transition metal surface dependent methane decomposition in graphene chemical vapor deposition growth. *Nanoscale* (2017) 9: 11584–11589. doi:10.1039/c7nr02743e.
- [18] G. Wang, M. Zhang, Y. Zhu, G. Ding, D. Jiang, Q. Guo, S. Liu, X. Xie, P. K. Chu, Z. Di, X. Wang. Direct growth of graphene film on germanium substrate. *Sci. Rep.* (2013) 3: 2465. doi:10.1038/srep02465.
- [19] J. Dabrowski, G. Lippert, J. Avila, J. Baringhaus, I. Colambo, Y. S. Dedkov, F. Herzigler, G. Lupina, J. Maultzsch, T. Schaffus, T. Schroeder, M. Kot, C. Tegenkamp, D. Vignaud, M.-C. Asensio. Understanding the growth mechanism of graphene on Ge/Si (0 0 1) surfaces. *Sci. Rep.* (2016) 6: 31639. doi:10.1038/srep31639.
- [20] J. Villacampa, C. Royo, E. Romeo, J. A. Montoya, P. Del Angel, A. Monzón. Catalytic decomposition of methane over Ni-Al<sub>2</sub>O<sub>3</sub> coprecipitated catalysts. *Appl. Catal., A* (2003) 252: 363–383. doi:10.1016/s0926-860x(03)00492-7.
- [21] G. Lippert, J. Dąbrowski, T. Schroeder, M. A. Schubert, Y. Yamamoto, F. Herzigler, J. Maultzsch, J. Baringhaus, C. Tegenkamp, M. C. Asensio, J. Avila, G. Lupina. Graphene grown on Ge (0 0 1) from atomic source. *Carbon* (2014) 75: 104–112. doi:10.1016/j.carbon.2014.03.042.
- [22] I. Hernández-Rodríguez, J. M. García, J. A. Martín-Gago, P. L. de Andrés, J. Méndez. Graphene growth on Pt (1 1 1) and Au (1 1 1) using a MBE carbon solid-source. *Diamond Relat. Mater.* (2015) 57: 58–62. doi:10.1016/j.diamond.2015.03.004.
- [23] <http://minotlab.physics.oregonstate.edu/content/image-gallery>. Web Site. Minot Group, Oregon State University.
- [24] J. M. Garcia, U. Wurstbauer, A. Levy, L. N. Pfeiffer, A. Pinczuk, A. S. Plaut, L. Wang, C. R. Dean, R. Buizza, A. M. van der Zande, J. Hone, K. Watanabe, T. Taniguchi. Graphene growth on h-BN by molecular beam epitaxy. *Solid State Commun.* (2012) 152: 975–978. doi:10.1016/j.ssc.2012.04.005.
- [25] M. Peplow. Graphene booms in factories but lacks a killer app. *Nature* (2015) 522: 268–269. doi:10.1038/522268a.
- [26] F. Bonaccorso, A. Lombardo, T. Hasan, Z. Sun, L. Colombo, A. C. Ferrari. Production and processing of graphene and 2D crystals. *Mater. Today* (2012) 15: 564–589. doi:10.1016/s1369-7021(13)70014-2.
- [27] S. Nie, A. L. Walter, N. C. Bartelt, E. Starodub, A. Bostwick, E. Rotenberg, K. F. McCarty. Growth from below: Graphene bilayers on Ir (1 1 1). *ACS Nano* (2011) 5: 2298–2306. doi:10.1021/nn103582g.
- [28] E. Loginova, N. C. Bartelt, P. J. Feibelman, K. F. McCarty. Evidence for graphene growth by C cluster attachment. *New J. Phys.* (2008) 10: 093026. doi:10.1088/1367-2630/10/9/093026.
- [29] E. Loginova, N. C. Bartelt, P. J. Feibelman, K. F. McCarty. Factors influencing graphene growth on metal surfaces. *New J. Phys.* (2009) 11: 063046. doi:10.1088/1367-2630/11/6/063046.
- [30] H. Tetlow, J. Posthuma de Boer, I. J. Ford, D. D. Vvedensky, D. Curcio, L. Omiciuolo, S. Lizzit, A. Baraldi, L. Kantorovich. Ethylene decomposition on Ir (1 1 1): initial path to graphene formation. *Phys. Chem. Chem. Phys.* (2016) 18: 27897–27909. doi:10.1039/c6cp03638d.
- [31] L. Zhong, J. Li, Y. Li, H. Lu, H. Du, L. Gan, C. Xu, S. W. Chiang, F. Kang. Unraveling the influence of metal substrates on graphene nucleation from first-principles study. *J. Phys. Chem. C* (2016) 120: 23239–23245. doi:10.1021/acs.jpcc.6b06750.

- [32] P. Wu, H. Jiang, W. Zhang, Z. Li, Z. Hou, J. Yang. Lattice mismatch induced nonlinear growth of graphene. *J. Am. Chem. Soc.* (2012) 134: 6045–6051. doi:10.1021/ja301791x.
- [33] O. V. Yazyev, Y. P. Chen. Polycrystalline graphene and other two-dimensional materials. *Nat. Nanotechnol.* (2014) 9: 755–767. doi:10.1038/nnano.2014.166.
- [34] S. Riikonen, A. V. Krashennnikov, L. Halonen, R. M. Nieminen. The role of stable and mobile carbon adspecies in copper-promoted graphene growth. *J. Phys. Chem. C* (2012) 116: 5802–5809. doi:10.1021/jp211818s.
- [35] T. Niu, M. Zhou, J. Zhang, Y. Feng, W. Chen. Growth intermediates for CVD graphene on Cu(111): Carbon clusters and defective graphene. *J. Am. Chem. Soc.* (2013) 135: 8409–8414. doi:10.1021/ja403583s.
- [36] H. Chen, W. Zhu, Z. Zhang. Contrasting behavior of carbon nucleation in the initial stages of graphene epitaxial growth on stepped metal surfaces. *Phys. Rev. Lett.* (2010) 104: 186101. doi:10.1103/physrevlett.104.186101.
- [37] M. Gao, Y.-F. Zhang, L. Huang, Y. Pan, Y. Wang, F. Ding, Y. Lin, S.-X. Du, H.-J. Gao. Unveiling carbon dimers and their chains as precursor of graphene growth on Ru(0001). *Appl. Phys. Lett.* (2016) 109: 131604. doi:10.1063/1.4963283.
- [38] J. Gao, Q. Yuan, H. Hu, J. Zhao, F. Ding. Formation of carbon clusters in the initial stage of chemical vapor deposition graphene growth on Ni(111) surface. *J. Phys. Chem. C* (2011) 115: 17695–17703. doi:10.1021/jp2051454.
- [39] J. Li, E. Croiset, L. Ricardez-Sandoval. Carbon clusters on the Ni(111) surface: a density functional theory study. *Phys. Chem. Chem. Phys.* (2014) 16: 2954. doi:10.1039/c3cp54376e.
- [40] L. Xu, Y. Ma, Z. Wu, B. Chen, Q. Yuan, W. Huang. A photoemission study of ethylene decomposition on a Co(0001) surface: Formation of different types of carbon species. *J. Phys. Chem. C* (2012) 116: 4167–4174. doi:10.1021/jp210500p.
- [41] L. Xu, Y. Jin, Z. Wu, Q. Yuan, Z. Jiang, Y. Ma, W. Huang. Transformation of carbon monomers and dimers to graphene islands on Co(0001): Thermodynamics and kinetics. *J. Phys. Chem. C* (2013) 117: 2952–2958. doi:10.1021/jp400111s.
- [42] Z. Fu, Y. Zhang, Z. Yang. Growth mechanism and controllable synthesis of graphene on Cu–Ni alloy surface in the initial growth stages. *Phys. Lett. A* (2015) 379: 1361–1365. doi:10.1016/j.physleta.2015.03.009.
- [43] A. Föhlisch, N. Wassdahl, J. Hasselström, O. Karis, D. Menzel, N. Mårtensson, A. Nilsson. Beyond the chemical shift: Vibrationally resolved core-level photoelectron spectra of adsorbed CO. *Phys. Rev. Lett.* (1998) 81: 1730–1733. doi:10.1103/physrevlett.81.1730.
- [44] M. Bianchi, D. Cassese, A. Cavallin, R. Comin, F. Orlando, L. Postregna, E. Golfetto, S. Lizzit, A. Baraldi. Surface core level shifts of clean and oxygen covered Ir(111). *New J. Phys.* (2009) 11: 063002. doi:10.1088/1367-2630/11/6/063002.
- [45] S. Lizzit, A. Baraldi, A. Groso, K. Reuter, M. V. Ganduglia-Pirovano, C. Stampfl, M. Scheffler, M. Stichler, C. Keller, W. Wurth, D. Menzel. Surface core-level shifts of clean and oxygen-covered Ru(0001). *Phys. Rev. B* (2001) 63: 205419. doi:10.1103/physrevb.63.205419.
- [46] M. V. Ganduglia-Pirovano, M. Scheffler, A. Baraldi, S. Lizzit, G. Comelli, G. Paolucci, R. Rosei. Oxygen-induced Rh  $3d_{5/2}$  surface core-level shifts on Rh(111). *Phys. Rev. B* (2001) 63: 205415. doi:10.1103/physrevb.63.205415.

- [47] L. Bianchettin, A. Baraldi, E. Vesselli, S. de Gironcoli, S. Lizzit, L. Petaccia, G. Comelli, R. Rosei. Experimental and theoretical surface core level shift study of the S-Rh(1 0 0) local environment. *J. Phys. Chem. C* (2007) 111: 4003–4013. doi:10.1021/jp0677593.
- [48] A. Baraldi. Structure and chemical reactivity of transition metal surfaces as probed by synchrotron radiation core level photoelectron spectroscopy. *J. Phys.: Condens. Matter* (2008) 20: 093001. doi:10.1088/0953-8984/20/9/093001.
- [49] Y. Niimi, T. Matsui, H. Kambara, K. Tagami, M. Tsukada, H. Fukuyama. Scanning tunneling microscopy and spectroscopy of the electronic local density of states of graphite surfaces near monoatomic step edges. *Phys. Rev. B* (2006) 73: 085421. doi:10.1103/physrevb.73.085421.
- [50] J. Y. Huang, F. Ding, B. I. Yakobson, P. Lu, L. Qi, J. Li. In situ observation of graphene sublimation and multi-layer edge reconstructions. *Proc. Natl. Acad. Sci.* (2009) 106: 10103–10108. doi:10.1073/pnas.0905193106.
- [51] B. Borca, S. Barja, M. Garnica, M. Minniti, A. Politano, J. M. Rodriguez-García, J. J. Hinarejos, D. Farías, A. L. Vázquez de Parga, R. Miranda. Electronic and geometric corrugation of periodically rippled, self-nanostructured graphene epitaxially grown on Ru(0 0 1). *New J. Phys.* (2010) 12: 093018. doi:10.1088/1367-2630/12/9/093018.
- [52] A. T. N'Diaye, M. Engler, C. Busse, D. Wall, N. Buckanie, F.-J. M. zu Heringdorf, R. van Gastel, B. Poelsema, T. Michely. Growth of graphene on Ir(1 1 1). *New J. Phys.* (2009) 11: 023006. doi:10.1088/1367-2630/11/2/023006.
- [53] E. Miniussi, M. Pozzo, T. O. Menteş, M. A. Niño, A. Locatelli, E. Vesselli, G. Comelli, S. Lizzit, D. Alfè, A. Baraldi. The competition for graphene formation on Re(0 0 1): A complex interplay between carbon segregation, dissolution and carburisation. *Carbon* (2014) 73: 389–402. doi:10.1016/j.carbon.2014.02.081.
- [54] J. Wintterlin, M.-L. Bocquet. Graphene on metal surfaces. *Surf. Sci.* (2009) 603: 1841–1852. doi:10.1016/j.susc.2008.08.037.
- [55] H. Hattab, A. N'Diaye, D. Wall, G. Jnawali, J. Coraux, C. Busse, R. van Gastel, B. Poelsema, T. Michely, F.-J. Meyer zu Heringdorf, M. Horn-von Hoegen. Growth temperature dependent graphene alignment on Ir(1 1 1). *Appl. Phys. Lett.* (2011) 98: 141903. doi:10.1063/1.3548546.
- [56] X. Feng, S. Maier, M. Salmeron. Water splits epitaxial graphene and intercalates. *J. Am. Chem. Soc.* (2012) 134: 5662–5668. doi:10.1021/ja3003809.
- [57] S. Nie, W. Wu, S. Xing, Q. Yu, J. Bao, S.-s. Pei, K. F. McCarty. Growth from below: bilayer graphene on copper by chemical vapor deposition. *New J. Phys.* (2012) 14: 093028. doi:10.1088/1367-2630/14/9/093028.
- [58] M. P. Seah, W. A. Dench. Quantitative electron spectroscopy of surfaces: A standard data base for electron inelastic mean free paths in solids. *Surf. Interface Anal.* (1979) 1: 2–11. doi:10.1002/sia.740010103.
- [59] M. Pozzo, D. Alfè, P. Lacovig, P. Hofmann, S. Lizzit, A. Baraldi. Thermal expansion of supported and freestanding graphene: Lattice constant versus interatomic distance. *Phys. Rev. Lett.* (2011) 106: 135501. doi:10.1103/physrevlett.106.135501.
- [60] P. A. Brühwiler, A. J. Maxwell, C. Puglia, A. Nilsson, S. Andersson, N. Mårtensson.  $\pi^*$  and  $\sigma^*$  excitons in C 1s absorption of graphite. *Phys. Rev. Lett.* (1995) 74: 614–617. doi:10.1103/physrevlett.74.614.

- [61] B. Wang, S. Günther, J. Wintterlin, M.-L. Bocquet. Periodicity, work function and reactivity of graphene on Ru (0 0 0 1) from first principles. *New J. Phys.* (2010) 12: 043041. doi:10.1088/1367-2630/12/4/043041.
- [62] A. Martín-Recio, C. Romero-Muñiz, A. J. Martínez-Galera, P. Pou, R. Pérez, J. M. Gómez-Rodríguez. Tug-of-war between corrugation and binding energy: revealing the formation of multiple moiré patterns on a strongly interacting graphene-metal system. *Nanoscale* (2015) 7: 11300–11309. doi:10.1039/c5nr00825e.
- [63] J. W. May. Platinum surface LEED rings. *Surf. Sci.* (1969) 17: 267 – 270. doi:http://dx.doi.org/10.1016/0039-6028(69)90227-1.
- [64] P. Merino, M. Švec, A. L. Pinardi, G. Otero, J. A. Martín-Gago. Strain-driven moiré superstructures of epitaxial graphene on transition metal surfaces. *ACS Nano* (2011) 5: 5627–5634. doi:10.1021/nn201200j.
- [65] N. Ferralis, K. Pussi, S. E. Finberg, J. Smerdon, M. Lindroos, R. McGrath, R. D. Diehl. Low-energy electron diffraction study of potassium adsorbed on single-crystal graphite and highly oriented pyrolytic graphite. *Phys. Rev. B* (2004) 70: 245407. doi:10.1103/physrevb.70.245407.
- [66] H. Kazi, Y. Cao, I. Tanabe, M. S. Driver, P. A. Dowben, J. A. Kelber. Multi-layer graphene on Co (0 0 0 1) by ethanol chemical vapor deposition. *Mater. Res. Express* (2014) 1: 035601. doi:10.1088/2053-1591/1/3/035601.
- [67] A. J. Mannix, X.-F. Zhou, B. Kiraly, J. D. Wood, D. Alducin, B. D. Myers, X. Liu, B. L. Fisher, U. Santiago, J. R. Guest, M. J. Yacaman, A. Ponce, A. R. Oganov, M. C. Hersam, N. P. Guisinger. Synthesis of borophenes: Anisotropic, two-dimensional boron polymorphs. *Science* (2015) 350: 1513–1516. doi:10.1126/science.aad1080.
- [68] B. Feng, J. Zhang, Q. Zhong, W. Li, S. Li, H. Li, P. Cheng, S. Meng, L. Chen, K. Wu. Experimental realization of two-dimensional boron sheets. *Nat. Chem.* (2016) 8: 563–568. doi:10.1038/nchem.2491.

## Chapter 6

# Graphene-supported nanoclusters and nanoparticles: the role of the substrate

In the previous chapters, I have treated the interaction of Gr with atoms and molecules, with a specific focus on how the substrate supporting this 2D material affects it. In addition, I have shown the consequences of this interaction and its effects on some possible applications of Gr. In this chapter, I will move to the study of a different category of adsorbates on Gr, namely nanoclusters and nanoparticles. In particular, I will describe an example of a system where their properties are strongly influenced by the composition of the substrate below Gr: TiO<sub>2</sub> nanoparticles on Gr.

Nanoclusters are aggregates composed of a small number of atoms, *i.e.* from a few to few hundreds; their size is therefore in the nanometre (or sub-nanometre) range. Their peculiarity arises from their scale being intermediate between that of molecules and solids. For this reason, their electronic structure still exhibits discrete levels, rather than the continuous bands which characterize solids, yet for increasing size the energy distribution of their levels becomes more and more dense and their behaviour becomes increasingly similar to that of their bulk counterparts<sup>1,2</sup>. Many properties in nanoclusters, therefore, differ from those of the bulk form: in particular, these properties depend on the exact number of atoms constituting them, as will be discussed in the next chapter. This is due to the fact that as long as the electronic levels can be considered discrete, their number and separation depends on the linear combination of each orbital of each atom belonging to the cluster.

On the other hand, in aggregates of larger size, composed of several hundreds or even thousands of atoms, the electronic structure is already characterised by bands. These structures, whose size is between a few nanometres and 1  $\mu\text{m}$ , are known as nanoparticles. The properties of nanoparticles are not as dramatically dependent on size as those of nanoclusters, as the addition of a single atom is not able to significantly modify the band structure, unlike was the case for discrete levels. Nevertheless, their properties are significantly different from those of bulk materials, and gradually converge to those for increasing size.

Nanoclusters and nanoparticles can be produced with a wide variety in their chemical composition, as they can be composed of materials which are metals, semiconductors or insulators in their bulk phase. Moreover, they can either have elemental composition or contain compound species, such as in the case of metal-oxide or metal-alloy clusters<sup>2</sup>.

A very important consequence of the reduced size of nanoclusters and nanoparticles is their enhanced surface-to-bulk ratio. This is due to a purely geometrical consideration, as the former scales with  $N^2$  and the latter with  $N^3$ . For example, in a macroscopic solid with a volume of the order of the cubic centimetre, the bulk atoms are of the order of the Avogadro number ( $10^{23}$ ), while the surface atoms are only about  $10^{15}$ , or a fraction of  $10^{-8}$  of the total mass. Instead, in a nanoparticle of slightly less than 1000 atoms, almost half of the atoms are on the surface. This is particularly important for applications in heterogeneous catalysis, as only atoms exposed on the surface are accessible to the reactants and therefore contribute to the catalytic activity. Maximising the surface to bulk ratio is therefore a powerful tool to reduce the amount (and therefore the cost) of the catalyst required.

However, the high surface-to-bulk ratio alone is not sufficient to explain the extraordinary catalytic ac-

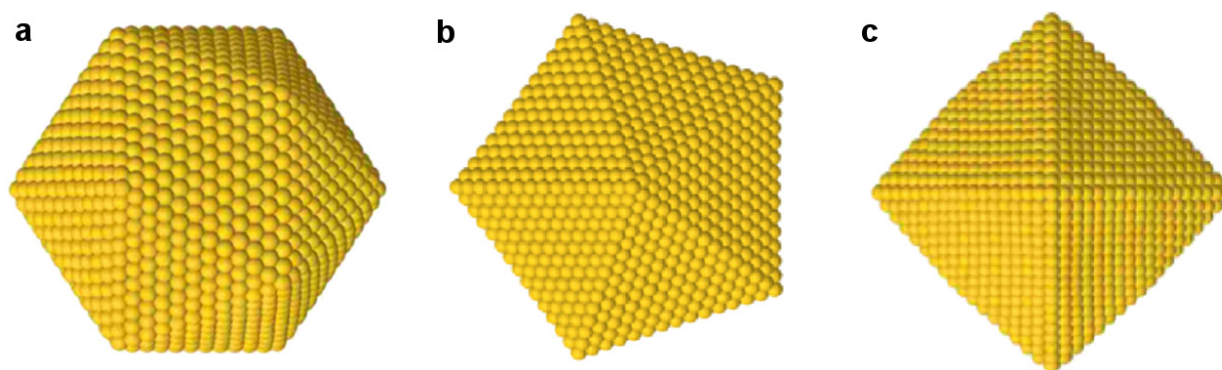


**Figure 6.1:** Calculated geometry of gold nanoparticles as a function of their size. a:  $\text{Au}_{3871}$  nanoparticle, having an icosahedral geometry. b:  $\text{Au}_{2815}$  nanoparticle with dodecahedral geometry. c:  $\text{Au}_{2894}$  nanoparticle, with octahedral geometry<sup>6</sup>.

tivity of nanoparticles. A very important example, in this respect, is the case of gold. In fact, while extended Au surfaces are known to be chemically inert (for example, it is the only metal where the chemisorption of oxygen is thermodynamically unfavoured), Au nanoparticles have shown a significant reactivity and a very high activity for the CO oxidation reaction, even at room temperature, which is dramatically dependent on size<sup>3,4</sup>. This surprisingly different behaviour with respect to the bulk material has been attributed to the high density of undercoordinated atoms, such as those found in the edges and corners of the nanoparticles, which can have as little as four nearest neighbours (whereas the atoms of an ideal surface have a coordination of 9). In fact, the increased reactivity of atoms depending on their coordination is well explained by the *d*-band model, described in Chapter 2<sup>4,5</sup>.

The coordination of the atoms in nanoparticles is intimately related to their geometric structure, which can also be dramatically dependent on their size. In fact, being their size finite, nanoclusters are not limited to the symmetries allowed by Bravais lattices, but can also organise into geometrical forms which are not able to form infinite periodic structures, such as dodecahedra or icosahedra, as shown in Figure 6.1<sup>2,7</sup>.

Besides these aspects related to their geometry, also the electronic structure of nanoparticles can be strongly influenced by their size. As the number of atoms in nanoparticles (unlike nanoclusters) is such that they have a band structure, the main mechanism by which the size affects it is quantum confinement. Basically, when the size of a system reaches the nanometre scale, the potential determining the electronic levels can not be approximated to a periodic potential as in extended solids, but must also take into account the boundary conditions given by the edges of the particles<sup>8,9</sup>. The generic effect of this different potential on their electronic structure is a shift in the bands with respect to those of the bulk counterpart, which, for the case of semiconductors, can lead to a modification in the band gap, as well as in the absolute HOMO and LUMO energies<sup>8,10,11</sup>. This has in turn consequences on the optical response of the system, with the optical absorption spectrum dramatically depending on the particle size<sup>8</sup>. An example of the outstanding optical properties of nanoparticles can be seen in the Lycurgus cup, a Roman item made of a dichroic glass, which is shown in Figure 6.2<sup>12</sup>. Due to the presence of gold nanoparticles in the glass, this cup, which is normally seen as green, changes to a bright red colour when illuminated in transmission rather than in reflection. Another consequence of the unique electronic structure of nanoclusters and nanoparticles are their remarkable magnetic properties, such as the giant magnetoresistance which is often observed in metal clusters<sup>13</sup>.

Thanks to these outstanding physical and chemical properties, nanoclusters and nanoparticles are widely used in many fields of materials science. For example, the chemical industry makes use of nanoparticles because of their enhanced chemical reactivity, as discussed above<sup>14–16</sup>. Other fields which could greatly benefit from the unique characteristics of nanoclusters and nanoparticles include biology<sup>17</sup>, optics<sup>9</sup>, and applications as light sources<sup>8</sup> or for nanoscale magnetic devices<sup>18</sup>.

The use of nanoclusters and nanoparticles, however, presents several difficulties. One important issue, related to their production, is the difficulty to precisely control their size, a key ingredient to fully exploit their potential by tuning this degree of freedom to achieve maximum performance. Another of the major





**Figure 6.2:** The Lycurgus cup, a 4<sup>th</sup>-century Roman cup made of glass, illuminated from the front (left) and from the back, in transmission (right). This dichroic effect is due to the presence of gold nanoparticles in its glass.

drawbacks in the use of these nanostructures on supporting surfaces is their thermal stability. Nanoclusters are in fact characterised by a very high mobility, which allows them to migrate on the substrates where they are deposited and sinter. This leads to an increase in their size and therefore to a degradation of their properties. Sintering is a thermodynamically favoured process: the only method to prevent it, therefore, is by addressing the kinematic factors of this process. The most obvious route to achieve this is by reducing the temperature, which is however not feasible for some applications. In alternative, reducing the density of nanoclusters increases their average separation, therefore reducing the probability that two particles diffuse towards each other. A much more viable and effective route to modify the mobility of nanoparticles and nanoclusters is by selecting an appropriate substrate, capable to fix their position or to reduce their mobility.

In this respect, the use of Gr as a substrate has proven a powerful tool to address both these issues. In particular, the moiré superstructure and moiré-induced corrugation formed by Gr on some metallic surfaces has been shown to induce a templating effect on nanoclusters supported on it<sup>19,20</sup>. In fact, due to the non-equivalence of the Gr atoms in the hills and valleys of the corrugation, adsorption on Gr is favoured in specific sites of this corrugation, while the mobility across different supercells is often reduced, as already discussed in Chapter 3.

In this chapter, I will describe a research work on a prototypical system where Gr was used as a template for the growth of titanium dioxide nanoarchitectures, which were specifically devised for an application in the field of catalysis – in particular, for the photocatalytic water splitting reaction –. The main focus of this work was to understand to which extent the interactions between the nanoclusters, the Gr layer and its substrate affect the properties of nanoclusters, and therefore to identify the main factors which can be tuned to improve the performance of such systems.

## 6.1 Graphene-titania nanoarchitectures for enhanced photocatalytic applications

Among the possible applications of nanoclusters, the one I have most extensively focussed on during my PhD research work is photocatalysis. Photocatalysis is a process by which a material is able to harvest

energy from electromagnetic radiation and employ it to activate a chemical reaction, thereby storing it as chemical energy. This process has been playing a major role on our whole ecosystem for billions of years: in fact, the most wide-spread photocatalytic process taking place on Earth is photosynthesis, where the excitation of chlorophyll organic molecule by light is converted into chemical energy through the splitting of a water molecule. Photocatalysis by inorganic materials was first demonstrated in 1972 by Fujishima and Honda, who observed the production of hydrogen and oxygen gas from an electrolytic cell when one electrode, composed of titanium dioxide ( $\text{TiO}_2$ , also known as titania), was exposed to ultraviolet radiation<sup>21</sup>.

Photocatalytic processes are usually found to occur on semiconductors, and depend on their band structure, which is characterised by a gap of the order of a few eV<sup>22</sup>. A schematical representation of the process is shown in Figure 6.3. Following the absorption of a photon having at least such an energy, an electron-hole pair can form following an electronic transition from the valence to the conduction band. The electron and hole thus created can separately participate to a redox reaction: in particular, the electron can participate to the reduction half-reaction, while the hole can participate to the oxidation. The redox potentials of the electrons and holes are respectively given by the absolute potentials of the valence band minimum (VBM) and conduction band maximum (CBM).

Titania, in particular, has a band gap of about 3 eV; the exact value depends on its crystal structure, with differences between them of the order of a few hundred meV. It has a relatively high oxidation potential, yet its reduction potential is modest when compared to the one required for several common reactions, including water splitting<sup>23</sup>. For this reason, its photocatalytic activity has been successfully employed for the oxidation of some species of pollutants<sup>22</sup>. However, the main objective of photocatalysis nowadays is the development of clean energy sources and of a hydrogen-based economy. In fact, photocatalysis represents a method for hydrogen production which uses exclusively renewable energy sources, and is therefore a powerful tool to address the problem of greenhouse emissions. However, no photocatalyst discovered up to now has a sufficient activity to make its application at industrial scale feasible<sup>22</sup>.

Among the main factors limiting the activity and applicability of photocatalysts, one of the most important is their low efficiency. This not only depends on the photon absorption probability, but is also significantly limited by the process of electron-hole recombination, which is in competition with the photocatalytic reaction. Other issues limiting the applicability of titania at the industrial scale include its wide band gap, which requires the use of ultraviolet radiation to generate electron-hole pairs, and the low reduction potential of its electrons, which impacts the efficiency of the reduction half-reaction.

Several approaches have been developed to improve the photocatalytic activity of titania and other photocatalytically active materials<sup>22,23</sup>. Firstly, generic approaches, commonly employed for any kind of catalyst, are based on increasing their surface to bulk ratio by reducing their size or increasing their porosity. For the specific case of photocatalysts, the use of a co-catalyst (which is usually an electrocatalyst) allows to address inefficiencies due to a lower activity for one of the two half-reactions. For example, connecting titania to a platinum electrode improves its activity towards water splitting, as the electrons can travel to this electrode and perform the hydrogen half-reaction on its surface, which is more active for that half-reaction<sup>21</sup>. The use of sensitizing dyes or of doping impurities provides a tool to allow the electron-hole excitation to occur even under exposure to radiation with a lower photon energy than the band gap, by providing intermediate states to which the electron can be promoted by low-energy photons, and from

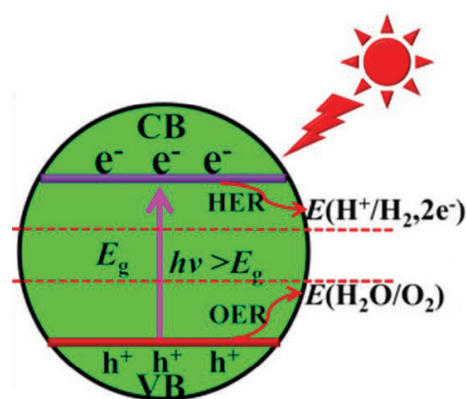


**Figure 6.3:** Schematic representation of the photocatalytic process<sup>23</sup>. The continuous violet and red lines represent the conduction band minimum and valence band maximum, respectively, separated by a band gap  $E_g$ . A photon (pink), of energy  $h\nu$ , generates an electron-hole pair. These, in turn, are involved in a reduction and oxidation reaction, respectively, provided their oxidation and reduction potentials (dashed lines) are both within the band gap.

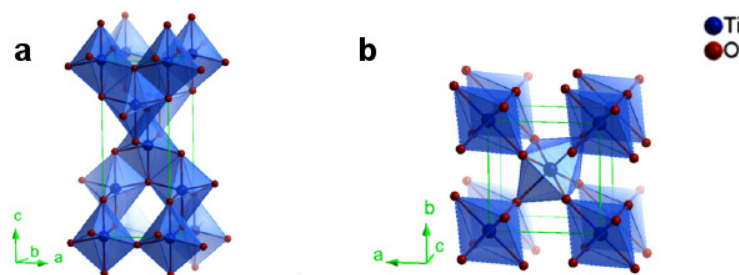


**Figure 6.4:** Crystal structure of the most common allotropes of titania<sup>22</sup>. a: anatase. b: rutile.

there reach the conduction band. Another route for modifying the photocatalytic activity of materials is by tuning their band structure in such a way to align the CBM and VBM to the redox potentials required by a specific reaction. This band structure engineering can be achieved by several approaches including nanoscale confinement and the formation of Schottky barriers by using a suitable substrate<sup>23</sup>. Moreover, for the particular case of titania – and other metal-oxide photocatalysts –, another important factor is the density of oxygen vacancies, as these defective sites introduce additional energetic levels into the band-gap region<sup>22,24,25</sup>. Finally, a very important property which is known to affect the photocatalytic activity of titania is its crystal structure. In fact, several allotropes of titania are stable in ambient conditions, the most commonly found being rutile (the thermodynamically stable one) and anatase (which is metastable), whose crystal structure is shown in Figure 6.4. Due to the different crystal structure, also the band structure is different in the two systems. Among the crystal structures formed by titania, the one which shows the highest photocatalytic activity is anatase<sup>22</sup>.

In this respect, carbon-based nanomaterials including Gr have proved very effective substrates for nanoclusters. For example, Gr oxide based titania nanocomposites have an outstanding photocatalytic performance, whose reason is still not fully understood yet, as the reduced size of these materials alone is not sufficient to account for it<sup>26</sup>. It has been proposed that the high mobility of charge carriers inside Gr acts by ensuring that the electron-hole pairs generated by photon absorption in titania are promptly separated, therefore reducing the probability of their recombination<sup>27</sup>. On the other hand, the charge transfer between titania and Gr could also contribute to a decrease in the catalyst's band gap, therefore lowering the absorption threshold<sup>28,29</sup>, or to a shift in the CBM and VBM<sup>23</sup>. Another possible route by which titania nanostructures stabilised by carbon-based nanomaterials acquire a higher activity is an increase in the density of oxygen vacancies<sup>25</sup>.

The aim of our experiment was therefore to evaluate the opportunities provided by the use of Gr as a substrate for titania nanoarchitectures, and explore the space of parameters which can be tuned to improve their photocatalytic efficiency. The choice of titania was due to the fact that it is a prototypical and well known system for photocatalysis: the aim of this experiment, however, was to derive some more generic conclusions on the effects of Gr on photocatalysts. In particular, we investigated the way in which modifying the electronic structure of Gr, by an approach based on a modification of the Gr-substrate interface similar to that described in Chapter 2, affects the photocatalytic activity of supported nanoparticles. This experiment was based on the synthesis of two different titania/Gr nanoarchitectures, shown in Figure 6.5b and c, where nanoclusters were supported respectively on metal- and metal-oxide-supported Gr, and their comparison

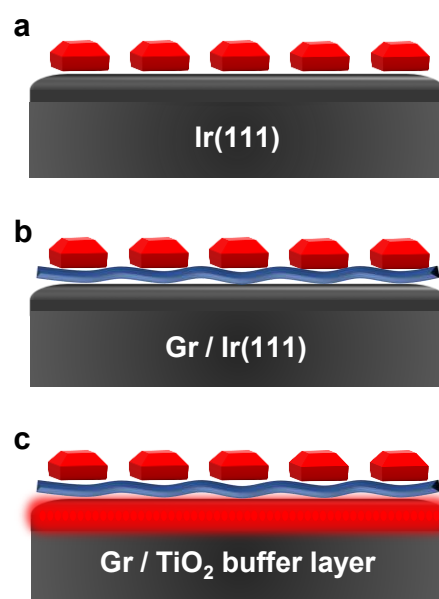


**Figure 6.5:** Schematic representation of the systems investigated in this experiment. a:  $\text{TiO}_2/\text{Ir}(111)$ . b:  $\text{TiO}_2/\text{Gr}/\text{Ir}(111)$ . c:  $\text{TiO}_2/\text{Gr}/\text{TiO}_x/\text{Ir}(111)$ .

with a control system composed of a titania thin film directly deposited on a metal substrate (Figure 6.5a). To investigate which of the mechanisms described above take place in these systems, and which of them play a major role on the photocatalytic activity of Gr, a systematic structural and electronic characterisation was performed by using a combination of several experimental techniques: these measurements were accompanied by photocatalytic measurements of hydrogen production from photocatalytic water splitting, performed by the research group of Prof. Fornasiero, at the Chemistry Department of the University of Trieste, to correlate the electronic and structural properties of the nanoparticles and their substrate with their effect on the formers' activity.

### 6.1.1 Experimental methods

The three different nanoarchitectures were obtained by Ti deposition from a high purity filament, followed by oxidation by exposure to oxygen pressures up to  $5 \times 10^{-6}$  mbar. The dose of Ti deposited was monitored by using a quartz microbalance; the same quantity of Ti was deposited in all three systems. The substrates which were chosen for the Gr-based systems were Gr/Ir (1 1 1) and Gr/1 ML  $\text{TiO}_x$ /Ir (1 1 1). The reason for this choice is that while Gr/Ir (1 1 1) still exhibits small perturbations to its band structure due to the (albeit weak) Gr-metal interaction, metal-oxide layers below Gr have proven effective in completely decoupling the carbon honeycomb from the substrate, as well as in modifying its doping level<sup>30–33</sup>. A control system was also synthesised, where titanium was deposited and oxidised on a clean Ir (1 1 1) surface. A schematic view of the three systems is shown in Figure 6.5. The Gr/ $\text{TiO}_x$  interface was obtained in two steps. Firstly, 1 ML metallic Ti was intercalated below Gr, following the same procedure described in Chapter 2.3. The titanium was subsequently oxidised by exposing the sample to about  $5 \times 10^{-3}$  mbar  $\text{O}_2$  (local pressure on the surface) introduced through a doser, while the sample was kept at a temperature of 573 K, following a procedure similar to the one adopted in previous experiments<sup>31,32</sup>.

Each sample was characterised by high energy resolution XPS and NEXAFS measurements. In addition, the work function of the samples was measured by Photoemission Spectroscopy, by measuring the kinetic energy of the onset of the secondary electrons: in fact, the lowest-energy electrons to be emitted from a surface are those whose total energy is just above its work function. To ensure that these electrons had sufficient energy to cross the vacuum and overcome the barrier represented by the analyser work functions, they were accelerated by applying a potential of  $-10$  V to the sample<sup>34</sup>.

Finally, a particular focus was dedicated to the characterisation of the valence band of the sample. In fact, the VBM (together with the CBM, which can be instead found by probing the unoccupied states with NEXAFS) represents one of the main factors determining the photocatalytic activity of a material<sup>23,35</sup>. In addition, the presence and density of the defect states in the valence band was investigated by valence band photoemission. In fact, previous studies on bulk and nanostructured  $\text{TiO}_2$ <sup>25,36</sup> have identified specific features associated with the presence of oxygen vacancies.

However, the electronic structure of our interfaces is quite complex and does not allow to distinguish most of its features, which prevents us from accurately calculating the density of oxygen vacancies which are present in the different systems. In order to overcome this issue, we have employed REsonant PhotoEmission Spectroscopy (RESPES) to improve chemical sensitivity in valence band photoemission spectra. This is a technique based on a combination of valence band photoemission and NEXAFS, which is performed by measuring the valence band photoemission spectrum while scanning the photon energy across an absorption edge<sup>37</sup>. A resonance condition occurs when the kinetic energy of a photoelectron from a specific valence state corresponds to that of an Auger electron from a participant decay process, described in Chapter 1.3. This leads to an increase in the photoemission signal from the valence states of an element when the photon energy corresponds to its absorption edge. Therefore, it allows to correlate a specific feature in the valence band to a specific NEXAFS edge and thus to a specific element and oxidation state<sup>35</sup>. RESPES, therefore, provides increased chemical sensitivity for valence band features and has proved particularly effective for investigating the electronic structure of transition metal oxides<sup>38,39</sup>.

Being a combination of photoemission and NEXAFS measurements, RESPES is also a powerful method to investigate both the occupied and unoccupied states, with elemental selectivity. For this reason, we also used it to calculate the band gap of our titania nanoparticles while preventing the electronic structure



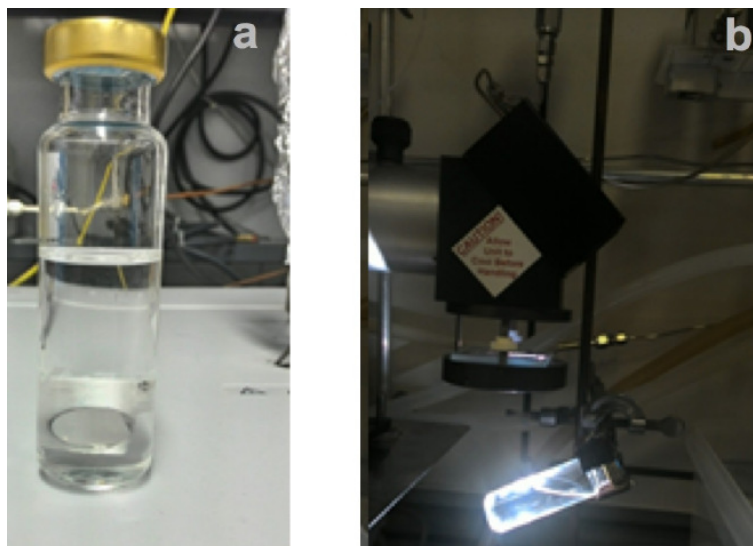


**Figure 6.6:** Setup employed for the photocatalytic activity measurements. a: Sample positioned and sealed in a vial, in a water-methanol solution. b: Sample exposed to visible radiation equivalent to 1 sun.

of the substrate from affecting the measurement. More in detail, the valence band spectrum allows to measure the VBM of the system, which corresponds to the BE onset of the resonant features, excluding those originated by defect-induced states. Likewise, the CBM can be obtained from the photon energy onset of the resonances of the features associated to the transitions to the lowest-lying unoccupied band, again excluding the defect-induced states. In fact, such photon energy corresponds to the BE difference of the initial and final state, and therefore allows to calculate the BE of the latter by subtracting the BE of the former from the photon energy. The band-gap is then equal to the sum of the absolute values of the VBM and CBM, referred to the Fermi level<sup>35</sup>.

In addition to the electronic characterisation of the titania nanostructures, their morphology and geometry was characterised by Scanning Tunnelling Microscopy, performed with a SPECS instrument. In addition, NEXAFS was also employed to determine the local crystalline configurations of the Ti atoms in the system, by comparing the modulation observed in the post-edge region with those of the most common allotropes of bulk titania<sup>40</sup>.

Finally, the photocatalytic activity measurements were performed by immersing the sample in a 12.5 mL solution with water and methanol in a 1:1 ratio and exposing it to visible radiation, using sensitizers in visible range. The setup is shown in Figure 6.6. In particular, the vial was first sealed using appropriate rubber septa and air was removed by bubbling Ar for 30 minutes. After this equilibrium period, the sealed vial was irradiated under radiation equivalent to 1 Sun for 20 hours. The analysis of the reaction products was performed by injecting 50  $\mu$ L of the gas phase into a gas chromatograph (Agilent 7890). A Thermal Conductivity Detector was used for the quantification of  $H_2$ , using a MoSIEVE 5A column with Ar as carrier gas.

### 6.1.2 Experimental results

#### Structural characterisation

Figure 6.7 shows selected STM images of the  $TiO_2/Gr/TiO_x/Ir(1\ 1\ 1)$  system. This image shows that the surface is homogeneously covered by particles with a diameter of the order of a few tens of nm; they are separated by narrow regions of bare Gr. In particular, the statistical distribution of the sizes of these aggregates is reported in Figure 6.8: this distribution is centred around an average value of 15 nm, indicating that titania forms nanoparticles when grown on Gr, with a size ranging from 10 to 30 nm.

The fact that the deposition of metallic Ti on Gr at room temperature results in the formation of nanoparticles has been observed before<sup>41</sup>. In addition, the size distribution of the  $TiO_2$  nanopar-

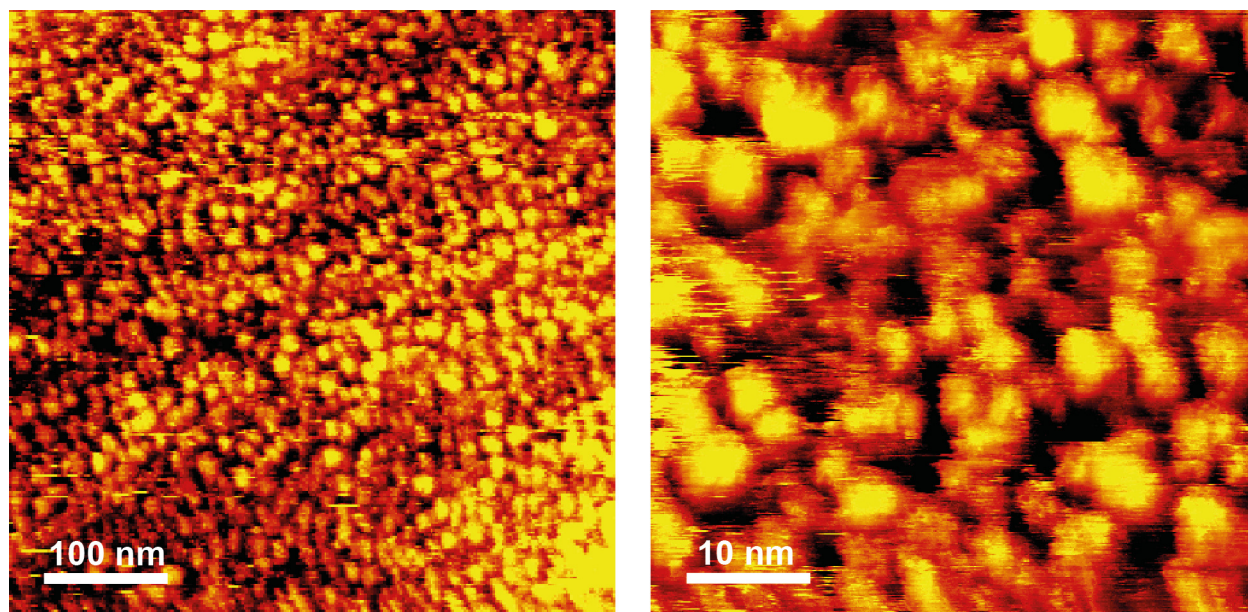


**Figure 6.7:** STM images of  $\text{TiO}_2$  nanoparticles grown on  $\text{Gr}/\text{TiO}_x/\text{Ir}(1\ 1\ 1)$ , acquired on regions of different lateral size.

ticles observed in our experiment is similar to the one reported for metallic Ti, even though the average size of the former is slightly larger. This indicates that the oxidation of the nanoparticles at room temperature did not induce coalescence phenomena.

Finally, also for the  $\text{TiO}_2/\text{Gr}/\text{Ir}(1\ 1\ 1)$  system a similar distribution in the nanoparticle sizes was found, indicating that the presence of the  $\text{TiO}_x$  layer below Gr does not affect the size of the nanoparticles supported on it.

The local crystal structure in these particles was investigated by the analysis of the NEXAFS spectra measured at the Ti  $L_{2,3}$ - and O K-edge, which are reported in Figure 6.9. In particular, the Ti  $L_{2,3}$ -edge spectra of the three systems investigated in this experiment are shown in Figure 6.9a. These spectra show two groups of features: one, found between about 455 and 461 eV, corresponds to the Ti  $L_3$ -edge, the other, between 461 and 468 eV, corresponds to the Ti  $L_2$ -edge. The features found in the latter region are generally broader than those of the former: this can be attributed to the larger intrinsic broadness of the initial state, *i.e.* the Ti  $2p_{1/2}$  core level. Each of these regions are characterised by a strong pre-edge feature, which are clearly structured, as it shows two distinct absorption maxima, which for the  $L_3$  edge are found at about 458.2 and 459.8 eV respectively. Their position on the energy scale, as well as their relative intensities, do not significantly change between the three different systems. These features can be both attributed to a transition from the Ti  $L_{2,3}$  shells, *i.e.* the  $2p_{1/2}$  and  $2p_{3/2}$  core levels respectively, to the unoccupied  $3d^*$  bound states<sup>38,40</sup>. The reason for the splitting can be ascribed to the crystal geometry, characterised by a distorted octahedron of O atoms around each Ti atom: this distortion in the geometry leads to a breaking of the degeneracy of the  $3d^*$  bands into two distinct bands, commonly denoted as  $t_{2g}$ , at lower energy, and  $e_g$ , at higher energy. However, the distortion in the octahedra is different depending on the crystal structure of  $\text{TiO}_2$ : for this reason, the energy position of these features can be used as a fingerprint to determine the local crystal symmetry around the Ti atoms<sup>40</sup>. While the energy of the feature

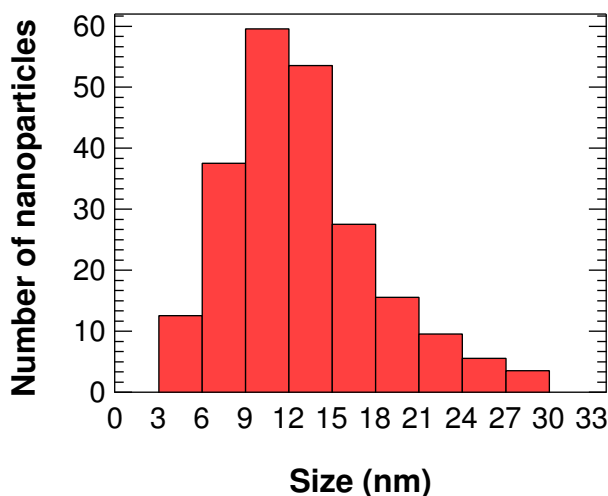


**Figure 6.8:** Size distribution of the  $\text{TiO}_2$  nanoparticles grown on  $\text{Gr}/\text{TiO}_x/\text{Ir}(1\ 1\ 1)$ , obtained from the STM image in Figure 6.7, left.

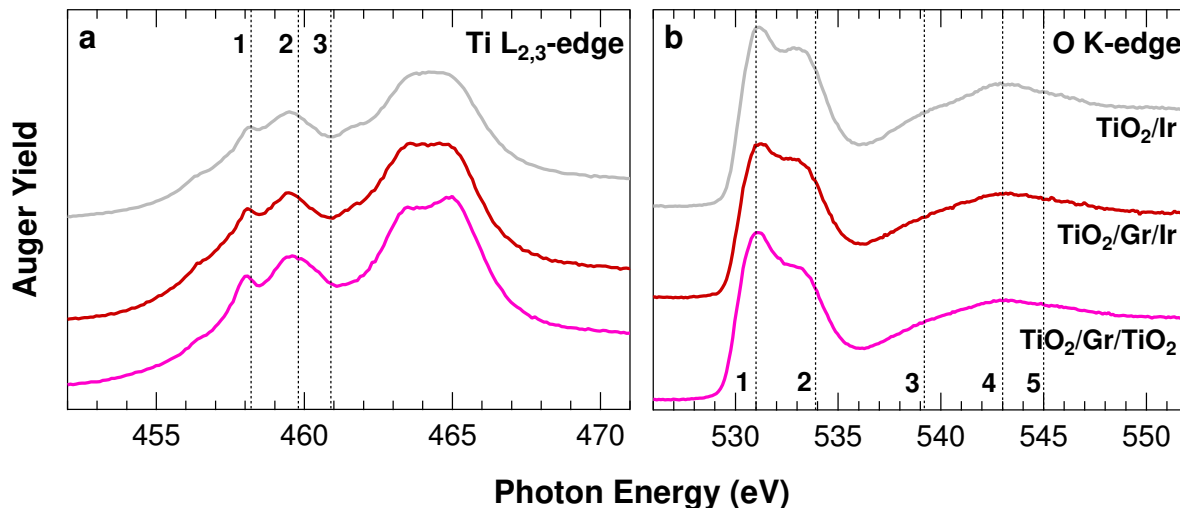


**Figure 6.9:** NEXAFS of the three titania-based nanoarchitectures. The energies at which the most prominent features are usually found in the spectra of bulk titania samples are indicated with dotted lines<sup>40</sup>. a: Ti  $L_3$  (feature at lower energy) and  $L_2$  (feature at higher energy) absorption edges. b: O K-edge.

originated by the  $t_{2g}$  final state, denoted as 1 in Figure 6.9a, is not significantly affected by the geometry, that of the  $e_g$  state increases by about 1.1 eV between anatase and rutile: in particular, it is found at an energy of 459.8 eV (indicated as 2 in the figure) in anatase, while it shifts to 460.9 eV in rutile (indicated as 3)<sup>38,40</sup>. While our spectrum is significantly broader than that of an extended titania surface, which can be attributed to a lower degree of order, it is clear from the spectra that all three systems show a maximum in their absorption spectra at 2 and a relative minimum at 3. This is a fingerprint that the local geometric structure around the Ti atoms is more similar to that of bulk anatase than rutile.

The absorption spectrum close to the O K-edge is reported in Figure 6.9b. As for the case of the Ti  $L_{2,3}$ -edge, the three spectra do not show significant differences from each other. Two distinct features (indicated as 1 and 2) are clearly visible at 531 and 533.9 eV, which, as for the case of the Ti L-edge, are due to a transition to the  $3d^*$  orbitals of  $t_{2g}$  and  $e_g$  symmetry. This transition is allowed even though in this case the initial state corresponds to an s orbital, as these  $3d^*$  bands are originated by the hybridisation of O  $2p$  and Ti  $3d$  states<sup>40</sup>. For the case of the O K-edge, no evident difference is reported in these two most prominent features allowing to distinguish between different crystal structures<sup>40</sup>. While some differences in the features indicated as 3, 4 and 5 are reported in literature, the broadness they show in our spectra does not allow to further refine the results obtained from the Ti  $L_{2,3}$ -edge, indicating an anatase-like local crystal structure.

### Electronic characterisation

The identification of the oxidation states of titanium in each system was performed by a quantitative analysis of the photoemission spectra of the Ti  $2p_{3/2}$  and O  $1s$  core levels. During the analysis of the Ti  $2p$  spectra, particular care was taken to the buried  $\text{TiO}_x/\text{Ir}$  (1 1 1) interface. In fact, those atoms at the interface with Ir can have significantly different properties, for various reasons. Firstly, as explained in Chapter 2, the first layers in contact with the interface may grow with a strained lattice parameter matching the one of the surface below<sup>42,43</sup>. Moreover, the different chemical environment of these atoms can lead to the formation of an oxide layer having a different composition from that found on either side of the interface<sup>44,45</sup>. This has been observed for example after the growth of titanium oxide films of few-layer thickness on the Pt (1 1 1) surface, which has properties very similar to those of Ir (1 1 1)<sup>44,46</sup>. In fact, in this system, the first layer Ti atoms are found in a much lower oxidation state, with a stoichiometry that depending on the growth conditions varies between  $\text{TiO}$  and  $\text{TiO}_{1.5}$ .

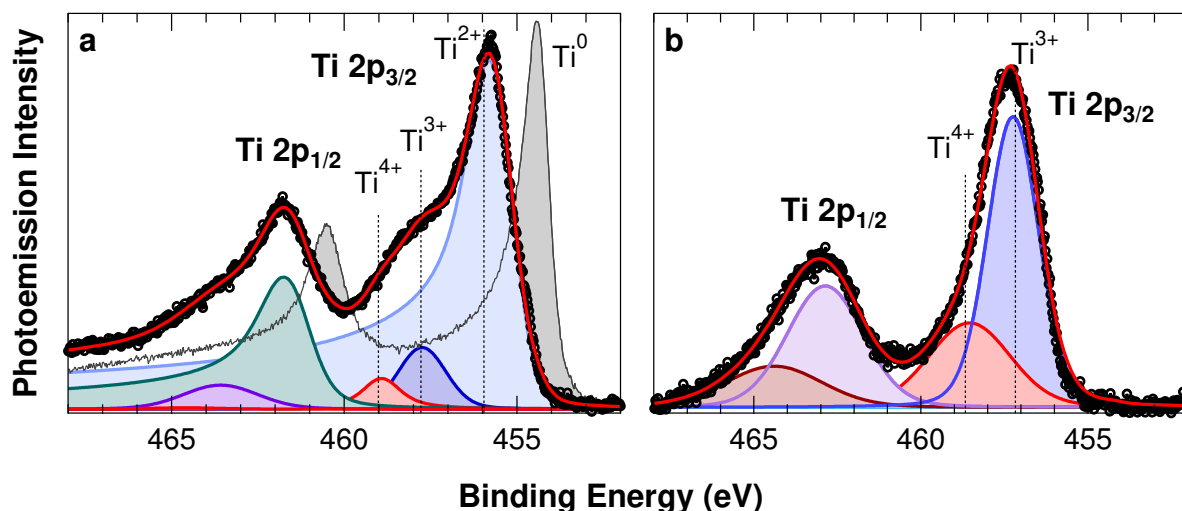


**Figure 6.10:** Ti  $2p$  photoemission spectra ( $h\nu = 550$  eV) of an oxidised single layer of Ti on Ir (1 1 1), with the de-convoluted components. a: oxidised titanium on bare Ir (1 1 1). The spectrum of the as deposited metallic titanium is shown in the background for comparison (grey curve). b: oxidised titanium intercalated below Gr/Ir (1 1 1).

For the case of our experiment, the study of the  $\text{TiO}_x/\text{Ir}$  interface was particularly important as it influences the properties of our oxide-supported Gr sample. In addition, this interface is also found buried below the  $\text{TiO}_2/\text{Ir}$  film in our control sample. To properly characterise these interfaces, the Ti  $2p$  spectra of a single layer of oxidised titanium on Ir (1 1 1), both covered by Gr or not, were studied. These spectra are reported in Figure 6.10. The Ti  $2p$  spectra are characterised by two main features, originated by the  $2p_{3/2}$  and  $2p_{1/2}$  spin-orbit splitting. The latter is significantly broader, due to the larger FWHM of the intrinsic lineshape: consequently, a quantitative analysis of the spectrum was only performed on the former. However, due to the fact that the separation between the core levels is very close to the chemical shifts observed in the spectrum, the fit had to be performed by including both spin components anyway, in order to properly deconvolute them; in any case, the components of the  $2p_{1/2}$  core level could not be reliably deconvoluted from each other.

The Ti  $2p_{3/2}$  spectrum of 1 ML  $\text{TiO}_x/\text{Ir}$  (1 1 1) is shown in Figure 6.10a. This spectrum is characterised by an intense feature at about 456 eV, with a FWHM of almost 2 eV, and some additional features at higher BE: one is found at about 458 eV, the other at about 459 eV. These three components can be associated to different oxidation states of Ti, in particular to  $\text{Ti}^{2+}$ ,  $\text{Ti}^{3+}$  and  $\text{Ti}^{4+}$  respectively<sup>47</sup>. The lineshape of the  $\text{Ti}^{2+}$  component shows a significant asymmetry ( $\alpha = 0.2$ ), which reflects its metallic character<sup>48</sup>. On the contrary, the lineshape of the components associated to higher oxidation states is symmetric, indicating the presence of a band gap. A quantitative analysis reveals that the  $\text{Ti}^{2+}$  component constitutes about  $(80 \pm 5)\%$  of the total spectral weight, while the remaining is in a higher oxidation state. The large FWHM of the components suggests that the system is actually more complex, as the oxidation state of the Ti atoms is better described by a distribution centred around a value slightly higher than +1 than by three discrete states, as was reported for the case of Pt (1 1 1)<sup>49</sup>.

Figure 6.10b shows the Ti  $2p$  spectrum of the intercalated layer of oxidised titanium below Gr. The Ti  $2p_{3/2}$  core level is clearly shifted towards higher BE with respect to the previous system. In particular, in this system, the component with the highest spectral weight ( $(67 \pm 5)\%$ ) is the one originated by  $\text{Ti}^{3+}$ ; additionally, a  $\text{Ti}^{4+}$  component is also visible, with a spectral weight of about  $(33 \pm 5)\%$ . This corresponds to an average oxidation state of Ti slightly higher than +3. The different oxidation state in this system could depend either on the presence of the Gr layer, which modifies the thermodynamics of the system, or to the higher temperature used for oxidation. Indeed, a stoichiometry of  $\text{Ti}_2\text{O}_3$  was observed for oxidised titanium films grown on Pt (1 1 1) at about 600 K, the same temperature we have employed for the oxidation of this system<sup>49</sup>.



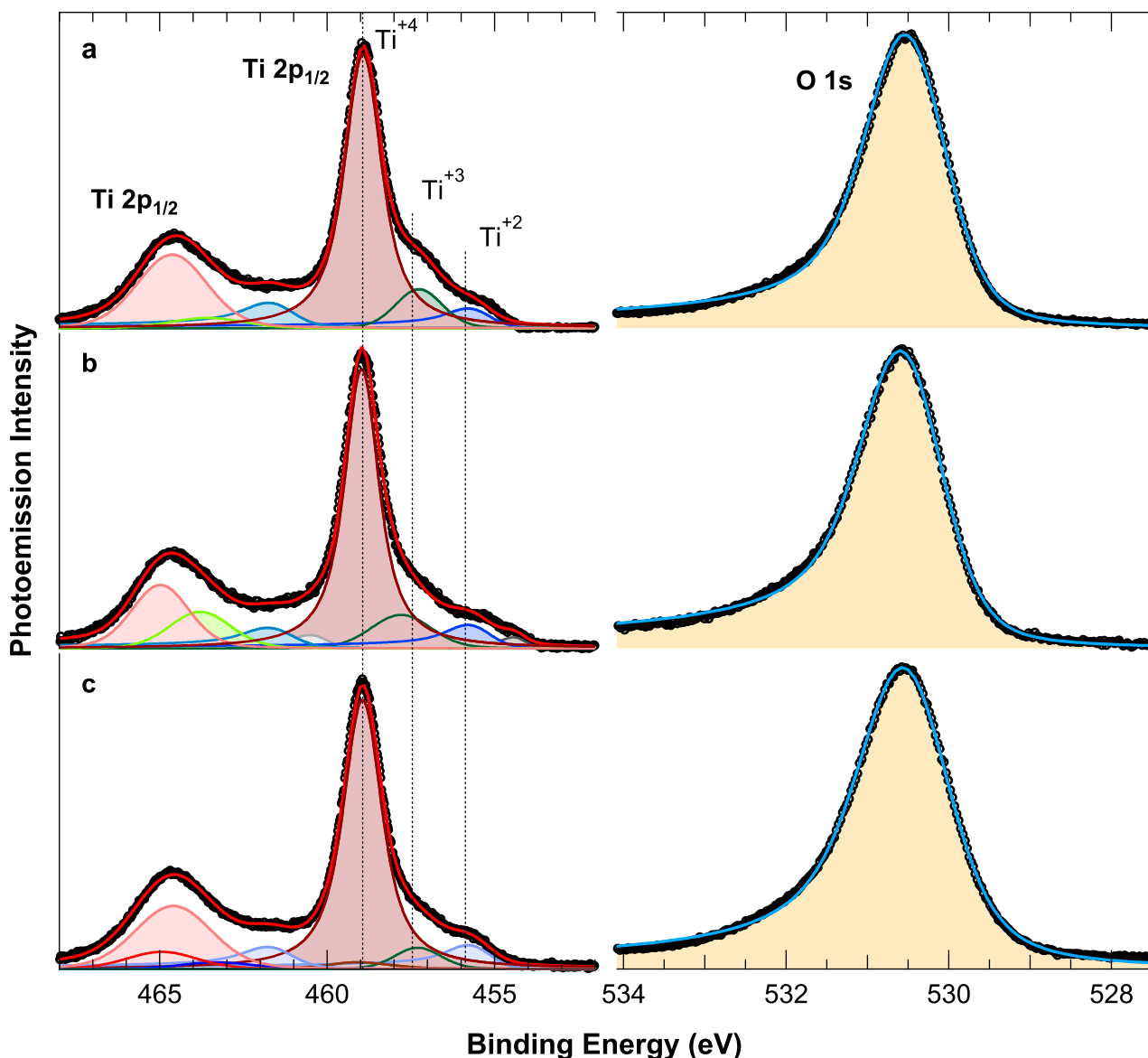


**Figure 6.11:** Ti 2p ( $h\nu = 550$  eV; left) and O 1s ( $h\nu = 650$  eV; right) photoemission spectra of the three titania/Gr and titania/Ir nanoarchitectures, together with the deconvoluted components. a: TiO<sub>2</sub>/Ir (1 1 1). b: TiO<sub>2</sub>/Gr/Ir (1 1 1). c: TiO<sub>2</sub>/Gr/TiO<sub>x</sub>/Ir (1 1 1).

Following this characterisation of the buried TiO<sub>x</sub>/Ir interface, we proceeded to the evaluation of the oxidation state of the surfaces of the three TiO<sub>2</sub> samples. The spectra of the Ti 2p region are shown on the left side of Figure 6.11. In all three systems, the main spectral feature is the one attributed to Ti<sup>4+</sup>, at about 459 eV. Additional components are present at lower BE, and are a fingerprint of the presence of oxygen vacancies on the exposed surface. For the case of the titania nanoparticles on the oxide-supported Gr, also the components originating from the buried interface below Gr were included in the fit (see above). However, due to the attenuation of the photoemission signal from this layer, the spectral weight of these components is small (few percent) with respect to those originating from the exposed surface and therefore their presence does not significantly affect our results. In all three systems, the relative spectral weight of the Ti<sup>4+</sup> is between  $(75 \pm 5)\%$  and  $(82 \pm 5)\%$ , indicating the presence of a significant density of oxygen vacancies in all systems. Based on the crystal structure of anatase, shown in Figure 6.4, where each O atom is coordinated to three Ti atoms, the number of O vacancies is one every three Ti atoms in +3 oxidation state. Therefore, the density of O vacancies on the surface in our nanoparticles is between  $(6 \pm 2)\%$  and  $(8 \pm 2)\%$ , not significantly different between the three systems.

To further characterise the oxidation state of these systems, we also analysed the O 1s core level, shown in Figure 6.11 on the right. All spectra can be fitted by a single component, centred at 530.49 eV. The lineshape of this component has a relatively large FWHM, namely 1.26 eV, while the asymmetry is 0.12. A component at this BE has been reported in studies of extended titania surfaces such as  $\text{TiO}_2(110)^{50,51}$  and  $\text{TiO}_2(001)^{52}$ . The large FWHM and asymmetric shape of the O 1s component can be attributed to several factors. For example, it could reflect a distribution of non-equivalent configurations of the O atoms found in the bulk, on surfaces with different termination or on the steps and edges of the nanoparticles, leading to small shifts in their core-levels which cannot be resolved individually. A further contribution to the broadening and asymmetry can originate from final state effects related to vibrational excitations. Finally, the tail at higher BE can also be originated by small traces of adsorbates such as OH groups, which are known to originate features at higher BE in the O 1s spectrum<sup>52,53</sup>.

Beside the characterisation of the oxidation state of titania, XPS was also employed to investigate the charge transfer occurring between Gr, its substrate and the clusters. In fact, as already mentioned, the doping of Gr is influenced by both these factors. On the other hand, a shift in the bands of the semiconductors, due to the junction which is formed between them and Gr due to a different degree of doping, is one of the mechanisms by which Gr can enhance the photocatalytic activity of the former<sup>23</sup>.

The C 1s level was therefore studied to analyse the effect of the titania deposited above or below Gr on its doping. In fact, for Gr weakly interacting with its substrate, the C 1s core level BE has been found to be in a linear relation with its doping<sup>54</sup>. Figure 6.12 shows the C 1s core level of Ir- and  $\text{TiO}_x$ -supported Gr, before and after the deposition of the titania nanoparticles. In particular, the C 1s spectrum of Gr/Ir is centred at 284.12 eV, indicating a weak p doping<sup>31</sup>. The intercalation of a layer of titanium oxide below Gr causes a shift of the C 1s core level to an even lower binding energy by about 0.50 eV, indicating that, in this configuration, Gr has a stronger degree of p doping. The deposition of titania on the two systems, instead, introduces a certain degree of n doping into Gr. In fact, when deposited on Gr/Ir, the nanoparticles induce a shift in the C 1s of Gr towards higher BE by 0.18 eV; while on the oxide-supported Gr they partially compensate the p doping effect of the substrate, reducing the shift with respect to Gr/Ir to only 0.18 eV towards lower BE.

We have also investigated the role of Gr and its substrate on the work function of the three systems. Figure 6.13 displays the work function of the three substrates, before (circles) and after (squares) the deposition of the nanoparticles. The work function of titania is of about 5 eV in all three systems. However, there are small differences of a few hundred meV between them. In particular, the work function of the Ir-

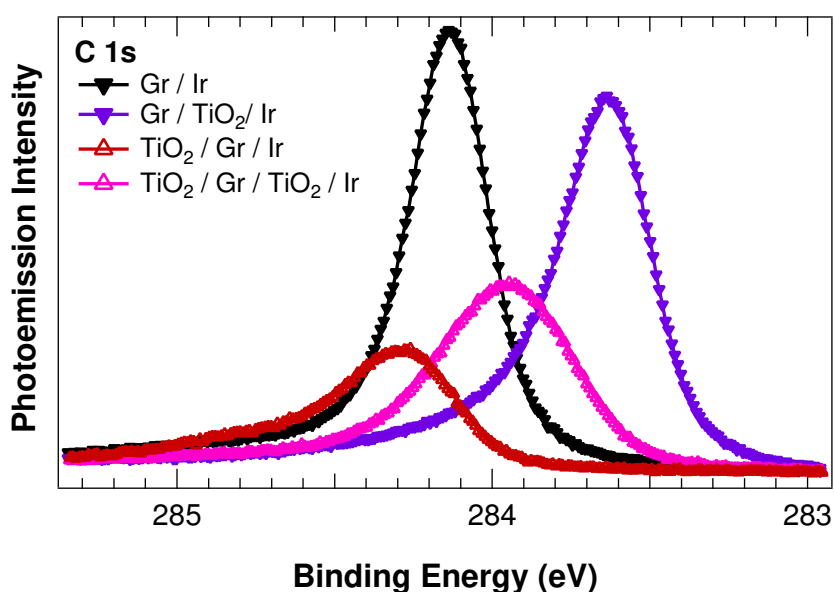


**Figure 6.12:** C 1s core level photoemission spectra ( $h\nu = 400$  eV) measured on the Gr/Ir(111) and Gr/ $\text{TiO}_x$ /Ir(111) systems, before and after the growth of the  $\text{TiO}_2$  nanoparticles.

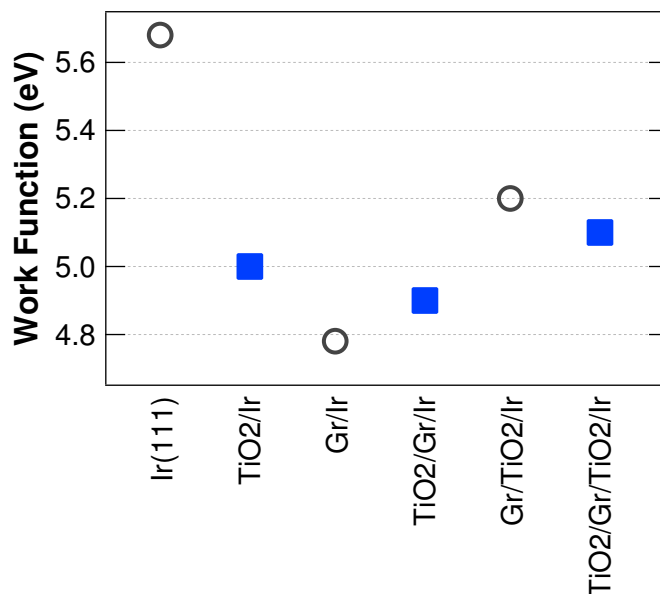


**Figure 6.13:** Work function of the three titania nanoarchitectures (blue squares), compared to that of their substrates (black circles).

and titania-supported Gr reflects the shift observed also in the C 1s core level. In fact, the work function of the former is lower than that of the latter by about 400 meV. On the other hand, the difference in the work function of these two Gr substrates also affects that of the nanoparticles supported on them, to a lesser degree, as those grown on the oxide-supported Gr have a lower work function by about 200 meV.

However, a similar consideration does not apply to the TiO<sub>2</sub>/Ir system, which shows a work function which is intermediate between these two values, even though that of Ir (1 1 1) is significantly higher than that of both Gr systems. This could be due to the fact that as, according to literature, titania forms larger islands in this system, their behaviour is less affected by the substrate than that of nanoparticles<sup>49</sup>.

Finally, RESPES has been used to identify and characterise the states originated by titania in the valence band of our three systems. The plot of the photoemission intensity is shown in a colour scale in Figure 6.14, as a function of the photon energy, which was scanned across the Ti L<sub>3</sub> absorption edge. In all three systems, three features are clearly visible which show a resonant enhancement in their photoemission intensity for photon energies between 458 and 460 eV. These photon energies correspond to the maxima in the absorption spectrum (Figure 6.9a). In particular, these resonating features are found at BEs between the Fermi level and 1 eV, between 4 and 9 eV and at about 23 eV. The latter two features are attributed respectively to hybridised O 2p-Ti 3d states and to the O 2s level<sup>25</sup>. The feature close to the Fermi level, on the other hand, is widely recognised as a fingerprint of the defect states which are introduced into the band gap by the self-doping of titania by Ti atoms in a lower oxidation state due to an adjacent oxygen vacancy<sup>22,38,39,55</sup>. A quantitative comparison does not show significant differences between the two Gr-supported titania nanoarchitectures (Figures 6.14b and c); also the TiO<sub>2</sub>/Ir structure, despite showing on average a stronger photoemission intensity, does not show appreciable differences in the relative spectral weight nor in the BE and photon energy position of these features.

From the RESPES measurements, we also calculated the band gap of titania in all three systems, as well as the potentials of the VBM and CBM with respect to the Fermi level, using the procedure described in Chapter 6.1.1. In particular, in all our systems, a VBM of -3.3 eV and a CBM of 1.0 eV were found. This, in turn, corresponds to a band-gap of 4.3 eV: these values are in agreement with the one measured for bulk anatase using the same method<sup>35</sup>. This value is actually overestimated, when compared to the one obtained from other methods, mainly due to the errors introduced by Koopmans' approximation and to final state effects. Nevertheless, differences between values calculated with this method can be calculated with high accuracy. Therefore, based on the values reported in literature for bulk anatase, we can estimate that the optical band-gap value would be the same of anatase, *i.e.* 3.2 eV<sup>22</sup>.

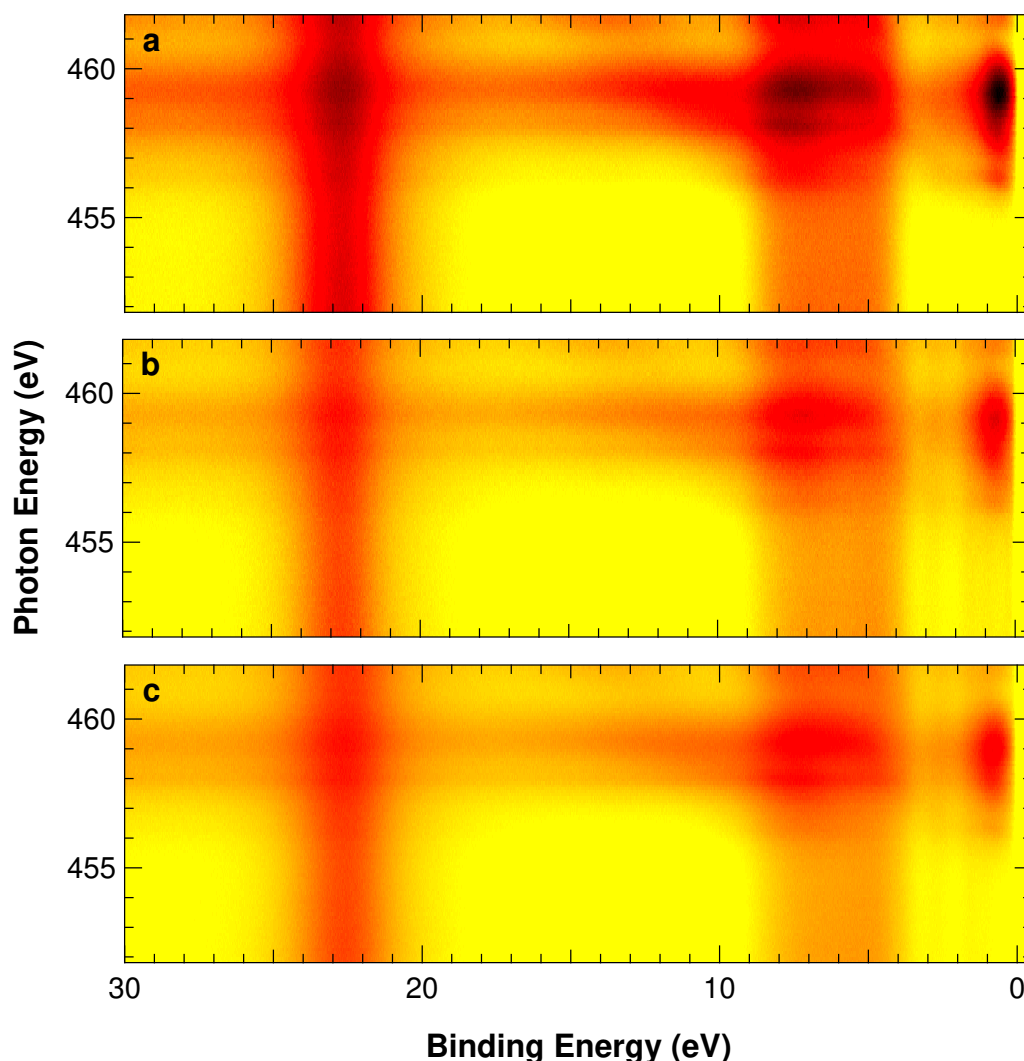


**Figure 6.14:** Resonant photoemission spectra of the three titania/Gr and titania/Ir nanoarchitectures, measured across the Ti  $L_3$ -edge. The photoemission intensity is plotted in colour scale: dark colours represent higher photoemission intensity. a:  $\text{TiO}_2/\text{Ir}$  (1 1 1). b:  $\text{TiO}_2/\text{Gr}/\text{Ir}$  (1 1 1). c:  $\text{TiO}_2/\text{Gr}/\text{TiO}_x/\text{Ir}$  (1 1 1).

### Photocatalytic activity

The results of the measurement of the photocatalytic activity of the three systems are reported in Table 6.1, which shows the hydrogen produced by the three different systems, normalised to the total moles of titania.

In particular, this dose was the same in all three systems, as verified with the quartz microbalance. Its precise value was calculated from the attenuation of the photoemission signal of the Ir  $4f_{7/2}$  core level due to inelastic scattering by the  $\text{TiO}_2$  layer, as described in Chapter 1.4. However, this calculation assumes that the thickness of the  $\text{TiO}_2$  layer is uniform on the surface: for this reason, it is not accurate in calculating the dose on the systems where  $\text{TiO}_2$  forms nanoparticles, where there are some uncovered Gr regions at the boundary where the attenuation is much lower. For this reason, the measurement of the  $\text{TiO}_2$  dose by this method was only performed on the  $\text{TiO}_2/\text{Ir}$  (1 1 1) system, as the oxide layer has a more uniform thickness and higher flatness there<sup>44</sup>; minimal differences in the exact amounts were accounted for by correcting this value by the quartz microbalance readings.

By comparing the first two systems, it is clear that the use of Gr as support has a significant effect on the activity of titania: for example, its activity shows an almost four-fold increase when the titania is

System	H <sub>2</sub> production (mol/mol(TiO <sub>2</sub> ))
TiO <sub>2</sub> /Ir (1 1 1)	3
TiO <sub>2</sub> /Gr/Ir (1 1 1)	11
TiO <sub>2</sub> /Gr/TiO <sub>x</sub> /Ir (1 1 1)	67

**Table 6.1:** Photocatalytic hydrogen production from a water/methanol 1:1 solution by the three different titania/Gr and titania/Ir interfaces, normalised by the quantity of titania.

supported on Gr/Ir rather than on Ir.

However, a much more dramatic effect is observed when comparing the activity of the Ti nanoparticles supported on metal- and oxide-supported Gr. In fact, the latter system has an activity which is larger by almost one order of magnitude than the former. In other words, the improvement obtained by the intercalation of an oxide layer below Gr is even larger than the one which is obtained by the use of metal-supported Gr as a support for the titania.

### 6.1.3 Discussion

The measurements performed in the reactor (Table 6.1) have shown that the use of Gr as a substrate can lead to a substantial improvement of the photocatalytic activity of titania. For example, titania on Ir-supported Gr shows a four-fold increase in the H<sub>2</sub> production with respect to Ir-supported titania. The reason for this improvement can depend on the fact that titania forms nanoparticles on Gr with a diameter of few tens of nm, as shown in our STM measurements, while it forms extended islands of larger size on metallic surfaces, as previously reported for example for the similar Pt (1 1 1) surface<sup>44</sup>.

However, a much more dramatic effect can be appreciated by comparing the activity of the TiO<sub>2</sub> nanoparticles supported on Gr/Ir (1 1 1) and Gr/TiO<sub>x</sub>/Ir (1 1 1). In fact, the latter system shows an activity towards hydrogen production higher by a factor 6, and therefore represents an improvement of a factor 20 with respect to the control system. Such an improvement, if replicated on a system which is already cutting edge – rather than on a prototypical photocatalyst as is TiO<sub>2</sub> –, would represent a major breakthrough in the development of photocatalysts for wide-scale application.

For this reason, our data analysis was dedicated primarily to unravel the possible contributions of the two different substrates, to understand which are those responsible for this increased activity. In fact, the understanding of these mechanisms is a key step towards the design of specifically tuned materials for highly efficient applications. In particular, as already mentioned, some of the properties of the nanoparticles which might be affected by the substrate and which might in turn influence their activity include the size of the clusters, their crystal structure, the density of oxygen vacancies, their band-gap and absolute values of the CBM and VBM, the recombination times of the charges generated by electron-pair excitations as well as their charge transfer time towards the substrate.

The characterisation of the sample allowed us to rule out most of these possible factors. For example, our structural characterisation indicated that the size and crystal structure of the nanoparticles was the same in the two systems. Likewise, no evidence was found of differences in the oxidation state of Ti, or in the density of oxygen vacancies. The band-gap was found to be the same in the two systems, as well as the energy of the VBM and CBM with respect to the Fermi level. On the other hand, we have observed a difference of 200 meV in the work function of the two systems, as well as in the doping level of Gr.

The doping observed in Gr can indeed improve the charge transfer from the nanoparticles, as strongly doped Gr is more efficient in accepting the charges, thereby separating them and preventing their recombination<sup>23,56</sup>. While our current measurements are not able to confirm whether this path might be responsible for the dramatic difference in photocatalytic activity observed between the two titania/Gr systems, we intend to perform theoretical calculations to determine the charge transfer dynamics between Gr and the nanoparticles, in order to shed further light on this system.

## Conclusion

In this chapter, I have shown another example of how the interaction between Gr and species supported on it can be used to improve the performance of the latter. In particular, we have characterised by a multidisciplinary approach a system in which Gr was used as a substrate to improve the photocatalytic performance of titania nanostructures. By direct measurements of the photocatalytic activity of different Gr- and Ir-supported titania nanoarchitectures performed in a reactor, we have shown that the Gr substrate leads to a substantial improvement in this process.

Most remarkably, we have proved that a dramatic role in this enhancement of the photocatalytic activity of a Gr-supported semiconductor is played by the substrate supporting Gr. In fact, we have shown that by tuning the properties of Gr by a different chemical composition of the substrate supporting it, the photocatalytic activity of our nanoarchitectures was increased by more than an order of magnitude with respect to the Gr-free control system.

By employing a combination of surface science experimental techniques, we were also able to attribute this result to an electronic effect, while showing that no differences are induced to the structural and morphological properties or to the oxidation state and density of oxygen vacancies of the nanoparticles by the chemical composition of the substrate below Gr. On the other hand, we have shown that some differences are found in the electronic structure of nanoparticles supported on metal- and oxide-supported Gr. In particular, while the absolute potentials of the CBM and VBM, and therefore the band-gap and reduction and oxidation potentials of the nanoparticles, do not significantly change, a significant dependence on the chemical species supporting Gr was found in the work function of both the nanoparticles and the Gr substrate. Based on this results, we believe that the enhanced photocatalytic activity of our systems is due to the efficient separation of the electron-hole pairs by Gr, which is influenced by its doping level affecting its efficiency as an electron acceptor. In fact, doping can thus improve the ability of Gr to promote electron-hole separation, thereby reducing their recombination rate which represent a major limitation to the efficiency of the system. To verify this hypothesis, theoretical calculations will be performed to shed further light on this process.

In conclusion, our experiments highlight how the interplay between the Gr-substrate and Gr-adsorbate interaction can be exploited for the development of Gr-based substrates to improve the efficiency of nanostructured photocatalysts. Our successful characterisation of a prototypical photocatalyst, namely titania nanoparticles, provides a tool to improve the performance of other nanoarchitectures based on metal-oxide or metal-free materials, towards the development of novel cost-effective photocatalysts.

## References

- [1] W. A. de Heer. The physics of simple metal clusters: experimental aspects and simple models. *Rev. Mod. Phys.* (1993) 65: 611–676. doi:10.1103/revmodphys.65.611.
- [2] F. Baletto, R. Ferrando. Structural properties of nanoclusters: Energetic, thermodynamic, and kinetic effects. *Rev. Mod. Phys.* (2005) 77: 371–423. doi:10.1103/revmodphys.77.371.
- [3] M. Haruta, T. Kobayashi, H. Sano, N. Yamada. Novel gold catalysts for the oxidation of carbon monoxide at a temperature far below 0 °C. *Chem. Lett.* (1987) 16: 405–408. doi:10.1246/cl.1987.405.
- [4] B. Hvolbæk, T. V. Janssens, B. S. Clausen, H. Falsig, C. H. Christensen, J. K. Nørskov. Catalytic activity of Au nanoparticles. *Nano Today* (2007) 2: 14–18. doi:10.1016/s1748-0132(07)70113-5.
- [5] A. Baraldi, L. Bianchettin, S. de Gironcoli, E. Vesselli, S. Lizzit, L. Petaccia, G. Comelli, R. Rosei. Enhanced chemical reactivity of under-coordinated atoms at Pt-Rh bimetallic surfaces: A spectroscopic characterization. *J. Phys. Chem. C* (2011) 115: 3378–3384. doi:10.1021/jp110329w.
- [6] H. Nakotte, C. Silkwood, K. Page, H.-W. Wang, D. Olds, B. Kiefer, S. Manna, D. Karpov, E. Fohtung, E. E. Fullerton. Pair distribution function analysis applied to decahedral gold nanoparticles. *Phys. Scr.* (2017) 92: 114002. doi:10.1088/1402-4896/aa8afd.
- [7] F. Baletto, R. Ferrando, A. Fortunelli, F. Montalenti, C. Mottet. Crossover among structural motifs in transition and noble-metal clusters. *J. Chem. Phys.* (2002) 116: 3856–3863. doi:10.1063/1.1448484.
- [8] A. P. Alivisatos. Semiconductor clusters, nanocrystals, and quantum dots. *Science* (1996) 271: 933–937. doi:10.1126/science.271.5251.933.
- [9] G. Schmid, M. Bäuml, M. Geerkens, I. Heim, C. Osemann, T. Sawitowski. Current and future applications of nanoclusters. *Chem. Soc. Rev.* (1999) 28: 179–185. doi:10.1039/a801153b.
- [10] J. Jasieniak, M. Califano, S. E. Watkins. Size-dependent valence and conduction band-edge energies of semiconductor nanocrystals. *ACS Nano* (2011) 5: 5888–5902. doi:10.1021/nn201681s.
- [11] L. Liao, Q. Zhang, Z. Su, Z. Zhao, Y. Wang, Y. Li, X. Lu, D. Wei, G. Feng, Q. Yu, X. Cai, J. Zhao, Z. Ren, H. Fang, F. Robles-Hernandez, S. Baldelli, J. Bao. Efficient solar water-splitting using a nanocrystalline CoO photocatalyst. *Nat. Nanotechnol.* (2013) 9: 69–73. doi:10.1038/nnano.2013.272.
- [12] D. J. Barber, I. C. Freestone. An investigation of the origin of the colour of the Lycurgus cup by analytical transmission electron microscopy. *Archaeometry* (1990) 32: 33–45. doi:10.1111/j.1475-4754.1990.tb01079.x.
- [13] J. Shi, S. Gider, K. Babcock, D. D. Awschalom. Magnetic clusters in molecular beams, metals, and semiconductors. *Science* (1996) 271: 937–941. doi:10.1126/science.271.5251.937.
- [14] C. R. Henry. Surface studies of supported model catalysts. *Surf. Sci. Rep.* (1998) 31: 231–325. doi:10.1016/s0167-5729(98)00002-8.
- [15] N. Tian, Z.-Y. Zhou, S.-G. Sun, Y. Ding, Z. L. Wang. Synthesis of tetrahedral platinum nanocrystals with high-index facets and high electro-oxidation activity. *Science* (2007) 316: 732–735. doi:10.1126/science.1140484.
- [16] S. Vajda, M. J. Pellin, J. P. Greeley, C. L. Marshall, L. A. Curtiss, G. A. Ballentine, J. W. Elam, S. Catillon-Mucherie, P. C. Redfern, F. Mehmood, P. Zapol. Subnanometre platinum clusters as highly active and selective catalysts for the oxidative dehydrogenation of propane. *Nat. Mater.* (2009) 8: 213–216. doi:10.1038/nmat2384.

- [17] A. P. Alivisatos, K. P. Johnsson, X. Peng, T. E. Wilson, C. J. Loweth, M. P. Bruchez, P. G. Schultz. Organization of 'nanocrystal molecules' using DNA. *Nature* (1996) 382: 609–611. doi:10.1038/382609a0.
- [18] G. C. Papaefthymiou. Nanoparticle magnetism. *Nano Today* (2009) 4: 438–447. doi:10.1016/j.nantod.2009.08.006.
- [19] A. T. N'Diaye, S. Bleikamp, P. J. Feibelman, T. Michely. Two-dimensional Ir cluster lattice on a graphene moiré on Ir(111). *Phys. Rev. Lett.* (2006) 97: 215501. doi:10.1103/physrevlett.97.215501.
- [20] A. T. N'Diaye, T. Gerber, C. Busse, J. Mysliveček, J. Coraux, T. Michely. A versatile fabrication method for cluster superlattices. *New J. Phys.* (2009) 11: 103045. doi:10.1088/1367-2630/11/10/103045.
- [21] A. Fujishima, K. Honda. Electrochemical photolysis of water at a semiconductor electrode. *Nature* (1972) 238: 37–38. doi:10.1038/238037a0.
- [22] Y. Ma, X. Wang, Y. Jia, X. Chen, H. Han, C. Li. Titanium dioxide-based nanomaterials for photocatalytic fuel generations. *Chem. Rev.* (2014) 114: 9987–10043. doi:10.1021/cr500008u.
- [23] X. Li, J. Yu, S. Wageh, A. A. Al-Ghamdi, J. Xie. Graphene in photocatalysis: A review. *Small* (2016) 12: 6640–6696. doi:10.1002/smll.201600382.
- [24] T. L. Thompson, J. T. Yates. Surface science studies of the photoactivation of TiO<sub>2</sub> new photochemical processes. *Chem. Rev.* (2006) 106: 4428–4453. doi:10.1021/cr050172k.
- [25] T. Caruso, C. Lenardi, T. Mazza, A. Policicchio, G. Bongiorno, R. G. Agostino, G. Chiarello, E. Colavita, P. Finetti, K. C. Prince, C. Ducati, P. Piseri, P. Milani. Photoemission investigations on nanostructured TiO<sub>2</sub> grown by cluster assembling. *Surf. Sci.* (2007) 601: 2688–2691. doi:10.1016/j.susc.2006.12.025.
- [26] X.-Y. Zhang, H.-P. Li, X.-L. Cui, Y. Lin. Graphene/TiO<sub>2</sub> nanocomposites: synthesis, characterization and application in hydrogen evolution from water photocatalytic splitting. *J. Mater. Chem.* (2010) 20: 2801. doi:10.1039/b917240h.
- [27] K. Ozawa, M. Emori, S. Yamamoto, R. Yukawa, S. Yamamoto, R. Hobara, K. Fujikawa, H. Sakama, I. Matsuda. Electron–hole recombination time at TiO<sub>2</sub> single-crystal surfaces: Influence of surface band bending. *J. Phys. Chem. Lett.* (2014) 5: 1953–1957. doi:10.1021/jz500770c.
- [28] N. Yang, Y. Liu, H. Wen, Z. Tang, H. Zhao, Y. Li, D. Wang. Photocatalytic properties of graphdiyne and graphene modified TiO<sub>2</sub>: From theory to experiment. *ACS Nano* (2013) 7: 1504–1512. doi:10.1021/nn305288z.
- [29] A. Du, Y. H. Ng, N. J. Bell, Z. Zhu, R. Amal, S. C. Smith. Hybrid graphene/titania nanocomposite: Interface charge transfer, hole doping, and sensitization for visible light response. *J. Phys. Chem. Lett.* (2011) 2: 894–899. doi:10.1021/jz2002698.
- [30] P. Sutter, J. T. Sadowski, E. A. Sutter. Chemistry under cover: Tuning metal-graphene interaction by reactive intercalation. *J. Am. Chem. Soc.* (2010) 132: 8175–8179. doi:10.1021/ja102398n.
- [31] R. Larciprete, S. Ulstrup, P. Lacovig, M. Dalmiglio, M. Bianchi, F. Mazzola, L. Hornekær, F. Orlando, A. Baraldi, P. Hofmann, S. Lizzit. Oxygen switching of the epitaxial graphene–metal interaction. *ACS Nano* (2012) 6: 9551–9558. doi:10.1021/nn302729j.
- [32] L. Omiciuolo, E. R. Hernández, E. Miniussi, F. Orlando, P. Lacovig, S. Lizzit, T. O. Menteş, A. Locatelli, R. Larciprete, M. Bianchi, S. Ulstrup, P. Hofmann, D. Alfè, A. Baraldi. Bottom-up approach for the low-cost synthesis of graphene–alumina nanosheet interfaces using bimetallic alloys. *Nat. Commun.* (2014) 5: 5062. doi:10.1038/ncomms6062.



- [33] R. Larciprete, P. Lacovig, F. Orlando, M. Dalmiglio, L. Omiciuolo, A. Baraldi, S. Lizzit. Chemical gating of epitaxial graphene through ultrathin oxide layers. *Nanoscale* (2015) 7: 12650–12658. doi:10.1039/c5nr02936h.
- [34] G. Ertl, J. Küppers. *Ultraviolet Photoelectron Spectroscopy (UPS)* (Wiley-VCH Verlag GmbH, 1985), Chapter 4. 87–146.
- [35] C. Das, M. Richter, M. Tallarida, D. Schmeisser. Electronic properties of atomic layer deposition films, anatase and rutile TiO<sub>2</sub> studied by resonant photoemission spectroscopy. *J. Phys. D* (2016) 49: 275304. doi:10.1088/0022-3727/49/27/275304.
- [36] K. C. Prince, V. R. Dhanak, P. Finetti, J. F. Walsh, R. Davis, C. A. Muryn, H. S. Dhariwal, G. Thornton, G. van der Laan. 2p resonant photoemission study of TiO<sub>2</sub>s. *Phys. Rev. B* (1997) 55: 9520–9523. doi:10.1103/physrevb.55.9520.
- [37] S. Hüfner. *Photoelectron spectroscopy: principles and applications*. (Springer-Verlag Berlin Heidelberg, 2003), 3rd edition. doi:10.1007/978-3-662-09280-4.
- [38] T. Caruso, C. Lenardi, R. G. Agostino, M. Amati, G. Bongiorno, T. Mazza, A. Policicchio, V. Formoso, E. Maccallini, E. Colavita, G. Chiarello, P. Finetti, F. Šutara, T. Skála, P. Piseri, K. C. Prince, P. Milani. Electronic structure of cluster assembled nanostructured TiO<sub>2</sub> by resonant photoemission at the Ti L<sub>2,3</sub> edge. *J. Chem. Phys.* (2008) 128: 094704. doi:10.1063/1.2832321.
- [39] M. Favaro, S. Agnoli, C. Di Valentin, C. Mattevi, M. Cattelan, L. Artiglia, E. Magnano, F. Bondino, S. Nappini, G. Granozzi. TiO<sub>2</sub>/graphene nanocomposites from the direct reduction of graphene oxide by metal evaporation. *Carbon* (2014) 68: 319–329. doi:10.1016/j.carbon.2013.11.008.
- [40] R. Ruus, A. Kikas, A. Saar, A. Ausmees, E. Nõmmiste, J. Aarik, A. Aidla, T. Uustare, I. Martinson. Ti 2p and O 1s X-ray absorption of TiO<sub>2</sub> polymorphs. *Solid State Commun.* (1997) 104: 199–203. doi:10.1016/s0038-1098(97)00300-1.
- [41] T. Mashoff, M. Takamura, S. Tanabe, H. Hibino, F. Beltram, S. Heun. Hydrogen storage with titanium-functionalized graphene. *Appl. Phys. Lett.* (2013) 103: 013903. doi:10.1063/1.4812830.
- [42] M. Ritter, W. Ranke, W. Weiss. Growth and structure of ultrathin FeO films on Pt (1 1 1) studied by STM and LEED. *Phys. Rev. B* (1998) 57: 7240–7251. doi:10.1103/physrevb.57.7240.
- [43] F. Allegretti, G. Parteder, L. Gagnaniello, S. Surnev, F. P. Netzer, A. Barolo, S. Agnoli, G. Granozzi, C. Franchini, R. Podloucky. Strained c(4×2) CoO (1 0 0)-like monolayer on Pd (1 0 0): Experiment and theory. *Surf. Sci.* (2010) 604: 529–534. doi:10.1016/j.susc.2009.12.018.
- [44] F. Sedona, G. A. Rizzi, S. Agnoli, F. X. Llabrés i Xamena, A. Papageorgiou, D. Ostermann, M. Sami, P. Finetti, K. Schierbaum, G. Granozzi. Ultrathin TiO<sub>x</sub> films on Pt (1 1 1): a LEED, XPS, and STM investigation. *J. Phys. Chem. B* (2005) 109: 24411–24426. doi:10.1021/jp0543173.
- [45] F. Allegretti, G. Parteder, M. G. Ramsey, S. Surnev, F. P. Netzer. The formation of sharp NiO (1 0 0)–cobalt interfaces. *Surf. Sci.* (2007) 601: L73–L76. doi:10.1016/j.susc.2007.05.008.
- [46] U. Bardi. On the composition and structure of thin layers of titanium oxide on platinum surfaces. *Catal. Lett.* (1990) 5: 81–88. doi:10.1007/bf00772097.
- [47] M. C. Biesinger, L. W. Lau, A. R. Gerson, R. S. C. Smart. Resolving surface chemical states in XPS analysis of first row transition metals, oxides and hydroxides: Sc, Ti, V, Cu and Zn. *Appl. Surf. Sci.* (2010) 257: 887–898. doi:10.1016/j.apsusc.2010.07.086.
- [48] S. P. Denker. Electronic properties of titanium monoxide. *J. Appl. Phys.* (1966) 37: 142–149. doi:10.1063/1.1707796.

- [49] G. Barcaro, S. Agnoli, F. Sedona, G. A. Rizzi, A. Fortunelli, G. Granozzi. Structure of reduced ultrathin  $\text{TiO}_x$  polar films on Pt (1 1 1). *J. Phys. Chem. C* (2009) 113: 5721–5729. doi:10.1021/jp811020s.
- [50] J. Haubrich, R. G. Quiller, L. Benz, Z. Liu, C. M. Friend. In situ ambient pressure studies of the chemistry of  $\text{NO}_2$  and water on rutile  $\text{TiO}_2$  (1 1 0). *Langmuir* (2010) 26: 2445–2451. doi:10.1021/la904141k.
- [51] H. Perron, J. Vandenborre, C. Domain, R. Drot, J. Roques, E. Simoni, J.-J. Ehrhardt, H. Catalette. Combined investigation of water sorption on  $\text{TiO}_2$  rutile (1 1 0) single crystal face: XPS vs. periodic DFT. *Surf. Sci.* (2007) 601: 518–527. doi:10.1016/j.susc.2006.10.015.
- [52] G. Silversmit, H. Poelman, D. Depla, N. Barrett, G. B. Marin, R. D. Gryse. A comparative XPS and UPS study of  $\text{VO}_x$  layers on mineral  $\text{TiO}_2$  (0 0 1)-anatase supports. *Surf. Interface Anal.* (2006) 38: 1257–1265. doi:10.1002/sia.2384.
- [53] F. Allegretti, J. P. W. Treacy, R. Lindsay. Visibility of  $\text{TiO}_2$  (1 1 0)(1×1) bridging oxygen in core level photoelectron spectroscopy. *Phys. Rev. B* (2012) 85: 205422. doi:10.1103/physrevb.85.205422.
- [54] A. Dahal, R. Addou, H. Coy-Diaz, J. Lallo, M. Batzill. Charge doping of graphene in metal/graphene/dielectric sandwich structures evaluated by C-1s core level photoemission spectroscopy. *APL Mater.* (2013) 1: 042107. doi:10.1063/1.4824038.
- [55] R. L. Kurtz, R. Stock-Bauer, T. E. Msdey, E. Román, J. D. Segovia. Synchrotron radiation studies of  $\text{H}_2\text{O}$  adsorption on  $\text{TiO}_2$  (1 1 0). *Surf. Sci.* (1989) 218: 178–200. doi:10.1016/0039-6028(89)90626-2.
- [56] S. Lizzit, R. Larciprete, P. Lacovig, K. L. Kostov, D. Menzel. Ultrafast charge transfer at monolayer graphene surfaces with varied substrate coupling. *ACS Nano* (2013) 7: 4359–4366. doi:10.1021/nn4008862.

## Chapter 7

# Development and characterization of a mass-selected nanocluster source

In the previous chapter, I have described some of the reasons why nanoclusters are very promising for applications in many fields. In particular, I have shown an example of an application of nanoclusters or nanoparticles in catalysis, which is one of the fields which has most widely taken advantage of the outstanding properties of these systems.

As already mentioned, one of the most intriguing properties of nanoclusters is the strong dependence of their physical and chemical properties from their size. In fact, the number of atoms composing the clusters affects their geometry (as shown for example in Figure 7.1a), as well as their electronic structure<sup>1-4</sup>. This, in turn, affects their macroscopic properties, including the chemical reactivity, optical absorption, and magnetic moment<sup>3,5-7</sup>. For example, it has been shown that the catalytic activity of nanoclusters, as well as their selectivity towards particular reaction products (Figure 7.1b), can be tuned by varying their size<sup>6,8,9</sup>. In some cases, this dependence can be relatively smooth, with properties changing with continuity from those of the single atom case to those of the bulk material. However, in other systems this dependence can be so dramatic that nanoclusters differing in size by just one atom can exhibit a completely different behaviour. This is mainly due to quantum effects related to the completion of shells in systems with

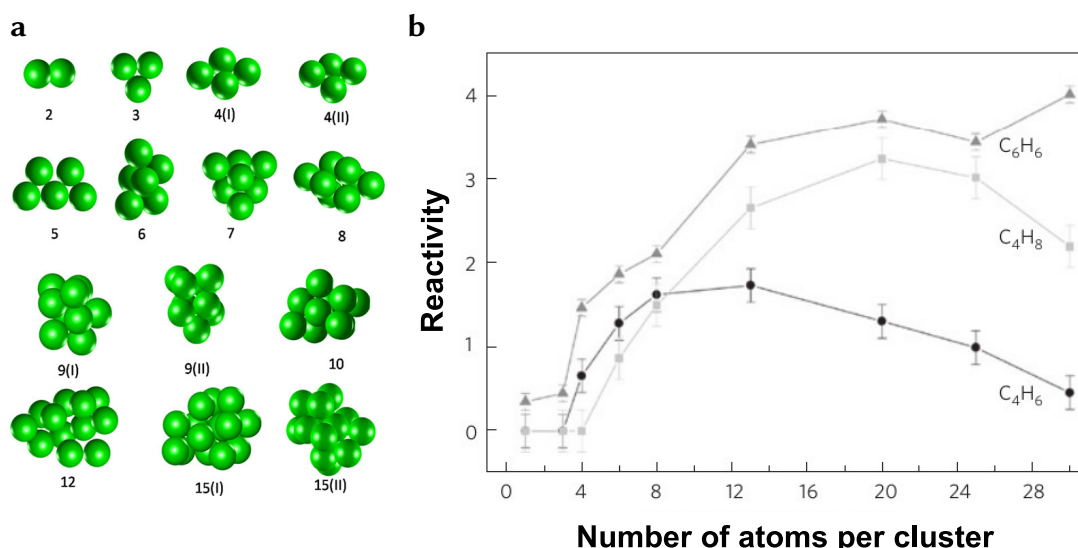


**Figure 7.1:** Examples of size-dependent properties in nanoclusters. a: Theoretically calculated most stable geometries for Ni nanoclusters, as a function of their sizes<sup>4</sup>. For some sizes, more than one stable geometry can exist. b: Selectivity of size-selected Pd<sub>N</sub> (N = 1 - 30) nanoclusters for the C<sub>2</sub>H<sub>2</sub> polymerization reaction<sup>9</sup>.

delocalized electrons<sup>3</sup>.

For this reason, the ability to isolate nanoclusters with a precise number of atoms (monodispersed clusters) is required firstly for performing research on them, especially for characterising the dependence of their properties on their size. This issue could be partially circumvented by characterising the properties of nanoclusters by means of microscopy techniques, thereby investigating the clusters one at a time and correlating the properties of each with its mass<sup>2</sup>. However, some properties of nanoclusters, such as their electronic properties, are not easily accessible to microscopy techniques; for this reason, they are usually studied by space-averaging techniques such as photoelectron spectroscopy. Such techniques, on the other hand, require to work on a homogeneous sample with monodispersed clusters<sup>2,5</sup>. Working on a monodispersed sample, moreover, presents further advantages, as it allows to correlate the macroscopic properties of the system (such as the chemical reactivity, which can be measured in realistic conditions in a device such as a reactor) with the geometric and electronic structure of the nanoclusters. This understanding, together with the methods allowing to mass-select nanoclusters, could then be employed to improve the efficiency in the applications of nanoclusters, by tailoring their size and properties depending on the requirements<sup>9</sup>.

The main issues which hinder the large scale investigation and utilisation of mass-selected nanoclusters are related to their production and their stability. The latter issue is due to the high mobility of nanoclusters, especially those having small sizes, and to their tendency to sinter already at moderate temperatures<sup>9</sup>. As a consequence of this, even when working with single-size nanoclusters, the formation of larger particles can occur, having completely different properties from the ones originally selected. This issue can be further exacerbated by exposure to chemicals, for example to the reactants of a catalytic reaction, which can modify the shape and mobility of nanoclusters<sup>9,10</sup>. A possible method to address this issue, which has been already discussed in the previous chapter, is the deposition of the nanoclusters onto a suitable substrate being able to reduce their mobility and improve their thermal stability, such as Gr<sup>10,11</sup>.

In this chapter, instead, I will focus on the issues related to the production of mass-selected nanoclusters. In particular, I will describe the construction and commissioning of a mass-selected nanocluster source at Surface Science Laboratory, which has been specifically designed to be interfaced with the SuperESCA beamline at Elettra. We intend to use it to produce nanoclusters with a precise number of atoms and deposit them onto a substrate such as Gr to be able to employ the techniques available there, which I have described and shown in the previous chapters, to study their properties as a function of their mass. The need to directly interface the source to the beamline arises from the requirement to produce and characterise them *in situ* to prevent contaminations, which would be unavoidable during transfer in atmosphere due to their high chemical reactivity. Furthermore, the possibility to deposit the nanoclusters directly on the liquid-nitrogen cooled manipulator of the experimental chamber allows to reduce their mobility as soon as they land on the surface, and therefore to study their thermal stability and evolution in a controlled way.

By using this approach, we intend to investigate, besides the fundamental role of the size on the characteristics of nanoclusters, also the interplay between the properties of the nanoclusters and of their substrate, with the final aim of finding reproducible conditions to synthesize thermally stable supported size-controlled nanoclusters. Such systems can be of interest for a wide range of applications in fields including catalysis, to further improve the performance of systems such as those studied in Chapter 6 by enhancing the surface-to-bulk ratio and tuning their electronic structure. Another field where nanoclusters have proven very promising is magnetism: for example, nanoclusters have been widely studied for applications in high density data storage, with similar perspectives as the ones of single-molecule magnets such as those described in Chapter 4.

The production of clusters with a homogeneous size can be achieved by several methods<sup>2,9</sup>. For example, wet methods can be used to synthesise monodispersed clusters of specific sizes from metal salts in solution or from colloids. However, this kind of techniques only work for selected elements: therefore, by using this approach, it is not always possible to obtain clusters of any material, nor of arbitrary size<sup>2</sup>. Besides the direct production of monodispersed clusters, another possible approach is to employ a less selective production technique, yielding clusters of different sizes, yet subsequently separate them

depending on their mass. This latter approach has the disadvantage of being in general less efficient, as a large part of the clusters produced are discarded, yet it is usually more versatile, as it can be applied to a wide variety of materials.

The main requirement when using this approach is therefore to be able to create a sufficient concentration of the desired species in the initial product, to still have an adequate density in the mass-filtered output<sup>9</sup>. In fact, a low flux would lead to an unacceptably long deposition time, as even in UHV conditions clusters can be contaminated by residual impurities. A high yield can be achieved if the mass distribution of the clusters originally produced is already relatively narrow, *i.e.* with a dispersion of their size of tens of atoms at most. Vaporisation or ion sputtering methods are often employed to provide the feedstock for the nanocluster generation, as they are effective on a wide variety of materials. A very efficient method to ensure a proper transport of the clusters from the place where they are generated to the mass filter is by employing the technology developed for ion beams. Also for the mass selection process, several well-established techniques can be used, such as time-of-flight or quadrupole mass spectrometry. The choice of the techniques for cluster generation and mass selection depends on the intended applications of the cluster source, more specifically, on the elements which will commonly be used and on the intended mass range. For example, time-of-flight mass spectrometers can be used to produce very large clusters, while quadrupole mass spectrometers (QMSs) are usually limited in the maximum mass they can select, yet more efficient in the low-mass region.

The approach employed in our source is based on separating the production and mass-selection stages, and it has been designed in order to allow the generation of clusters from a wide variety of elements, as well as to ensure compatibility with the UHV environment of the beamline. In addition, particular care has been taken to ensure that the procedure for switching to clusters with a different elemental composition can be performed in a relatively short time and does not require a major reoptimisation process.

## 7.1 Cluster source operating principles

The cluster source which we are building is based on the original design<sup>12</sup> developed by the group of Prof. Heiz at the Chemistry Department of the Technische Universität München, and has been developed as part of a collaboration with them. In addition, as part of the same collaboration, I have spent a period of traineeship there, where I have worked on a cluster source based on the same design, in order to acquire knowledge on its operation.

This cluster source is made up of separate stages, each consisting of a vacuum chamber with its own pumping system, as shown in Figure 7.2. There, the components of the cluster source are progressively labelled according to the order by which they are encountered by the nanoclusters. The most important stages are the cluster production (denoted as **a** in Figure 7.2) and mass selection (denoted as **d**) sections. In particular, the cluster production employs the laser vaporisation technique, while the mass selection is performed by a QMS. These two components will be described in detail in the sections below. In addition, a section with an electrostatic bender is present, to separate the clusters based on their charge before they enter the QMS (**c**). Finally, several stages of differential pumping are needed due to the different pressure requirements in different parts of the system (**b**).

### 7.1.1 Nanocluster production

As already mentioned, our cluster source relies on the laser vaporisation method for nanocluster production. In fact, the clusters are obtained from the rapid cooling of a plasma generated by evaporation from a solid target (an example is shown in the inset in Figure 7.3), in a vacuum environment. In particular, a focussed high power laser is used to heat a very small area of the target, while the rest is not significantly heated. This is possible thanks to the use of a pulsed laser with very low duty cycle (7 ns pulse duration, 120 Hz repetition rate) and high peak power (up to 140 mJ/pulse), which causes an immediate ionisation of the atoms hit by the pulse. This results in the formation of a plasma expanding out of the surface, while only a negligible amount of power is transmitted to the remaining solid body. The laser pulse has a wavelength of 532 nm, obtained from the second harmonic generation from a Nd-YAG laser. The choice of the

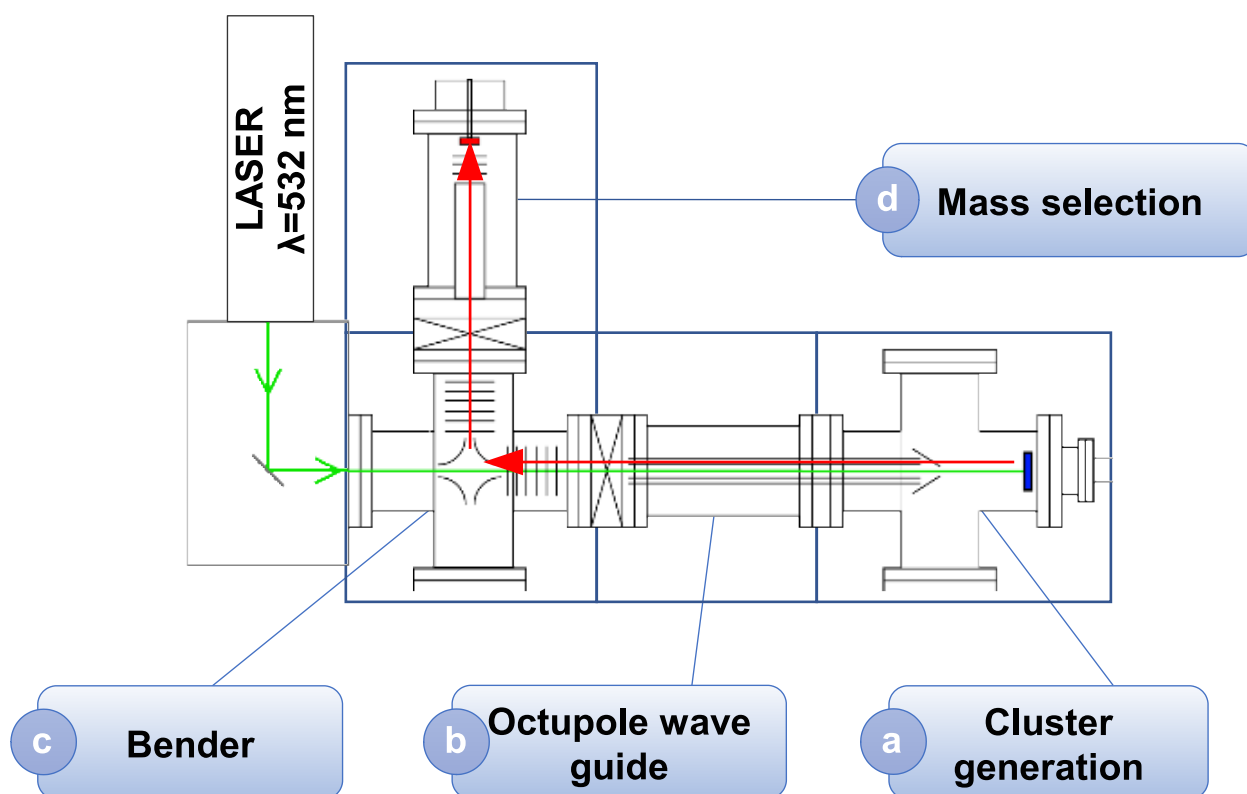


**Figure 7.2:** Scheme of the mass-selected nanocluster source. a: Nanocluster generation chamber, including the target assembly with its motor, piezo valve for the carrier gas, and nozzle. b: First stage of differential pumping, with octupole wave guide. c: Electrostatic bender chamber. d: QMS filter chamber. The path of the laser beam across the chamber is shown in green (from left to right), while the cluster path (right to left) is indicated in red.

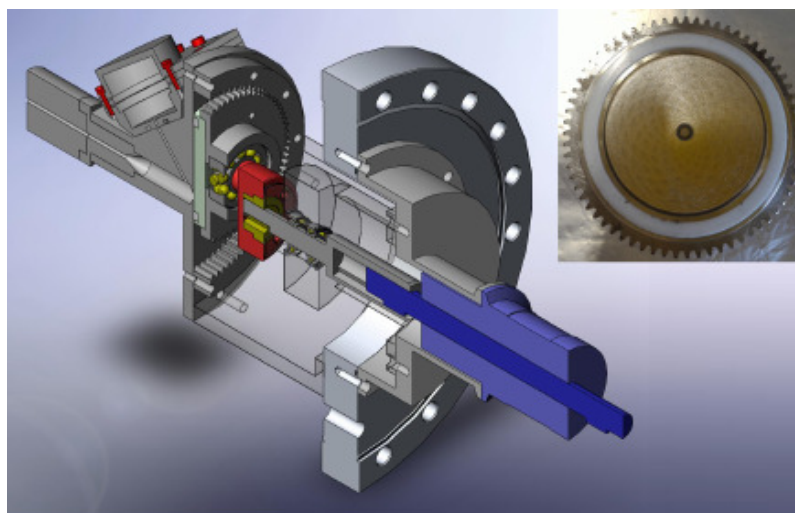


**Figure 7.3:** Schematic drawing of the gear assembly used to move the sample on a hypocycloidal curve during ablation. A stepper motor (blue; visible in the right part of the image) makes the sample rotate around the axis of the outer gear (seen on the left), while the coupling between two eccentric gears, the inner one being coaxial to the target and the outer one to the motor, allows the simultaneous rotation of the target around its own axis. The combination of the two movements is a cycloid drawn on the target by the laser, coaxial to the motor. The inset shows a typical target, composed of a metal disc glued to the inner gear assembly.

wavelength (and in particular of a harmonic in the visible range) is due to practical considerations, as the laser has to enter the vacuum chamber of the cluster source through a window. The chosen wavelength, when crossing a fused silica window, grants the maximum possible transmission of the laser beam and

therefore also minimal thermal stress to the window.

Another important point to address in the laser ablation of the target is that due to the high power density which is required to provide sufficient energy to ablate the target (which requires focussing the laser beam to a spot below 1 mm in diameter), only a minute fraction of the surface is ablated by each pulse. This, if the target were fixed, would rapidly lead to the complete ablation of the target in one point, while not using the remainder of the available material. To this aim, the target is constantly moved, to ensure that all the surface is subsequently exposed to the laser, so that the wear on the target is uniform, at least to a first approximation. This movement is achieved by letting the sample rotate simultaneously around two eccentric circles: the laser, therefore, draws a cycloidal path on the target, which, after a sufficiently long time, covers the whole target surface. The mechanism allowing this movement is illustrated in Figure 7.3.

In order to obtain nanoclusters from this plasma, the latter has to be cooled down. This is achieved by means of a carrier gas, which accelerates the plasma, carrying it away from the target surface, into a first expansion chamber where the atoms can cool and collide, forming some small, hot clusters. These clusters are further cooled down and allowed to aggregated by expanding supersonically through a nozzle, into the vacuum chamber constituting the first stage of the cluster source (Figure 7.2a). This cooling and condensation process is very complex from a theoretical perspective, as it is in a strongly non-equilibrium thermodynamic state. This supersonic expansion leads to the formation of nanoclusters, either neutral or charged; the charge is usually unitary, and can be either positive or negative. As will be shown later on, single atoms are always produced by this process, as well as small clusters. In addition, depending on the cluster generation conditions, a distribution of clusters of higher mass can also originate, whose broadness and average mass depend on the conditions used for their generation. Among the factors affecting the distribution and yield of the cluster generation, some of the most influential are the power of the laser pulse, the composition of the target, the timing of the carrier gas pulse (with respect to the laser pulse), the characteristics of the gas pulse (pressure and duration), the shape of the expansion region and nozzle, the species of the carrier gas. In our source, the carrier gas employed is helium: the use of an inert gas is necessary to ensure that it does not react with the nanoclusters, contaminating them. In fact, the use of reactive gasses, either added or replacing the carrier gas, can lead to the formation of compound clusters. This can be actually employed for altering the composition of the nanoclusters: for example, this can be used to generate oxide nanoclusters by adding oxygen to the carrier gas, as will be shown later.

The gas pulse is obtained and controlled by the use of a piezoelectrically-actuated needle valve. This valve consists of a metallic disk constrained to a piezoelectric disk, whose centre has a needle which normally seals an aperture by means of an elastic O-ring. The application of a potential to the piezoelectric disk leads to its deformation, and therefore also to that of the attached metal disk, which pulls the needle away from the aperture, allowing the gas to flow out of it.

To achieve supersonic expansion, the carrier gas pressure before and after the nozzle must be significantly different: the pressure of the in-coming gas is therefore of the order of a few bar. For this reason, even though the aperture through which it flows is relatively narrow (sub-millimeter diameter), the gas inflow in the first stage of the cluster source, *i.e.* just after the supersonic expansion area, is rather high, and requires a high pumping speed to be readily removed. In fact, the pressure must remain low enough in the chamber to ensure that the pressure gradient is high enough to achieve supersonic expansion. In reality, the supersonic expansion process is much more complicated, leading to a strongly non-uniform distribution of the pressure in the chamber. Anyway, a level of vacuum well below 1 mbar is required both to ensure that the supersonic expansion is not perturbed by the gas already in the first chamber, as well as to reduce the gas flow towards the following sections of the cluster source.

### 7.1.2 Mass-selection of nanoclusters

The second fundamental component in our cluster source is the one which is in charge of filtering the produced clusters, in order to allow only those with a specific number of atoms to reach the deposition target (Figure 7.2d). Our mass filter is a QMS designed for operation in a mass range between about 10 and 16 000 AMU, shown in Figure 7.4. This range allows us to select either single atoms of all elements except for the lightest, and of nanoclusters of any size up to hundreds of atoms for the case of light elements, and



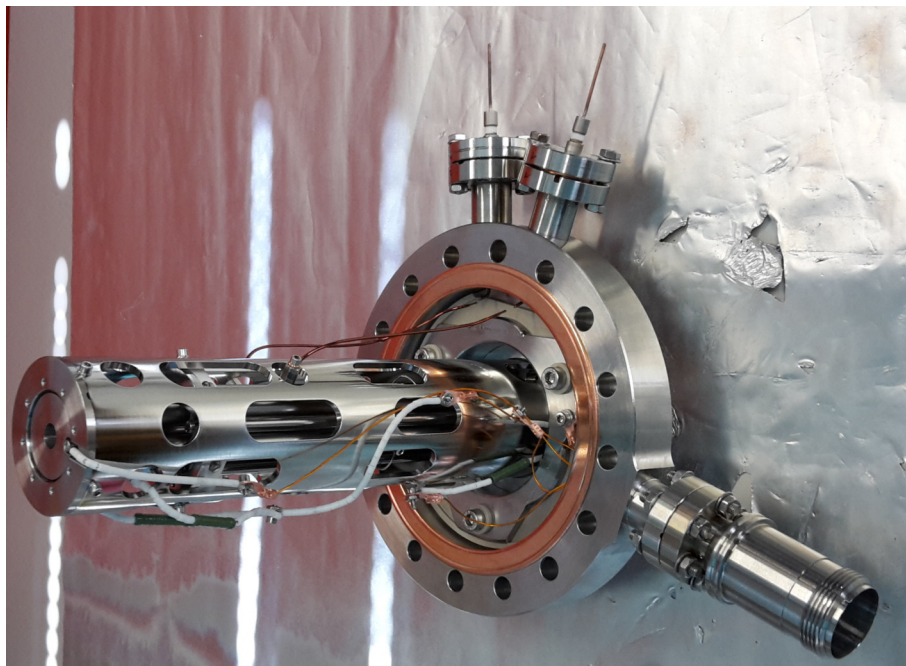


**Figure 7.4:** Picture of the QMS (by Extrel) in use in our nanocluster source, mounted on its support, which we have specifically designed for our cluster source.

several tens for the heaviest elements. For example, gold nanoclusters with up to 88 atoms can be selected.

The QMS is usually configured to act as a band-pass mass filter, enabling only particles with a specific charge-to-mass ratio to pass. In particular, in a typical QMS, the potential applied to the rods is given by the sum of a DC bias  $U$  with an RF potential  $V\cos(\omega t)$ . The equations of motion for a charged particle inside such a field are described by Mathieu's equations<sup>13</sup>. In summary, if we define the  $z$ -axis as the one parallel to the QMS axis, it can be shown that a QMS acts like a high pass mass filter in the  $x$ - $z$  plane and as a low pass mass filter in the  $y$ - $z$  plane<sup>14</sup>. By properly selecting  $U$  and  $V$ , it is therefore possible to operate the QMS as a narrow band pass filter.

Besides working as a band-pass filter, the QMS can also be operated in such a way that only the high-pass filtering action is present: this can be used, in our application, to be able to collect nanoclusters of any size, without mass selection, while filtering out ions originating from the carrier gas or common vacuum contaminants (such as CO and water), which are generally characterised by a lower mass.

From a qualitative point of view, the mass filtering by the field in the QMS is due to the fact that, given a certain  $U$  and  $V$  potentials, only the particles having a certain charge-to-mass-ratio will follow a non-diverging trajectory inside the QMS: particles with a different ratio will instead crash against the QMS rods.

### 7.1.3 Differential pumping and nanocluster transport

One of the main issues related to the operation of this cluster source is related to the very different pressure regimes found in the different stages. In fact, while the pressure in the first chamber (where the clusters are generated) can reach more than  $10^{-1}$  mbar due to the high gas flux required for the supersonic expansion, the maximum pressure allowed for a safe operation of the QMS is in the low  $10^{-5}$  mbar range, and an even lower pressure is required in the last stage of the source, where the clusters are deposited, in order to ensure that no significant amounts of contaminants are deposited. This is especially true if the deposition has to be performed at low temperature, due to the high sticking coefficients of most gasses at temperature below 100 K.

The task of allowing such a large difference in pressure, which almost amounts to 10 orders of magnitude, to exist between the first and last stages, while allowing the clusters to travel between them, is



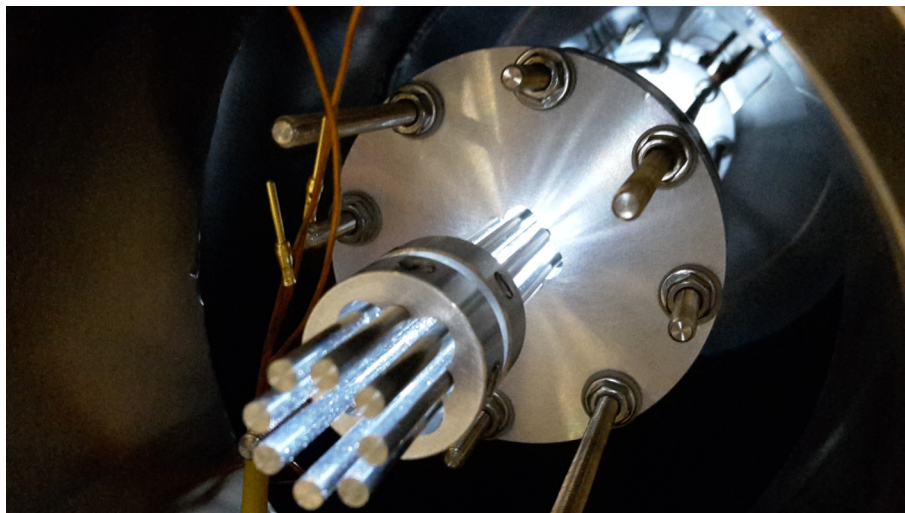


**Figure 7.5:** Picture of the octupole in use in the cluster source, mounted on its assembly.

achieved by a system of differential pumping stages. These consist of several consecutive vacuum chambers, communicating with each other only through a hole with a diameter of about 4 mm, slightly larger than the average diameter of the cluster beam. This approach represents a particularly effective obstacle against gas diffusion between nearby chambers, allowing differences in pressure of about one order of magnitude between each two.

Each stage is pumped by turbomolecular pump, whose pumping speed must be particularly high (about  $1000 \text{ m}^3/\text{s}$  at  $1 \times 10^{-3} \text{ mbar}$ ) in the second and third stage, where the residual carrier gas flux is still high. On the other hand, the later stages are exposed to a lower carrier gas flux, yet in this case the level of vacuum achievable is limited by another factor, *i.e.* the compression ratio of the pumps. In fact, momentum transfer pumps such as turbomolecular pumps are not particularly efficient in pumping light gasses such as He, with maximum compression ratios rarely as high as  $10^8$ : in order to reach the UHV regime, such pumps would require a forevacuum pressure well below the mbar range, which is difficult to achieve, in particular when using dry pumps to generate it. A possible workaround is to use a couple of turbomolecular pumps in series, where one creates the forevacuum for the other, thereby increasing the total compression ratio of the system.

The use of several stages of differential pumping leads to long distances between the components of the cluster source, which the clusters must be able to cross without dispersing far away from the axis of the chamber. In particular, the passage through the narrow apertures placed between each differential pumping stage requires the beam to be precisely refocussed in these points.

Such a guiding and focussing of the cluster beam can be easily achieved for charged clusters, by the use of electrostatic or radio-frequency potentials. In particular, two types of elements have been employed in our cluster source. The first is an octupole wave guide (found in the position indicated in Figure 7.2b)<sup>15</sup>. This device (shown in Figure 7.5) is composed of 8 cylindrical and parallel rods, of which every consecutive two have opposite polarity, and so on with alternating polarity, thereby dividing the rods in two subgroups, composed of non-adjacent rods, which are connected to each other. Each of these two subgroups, is connected to the opposite pole of an AC potential, while a DC offset is then added to both<sup>16</sup>. This device works as a wave guide for charged particles beams, which, as long as their trajectory remains close to the octupole centre, are efficiently transported even across large distances. In fact, by a principle similar to that of the QMS, the DC and AC voltages, as well as the AC frequency, determine a relatively wide interval of charge-to-mass ratio values which are efficiently transported across the field.

The second type of element which has been diffusely employed in our cluster source to guide the charged nanocluster beam inside our system are electrostatic lenses. These are based on the typical Einzel lenses, which are systems composed of three coaxial conductive elements with cylindrical symmetry<sup>17</sup>. In

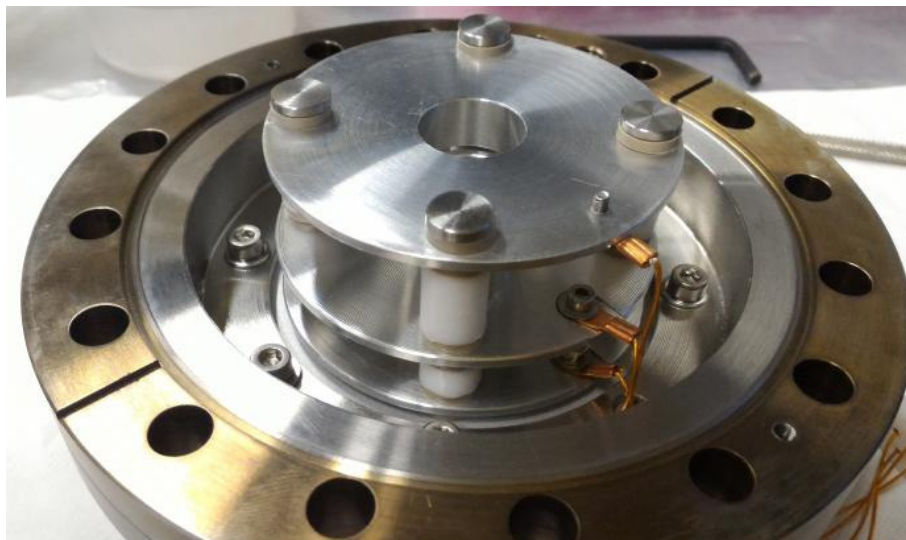


**Figure 7.6:** Picture of an electrostatic lens in use in the cluster source, with its assembly.

their original design, the first and last elements are placed at the same potential, while the central element is at a different one: this generates an electrostatic field, which is ideally fully contained between the first and last element, which acts to refocus a beam of charged particles crossing this area. The relative potential of the second lens with respect to the first and last ones determines the focal distance. More complex lenses, allowing for an asymmetric position of the two focal points and a higher degree of manipulation on the beam size and divergence, can be obtained by introducing a further potential difference between the first and last element, and by adding couples of additional elements to the lens. For example, in the electron optics of our system, electrostatic lenses with 5 and 7 elements are found (Figure 7.6).

In particular, the first lens in our system is positioned just before the octupole (the skimmer), with the aim to collect and collimate the clusters entering it. Further lenses are located between each stage of the differential pumping, where the metallic plates constituting them are shaped and mounted in order to also act as the aperture for the differential pumping. In fact, this double function allows the nanoclusters to be efficiently guided through the aperture, by properly adjusting the lens potentials. A set of electrostatic lenses is also present at the entrance and exit of the QMS, the former to ensure that the nanoclusters cross it close to its axis, which is necessary to ensure that it can efficiently filter them, the latter to refocus the filtered clusters onto the deposition substrate.

From a qualitative point of view, both the elements described above can be viewed as the electronic counterparts of some optical elements typically used for light: in fact, as also suggested by their names, the octupole wave guide works in a similar way as an optical fibre, and electrostatic lenses have a behaviour similar to refractive lenses for visible light. An important distinction for the latter case, however, is that the unitary element in an electrostatic lens system, which would correspond to a single optical lens, is not given by a single electrostatic plate, but by a full set of them, as the deflection of the beam by the lenses depends on the electrostatic potential difference between consecutive plates, rather than from their absolute values.

Finally, another important component in the cluster source is the electrostatic bender (Figure 7.2c), whose task is the separation of positively and negatively charged ions from each other and from neutral ones. This device consists of a quadrupole whose axis is oriented perpendicularly to the plane over which the cluster beam moves. The clusters enter laterally, passing between two bars and with their direction towards the axis. Two different electrostatic potentials are applied to each couple of bars opposite to each other. The potential difference between them generates constant-potential surfaces, which are symmetrical with respect to the plane connecting opposite rods (*i.e.* those at the same polarity). The average between the two potentials, instead, determines the value of the potentials of these surfaces. Ions entering the bender will proceed along different ones depending on their charge, and are therefore deflected in opposite

directions, while the neutral particles are not affected by the field and proceed straight through it. The interplay between the rod potentials modifies the position and curvature of the potential energy surfaces. By properly tuning them, therefore, a condition can be found such that ions with a specific charge-to-mass ratio are deflected at a right angle, in opposite directions depending on the sign of their charge<sup>18</sup>. The cluster will then exit the bender by passing in the middle between an adjacent couple of rods.

The principal aim of this bender, in our cluster source, is to filter out the neutral nanoclusters, which would not be filtered by the QMS, leading to an unselected contribution to the cluster beam. For this reason, the chamber with the QMS, and all subsequent stages of the cluster source, are mounted on one side of the bender, with respect to the axis of the octupole and of the target, so that only the charged particles, being actively deflected by the bender, can reach it. On the opposite side of the bender with respect to the octupole, moreover, the laser entrance window is found: the laser beam, in fact, enters the machine passing through the bender and along the octupole, basically following the first part of the path made by the clusters in opposite direction, as can be better understood in Figure 7.2.

## 7.2 Design of the nanocluster source

The design of our cluster source at SSL required some specific adaptations with respect to its original design, originating in particular from our intention to interface it to the SuperESCA beamline – in particular, to its preparation chamber. This firstly imposes stringent constraints on the geometry of this source, due to the presence of the optics of the beamline and the pre-existing equipment of its experimental chambers. Moreover, the cluster source is required to be moveable: in fact, for optimum cluster transport, its optics must be able to get within few centimetres from the sample, during its operation, yet they must also be easily removable from the beamline, in order not to interfere with other experiments.

Due to these requirements, a distance larger than 0.5 m is needed between the exit lens of the QMS and the sample position (as can be seen from the CAD drawing of the system, in Figure 7.7), through which the clusters have to be guided using methods similar to those already described. In particular, due to the distance involved, we have chosen to use a second octupole wave guide, followed by an Einzel lens

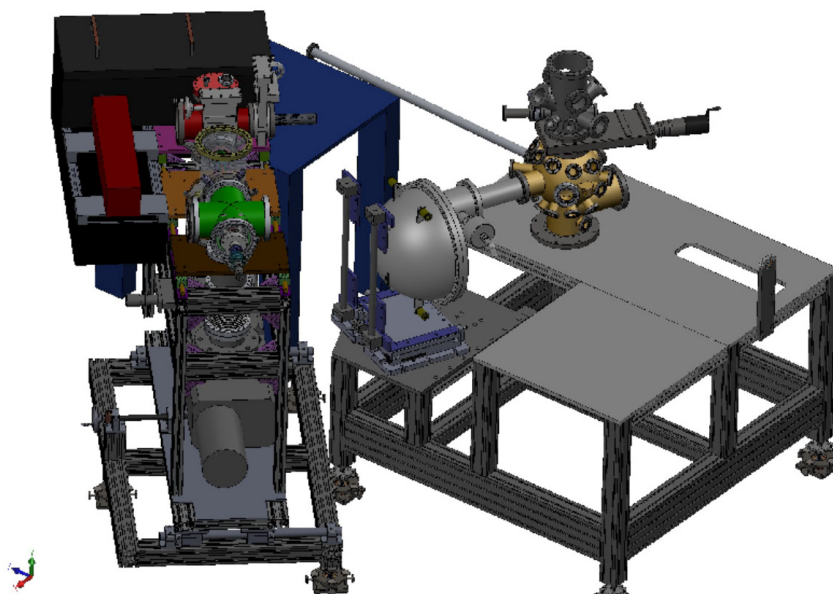


**Figure 7.7:** CAD drawing of the cluster source together with the SuperESCA experimental chamber, in the position which we have selected for their future interfacing. The position of the QMS, on the side of the bender (red cylinder) and pointing towards the experimental chamber, is shown. In the space between the QMS and the sample, further elements for guiding the ion beam will be introduced.

for the final focussing of the ions on the sample. Moreover, due to the need to keep the final lens within centimetres from the sample, its elements have to penetrate inside the SuperESCA preparation chamber. On the other hand, as mentioned before, it must be possible to extract it from there when the cluster source is not in use. For this reason, the whole cluster source will be mounted on a moveable stage, in order to be able to enter and exit the experimental chamber on need. The movement required to this aim will be of the order of about 150 mm. To allow for this movement, the octupole will be contained within a metal bellows which compresses when the source is inserted into the chamber, exposing the final part of the octupole and the lenses, and completely contains them when the source is fully retracted. A gate valve between the bellows and the preparation chamber will allow the two systems to be vented independently.

A further limitation for the interfacing of our cluster source is due to the pressure requirements in the SuperESCA experimental chamber, which must be in the UHV range. Furthermore, the high requirements of cleanliness of the beamline vacuum require that wet pumps, which are prone to introduce oil contaminations into the experimental chamber, have to be used with extreme care. For this reason, dry pumps are used for the vacuum generation of all stages of the cluster source, with the exception of the first stage where the high gas throughput required (about  $1000 \text{ m}^3/\text{s}$ ) requires the use of a rotary vane pump backing a dry (roots) booster pump. Even there, a zeolite trap is used to further reduce oil backstreaming from the rotary vane pump, which is also employing a mineral oil characterised by a vapour pressure below  $1 \times 10^{-7}$  mbar at room temperature. While its pressure increases when the pump is hot, the high gas flux during the cluster source operation prevents backstreaming during most of the system operation, while isolating the rotary pump from the vacuum chamber as soon as the cluster source is turned off is a further way to improve the quality of the vacuum in the cluster source.

### 7.3 Characterisation of the nanocluster source

The commissioning of the cluster source in construction at SSL is being currently performed in a gradual way. To be able to better pinpoint any issue, each element was firstly tested and optimised separately.

With respect to the first part of the testing, this is a demanding process, as the parameters of each stage affect the characteristics of the cluster beam in the next ones. For this reason, the optimisation of the parameters of the cluster source has to be performed in an iterative procedure, to ensure the maximum efficiency in the cluster production and transport depending on the desired mass.

In addition to the work performed at SSL, I will describe my work on the cluster source at TUM, to briefly explain its routine operation and provide some data on the actual performance of this type of cluster sources, which we expect to be able to achieve after installing our new cluster source at the SuperESCA beamline.

#### 7.3.1 Commissioning of the Surface Science Laboratory cluster source

To separately test the individual components of the cluster source, the first step was to decouple the clusters' generation from their transport through the different stages of the machine. To this aim, the cluster current was initially measured on the first element of the electrostatic transport system, which is the skimmer. By setting it to a negative potential, we were able to attract all positive charges produced by the ablation process, and by measuring the drain current on this element we could tune the degrees of freedom to maximise the cluster production rate. In particular, the parameters which we were able to modify were the laser power, the delay between the laser and He pulse, and the characteristics of the He pulse, which further depend on the pressure of the He gas behind the piezo valve and on the amplitude and duration of the electric pulse triggering the piezo valve.

After successfully obtaining a stable and reproducible current on this first element, the clusters were allowed to enter the transport system, whose parameters were optimised by adopting a similar strategy: one element at a time, while keeping the values already found for the previous elements fixed. Again, the parameters required to cross each element (octupole or electrostatic plate) were found by attracting the clusters towards the following element by applying a negative potential, and maximising the drain current on that element.





**Figure 7.8:** Panoramic photo of the mass selected nanocluster source at SSL. The laser is visible on the right, with the optics enclosed in the black box. The motor of the target is visible on the left. The cluster generation and first differential pumping stages are behind the He gas line, while the bender chamber is visible to their right, close to the laser optics box.

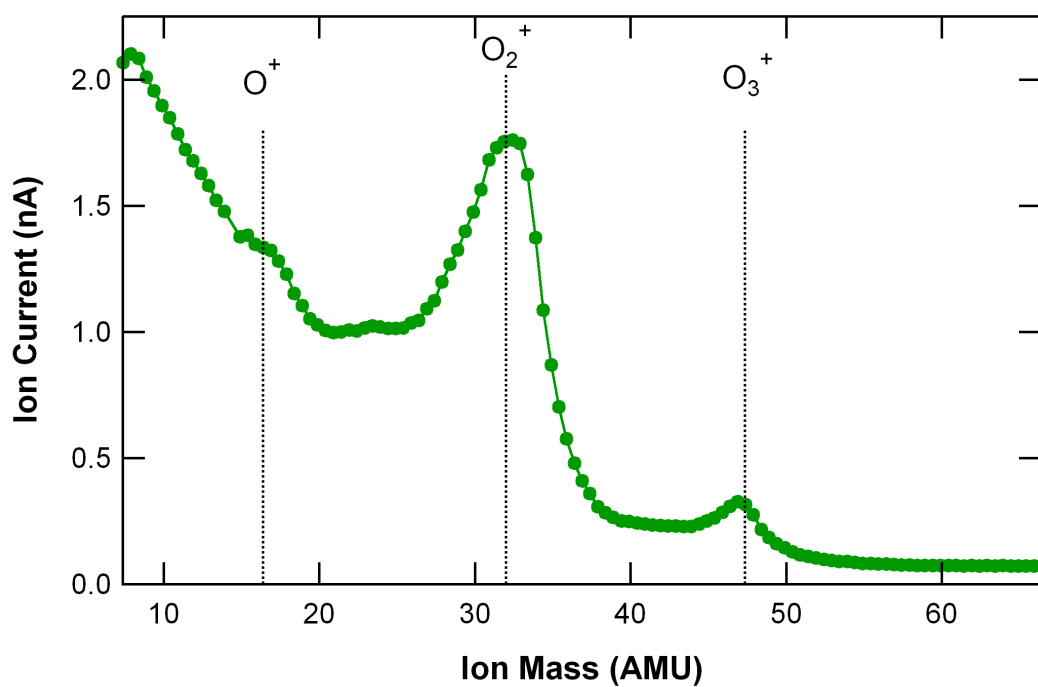


**Figure 7.9:** Mass spectrum of an oxygen plasma produced by a Tectra plasma source, measured by the QMS.

This technique was employed to find adequate values of the parameters for each element, until we were able to successfully carry the ions to a target placed in front of the entrance lens of the QMS. In particular, the drain current read on that element was 10 nA, which, supposing that all the particles impinging are positively charged by 1e (as is expected in a first approximation from this kind of machine, after neutral and negative clusters have been filtered out by the bender), corresponds to  $6 \times 10^{-10}$  particles per second.

Due to the more complex operating principles and higher number of degrees of freedom of the QMS with respect to the other components, and to the fact that the composition of the cluster beam was not yet known, this latter element was instead tested separately, in order to characterise its behaviour and calibrate it on an ion beam of known composition. In particular, the calibration of the QMS was performed by exposing it to a high-purity oxygen plasma, produced by a commercial source which had been placed in front of it for this purpose. The mass spectrum obtained by the QMS of the plasma is reported in Figure 7.9. This mass spectrum clearly shows distinct peaks at about 16, 32 and 48 AMU, which can be attributed to  $O_1^+$ ,  $O_2^+$  and  $O_3^+$  species. The FWHM of the components observed in the spectrum is of the order of few AMU, which indicates that the resolution of this instrument will be sufficient to resolve clusters with a different number of atoms, even if composed of light elements, at least as long as the clusters have a small size.

This test, therefore, allowed us to verify the efficiency of the transport of the ions through the whole QMS assembly, as well as to characterise its resolution capabilities for the low end of its mass range.

### 7.3.2 Set-up and commissioning of the cluster source at Technische Universität München

During my traineeship at TUM, I have worked on the commissioning of the cluster source at the Spectroscopy Lab at the Chair of Physical Chemistry, Chemistry Department, in the group of prof. Heiz. This procedure was necessary after the machine had been moved to a new laboratory, and involved the re-alignment and re-optimisation of the cluster generation conditions and potentials used for the cluster's transport. More specifically, the parameters were optimised for silver nanoclusters of few tens of atoms.

This re-optimisation procedure was performed in two steps. Firstly, a starting value for each tunable parameter was found by an approach similar to the one described in the previous paragraph. In this first step, the QMS was operated in high-pass mode, as the cluster synthesis stage produces a mass distribution which cannot be predicted *a priori*, and can only be characterised once the clusters can be guided to the QMS.

The transport efficiency was then optimised for a specific mass value by an iterative procedure, consisting of the following three steps:

- characterisation of the mass distribution of the unselected nanoclusters, by measuring the mass spectrum with the QMS.
- choice of a mass on which the current optimisation cycle will be performed.
- optimisation of the cluster generation and transport parameters to maximise the yield of the selected mass.

The mass spectrum is measured by landing the clusters on a conducting surface located just after the QMS exit lens, which must be only connected to ground through a picoamperometer. The clusters exiting the QMS impinge on this surface, where they are neutralised: the drain current measured on this surface, corresponding to the flux of the charges neutralising the clusters, is then proportional to the number of clusters impinging the surface per unit of time.

Once the mass distribution of the unselected nanocluster beam is known, optimisation can be performed for a specific value of the cluster mass, in order to find the cluster source parameters allowing to obtain the highest possible flux of size-selected nanoclusters of the desired mass. The aim of this process is to align the maximum of the mass distribution of the unfiltered clusters to the selected mass. This distribution is mainly determined by two factors: the distribution of the clusters as produced by the first

stage of the source, and the mass-dependence of the transport efficiency. Both can be maximised by tuning one parameter at the time, in order to maximise the current of mass-selected clusters. However, since the parameters of the cluster source are correlated, this process requires multiple iterations.

This optimisation procedure is performed by observing gradients in the cluster source yield as a function of its parameters: thus, a cluster current must be present and be maintained throughout this process. For this reason, once the mass distribution of the nanoclusters is known, only masses which are already observed in the cluster beam mass distribution spectrum can be optimised. If, instead, the signal of the desired mass is not sufficiently discernible from the noise, the optimisation must be performed gradually. Firstly, a mass has to be chosen, having a value in between the desired mass and the centre of the measured distribution and being produced in appreciable concentrations in the current conditions. The source must then be optimised for this new mass value. This process must be iterated in order to progressively shift the mass distribution to include the required cluster species.

An example of a mass spectrum, acquired during the optimisation of the cluster source at TUM for silver nanoclusters, is shown in Figure 7.10a. This spectrum is clearly composed of several, distinct components, equispaced by about 108 AMU. This separation corresponds to the mass of a single Ag atom: therefore, each component is originated by clusters having one atom more (or less) than their neighbours. In particular, a very intense peak can be observed, in a position compatible with the mass of single Ag atoms at 108 AMU. Further components, originated by ionized  $\text{Ag}_2$  and  $\text{Ag}_3$  species, can be seen. At higher masses, a wide distribution is found, centred between 3000 and 4000 AMU, originated by larger clusters.

However, the shape of these peaks is quite broad, as can be observed in Figure 7.10b, which shows the lineshape of a selected component. This component can be fitted to the sum of three Gaussian peaks, separated from each other by about 30 AMU. This particular shape can be attributed to the fact that contaminants are present on some nanoclusters, thereby increasing their mass. A possible source of contamination is molecular oxygen which, if present in the first stages of the source, can oxidise the clusters: this hypothesis is verified by the fact that the data can be very well fitted by three components with a 32 AMU separation, as shown in Figure 7.10b. According to these results, only clusters with an even number of oxygen atoms exist. This might be explained by the fact that the oxygen molecules adsorb on the clusters without having been previously dissociated either by the laser beam or by collisions with other ions in the cluster production region.

A new mass spectrum of Ag clusters, produced in similar conditions after the purification of the He

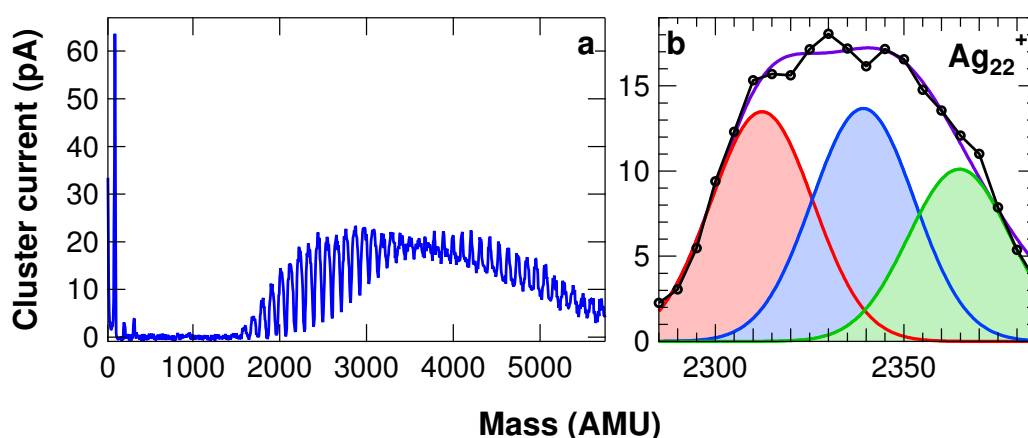


**Figure 7.10:** Mass spectrum of silver nanoclusters produced by the cluster source at TUM after the first iteration of the optimisation procedure. a: Mass spectrum of an extended mass region. The signal of Ag monomers, dimers and small clusters is visible, together with a wide distribution centred at about 3500 AMU, corresponding to clusters of about 30 Ag atoms. b: Zoom of a narrow region, corresponding to clusters all having 22 Ag atoms. Components due to oxidised nanoclusters are also observed and resolved: the de-convoluted components are superimposed in different colours.

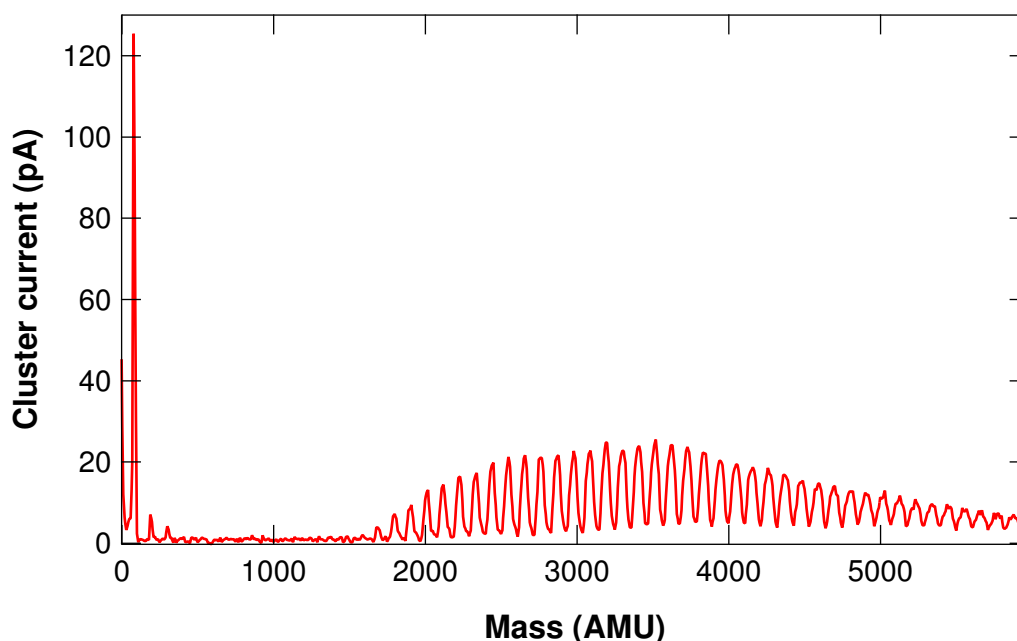


**Figure 7.11:** Mass spectrum of silver nanoclusters produced by the cluster source at TUM after further optimisation. Each component in the mass spectrum now shows a single, sharp component, indicating that no oxidised species are present.

in the gas line (which was identified as the most probable source of the contamination), is shown in Figure 7.11. The shape of the peaks is clearly narrower, as is particularly evident at high masses, where nearby components no longer overlap, and can now be well described by a single Gaussian component, characterised by a FWHM of the order of 50 AMU for masses of about 3000 AMU.

While this resolution is clearly sufficient to resolve clusters with different number of atoms, a much more important quantity to consider in this case is the overlap between the mass distributions of nanoclusters differing by a single atom. More specifically, this overlap corresponds to the contribution – due to the tails of the distributions centred on nearby masses – to the cluster signal measured at the selected mass value. For our case, this value is well below 0.5%, which means that the concentration of clusters with a number of atoms different from the selected value is negligible.

The characterisation of a cluster source similar to the one under commissioning in SSL provides a demonstration of its expected behaviour. In particular, I have shown that a cluster source based on this design is able to produce monodispersed clusters with very high reproducibility and selectivity. Thanks to the very low density of differently-sized nanoclusters, this machine will allow a very accurate characterisation of mass-selected nanoclusters with the use of space-averaging techniques. Finally, the description of my work performed at TUM provides a picture of the procedures which will be at the base of the operation of our source during its everyday use.

## Conclusions

In this chapter, I have described my work on the development of a new experimental setup for the production of nanoclusters with a precise number of atoms. While this machine is still under commissioning, the separate testing of its components, as well as my work on a machine based on the same design, suggest that it will have the suitable characteristics to allow the production of mass-selected nanoclusters and their deposition on a suitable substrate.

This machine, when fully operational, will represent an important step forward for the understanding on the properties of nanoclusters, by enabling full control on one of the most important degrees of freedom in nanoclusters: the number of atoms. The capability to measure *in situ* the electronic properties of mass



selected nanoclusters, as well as to investigate their reactivity and the sites involved in their catalytic activity, using the techniques already described in this thesis, will be provided by the unique characteristics of the SuperESCA beamline.

This machine will be particularly appropriate to improve our knowledge on some of the systems which I have addressed in this thesis. Firstly, as already mentioned, it will allow to study the role of the clusters' size on their catalytic activity. By coupling a careful optimisation of the cluster size with an investigation of the role of the substrate on the catalytic properties of nanoclusters – as shown in Chapter 6 – and of their stability, we can employ this machine to explore new paths for improving the efficiency of nanoclusters for applications in catalysis.

In addition, by being able to selectively produce monomers, dimers and larger clusters from any solid source, it would allow to further improve our understanding on the role of different carbon species during Gr nucleation, which has been addressed in Chapter 5. Moreover, it would allow to select a single species to provide the carbon feedstock, which can be a further degree of freedom to improve the quality of the final product.

Finally, by further upgrading this system and collaborating with other beamlines, it could be possible to also perform measurements of the magnetic properties of nanoclusters as a function of their size, and of their magnetic interaction to the substrate, to compare the performance of mass-selected nanoclusters with those of single molecule magnets like the ones described in Chapter 4, in view of applications such as for high density data storage.

## References

- [1] F. Baletto, R. Ferrando. Structural properties of nanoclusters: Energetic, thermodynamic, and kinetic effects. *Rev. Mod. Phys.* (2005) 77: 371–423. doi:10.1103/revmodphys.77.371.
- [2] J. P. Wilcoxon, B. L. Abrams. Synthesis, structure and properties of metal nanoclusters. *Chem. Soc. Rev.* (2006) 35: 1162. doi:10.1039/b517312b.
- [3] E. Roduner. Size matters: why nanomaterials are different. *Chem. Soc. Rev.* (2006) 35: 583. doi:10.1039/b502142c.
- [4] A. Kumar, S. Kang, C. Larriba-Andaluz, H. Ouyang, C. J. Hogan, R. M. Sankaran. Ligand-free Ni nanocluster formation at atmospheric pressure via rapid quenching in a microplasma process. *Nanotechnology* (2014) 25: 385601. doi:10.1088/0957-4484/25/38/385601.
- [5] W. A. de Heer. The physics of simple metal clusters: experimental aspects and simple models. *Rev. Mod. Phys.* (1993) 65: 611–676. doi:10.1103/revmodphys.65.611.
- [6] M. Che, C. O. Bennett. The influence of particle size on the catalytic properties of supported metals. *Adv. Catal.* (1989) 36: 55–172. doi:10.1016/s0360-0564(08)60017-6.
- [7] P. Gambardella, S. Rusponi, M. Veronese, S. S. Dhesi, C. Grazioli, A. Dallmeyer, I. Cabria, R. Zeller, P. H. Dederichs, K. Kern, C. Carbone, H. Brune. Giant magnetic anisotropy of single cobalt atoms and nanoparticles. *Science* (2003) 300: 1130–1133. doi:10.1126/science.1082857.
- [8] U. Heiz, F. Vanolli, A. Sanchez, W.-D. Schneider. Size-dependent molecular dissociation on mass-selected, supported metal clusters. *J. Am. Chem. Soc.* (1998) 120: 9668–9671. doi:10.1021/ja981181w.
- [9] E. C. Tyo, S. Vajda. Catalysis by clusters with precise numbers of atoms. *Nat. Nanotechnol.* (2015) 10: 577–588. doi:10.1038/nnano.2015.140.
- [10] T. Gerber, E. Grånäs, U. A. Schröder, P. Stratmann, K. Schulte, J. N. Andersen, J. Knudsen, T. Michely. Stability and reactivity of graphene-templated nanoclusters. *J. Phys. Chem. C* (2016) 120: 26290–26299. doi:10.1021/acs.jpcc.6b07828.
- [11] A. T. N'Diaye, S. Bleikamp, P. J. Feibelman, T. Michely. Two-dimensional Ir cluster lattice on a graphene moiré on Ir(1 1 1). *Phys. Rev. Lett.* (2006) 97: 215501. doi:10.1103/physrevlett.97.215501.
- [12] U. Heiz, F. Vanolli, L. Trento, W.-D. Schneider. Chemical reactivity of size-selected supported clusters: An experimental setup. *Rev. Sci. Instrum.* (1997) 68: 1986–1994. doi:10.1063/1.1148113.
- [13] D. A. McQuarrie. Handbook of mathematical functions. *Am. J. Phys* (1966) 34: 177–177. doi:10.1119/1.1972842.
- [14] P. E. Miller, M. B. Denton. The quadrupole mass filter: Basic operating concepts. *J. Chem. Educ.* (1986) 63: 617. doi:10.1021/ed063p617.
- [15] Y. Huang, S. Guan, H. S. Kim, A. G. Marshall. Ion transport through a strong magnetic field gradient by r.f.-only octupole ion guides. *Int. J. Mass Spectrom. Ion Processes* (1996) 152: 121–133. doi:10.1016/0168-1176(95)04334-9.
- [16] M. A. Röttgen, K. Judai, J.-M. Antonietti, U. Heiz, S. Rauschenbach, K. Kern. Conical octopole ion guide: Design, focusing, and its application to the deposition of low energetic clusters. *Rev. Sci. Instrum.* (2006) 77: 013302. doi:10.1063/1.2162439.
- [17] A. Adams, F. H. Read. Electrostatic cylinder lenses II: Three element einzel lenses. *J. Phys. E* (1972) 5: 150–155. doi:10.1088/0022-3735/5/2/019.
- [18] H. D. Zeman. Deflection of an ion beam in the two-dimensional electrostatic quadrupole field. *Rev. Sci. Instrum.* (1977) 48: 1079–1085. doi:10.1063/1.1135188.

# Conclusion

In conclusion, the results presented in this work provide wide evidence on the fundamental role played by the substrate supporting Gr on its interaction with adsorbed species and on the properties of those.

More specifically, we have firstly proven that the interaction between Gr and metal substrates is originated by the coupling between the  $d$ -band of the latter and the  $\pi$  bands of the former. We have then shown how the alterations induced by this process to the band structure and charge distribution of Gr causes significant modifications in its interaction with adsorbed species, for the case of physisorbed atoms and molecules.

Following these results, we have investigated a variety of Gr-based systems where this interplay between the interaction of Gr with the substrate and with its adsorbates plays an important role. In particular, we have shown how this interplay has a remarkable effect on the response of magnetic molecules deposited on Gr supported on a cobalt interface, thanks to a super-exchange process involving the mixing of the bands of Gr with both the  $d$ -band of the substrate and the  $d$  orbitals of the molecules. Another example of the role of the substrate supporting Gr was demonstrated for the case of nanostructured photocatalysts deposited on this material. In fact, we have shown that decoupling Gr from its substrate by intercalation of an oxide layer leads to a remarkable enhancement of their reactivity. Our results suggest that this phenomenon can be again explained by the charge transfer and redistribution induced into Gr by its substrate.

Finally, we have shown that the interaction of Gr with its adsorbates plays an important role even during its synthesis. In fact, we have proven that the growth dynamics of Gr are strongly influenced by the interaction of the precursors used for its growth with the still-expanding islands.

In summary, the work presented here demonstrates that the interaction of Gr with its substrate is deeply interconnected with that of Gr with its adsorbates, and that this interplay plays an important role in many processes occurring on Gr. This understanding provides a tool for predicting and tuning the properties of Gr-based systems, for a wide range of applications.

The most intriguing future development of my research work is the study of the properties of nanoclusters deposited on Gr, which has proven a very promising substrate for nanostructured materials. In fact, these nanostructured materials display even more remarkable properties than the nanoparticles I have investigated in this work, as they can be significantly modified and tuned by selecting the number of atoms composing them. In order to be able to synthesise and characterise these very intriguing systems, as well as their interaction with their Gr substrate, and to investigate the dependence of their properties on their size, we have recently commissioned a mass-selected nanocluster source, as described in this work. In the near future, we intend to combine this instrument with the SuperESCA beamline at Elettra-Sincrotrone Trieste, in order to proceed to a new phase of this project: the characterisation of mass-selected nanoclusters by a combination of spectroscopic experimental techniques exploiting the unique properties of synchrotron radiation.



# Publications

## Published on peer-reviewed journals

1. F. Presel, N. Jabeen, M. Pozzo, D. Curcio, L. Omiciuolo, P. Lacovig, S. Lizzit, D. Alfè, A. Baraldi. Unravelling the roles of surface chemical composition and geometry for the graphene-metal interaction through C 1s core-level spectroscopy. *Carbon* (2015) 93: 187-198.
2. F. Presel, C. A. Tache, H. Tetlow, D. Curcio, P. Lacovig, L. Kantorovich, S. Lizzit, A. Baraldi. Spectroscopic Fingerprints of Carbon Monomers and Dimers on Ir (1 1 1): Experiment and Theory. *J. Phys. Chem. C* (2017) 121: 11335-11345.

## In preparation

1. F. Presel, E. R. Hernandez, D. Alfè, P. Lacovig, S. Lizzit, A. Baraldi. Not a real transparency: indirect mechanism for substrate-induced increase in the adsorption energy of molecules on graphene. Submitted.
2. H. Bana, E. Travaglia, L. Bignardi, P. Lacovig, C. E. Sanders, M. Dendzik, M. Michiardi, M. Bianchi, N. Apostol, D. De Angelis, F. Presel, P. K. Das, J. Fujii, I. Vobornik, R. Larciprete, A. Baraldi, P. Hofmann, S. Lizzit. Synthesis of Single-Orientation High-Quality MoS<sub>2</sub> Monolayers with Complete Spin Polarization. Submitted.
3. F. Presel, H. Tetlow, C. A. Tache, L. Bignardi, P. Lacovig, L. Kantorovich, S. Lizzit, A. Baraldi. Factors governing single- and multi-layer graphene growth on Ir (1 1 1) from a solid state carbon source. In preparation.
4. D. De Angelis, F. Presel, N. Jabeen, L. Bignardi, D. Lizzit, P. Lacovig, S. Lizzit, T. Montini, P. Fornasiero, A. Baraldi. Titania/graphene nanoarchitectures for enhanced photocatalytic activity. In preparation.



# Acknowledgements

This thesis represents the conclusion of an experience which has taken up a significant part of the past three years of my life. In this last page, I would like to thank all the people who have supported me during this period and have contributed to make this experience so positive.

Firstly, I would like to express my most heartfelt gratitude to my Supervisor Alessandro Baraldi, not only for giving me the opportunity to work on this stimulating project and always providing guidance and motivation to my work: I would also like to thank him as a person, for always being available and ready to help when needed, even in difficult times, and for his friendship and earnestness. I am also truly grateful for his fundamental role in my growth as a scientist. Thank you for all!

I would also like to sincerely thank my former and present colleagues at the Surface Science Laboratory, in particular Luca, Davide and Dario, for their friendship, helpfulness and stimulating discussions, but also Naila, Cristian, Gian and Luca, as well as the SuperESCA staff, Silvano, Paolo, Luca, Daniel, Harsh and Betta, for their invaluable assistance during our beamtimes and fruitful discussions. I am very grateful to our technician Eugenio for his invaluable help in the development of the cluster source.

My sincere thanks to Dr. Aras Kartouzian and Prof. Ueli Heiz, for providing me the opportunity to work on their cluster source at TUM, for teaching me about its operating principles, and for their precious hints and fruitful discussions during the whole design and commissioning phases of our cluster source. Many thanks to their whole research group for warmly welcoming me in Garching. I would like to also thank Prof. Betti for allowing me to take part in the intriguing research activity of her group and for introducing me to the magnetic properties of matter, and to Giulia for her precious help and stimulating discussions. Further thanks to all our national and international collaborators who have provided a fundamental contribution to my research work, including the research groups of Prof. Alfè at UCL, Prof. Kantorovich at KCL, Eduardo Hernández at CSIC and Prof. Fornasiero at the University of Trieste.

Thanks to my office mates with whom I have spent much of my time at Elettra, for your patience and for always keeping the atmosphere so nice – Betta and Harsh *in primis*, Clara, Vero, Matteo –, and thanks to all the other people who have made my work at Elettra more pleasant.

A special thanks goes to my friends, and in particular to the “Physicists Worth Knowing” friends from the University, with whom I have spent a good part of my time in the past few years.

Last but not least, I would like to express my most heartfelt gratitude to my family, for their constant love and support. I would never have arrived here without your constant help and backing.

The contribution of all of you has been fundamental in shaping different aspects of my past three years.